Modeling and characterization of the effects of nanocompliance for localized epitaxial growth of GaN on Si substrates.

Maya Wehbe

THÈSE

Pour obtenir le grade de

DOCTEUR DE L'UNIVERSITÉ GRENOBLE ALPES

École doctorale : PHYS - Physique
Spécialité : Physique de la Matière Condensée et du Rayonnement
Unité de recherche : Laboratoire d'Electronique et de Technologie de l'Information (LETI)

Modélisation et caractérisation des effets de nanocompliance pour la croissance épitaxiale localisée de GaN sur substrats Si.

Modeling and characterization of the effects of nanocompliance for localized epitaxial growth of GaN on Si substrates.

Présentée par :

Maya WEHBE

Direction de thèse :

Patrice GERGAUD DIRECTEUR DE RECHERCHE, CEA – Centre de Grenoble	Directeur de thèse
Daniel PINO MUÑOZ Chargé de Recherche, Mines Paris – PSL	Co-encadrant de thèse
Matthew CHARLES DIRECTEUR DE RECHERCHE, CEA – Centre de Grenoble	Co-directeur de thèse

Rapporteurs :

Stéphanie ESCOUBAS
PROFESSEURE DES UNIVERSITES, Aix-Marseille Université
Nicolas GRANDJEAN
FULL PROFESSOR, École Polytechnique Fédérale de Lausanne

Thèse soutenue publiquement le **29 novembre 2024**, devant le jury composé de :

Vincent CONSONNI, DIRECTEUR DE RECHERCHE, CNRS Délégation Alpes	Président
Stéphanie ESCOUBAS, PROFESSEURE DES UNIVERSITES, Aix-Marseille Université	Rapporteure
Nicolas GRANDJEAN, FULL PROFESSOR, École Polytechnique Fédérale de Lausanne	Rapporteur
Stephane MOREAU, INGENIEUR DE RECHERCHE, CEA – Centre de Grenoble	Examinateur
Maud NEMOZ, INGENIEURE DE RECHERCHE, CNRS Délégation Côte d'Azur	Examinatrice
Eirini SARIGIANNIDOU, PROFESSEURE DES UNIVERSITES, Grenoble INP – UGA	Examinatrice

To My Mother and Father

For Their Endless Love

Acknowledgments

First, I would like to thank the jury members, Prof. Nicolas Grandjean, Prof. Stéphanie Escoubas, Prof. Eirini Sarigiannidou, Dr. Vincent Consonni, Dr. Maud Nemoz and Dr. Stephane Moreau for accepting to review this PhD work and providing insightful feedback.

It has been an enriching experience to have my three PhD supervisors, each expert in a distinct discipline. I would like to thank my PhD director Patrice Gergaud for his knowledge, wisdom and guidance. I thank my co-supervisor Matthew Charles for his support, leadership and positivity. And, I want to thank my co-supervisor Daniel Pino Muñoz for his guidance, kindness, and constant encouragement.

The dedicated efforts of the PEGADIS team members from the four laboratories CEA, CEMEF, LTM and CRHEA has been crucial in shaping the outcome of this thesis, so I would like to thank the entire team for all the hard work in preparing the greatest samples of all time and for all the insightful discussions we had.

I would also like to thank Alexis Nicolaÿ from CEMEF for his help and advice during the EBSD measurements.

During these three years, I had the enriching opportunity to work with inspiring scientists from the ESRF who provided me with invaluable assistance both during and after the experiment. Thank you to Edoardo Zatterin from ID01 beamline, Can Yildirim from ID06 and Gilbert Chahine from BM02.

My sincere thanks to all my friends and colleagues from CEMEF and CEA for all the good moments spent together. Paul Martin, “j’en ai ras la casquette” ;) it was a journey full of memories, thank you for all the laughs that made it this much enjoyable. To Cynthia, Eliane and Joya, my sincere thank you for the love and support you have given me!

To my best friend Rim, thank you for your unconditional love and support! To my valuable friend Jana, thank you for encouraging me with your wisdom! To Jimmy and Maroun, a sincere appreciation for your constant encouragement since day one.

Finally, to my sisters and my best friends, Maria and Lea, thank you for consistently listening to me, for being so proud of me, and for loving me during the highs and lows of this ride! To my parents, thank you for guiding me, and encouraging me every single day, this work is the fruit of your endless love. As I take on new challenges, your love will always guide me back to what truly matters in this “life”.

Maya

Table of Contents

List of Acronyms **1**

General Introduction **2**

Chapter 1 : Fundamentals of GaN **4**

1.1 III-Nitride materials characteristics **4**

1.1.1 Crystalline Structure *4*

1.1.2 Optoelectronic properties and applications *6*

1.1.3 Polarity *7*

1.2 Crystal defects **8**

1.2.1 Point defects *9*

1.2.2 Line defects *9*

1.2.3 Planar defects *12*

1.3 Stress and strain distribution in the epitaxial layer **13**

1.3.1 Stress distribution *13*

1.3.2 Strain distribution *17*

1.4 Challenges facing GaN growth on foreign substrate **18**

1.4.1 Melt-back etching *19*

1.4.2 Cracking of the GaN epitaxial layer *19*

1.4.3 Dislocations density *20*

1.5 Growth approach studied in this thesis **23**

1.5.1 Motivation behind the proposed growth approach *23*

1.5.2 Objectives of this thesis *26*

1.5.3 Nanopillars etching process *27*

1.5.4 GaN platelet epitaxy process *29*

Chapter 2 : Characterization techniques **33**

2.1 Introduction **33**

2.2 Basics of X-ray diffraction **33**

2.2.1 Synchrotron X-ray *33*

2.2.2 Bragg diffraction *36*

2.2.3 Diffraction in reciprocal Space *37*

2.2.4 Different scan types and measurement geometries *40*

2.3 Synchrotron X-ray diffraction techniques **43**

2.3.1 Macroscopic X-ray diffraction technique: BM02 ..... *43*

2.3.2 Dark field X-ray microscopy: ID06 ..... *45*
2.3.3 Scanning X-ray diffraction microscopy: ID01 ..... *50*
2.4 Electron backscatter diffraction technique **57**
2.4.1 Set up and description of the technique *57*
2.4.2 Post-processing tool *60*
2.5 Scanning electron microscopy **62**
2.6 Cathodoluminescence microscopy **63**
2.7 Conclusion **64**
Chapter 3 : Experimental assessment of pillars rotation and GaN quality 65
3.1 Introduction **65**
3.2 Verification of the pillar's rotation in a set of three pillars **65**
3.2.1 Orientation of coalesced GaN lines *65*
3.2.2 Orientation of the corresponding Si pillars underneath the GaN lines *73*
3.3 Evolution of the epitaxial GaN from pillars to coalesced domains **76**
3.3.1 Reference sample: crystalline orientation of GaN pillars before coalescence *76*
3.3.2 Reorientation of the GaN during coalescence *78*
3.3.3 Grain boundaries formation at the early stage of coalescence *79*
3.3.4 Validation by EBSD measurements *81*
3.3.5 Geometrically necessary dislocations *83*
3.3.6 Testing model to compute the tilt between neighboring pillars *85*
3.4 Demonstration of highly oriented GaN lines on top of a set of ten pillars **89**
3.4.1 Crystalline GaN orientation *89*
3.4.2 Dislocation density in the GaN lines *91*
3.5 Promising results of small highly oriented islands of GaN on Si suitable for µLEDs 92
3.5.1 Measurements of the quality of GaN platelets up to 40 x 40 µm² *92*
3.5.2 Growth through cluster formation *94*
3.5.3 Measurement of the pillar's rotation on a macro scale *95*
3.6 Conclusion **96**
Chapter 4 : Finite element mechanical modeling of GaN pillars coalescence 98
4.1 Introduction **98**
4.2 Modeling of the test model **100**
4.2.1 Purpose of the test model *100*
4.2.2 Geometrical model and boundary conditions *100*
4.2.3 Limitations of the model *102*

4.2.4 Mechanical anisotropic properties *103*
4.2.5 Validation of the model *105*
4.3 Modeling of the twist and tilt of GaN hexagons **106**
4.3.1 Purpose of simulating the hexagons rotation *106*
4.3.2 Testing different twist approaches *107*
4.3.3 Twist and Tilt model *114*
4.4 Computation of the rotation energy **116**
4.4.1 Purpose of computing the rotation energy *116*
4.4.2 Energetic feasibility of the experimental tilt results *116*
4.4.3 Optimization of the pillars pitch *120*
4.4.4 Optimization of the GaN thickness *121*
4.5 Analytical study of pillars rotation **122**
4.5.1 Twist case *122*
4.5.2 Tilt case *125*
4.6 Conclusion **128**
Chapter 5 : New perspectives from optimization of pillars **129**
5.1 Introduction **129**
5.2 Towards new promising pillars pattern **129**
5.2.1 Study of GaN reorientation within a star-shaped pillars pattern *129*
5.2.2 Study of GaN reorientation within a spiral-shaped pillars pattern *133*
5.3 Conclusion and perspectives **135**
General Conclusion **138**
Scientific Communications and Award **140**
Bibliography **141**
Résumé **148**

List of Acronyms

SEM	Scanning electron microscopy
CL	Cathodoluminescence
AFM	Atomic force microscopy
EBSD	Electron backscatter diffraction
XRD	X-ray diffraction
FWHM	Full width at half maximum
DFXM	Dark field X-ray diffraction microscopy
SXDM	Scanning X-ray diffraction microscopy
COM	Center of mass
CRL	Compound reflective lens
ROI	Region of interest
VOI	Volume of interest
LED	Light emitting diode
ELOG	Epitaxial lateral overgrowth
PE	Pendo-epitaxy
MOVPE	Metal organic vapor phase epitaxy
NIL	Nanoimprint lithography
TD	Threading dislocation
GROD	Grain reference orientation deviation
GND	Geometrically necessary dislocation
EBSP	Electron backscatter pattern
FEM	Finite element method
BC	Boundary condition

General Introduction

The market for high-resolution micro-displays has experienced rapid growth, particularly for micro light-emitting diodes (µLEDs) with better emission properties than traditional LEDs. This growth is driven by the increasing demand for enhanced visual technologies in applications such as virtual and augmented reality, wearables, smart devices, and automotive displays. III-Nitride semiconductors such as Gallium Nitride (GaN) are extremely attractive materials for µLEDs due to their exceptional optoelectronic properties. The high requirements for display applications demand high emissive efficiency of the nitride based µLEDs, which pose significant challenges in the fabrication process. The emissive efficiency significantly decreases when the chip undergoes a top-down based process to reduce its size from a few hundreds of µms down to a few µms. Furthermore, the dislocation density of the initial epitaxial wafer determines that of the µ-LEDs active layers, which might also affect its emissive efficiency.

This thesis is part of a project called PEGADIS (Pendeo-Epitaxy of GaN for µDisplays) that proposes an innovative growth approach of GaN on SOI (Silicon-On-Insulator) substrate that overcomes these important technological issues and thus, allows the fabrication of low dislocation density GaN based µLEDs. The proposed method consists of growing non-doped GaN layers on top of GaN/AlN/Si(111)/SiO_2 etched nanopillars on SOI substrate, and expects the pillars to rotate so that the GaN on the top align, to achieve a high quality GaN layer. This is then followed by the growth of the active layers. The low mechanical strength of the pillars after growth should facilitate µLED transfer. The PEGADIS project is funded by the National Research Agency (ANR) and is a collaboration among four laboratories: LTM (Laboratoire des technologies de la microélectronique) for the sample patterning part, CRHEA (Centre de recherche sur l'hétéro-épitaxie et ses applications) for the growth part of the material, CEA-LETI (Laboratoire d'électronique et de technologie de l'information) for the fabrication and characterizations of µ-LEDs and CEMEF (Centre de mise en forme des matériaux) for the numerical mechanical simulations part.

This PhD work was performed at CEA and CEMEF; it aims at performing nano-characterization of the epitaxial non-doped GaN layer grown on top of the nanopillars for a better understanding of the phenomena taking place during the process of nano-pendeo epitaxy in order to control it and improve the quality of the epitaxial GaN layers. The characterization primarily employed advanced X-ray diffraction techniques at the European Synchrotron Radiation Facility (ESRF). Finite element simulations were also conducted to assess the mechanical behavior of the nano-structured systems and optimize different pillars parameter. This thesis is organized into five chapters, outlined as follows:

The first chapter provides a description of the essential physical properties of GaN and the concept of GaN based µLEDS necessary for a good understanding of the manuscript. It

introduces the concept of defects obtained in crystals during epitaxy and the different challenges facing GaN growth on foreign substrate. The most common growth techniques that help reducing defect density are then presented followed by a description of the growth technique proposed in PEGADIS, the objectives of this thesis and lastly the etching and growth procedures.

The second chapter presents the various characterization techniques employed in this thesis (macroscopic X-ray diffraction, dark field X-ray microscopy, scanning X-ray diffraction microscopy, electron backscatter diffraction, scanning electron microscopy and cathodoluminescence microscopy). It introduces the potential as well as the limitations of each one, followed by detailed description of the data processing performed after each experiment. Numerous experiments were carried out at the synchrotron, so this chapter covers also the fundamentals of X-ray diffraction and synchrotron facilities.

The third chapter discusses the results of the experimental characterization work. It provides an assessment of the pillars rotation and the GaN quality at different growth stages and on various types of samples.

The fourth chapter covers the findings obtained from finite element simulations using Abaqus software. It defines a test model, introduces its boundary conditions, the mechanical properties of each material and its limitations. Once the test model is validated, it introduces different approaches to model the mechanical rotation of the pillars for energy calculations to provide an explanation for the pillars maximum rotation values acquired from the experimental data. These numerical results allowed to propose a simplified analytical model that allows to determine the impact of the pillar's physical parameters on the maximum energetically possible nanopillar rotation.

The fifth chapter addresses the conclusions and perspectives that this work has produced. It proposes new optimized samples that had promising primary characterization results. Based on the findings, this chapter outlines three key elements that can be developed to optimize the proposed growth approach and produce high quality GaN layers suitable for µLEDs.

Chapter 1: Fundamentals of GaN

1.1 III-Nitride materials characteristics

1.1.1 Crystalline Structure

Crystalline materials have atoms arranged periodically in all three dimensions and the III-Nitride materials crystals such as GaN, AlN, InN are formed by equal parts of group-V atoms (nitrogen atoms in this case) and group-III atoms (Ga, Al, In...). Cubic zinc-blende, rock-salt and the hexagonal wurtzite are the three distinct structures that III-N materials and their ternary and quaternary alloys can crystallize into depending on the growth conditions. The zinc-blende structure occurs when III-N materials are grown on cubic substrates like GaAs(001), Si(001) or MgO [1]. The rock-salt structure, can only be induced under very high pressure conditions (> 30 GPa) unreachable during epitaxial growth [2] which makes it unsuitable for industrial applications [3]. The wurtzite structure is the most thermodynamically stable at ambient conditions [4] and is generally preferred. It has a hexagonal lattice system that consists of two interpenetrating hexagonal sublattices as shown in figure 1.1. The hexagonal wurtzite sublattice of gallium (the group III atom considered in this study) is colored in black with gallium (Ga) atom colored in red and the hexagonal wurtzite sublattice of nitrogen is colored in orange with nitrogen (N) atom colored in blue. The nearest neighbor bonds are indicated by purple lines and for simplicity, the atoms displayed are limited to only one unit cell.

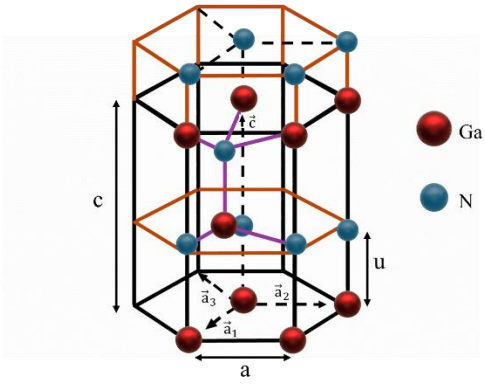

Figure 1.1: Illustration of one unit cell of GaN wurtzite structure inside two interpenetrating hexagonal sublattice.

The GaN wurtzite structure has four unit vectors: $\overrightarrow{a_1}$,$\overrightarrow{a_2}$, $\overrightarrow{a_3}$ of the same length $|\overrightarrow{a_1}|$ =$|\overrightarrow{a_2}|$ =$|\overrightarrow{a_3}|$ =a = 3.189 Å and an orthogonal vector $\vec{c}$ with $|\overrightarrow{c}|$= c= 5.185 Å [5] at ambient temperature (T) where a and c are defined as lattice parameter referring to the length of the uFnit cell in the basal plane and in the c-plane respectively. The angle between the basal unit vectors is 120° and

the basal vectors are perpendicular to the c axis. The two sub-lattices are shifted by u = $\frac{3c}{8}$ from each other along the c-axis. The atoms planes of Ga and N alternate to form an ABAB type stack.

For the cubic, tetragonal and orthorhombic structures, the crystallographic planes in a crystal lattice are described by three Miller indices (h k l) such that (h, k, l) = n*($\frac{1}{x_0}$, $\frac{1}{y_0}$, $\frac{1}{z_0}$) where x_0, y_0 and z_0 are the interception made by the plane with each unit cell of the three axis $\vec{a_1}$, $\vec{a_2}$ and $\vec{c}$ with (h k l) being a combination of the smallest integer possible. On the other hand, crystallographic directions are written in square brackets as [u v w] where u, v and w are the coordinates of the vector parallel to the crystallographic direction in the three-axis system. In the cubic system a [u v w] direction is always normal to the corresponding (h k l) plane which means h=u, k=v and l=w. Equivalent directions are those related by symmetry and are written with angle brackets ⟨u v w⟩ representing an identical direction family and equivalent planes are expressed in curly brackets{h k l} representing an identical plane family. For example, in the cubic system, six different directions belong to the same directional family <100>: [100], [010], [001], [$\bar{1}$00], [0$\bar{1}$0] and [00$\bar{1}$]. We note that the negative indices are noted with a bar over the number (e.g. -1 is denoted $\bar{1}$). It is important to note that when we are using the ⟨h k l⟩ notation we must be aware of the type of crystal system we are working with, as different crystals have varying symmetry.

For the III-N crystals with a hexagonal structure, four indices [u' v' t' w'] Miller-Bravais notation [6] is frequently used to represent directions and planes and this because the Miller indexation in hexagonal systems does not allow a correct distinction of the directions and planes families, and does not clearly show the symmetry of the planes and directions. The relationship between a three-axis system and a four-axis system for the crystallographic directions is given by [6]:

- u'= $\frac{1}{3}$ (2u-v)
- v'= $\frac{1}{3}$ (2v-u)
- t'= - (u+v)
- w'=w

The planes in this four-axis system are indexed as (h' k' i' l') where h' k' and l' are the same as in the three-axis system which means h'=h, k'=k and l'=l and i' is defined as i'= - (h'+ k'). Using the Miller-Bravais notation, the crystallographic directions in the basal plane of a hexagonal crystal are shown in figure 1.2.

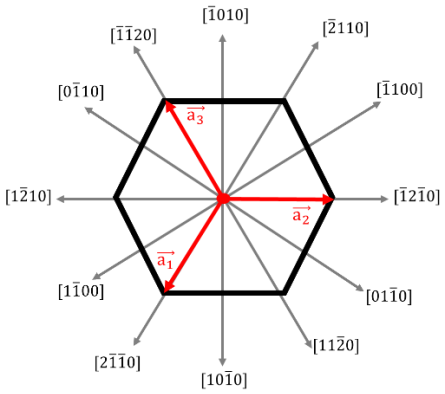

Figure 1.2: Crystallographic directions in the basal plane of a hexagonal crystal in the four-axis system.

1.1.2 Optoelectronic properties and applications

Optoelectronic devices (emitters, detectors) based on III-V semiconductors, provide distinct benefits such as low power consumption, high quantum efficiency, increased speed, lower lasing threshold, and lower cost [7]. GaN is a wide bandgap III-V semiconductor commonly used in light emitting diodes (LEDs) which fabrication began in 1927, thanks to the work of Oleg Losev [8] but it was not very bright and was not suitable for any application. In 1962, Nick Holonyak Jr. [9] invented the first practical LED, emitting red light. From there, continuous efforts and studies were made over the years to finally fabricate LEDs in all colors, leading to a blue light emitting LED by Nakamura et al. [10], achieved with the growth and activation of good quality p-doped GaN layers [11][12]. From this it was possible to obtain white LEDs.

A new application for GaN semiconductors has emerged and studies are ongoing to produce highly efficient micro-light emitting diodes (µLEDs) based on GaN. MicroLEDs are LEDs with small dimensions, and if they are used as pixels, they can reach high resolution due to their size reduction. µLEDs can be used in large number of applications mainly in micro-display applications which cover not only the conventional displays such as projection displays and small displays for cameras but also newly coming-up displays, such as smart watches, virtual reality (VR) and augmented reality (AR) products where pixel size reduction is necessary [13]. They can also be spaced out and used in macro-scale screens. Compared to other technologies used in the field of micro-display applications such as liquid-crystal display (LCD) on silicon, organic light-emitting diode (OLED), semiconductor µLEDs present better performance in contrast, response time luminance, efficiency, power consumption and lifetime [14][15]. However they present technological challenges like low external quantum efficiency (EQE), in particular due to the defects created at their edges during etching [15][16][17]. MicroLEDs have a size of 10 to 30 µm [18] while the standard size was 300 x 300 µm² for indicators and 1

x 1 mm² for power LEDs used for lighting [19]. In this thesis, we will study GaN samples grown using an original approach that we propose in order to fabricate high quality GaN layers suitable for µLED without requiring any pixel etching procedure. The proposed growth approach will be introduced and explained in section 1.5.

GaN is a very promising semiconductor highly relevant for µLEDs due to its electronic properties and particularly its optoelectronic properties. It has a direct and wide band gap (3.4 eV in contrast to the Si band gap that is 1.1 eV [20]) which means that it can efficiently emit light when electrons in the conduction band recombine with holes in the valence band. It also has the possibility to emit from ultraviolet to near red in the 400–625 nm range by incorporating indium (In),and creating InGaN quantum wells with different alloy compositions. The n-type layers typically use Si doping p-type layers Mg doping.

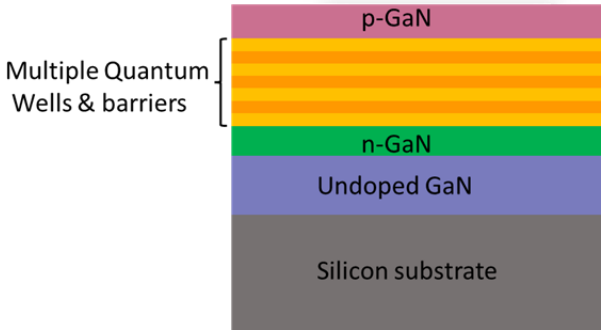

Figure 1.3: Schematic structure of multiple quantum wells grown on top of epitaxial GaN.

The multiple quantum wells (MQW) are located in the active region that emits light. One quantum well consists of a thin layer of InGaN with low bandgap energy positioned between two layers of GaN serving as barriers layers with greater bandgap energy. (The bandgap energy equal to the difference between the maximum of the covalence band and the minimum of the conduction band). The electrons and holes are confined in these QWs increasing their probability of recombining. After epitaxial growth, various etching, metallization, and separating processes are performed to manufacture the µLED.

It is interesting to note that gallium nitride is also suitable for high power devices because it has a large critical breakdown field of 4.0 MV cm^{-1} [21], high electron mobility enabling faster switching speeds and it can withstand the high temperatures associated to high power electronics because of its high thermal conductivity. However, this study is focused principally on the development of GaN layers for µLEDs.

1.1.3 Polarity

The polar planes in GaN wurtzite are the planes that possess a net electric dipole moment due to an unequal distribution of charges. These planes are characterized by having different

numbers of gallium and nitrogen atoms on their surfaces, resulting in an asymmetrical arrangement. The presence of a dipole moment in these planes is then caused by the difference in electronegativity between the cations (gallium in our case) and the anions (nitrogen), the induced dipole moment is oriented from anions toward cations. In wurtzite GaN, the polar plane is the (0001), also known as the c-plane. The non-polar planes are those with zero net electric dipole moment due to the cancellation of the individual dipole moments associated with the bonds between atoms [22]. Two important non-polar planes in GaN wurtzite are the $(10\bar{1}0)$ plane and the $(11\bar{2}0)$ known also as the m-plane and a-plane respectively. In addition, semi-polar planes are present in GaN and they are characterized by having an intermediate degree of polarity, meaning they possess a partial electric dipole moment. Figure 1.4 shows polar, semi-polar and non-polar planes in the III-nitrides material.

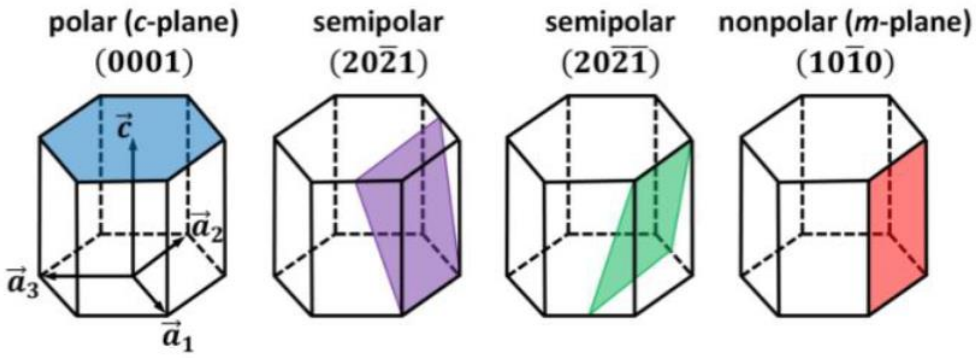

Figure 1.4: Schematic of different crystallographic planes in III-nitrides material. The figures are taken from reference [23].

In this thesis, the growth of GaN has been produced along the c axis, therefore we will have a polar growth for all the studied samples.

1.2 Crystal defects

The arrangement of the atoms in the III-N semiconductors contains imperfections and local deviations from the perfect lattice due to the growth conditions and methods. These defects can have a profound effect on the behavior of the materials, and they can be sorted into three main types:

- Point defects (vacancies, interstitial defects, and substitution defects)
- Line defects (screw dislocations, edge dislocations, mixed dislocations, and misfit dislocations)
- Planar defects (stacking faults, and grain boundaries)

1.2.1 Point defects

Point defects occur commonly in semiconductors and they are manifested by a local perturbation at the atomic scale of the atomic sequence. They may be unintentionally present, or deliberately introduced to achieve certain properties.
Points defects can be classified into three categories (figure 1.5):

- Interstitial: an extra atom is inserted between the lattice sites at a normally unoccupied position.
- Substitutional: a cation sitting on an anion site, or vice versa
- Vacancy: an atom missing from the lattice normal site.

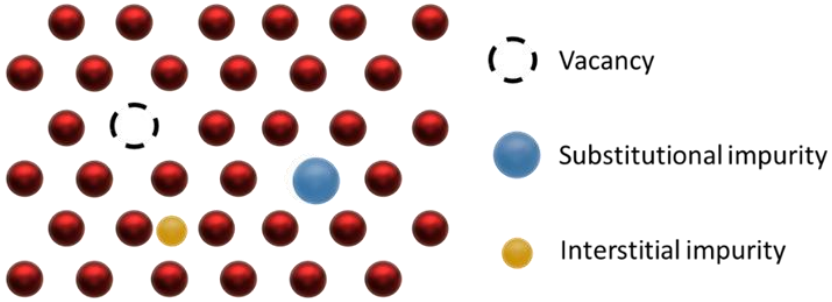

Figure 1.5: Schematic representation of the three types of point defects.

These defects can strongly affect the electrical and optical properties of the semiconductors:

- The electronic conductivity in semiconductors is controlled by substitution defects: a doped atom with a different number of valence electrons compared to the host semiconductor will substitute a host atom in the crystal and therefore will introduce more or less deep energy levels in the band gap of the semiconductor which will increase its conductivity [24]. To obtain n-type doped GaN, which means to have an extra electron, Si can be used, while for p-type GaN, which means to have extra hole, Mg can be introduced.
- Diffusion and the ionic conductivity are facilitated by the presence of vacancies.

1.2.2 Line defects

One-dimensional defects are known as dislocations. They are defined by a line vector “l” and Burgers vector “b” [25]. The Burgers vector describes the magnitude and direction of the lattice distortion resulting from a dislocation in a crystal lattice - it is the vector required to close an atomic drawn around the dislocation. The line vector represents the propagation direction of the dislocation.
Mis-fit dislocations are in plane dislocations that arise during epitaxy due to stress caused by the lattice mismatch at the interface between two materials and they might recombine into

threading dislocations. There are three types of dislocations: edge-type, screw-type and mixed dislocation:

- Edge-type dislocations originate from the insertion or removal of a partial plane of atoms from the crystal structure shown in green in figure 1.6(a). The area around the dislocation line is the most strained area where the atoms are shifted out of their natural equilibrium positions and causing a lattice distortion. Its Burgers vector is perpendicular to its line vector.
- Screw-type dislocations shown in figure 1.6(b) follows the shape of a helicoid and take place when the elastic limits of the crystal are surpassed due to high stress. Its Burgers vector and line vector are parallel to each other.
- Mixed dislocations are a combination of the screw and the edge dislocation. It has a Burgers vector with two components in the directions normal and parallel to the dislocation line.

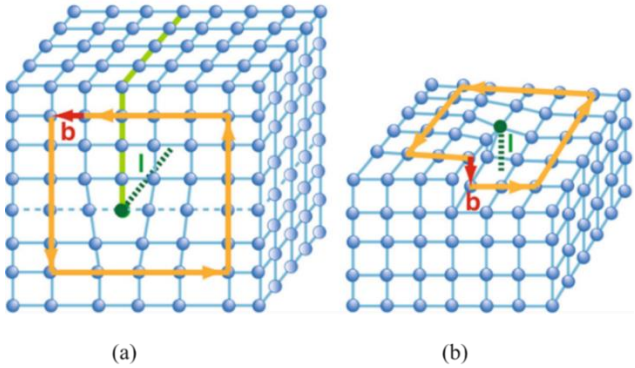

Figure 1.6: (a) An edge dislocation, the extra half plane of atoms is outlined in green, the dislocation line is the dashed line colored in green perpendicular to the Burgers vector $\vec{b}$ colored in red, and (b) screw dislocation with the Burgers vector $\vec{b}$ in red parallel to the dislocation line dashed in green. The Burgers vectors are one lattice spacing long and their construction paths are outlined in yellow. Both figures are taken from reference [26] .

The growth of GaN on GaN (homoepitaxy) is not very common as only small diameter GaN substrates are available and the GaN substrates are expensive [27]. Therefore, the growth of GaN on low-cost foreign substrates (sapphire, silicon and silicon carbide-heteroepitaxy) is more common. However, the growth of GaN on foreign substrates leads to the generation of defects such as dislocations in the GaN layer with high density in the order of 10^{10} cm² in the initial growth layers on silicon or sapphire. The growth of GaN on SiC is naturally better quality, due to the lower lattice mismatch, but SiC wafers are expensive.

The dislocations are mainly caused by the large lattice parameter mismatch between the film and the substrate, which will lead to strain generation in the epitaxial layer as it tries to conform to the substrate's lattice structure. If the strain becomes too large to be accommodated elastically, defects such as dislocations that will form in order to release some of the built-up strain.

It is not possible to grow directly GaN on Si, so we start with the growth of AlN on Si. The growth takes place through the formation of small AlN nucleation sites disoriented with respect to each other due to the lattice parameter mismatch that will introduce dislocations causing the nucleation sites to tilt or/and twist. When the nucleation sites coalesce, dislocations will be created at the grain boundaries to accommodate the misorientation present between adjacent grains (sites), these dislocations are referred to as threading dislocations (TDs). They grow through the developing layers in a direction normal to the growth surface as the epitaxy process advances to reach the active device layer.

For the [0001]-oriented (c plane) GaN films, the Burgers vectors of threading screw, edge and mixed dislocations are $b_{edge} = \frac{1}{3} < 11\bar{2}0 >$, b_{screw} = <0001> and $b_{mixed} = \frac{1}{3} < 11\bar{2}3 >$. The Burgers vector of the edge dislocation is parallel to $\vec{a}$ (parallel to the surface) with $|\overrightarrow{b_{edge}}|$ = a, the Burgers vector of the screw dislocation is parallel to $\vec{c}$ (normal to the surface). The mixed Burgers vector is the vector forming an intermediate angle between the screw and edge Burgers vectors with $|\overrightarrow{b_{screw}}|$ = c and $|\overrightarrow{b_{mixed}}| = \sqrt{a^2+c^2}$. The screw dislocations are the least present (2%) [28][29]. Figure 1.7 shows the three distinct groups of dislocations that coexist in hexagonal (0001) GaN layers.

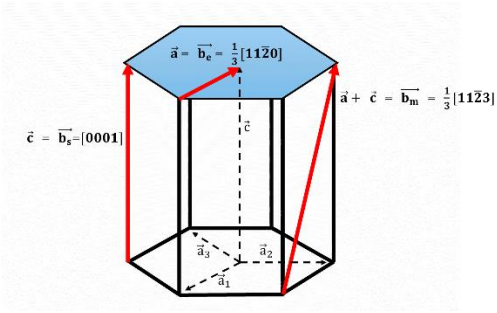

Figure 1.7: GaN and AlN Wurtzite structure presenting three Burgers vectors of a screw, edge and mixed dislocations: $\vec{a} = \overrightarrow{b_e} = \overrightarrow{b_{edge}}$, $\vec{c} = \overrightarrow{b_s} = \overrightarrow{b_{screw}}$ and $\vec{a} + \vec{c} = \overrightarrow{b_m} = \overrightarrow{b_{mixed}}$.

Dislocations must have defined start and end points, so they will either move though the crystal lattice to reach the surface or they will form closed loops [30]. This displacement of the dislocation occurs in a slip plane which is a plane containing its line and its Burgers vector and is the reason for plasticity of crystalline materials and has high atom density [31]. In hexagonal wurtzite structures, the most favorable GaN slip systems for the (a+c) -type dislocation are $\{10\bar{1}1\}$ <$11\bar{2}3$>, $\{11\bar{2}2\}$ <$11\bar{2}3$>, and for the a-type dislocation are {0001} <$11\bar{2}0$> [32][33].

These dislocations cause a degradation in the emission efficiency of LEDs. In the GaN, the non-radiative coefficient “A” related to the Shockley-Read-Hall (SRH) mechanism and which represents the rate at which charge carriers (electrons and holes) recombine non-radiatively through defects in the material was shown to increase with the increase of the dislocations densities: from 6 x 10^8 s^{-1} to 2 x 10^8 s^{-1} for dislocation densities ranging from 5.3 x 10^8 cm^{-2} to 5.7 x 10^8 cm^{-2} [34][35]. This leads to a reduction of the internal quantum efficiency (IQE) which

determines the ratio between the number of radiative recombination over the sum of all recombination and a thus reduction in the light emission efficiency of the µLED as seen in figure 1.8. There have been numerous methods implemented to lower the dislocation density in the epitaxial films; these methods will be discussed in section 1.4.

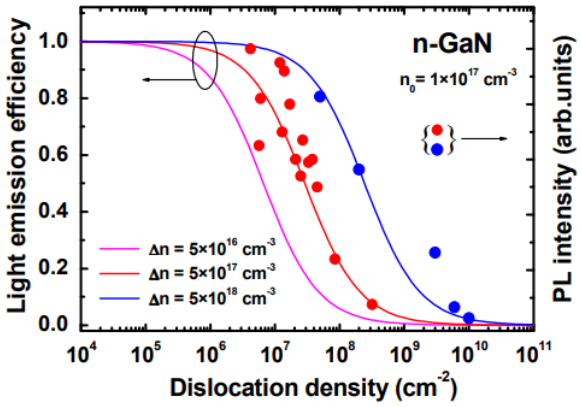

Figure 1.8: (a) Light emission efficiency in GaN for different non-equilibrium carrier concentrations (lines, left axis) and the PL intensity (circles, right axis) as a function of dislocation density [36].

It is therefore crucial to reduce the density of dislocations to values around 1 x 10^8 cm^{-2} in the epitaxial GaN layers for photo emission applications such as LEDs. Therefore, in the thesis, a study of the quality of the GaN thin films obtained with the proposed growth approach will be presented and discussed, to confirm the ability to grow high quality GaN layers with low dislocation densities.

1.2.3 Planar defects

Planar defects are due to a two-dimensional atom deviation from their initial site. There are different forms of planar defects: basal-plane stacking faults (BSFs) and grain boundaries.

- Basal-plane stacking faults interrupt the ideal stacking sequence (ABAB hexagonal closed pack stacking) along the c-axis by inserting faulted planes to the stacking rules and therefore the face-centered cubic close packed ABCABC sequence will be obtained. They can be detected by photoluminescence and cathodoluminescence since they are optically active [37]. This type of defect does not play a major role for c-plane GaN but is more common in semi-polar and non-polar GaN [38]. Hence, this type of defect will not be studied for the [0001]-grown layers characterized in this thesis.
- Grain boundaries are the interface that separates two adjacent crystalline regions that have different crystallographic orientation forming a polycrystalline material. They are formed during the growth process due to the mosaic structure of tiny crystalline regions and there are three types of grain boundary: tilt boundary, twist boundary and twin. The

tilt boundary is when the grains are bent away from an axis that is parallel to the grain boundary plane. As mentioned above, edge dislocations can be added so the extra planes fill the free part of the crystal (figure 1.9(a)). The twist boundary occurs when the grains undergo a rotation around an axis that is perpendicular to the grain boundary plane (figure 1.9(c)).

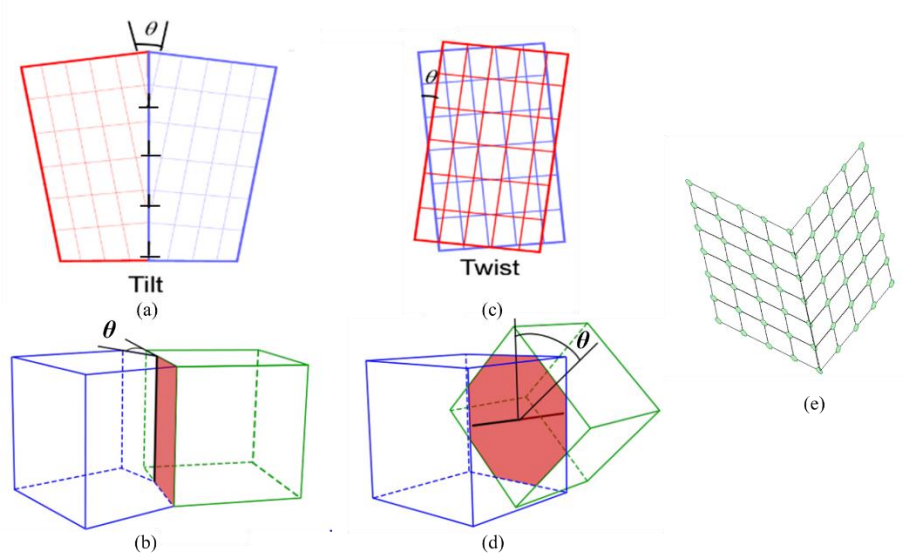

Figure 1.9: Schematic representation of (a) & (b) a tilt boundary, (c) & (d) a twist boundary, and (e) a twin boundary [39].

The twin Boundary is a single plane of atoms between two twinned crystals. It occurs when the crystals on both sides of a plane are mirror images of each other during crystallization, or due to a mechanical or thermal work. No disordered border is seen (figure 1.9(e)) and the boundary atoms can be viewed as belonging to the crystal structures of both twins. There is little information on the twins plane in GaN, the authors of [40] talk about twin boundary that is likely to appear in the GaN grown on the $(11\bar{2}0)$ plane. Therefore, grain boundaries in GaN are mainly a combination of tilt and twist boundary.

1.3 Stress and strain distribution in the epitaxial layer

1.3.1 Stress distribution

The precise description of the mechanical behavior of the crystalline material requires an understanding of two fundamental concepts: stress and strain at the crystal lattice scale. Stress refers to the internal resistance experienced by a material when subjected to an external force or load. Stress can cause the atoms or ions in a crystal lattice to shift from their equilibrium

positions, resulting in changes in the material's structure and properties. Stress can also exist within a material even in the absence of any external load, this type of stress is called residual stress, and it is commonly present in heteroepitaxial III-Nitride materials due to the difference in lattice parameter and CTE difference between the substrate and the epitaxial layer.

Stress in a body is defined as: $\sigma = \frac{F}{A}$ with F the force or load and A the area where the force is applied. When studying a material point (in the context of continuum mechanics), the applied force is not necessarily perpendicular to the surface it is applied to, thus in order to fully describe the loading state of a material point, nine components of stress should be defined. Each component is denoted with two subscripts i and j: by convention, the first subscript denotes the direction normal to the plane on which the force acts and the second subscript denotes the direction of the force. The figure below presents the nine components of the stress and their direction:

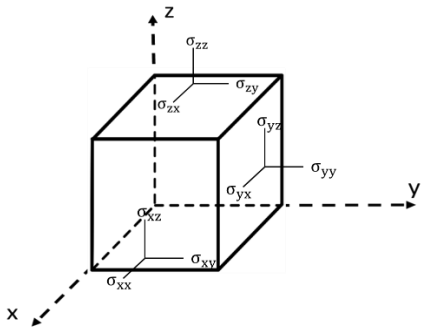

Figure 1.10: Representation of the nine stress components acting on an infinitesimal element.

A stress tensor is then expressed as follows:

$$\sigma_{ij} = \begin{bmatrix} \sigma_{xx} & \sigma_{yx} & \sigma_{zx} \\ \sigma_{xy} & \sigma_{yy} & \sigma_{zy} \\ \sigma_{xz} & \sigma_{yz} & \sigma_{zz} \end{bmatrix} \quad \textit{Equation 1.1}$$

For elastic deformation, the relation between the stress and strain is given by Hooke's law [41] and can be expressed by

$$\sigma_{ij} = C_{ijkl}\varepsilon_{kl} \quad \textit{Equation 1.2} \qquad \text{with i, j, k, l=1,2,3}$$

This formula is general for any anisotropic material where σ_{ij} is the stress tensor and ε_{kl} is an infinitesimal strain tensor (both tensors are second rank). C_{ijkl} is a stiffness fourth order tensor with 81 components that represent the elastic stiffness coefficients. The stress tensor σ_{ij} is symmetric which means the maximum number of independent components of C_{ijkl} is reduced to is 21 [42]. Furthermore, depending on the crystal symmetries, the number of independent components can be further reduced. Where the most extreme case would be an isotropic material which only has two independent components.
Using Voigt notation [43], equation (1.2) can be explicitly written as:

$$\sigma_{ij} = C_{ij}\varepsilon_j \quad \textit{Equation 1.3} \qquad i,j=1,2,\ldots,6$$

where,

$\sigma_1=\sigma_{11}=\sigma_{xx}$

$\sigma_2=\sigma_{22}=\sigma_{yy}$

$\sigma_3=\sigma_{33}=\sigma_{zz}$

$\sigma_4=\sigma_{23}=\sigma_{zy}$

$\sigma_5=\sigma_{13}=\sigma_{zx}$

$\sigma_6=\sigma_{12}=\sigma_{yx}$

and,

$\varepsilon_1=\varepsilon_{11}$

$\varepsilon_2=\varepsilon_{22}$

$\varepsilon_3=\varepsilon_{33}$

$\varepsilon_4=2\varepsilon_{23}=\gamma_{23}$

$\varepsilon_5=2\varepsilon_{13}=\gamma_{13}$

$\varepsilon_6=2\varepsilon_{12}=\gamma_{12}$

Then equation (1.3) can be explicitly written as:

$$\begin{bmatrix}\sigma_{11}\\ \sigma_{22}\\ \sigma_{33}\\ \sigma_{23}\\ \sigma_{13}\\ \sigma_{12}\end{bmatrix} = \begin{bmatrix} C_{11} & C_{12} & C_{13} & C_{14} & C_{15} & C_{16} \\ & C_{22} & C_{13} & C_{24} & C_{25} & C_{26} \\ & & C_{33} & C_{34} & C_{35} & C_{36} \\ & & & C_{44} & C_{45} & C_{46} \\ & \text{Symmetry} & & & C_{55} & C_{56} \\ & & & & & C_{66} \end{bmatrix} \begin{bmatrix}\varepsilon_{11}\\ \varepsilon_{22}\\ \varepsilon_{33}\\ \gamma_{23}\\ \gamma_{13}\\ \gamma_{12}\end{bmatrix} \quad \textit{Equation 1.4}$$

The number of independent elastic constants can be reduced further if the material exhibits certain crystallographic symmetries such as isotropic symmetry, transverse isotropy, orthotropic symmetry, and anisotropic symmetry. GaN presents a transverse isotropy [44][45] with (x y) the plane of symmetry, therefore we can write its stiffness matrix as follows:

$$[C] = \begin{bmatrix} C_{11} & C_{12} & C_{13} & 0 & 0 & 0 \\ & C_{11} & C_{13} & 0 & 0 & 0 \\ & & C_{33} & 0 & 0 & 0 \\ & & & \frac{C_{11}-C_{12}}{2} & 0 & 0 \\ & \text{Symmetry} & & & C_{44} & \\ & & & & & C_{44} \end{bmatrix} \quad \textit{Equation 1.5}$$

In chapter 4, we will present the symmetries of all the different materials we used in our numerical model as well as their elastic constant values.

The inverse of the stiffness matrix is called the compliance matrix and is denoted $[S] = [C]^{-1}$ and in the general case contains 21 independent compliance matrix components S_{ij} from which we can derive the engineering constants. For isotropic materials, we have only two independent coefficients: Young's modulus (E) and Poisson's ratio (υ):

- Young's modulus is a measure of a material stiffness in the linear elastic domain. In other words, it describes the material's response under axial or linear deformation. Materials with a high Young's modulus are stiff and resistant to deformation under load while materials with low Young's modulus are flexible. The unit is usually expressed in gigapascals (GPa).
- Poisson's ratio is a dimensionless material property that quantifies the relationship between the lateral (transverse) strain and axial (longitudinal) strain when a material is subjected to a uniaxial stress. In other words, it measures the deformation (expansion or contraction) of a material in directions perpendicular to the specific direction of loading.
-

We define as well shear modulus (G):

- Shear modulus, often referred to as the modulus of rigidity, describes a material's response to shearing deformation, which occurs when forces are applied parallel to a surface of the material but in opposite directions. It is the ratio of shear stress to shear strain. A large shear modulus means a highly rigid solid that requires a large force to be deformed. A small shear modulus means a flexible solid easy to deform. It is also expressed in gigapascals (GPa).

The engineering constants are related through equation (1.6):

$$G = \frac{E}{2(1+\upsilon)} \quad \textit{Equation 1.6}$$

When the material is not isotropic, the Young's modulus and the Poisson ratio can be measured in different directions. Since GaN is transversely isotropic, different parameters can be measured:

- In-plane Young's modulus: E_1
- Out-plane Young's modulus: E_3
- Two Poisson rations: υ_{12} and υ_{13}

From these coefficients, we can obtain the corresponding shear modulus G_{12} and G_{13}. In this case, the stress-strain relation as function of the engineering constant is written as:

$$\begin{bmatrix}\varepsilon_{11}\\ \varepsilon_{22}\\ \varepsilon_{33}\\ \gamma_{23}\\ \gamma_{13}\\ \gamma_{12}\end{bmatrix} = \begin{bmatrix} \frac{1}{E_1} & -\frac{\vartheta_{12}}{E_1} & -\frac{\vartheta_{31}}{E_3} & 0 & 0 & 0 \\ -\frac{\vartheta_{12}}{E_1} & \frac{1}{E_1} & -\frac{\vartheta_{31}}{E_3} & 0 & 0 & 0 \\ -\frac{\vartheta_{13}}{E_1} & -\frac{\vartheta_{13}}{E_1} & \frac{1}{E_3} & 0 & 0 & 0 \\ 0 & 0 & 0 & \frac{1}{G_{12}} & 0 & 0 \\ 0 & 0 & 0 & 0 & \frac{1}{G_{13}} & 0 \\ 0 & 0 & 0 & 0 & 0 & \frac{1}{G_{13}} \end{bmatrix} \begin{bmatrix}\sigma_{11}\\ \sigma_{22}\\ \sigma_{33}\\ \sigma_{23}\\ \sigma_{13}\\ \sigma_{12}\end{bmatrix}$$ *Equation 1.7*

Values of the engineering constants for the GaN and for the rest of the materials will be presented in chapter 4.

1.3.2 Strain distribution

Strain, on the other hand, is a measure of the amount of deformation that occurs in a material due to stress. It quantifies the relative change in size and/or shape of a material when subjected to an external load. Strain is defined as the ratio of the change in length (or other dimensions) of a material to its original length (or dimension) and is expressed as a unitless quantity or as a percentage. In crystalline materials, strain can manifest as changes in the lattice parameters, which can affect the material's mechanical properties, electronic behavior, and optical properties.

Strain due to lattice mismatch between a substrate and a deposited layer arises when the crystal lattice of the layer being deposited does not perfectly match the lattice spacing of the substrate onto which it is grown. In this case, it is the lattice parameter of the substrate which is imposed on the layer being grown:

- If $a_l < a_s$ (Figure 1.11(a)) the layer is under tensile strain (Figure 1.11(b)) with the atoms attempting to expand to match the substrate lattice.
- If $a_l > a_s$ (Figure 1.11(c)) the layer is under compressive strain (Figure 1.11(d)) with the atoms being forced to be closer together than they would be in their relaxed state to match the substrate lattice.

where a_l refers to the lattice constant of the relaxed layer and a_s refers to the lattice constant of the substrate. A compressive strain is indicated by a negative strain value, while a tensile strain is indicated by a positive strain value.

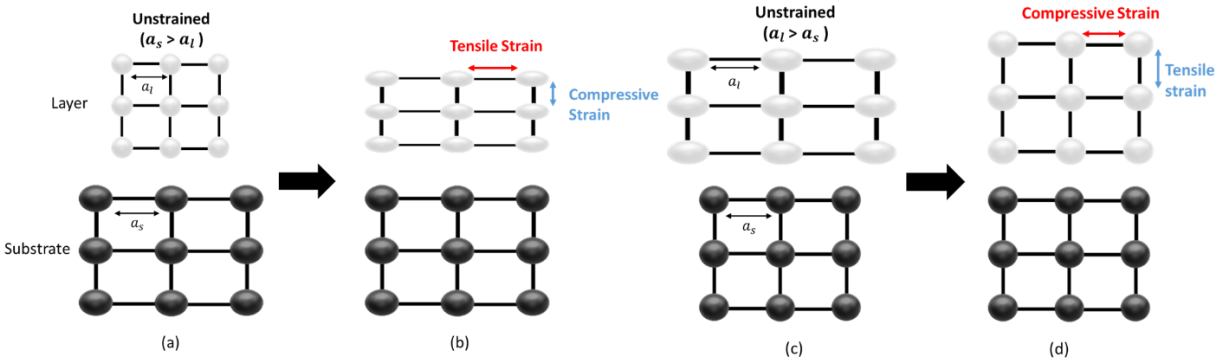

Figure 1.11: Schematic for the strain resulting from the lattice mismatch between the layer and the substrate: (a) unstrained layer with $a_s > a_l$, (b) corresponding layer deformation in both horizontal and vertical direction, (c) unstrained layer with $a_l > a_s$, and (d) corresponding layer deformation in both horizontal and vertical direction.

The strain components in the epitaxial layer are defined as $\varepsilon_{xx} = \varepsilon_{yy} = \frac{a-a_0}{a_0}$ and $\varepsilon_{zz} = \frac{c-c_0}{c_0}$ where a_0 and c_0 represent the lattice parameters of the unstrained relaxed layer, on the other hand a and c represent the lattice parameters of the epitaxial strained layer.

This strain induced by lattice mismatch during epitaxial growth can lead to the formation of crystallographic defects such as dislocations and stacking faults at the interface between the layer and the substrate. As discussed in section 1.2.2, these defects are introduced to reduce the strain by allowing atoms to rearrange in a way that partially relieves the mismatch. The strain can also affect the bandgap of semiconductors, leading to changes in their electronic properties [46].

Strain due to a coefficient of thermal expansion (CTE) mismatch between a substrate and an epitaxial layer is a common occurrence when materials with different CTEs are combined in a layered structure that undergoes a change in the temperature. After the growth, the epitaxial material and the substrate will be subjected to a cool down process so they will expand or contract at different rates which might lead to cracks in the layer under stress. This in-plane thermal strain is expressed as:

$$\varepsilon_{th} = \int_{Tg}^{Tamb} (\alpha_s(T) - \alpha_l(T)) dT \quad \textit{Equation 1.8}$$

In this equation, α_s denotes the CTE of the substrate, α_l denotes the CTE of the epitaxial layer, T_{amb} represents the ambient temperature and T_g the growth temperature.

1.4 Challenges facing GaN growth on foreign substrate

As we have already discussed in section 1.1.3, GaN is a very commonly used semiconductor for the fabrication of highly efficient light-emitting diodes (LEDs) from ultraviolet to blue,

green and even red wavelengths [47]. The growth of GaN on foreign substrates is more suitable for industrial applications because of the high cost of GaN bulk substrates and its limitation in size. In addition, as we have seen in section 1.2.2 the heteroepitaxy approach generates dislocations that are responsible for the degradation in the emission efficiency of GaN-based devices. However, the high dislocation density is not the only challenge that the research community is trying to solve. Other difficulties such as melt-back etching, GaN cracking issues and GaN platelet transfer are also significant problems that the researchers are working to solve. We will present the different approaches that have been implemented over the years to face these different challenges and improve the fabrication of efficient GaN-based devices.

1.4.1 Melt-back etching

Sapphire is widely used as substrate for GaN-based optoelectronic devices because it is not expensive, it does not react chemically with the GaN and the dislocation density for GaN on sapphire is in the order of 4×10^8 cm^{-2} [48]. However, silicon is more advantageous as a substrate for GaN because it is available with larger diameter (300 mm) than sapphire, which makes it more suitable for industrial application and reduces more the manufacturing cost making the Si even cheaper.

A common problem for the growth of GaN on Si substrate is melt-back etching. Melt-back etching is a chemical reaction that occurs when the Ga atoms and the Si atoms come in contact at high growth temperature [49]. This reaction deteriorate the surface morphology of the GaN and makes the post-growth device processing too complicated [50]. Therefore, in order to obtain clean GaN surfaces, it is necessary to eliminate the contact between gallium and silicon during the growth. This is done by inserting a layer of a third material in between. Various materials have been evaluated such as GaAs and SiC [51][52][53][54] but Aluminum nitride (AlN) has become the standard nucleation layer [55]. The deposited AlN layer should have a high quality with a smooth surface to avoid any holes on its surface that might allow the Si atoms to come in contact again with the Ga atoms.

1.4.2 Cracking of the GaN epitaxial layer

As discussed in section 1.3.1, the large thermal coefficient mismatch between the epitaxial layer and the substrate generate stress in the epitaxial material. If the stress is too high and cannot be relaxed with the formation of defects such as dislocations, the material is likely to crack. Table 1.1 shows the in-plane thermal coefficient α_a of GaN and Si at high growth temperature (1300K) and room temperature.

Material	T(K)	α_a $(10^{-6}k^{-1})$	Reference
GaN	1300	5.54	[48]
	300	3.94	
Si	1300	4.44	[62]
	300	2.57	

Table 1.1: Thermal coefficient values of GaN and Si at T=300K and T=1300K.

Therefore, during the cooling-down process from growth to room temperature, the GaN will be under tensile stress which might generate cracks for GaN films with thickness exceeding 1 µm [56], because as the thickness of GaN increases, the less compressive stress in its layers decreases, which reduces the ability to compensate the tensile stress that was generated during cooling down, potentially leading to cracks in the GaN. Most of the devices usually demand a thick layer because a thicker layer has fewer dislocations, and thicker layers are frequently required for processing and current spreading in LEDs.

Several methods have been found that allowed to grow thick crack-free GaN on Si [57].

The first method started from the idea of Watanabe et al. [58] on inserting AlN layer on top of the Si in an attempt to adopt the in-plane lattice parameter who present at the interface. Then two to three AlGaN layers are formed on top of the AlN, with the Al concentration gradually decreasing, in order to gradually adjust the AlN and GaN lattice characteristics. These graded AlN-AlGaN buffer layers will put the GaN under compression stress which will compensate the tensile stress that comes from the cooling process. This method allowed the growth of 6.7 µm thick crack-free GaN layers [59].

The second technique is patterning the substrate to cover part of its surface with dielectric, allowing for localized growth in the areas that are left unmasked. This way, the growth areas will have free lateral sides that will enhance the lateral strain relaxation and prevent the epitaxial zones from cracking.

1.4.3 Dislocations density

Efforts to lower the dislocations densities in GaN on foreign substrates started in the early 2000s through research and remains active until today in order to find the optimal approach that allows the growth of high quality heteroepitaxial GaN for electronic and optoelectronic applications. Two main methods are widely used : epitaxial lateral overgrowth (ELOG) [47][48] and pendeo-epitaxy (PE) [60][61].

- Epitaxial lateral overgrowth (ELOG):

Epitaxial lateral overgrowth consists of four steps that are shown in figure 1.12:

1) Two-dimensional GaN growth on foreign substrate with a low temperature AlN buffer layer placed in between since it contributes to the reduction of the dislocation density [62][63].

2) Then we create windows by lithography and etching of a SiO_2 or SiN mask that will cover the GaN epilayer. This mask will delimit the zones of GaN nucleation and block the dislocations originating from the heteroepitaxy beneath it.

3) The third step is the lateral growth of the GaN that grows from the different masks.

4) The final step occurs after sufficient growth time, where the GaN from different windows will coalesce to form a fully coalesced GaN platelet. To guarantee that the coalescence occurs, the width of the windows should be small (in the order of tens of microns).

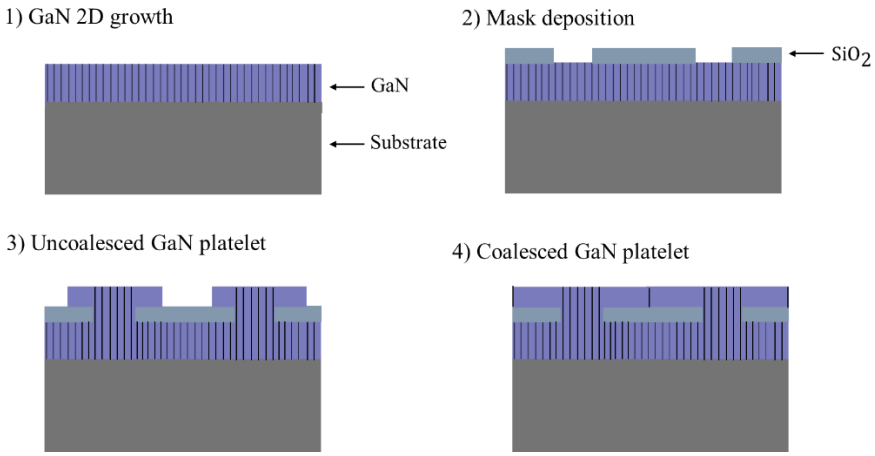

Figure 1.12: Schematic representation of lateral epitaxial overgrowth approach of GaN on substrate. Each dark line corresponds to the propagation of one dislocation.

This technique will therefore reduce the dislocations coming from the lateral nucleation sites, nevertheless, the GaN islands which nucleated on top of each independently, will be slightly disoriented which means further dislocations will form when they coalesce laterally. Dislocations densities in the order of 10^7 cm^{-2} were reached with this method [64][65] but the remaining transversal dislocations are distributed inhomogeneously in the GaN layer and the epitaxial layer needs to be thick.

This method can be improved with a two-step ELOG method: a 3D growth step (Volmer-Weber mechanism (island formation)) followed by a 2D step (coalescence mechanism).
Growth conditions can be adapted such that inclined planes are favored. We can then grow GaN in the shape of pyramids and this will be the first step (the 3D step). Initially, during the growth, the dislocation lines will spread vertically along the +c-axis with the progressive formation of the pyramids. However, as the growth progresses, the top c-plane's size gradually decreases, causing the vertical dislocation lines to intersect a semi-polar facet of the pyramid and bend in the direction of the free surface, adopting a new direction in the basal plane [66][67] which will then reduce the density of threading dislocations observed at the surface. After that comes the second step (2D step) where the coalescence between the GaN pyramids takes place laterally

and the bended dislocations will come in contact and form a loop that will not propagate to the top.

Vennéguès and al. [68] showed that it is possible to reduce the dislocations still present in the GaN grown on top of the unmasked areas of the ELOG through this 3D growth step (figure 1.13 (a)) and followed by a 2D step (figure 1.13(c)) and they obtained a dislocation density over the entire material of 1.7 x 10^7 cm^{-2}.

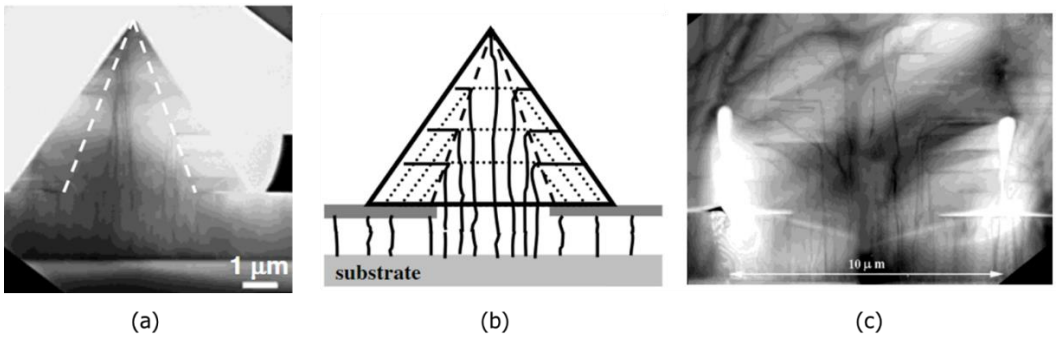

Figure 1.13: (a) Cross-section TEM image along the [10$\bar{1}$0] zone axis of a GaN window grown by ELOG after the 3D growth step [68]*, (b) its schematic representation and (c) Cross-section TEM image along the [10$\bar{1}$0] zone axis of coalesced GaN film after step 2 in the ELOG* [68].

This two-step ELOG approach is schematically represented in Figure 1.14.

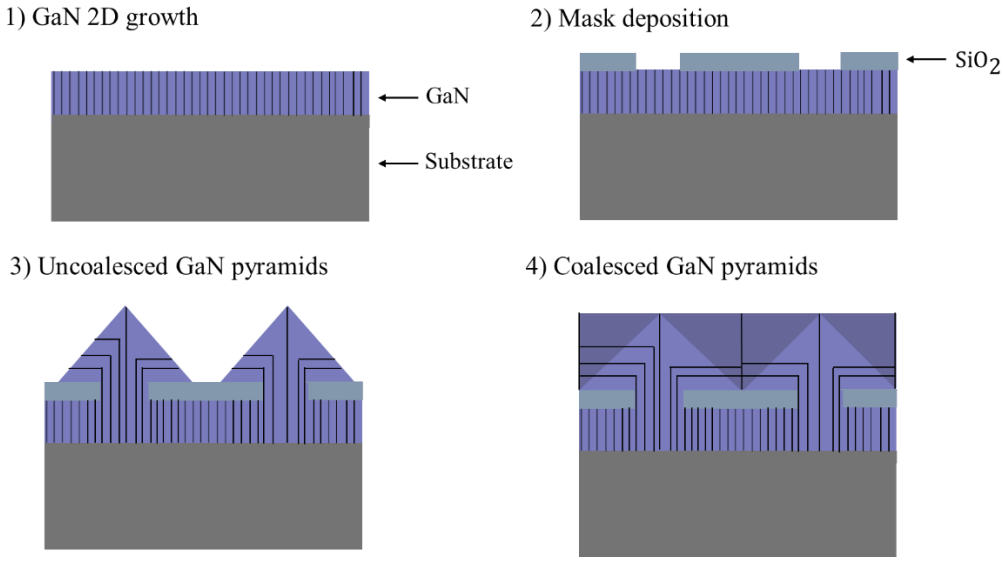

Figure 1.14: Schematic representation of two-step lateral epitaxial overgrowth approach of GaN on Si substrate. Each dark line corresponds to one dislocation.

- Pendeo-epitaxy (PE):

Pendeo-epitaxy is another growth technique that was developed in order to grow high quality GaN on foreign substrate. This approach consists of three major steps presented in figure 1.15:

1) Two-dimensional GaN growth on foreign substrate with a low temperature AlN buffer layer placed in between.
2) Selective etching to a certain depth in the substrate to from separated GaN/AlN/substrate columns in the substrate.
3) The GaN will grow both vertically and laterally with an empty space under the coalesced layer. The lateral component of the GaN film is able to grow independently from the sidewalls of the columns and from the etched substrate. We would also expect meltback etching on silicon because the GaN sees the silicon directly after etching into the substrate.

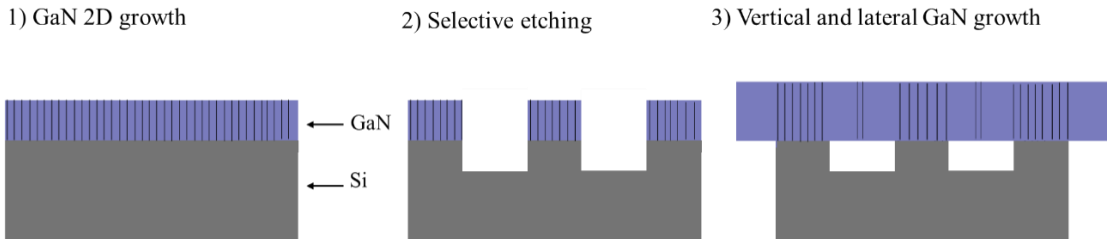

Figure 1.15: Schematic representation of Pendeo-Epitaxy approach of GaN on substrate. Each dark line corresponds to the propagation of one dislocation.

Figure 1.15: Schematic representation of Pendeo-Epitaxy approach of GaN on substrate. Each dark line corresponds to the propagation of one dislocation.

Morgan and al. [63] showed that using PE, the dislocations do not propagate laterally from the GaN columns when the structure coalesce laterally, which means the regions above the etched voids are usually defect free, but the dislocation density is very high in coalescence zones and nucleated zones directly on the substrate. Therefore, the disadvantage of the PE method is that the dislocation density is very inhomogeneous depending on the position on the surface.

1.5 Growth approach studied in this thesis

1.5.1 Motivation behind the proposed growth approach

As we have presented in section 1.4, many growth methods attempt to address different challenges facing the heteroepitaxy of GaN to improve its quality. In this thesis, we propose a new approach that combines a number of the earlier discussed techniques with the objective to

bring solutions for different problems that occurs during GaN growth for µLEDs applications. The advantages of our growth approach are:

- Reducing the dislocation density in the epitaxial GaN layer.
- Achieving mass production of small size GaN platelet without the need of an etching step to define the µLED.
- Using an architecture that facilitates the transfer of the GaN platelets for the use of µLEDs in screen fabrication.

We start from simple thin GaN layers on silicon using an AlN nucleation layer. The AlN plays a role in the reduction of the dislocation density [62] and in compensating the tensile stress during the cooling process [58]. It also helps in avoiding the melt-back etching problem by avoiding any contact between Ga and Si atoms that could launch a chemical reaction. Instead of silicon, we grow the layers on a specific SOI substrate using a silicon (111) layer above the oxide. These layers and the substrate are then etched to obtain GaN/AlN/Si(111)/SiO_2/Si(100) nanopillar arrays distributed in a hexagonal pattern as shown in figure 1.16(b). The etching process will be explained later in section 1.5.2. Furthermore, dislocations can be bent perpendicular to the growth direction throughout a two-step growth method (3D step followed by a 2D step) [68] which is why the samples studied in this thesis are grown with two steps as shown in figure 1.16(c) and (d).

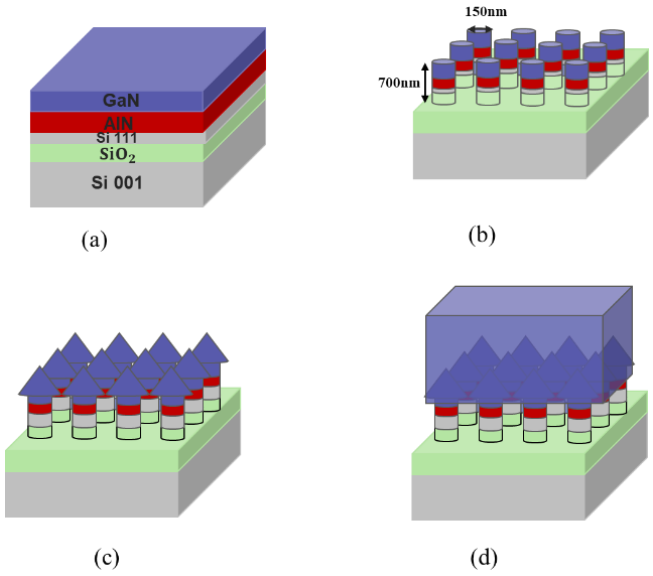

Figure 1.16: Fabrication process: a) growth of GaN/AlN on SOI, b) structure substrate: etching of nanopillars, c) growth step 1: nucleation of GaN pyramids, d) growth step 2: coalescence and formation of GaN microplatelets.

As shown in figure 1.16, there are four steps to our approach:

(a): Growth of GaN/AlN layer: A thin stack of GaN/AlN is grown on the SOI substrate.

(b): Etching: we etch to obtain a GaN/AlN/Si(111)/SiO_2/Si(100) nanopillar array with hexagonal symmetry and a pitch p (center-to-center distance between two consecutive pillars) varying from 300 nm to 1.5 µm. The buffer GaN layer, the AlN nucleation layer and the Si(111) layer have thicknesses of 250, 150 and 50 nm, respectively, while the SiO_2 is etched down to a depth of 300 nm.

(c): Pyramid growth: The growth of GaN pyramids on top of these nanopillars by metal organic vapor phase epitaxy (MOVPE), with trimethylgallium (TMGa) and ammonia (NH_3) as precursors for gallium and nitrogen, respectively. More details on the growth approach will be given in section 1.5.4.

(d): Coalescence: The pyramids touch and coalesce and GaN growth takes place to obtain a fully coalesced GaN platelet on which an LED structure will be grown.

The idea behind this method is based on the self-realignment of GaN on Si(111) nanopillars during GaN coalescence. This alignment is driven by the excess energy present at the interfaces between the two neighboring pyramids (indicated by double red arrow in figure 1.17(a)), once the two pyramids touch, this excess of energy might enable a rotation of the pillars which should allow the GaN pyramids on top to align once they come in contact. In this way the GaN crystallites can reorient themselves during coalescence. The tendency of the system to minimize its total energy should result in the formation of a low TD density GaN platelet. Additionally, at high growth temperatures (≃1000°C), the viscoelastic properties of SiO_2 allow its deformation [69][70], which will make the rotation of the pillars easier. Figure 1.17 displays a schematic showing the twist between two neighboring GaN pyramids.

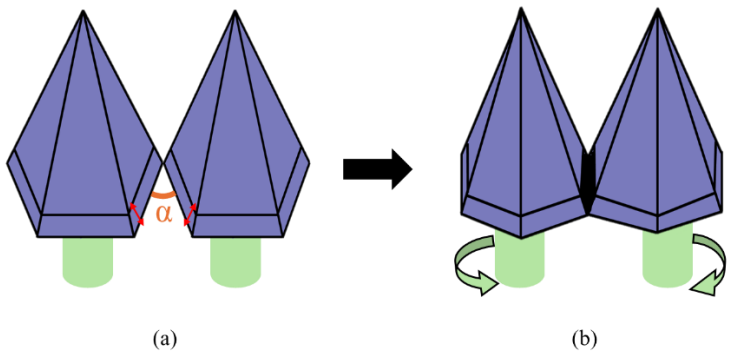

Figure 1.17: Schematic representation of (a) two twisted GaN pyramids by an angle α grown on SOI pillars and (b) the same GaN pyramids after realignment during coalescence.

As discussed in section 1.1.3, the new generation of high resolution and small dimension displays require µ-LEDs with micrometer sizes. In the proposed growth, we use a bottom-up approach that allows the production of small size GaN platelets without requiring an etching step. These platelets will serve as pixels when the complete LED structure is grown on top of them (figure 1.18) as schematized previously in figure 1.3. Additionally, there is a possibility

to have growth over a large area due to the availability of large SOI substrate (300mm) which allows us to meet the ever-increasing market demands.

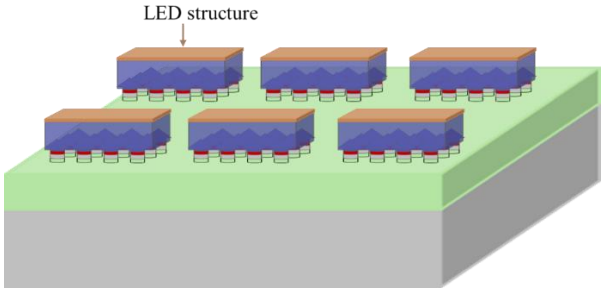

Figure 1.18: Schematic representation of individual micro-LEDs grown on top of GaN platelets.

An additional advantage of this method is that it makes it easier to transfer the micro-LEDs because the SOI pillars are weak, and the micro-LEDs detach from the pillars with ease.

Having outlined the motivation behind exploring this growth technique, we will present the objectives of the work done in this thesis followed by a description of the fabrication procedure used to produce the samples used in this thesis.

1.5.2 Objectives of this thesis

The objectives of this thesis will be to study the GaN crystalline orientation before coalescence, during coalescence and after coalescence, in order to gain a deeper physical understanding of the processes operating during our proposed growth approach and to determine the quality of the epitaxial GaN layer. We also aim to study the quality of the GaN grown on various pillars patterns to find the optimal one. Additionally, until now we do not have clear evidence that the principle of the rotation of the pillars that we talk about in our approach works. Therefore, another objective of this thesis is to address the concept of the pillars rotation by exploiting and understanding the behavior of the pillars (if they really tilt/twist and by how much). To reach these objectives, structural characterization techniques on different GaN samples at the nanometer-scale are needed, such as X-ray Diffraction techniques at the European Synchrotron Radiation Facility (ESRF) and Electron Backscattered Diffraction. In chapter 2, we provide an overview of the characterization approaches that were employed and the data treatment process, and in chapter 3 we present and discuss the results. This thesis also aims to find the optimal pillars parameter (pitch, height...) that would facilitate the pillars rotation; given the limited beamtime available at the ESRF, we performed finite element simulations with ABAQUS software to determine the impact of the pillars parameters, and to test different theories that could help us to understand and complete the experimental observations. These simulations and their outcomes are presented in chapter 4.

1.5.3 Nanopillars etching process

In this section, we will describe the etching process performed by Nabil Labchir and then the growth steps performed by Kilian Baril [35] in section 1.5.4. Before describing the nanopillars etching process, we will briefly present the preparation of the SOI substrate followed by GaN/AlN layer growth. The SOI substrates used in this thesis were fabricated in the CEA-LETI cleanrooms using SmartCut technology. The thicknesss of Si(001) is 750 µm , the SiO_2 500 nm and the Si(111) on top 50 nm. These SOI substrates were diced into samples 36x36 mm across and then sent to CRHEA for the growth of the GaN/AlN layer. The first step consists of cleaning the SOI substrate using BOE (Buffered Oxide Etch) solution that removes the protective oxide layer deposited on top of the SOI substrate. The second step is the deposition using MOVPE in a AIXTRON close coupled showerhead 6x2" tool of an AlN buffer layer of 150 nm thick at a high temperature (1010°C) followed by a 250 nm GaN layer at a lower temperature (1170°C). The obtained high dislocation density in the 2D GaN was found equal to $\sim 1 \pm 10^{10}$ cm^{-2}.This GaN layer grown on the 2D SOI substrate will serve as reference.

After this step, the sample is sent to the LTM in Grenoble, France to be structured into arrays of nanopillars using nanoimprint lithography (NIL) combined with a lift-off step and an inductively coupled plasma (ICP) etching. These techniques will be explained next.

(1) First, a Si master is created for each set of patterns by etching the Si down to 70 nm according to the pattern we desire to transfer to the sample. The etching is performed by ICP-RIE (an inductively coupled plasma - Reactive Ion Etching) after patterning by E-beam lithography (step (a) in figure 1.19). Then, a thin "anti-sticking" FDTS layer is deposited on the master to facilitate the demolding. The master is then put on a heated plate, after reaching 50°C, a PDMS is applied to the master surface for 48 h (step (b) in figure 1.19). After that, the patterned PDMS is removed easily thanks to the FDTS layer and used as a stamp (step (c) in figure 1.19)... Each stamp can be used to structure the surface of around ten of samples. The technique of NIL patterns the entire wafer in one single step, while giving very high resolution. This is a big advantage over electron beam lithography, which can be very time consuming.

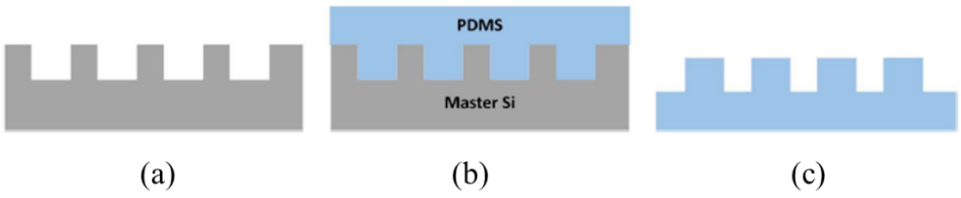

Figure 1.19: Schematic of steps for creating a PDMS stamp with (a) Si master, (b) PDMS deposition and (c) PDMS stamp after demolding. This schematic is taken from reference [71].

(2) A thin layer of SiO_2 is deposited on the surface of the GaN on SOI sample to protect it followed by a deposition of a resin TU /Ge (Germanium) /PMMA (poly acrylic methyl methacrylate) tri-layer system on the oxide layer used to improve the lift off [72]. The previously made PDMS stamp is then used to transfer the desired motifs onto this tri-layer by NIL using an EITRE6 Obducat tool. Once the pattern is transferred the PDMS stamp is removed manually. Then, the tri-layer is etched using plasma, and a Ti(5 nm)/Ni(75 nm) mask is deposited everywhere. The final step is the lift-off step where a solvent is used to attack the residuals of the tri-layer (resin) and remove it which will leave us with hard mask made from Nickel metal dots only. These steps are shown in figure 1.21.

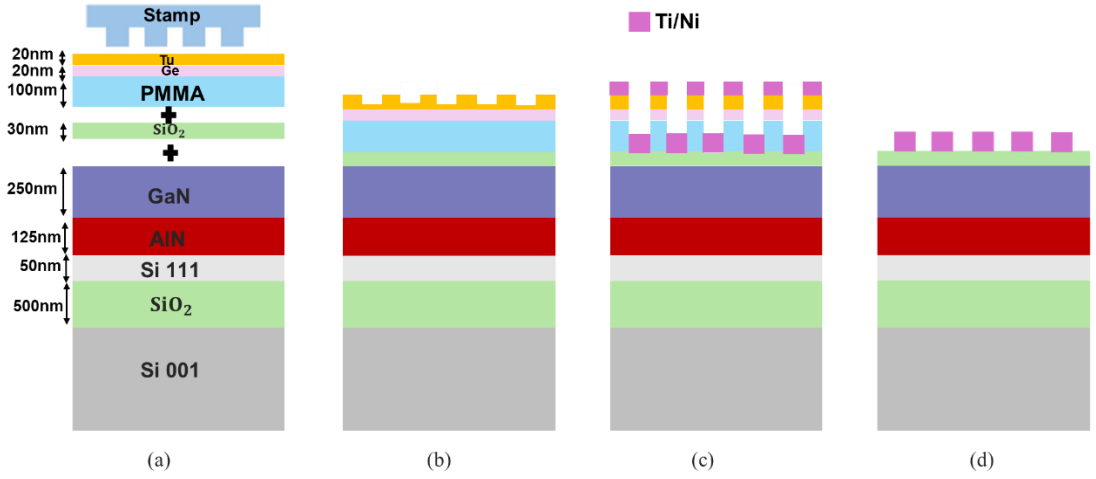

Figure 1.20: Schematic representation of the different deposition and etching steps leading to the creation of a Ti-Ni hard mask.

An SEM image of the final metal dots (Ti-Ni mask) corresponding to the Ti-Ni mask after lift-off (figure 1.21(a)) is shown in figure 1.22.

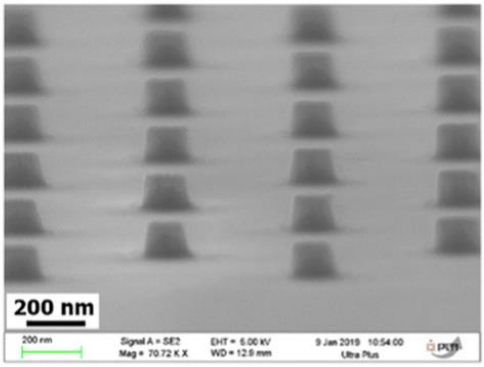

Figure 1.21: Patterning after Ti/Ni deposition and lift off on the sample surface [73].

(3) The last part is the etching of the pillars using again the dry plasma etching (ICP). The etch process is controlled using an end-point system, "EyeD" from Verity Instrument, allowing a real time monitoring of the etch depth and velocity using optical interferometry.

Finally, a cleaning of the sample using CARO's acid is required to remove the Ti-Ni mask still present on the surface.

1.5.4 GaN platelet epitaxy process

Following their structuring, the samples are returned to the CRHEA so that the epitaxy can be resumed. Prior to any growth, the samples are characterized in order to identify any defaults in the pillars (cracked pillars, lost pillars, chemical residue present on the surface) that might prevent a successful epitaxy. Figure 1.23 shows the SEM image of etched pillars prior to epitaxy that were later characterized in this thesis.

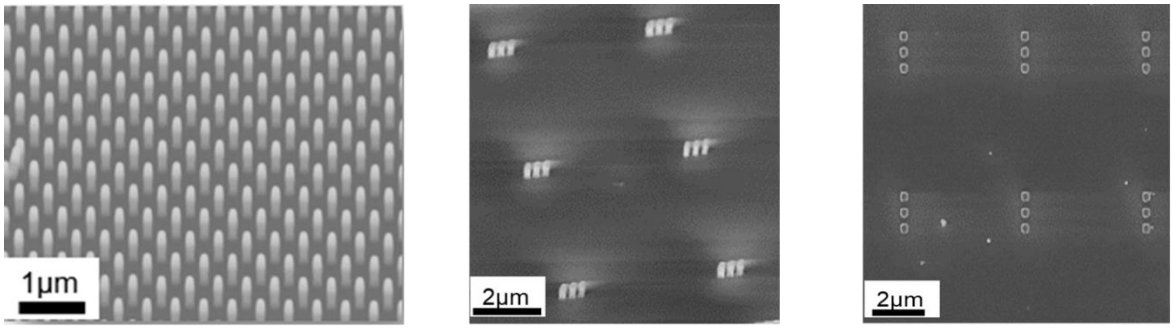

Figure 1.22: SEM images of (a) arrays of pillars in hexagonal pattern, (b) sets of three horizontal pillars lines and (c) top view image of sets of three vertical pillars lines.

Figure 1.23(a) shows an array of pillars distributed in a hexagonal pattern and with a pitch = 500 nm). Figure 1.23(b) shows six sets of pillars, each composed by three pillars aligned horizontally with a pitch=300 nm. Figure 1.23 (c) displays a top of view of six sets of pillars, each composed by three pillars aligned vertically with a pitch= 500 nm. The choice of the pillars pattern and pitch is chosen based on the characterization goals which will be presented and discussed in detail in the next chapters.

These figures demonstrate the potential of our patterning process to produce patterns of these types without flaws such as missing pillars or blank spaces. To reduce cost, as described above, a single stamp can be used multiple times. However, it is important to remember that using the same stamp too many times can lead to flaws in the samples. In figure 1.24, we show arrays with missing pillars in some areas and fallen pillars in others. These defaults result from using a stamp too many times. We can also notice broken pillars at the AlN/Si interface, and this is mainly due to the smaller diameter of the pillars on this level caused by the Caro etching.

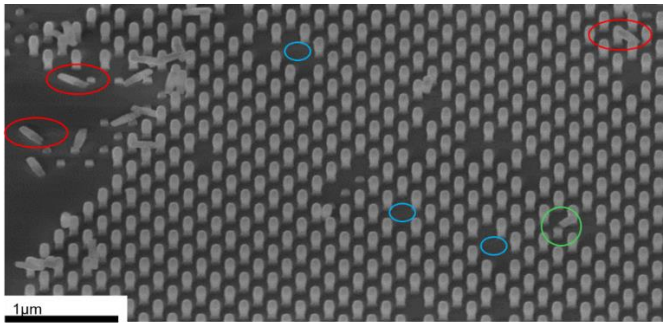

Figure 1.23: SEM photos displaying the defaults that were found in the pillars: blue circles indicate missing pillars in specific locations, green circles indicate broken pillars and red circles indicate fallen pillars.

The growth was resumed in a MOVPE Thomas Swann Reactor (Close Coupled Showerhead) with TMGa and NH_3 respectively as precursors of gallium and nitrogen. The growth conditions used for the 3D GaN growth have been studied by previously [74][75] and the ones used in this work are presented:

For our 3D growth of GaN, the reactor pressure was set constant at 100 Torr, with N_2 as the carrier gas, [75] as used in earlier work by R. Dagher et al. [76]. The duration of the growth is important because it controls the spacing between the GaN pyramids before the start of the 2D growth and a short duration might leave us with uncompleted pyramids. Temperature is a crucial factor, particularly during coalescence where a high temperature is required to make the SiO_2 soft and flexible to allow the accommodation of different orientations of pyramids. K. Baril studied the impact of the temperature on the GaN pyramids morphology by growing three samples at different growth temperature (figure 1.25).

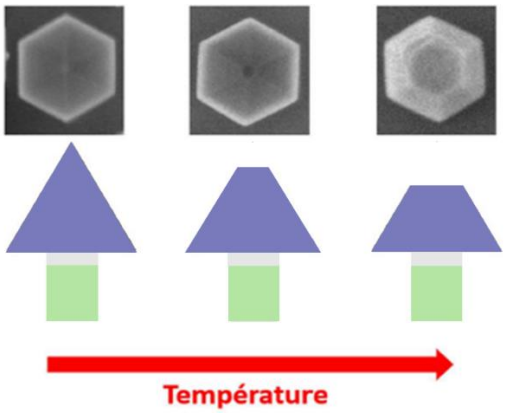

Figure 1.24: Impact of the growth temperature on the morphology of GaN pyramids for temperatures of 1130°C (a), 1170°C (b) and 1230°C (c) [71].

It was found that the higher the temperature, the more the growth of the c-plane is favored over semi-polar planes. However, these flattened top surfaces should be avoided for this first step as they permit dislocations to continue through the layers instead of being bent into the plane. Therefore, the growth cannot be done at a very high temperature.

Figure 1.26 shows a SEM image of an array of pillars after a long 3D growth (100s). The pyramids on top of the pillars are clearly distinguished, having six semi-polar facets $\{10\bar{1}1\}$ each. These facets are obtained due to the dependence of the growth speed on the different crystallographic planes [77].

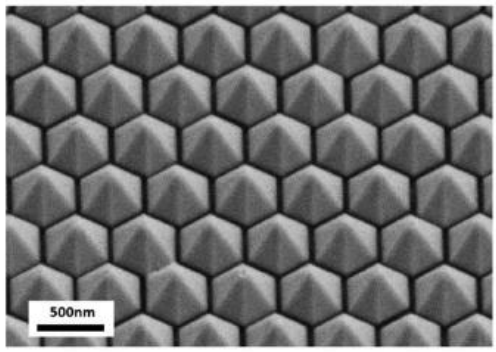

Figure 1.25: SEM image of a network of GaN pyramids after a 3D growth for 100 s [71].

For the 2D growth and coalescence, the optimal temperature found was 1170°C. Samples at higher and lower temperature presented incomplete nucleation and a rough surface. After 90 minutes, fully coalesced GaN platelets were obtained as shown in figure 1.27(a). The atomic force microscopy (AFM) image of this platelet is shown in figure 1.27(b) and the surface with an area of 15 x 15 µm² is found to have a roughness of 2 nm [35].

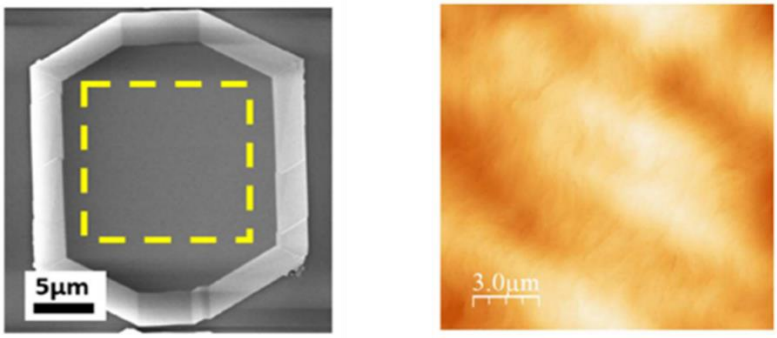

Figure 1.26: (a) SEM image of one fully coalesced GaN platelet grown on top of arrays of pillars spaced by 500 nm and (b) AFM image of the corresponding surface [35].

In order to verify the behavior of the dislocations inside the pyramids described in section 1.4.3, TEM observations were performed on a coalesced GaN sample (after the 2D growth step) following a preparation of a thin FIB section. Figure 1.28 shows a TEM image of one of the pillars. The yellow dotted lines represent the position of the semi-polar facets at the end of 3D GaN growth.

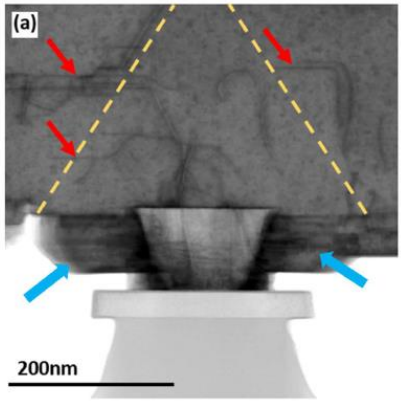

Figure 1.27: TEM image of a pillar with GaN coalesced on the top [71].

We clearly see the curvature of the dislocations (designated by red arrows) into the plane orthogonal to the growth direction. We also notice dislocations (designated by blue arrows) in the plane perpendicular to the growth direction at the AlN level and these dislocations appear to come from the nucleation of the GaN on the AlN. Even though these dislocations do not appear to propagate towards the surface, they can potentially curve back towards the surface, especially at the point of coalescence, leading to an increase in TDs density.

To summarize, this previous work focused on optimizing growth parameters to achieve GaN layers with reduced dislocation density using the proposed growth approach. K. Baril et al. [71] were able to obtain GaN platelets of 40 x 40 μm^2 and 20 x 20 μm^2 with a thickness of 5 µm and dislocation densities of the order of 4 x 10^8 cm^{-2}.

Chapter 2: Characterization techniques

2.1 Introduction

As described in chapter 1, an original method has been suggested for achieving low dislocation density gallium nitride films suitable for µLEDs applications. The proposed growth approach is based on the self-realignment of Si(111) nanopillars during nitride layer coalescence. In this thesis, we aim to (i) determine the degree of tilt and twist of the individual Si nanopillar, (ii) study the layers for various GaN growth times in order to better comprehend each step of the GaN pyramid coalescence, (iii) determine the GaN quality and (iv) predict the optimal structures by varying the geometry and the spatial distribution of the nanopillars. To obtain these kinds of information, X-ray diffraction is a crucial technique as it allows for the analysis of the crystal orientation and strain distribution by measuring the diffraction patterns of X-rays as they interact with the crystal lattice. Given the size of the pillars and the need of statistical information on large field of view, we require a high intensity beam with a nano size and a high spatial resolution, these requirements cannot be met by conventional X-ray diffractometers; this can only be achieved using synchrotron radiation. Therefore, in this thesis, we performed four X-ray diffraction experiments using three distinct X-ray diffraction techniques at ESRF in Grenoble and each time with different type of samples. Given the time limitations with the beam time at the ESRF, electron backscatter diffraction (EBSD), cathodoluminescence (CL) and scanning electron microscopy (SEM) techniques are also employed in this work to compare with the XRD results and to provide information on larger number of samples. The objectives of this chapter are to present the potentials as well as the limitations of the various characterization techniques we used followed by a description of the data treatment work following each experiment.

2.2 Basics of X-ray diffraction

2.2.1 Synchrotron X-ray

Discovered by the German physicist W.C. Roentgen [78] in 1895, X-rays are electromagnetic waves with zero charge and zero mass, similarly to visible light, but with far higher energies ranging from 124 keV to 124 eV and with wavelengths (λ) ranging from 0.01 to 10 nanometers. X-ray diffraction (XRD) is a powerful characterization technique used to investigate the structural properties of crystalline materials down to the atomic level. Information like lattice parameters can be extracted to study the strain fields and defects present in the crystal. Different

XRD techniques have been conducted in this thesis. As we need information at nanopillar scale, we used synchrotron radiation because brilliance, beam spot size, etc…

A powerful X-ray source with very interesting characteristics has become available with the invention of synchrotron in 1947 [79][80]. The idea of a synchrotron radiation source started back in 1898 with Alfred Lienard who calculated the energy dissipated by electrons moving in a circular trajectory within a homogeneous magnetic field [81]. This theory can be considered as the basis of synchrotron radiation. The core of a synchrotron source is a circular particle accelerator known as a synchrotron ring. Typically, electrons are injected into this ring and accelerated to nearly the speed of light using powerful electro-magnets. The accelerated electrons travel along a circular path due to bending magnets as well as insertion devices placed strategically around the ring to bend the electron trajectories. The accelerated electrons are forced to change direction by the magnetic fields, and therefore they emit electromagnetic radiation. The emitted radiation has distinctive properties such as high brightness, coherent power, very low divergence and can cover a broad energy spectrum [82][83]. The first use of synchrotron radiation was exclusively for particle physics, it is only from 1970 that synchrotron for other applications emerged. These are called first generation synchrotrons (e.g. SURF - USA, Frascati - Italy, INS - Japan, ACO – France) [84] and the radiation was produced only by the bending magnets. In the second generation synchrotrons, ring storage was used and in the third generation synchrotrons, insertion devices were added in the straight sections of the ring. This means that X-rays are produced not just within the bending magnets but also within the insertion devices, which means the brilliance of the radiation produced is now much higher. The first third generation synchrotron is ESRF located in Grenoble, France (1994) (figure 2.1 (a)), followed by the Advanced Photon Source in USA (1996), the Spring8 in Japan (1997) and Petra III in Germany (2009). The applications of synchrotron light are very wide covering different fields such as materials science, geoscience, archeology, biology, medicine, applications…

Since 1994, the ESRF has undergone continuous improvements and upgrades in the instrumentation and technology of the X-rays source and beamlines, and today it is a fourth-generation synchrotron with a ring of 844m circumference, a powerful energy of 6 GeV, and a maximum current of I=200 mA, containing more than 1000 magnets of various kinds [85][86]. The electrons travel through a bending magnet of 0.8 T and the produced X-ray beam is characterized by a vertical divergence of 0.2 mrad and a horizontal divergence of 3mrad.

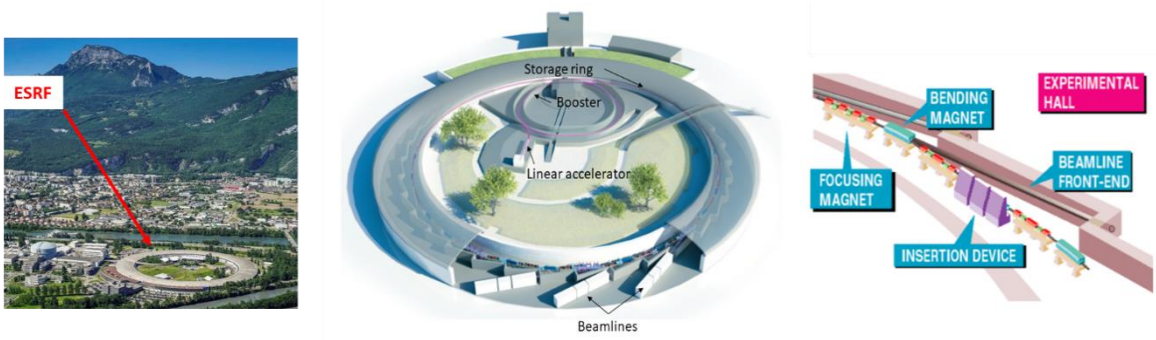

Figure 2.1: (a) European Synchrotron Radiation Facility (ESRF) in Grenoble where the synchrotron experiment were conducted in this thesis, photo taken from ref. [87], *(b) sketch of the ESRF taken from ref.* [88] *and (b) the storage ring, showing the principal geometry of bending magnets, insertion devices and beamlines taken from ref.*[89].

Insertion devices

Insertion devices consist of a series of magnetic dipoles with alternating orientation such that when charged particles pass through these alternating magnetic fields, they are forced to oscillate, emitting radiation in the form of intense and narrowly collimated X-ray beams. Two categories of insertion devices are used: wigglers and undulators. Figure 2.2 shows the electron trajectory inside the wiggler, the undulator and the bending magnet.

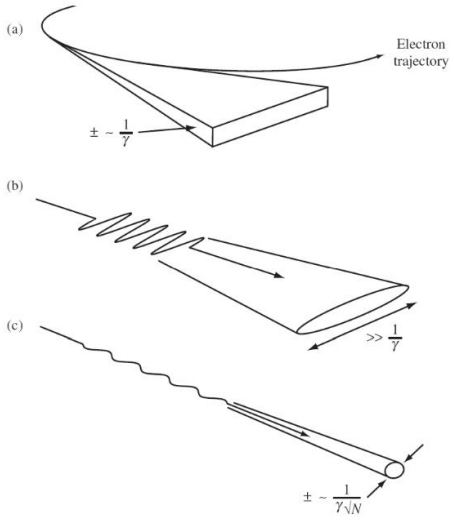

Figure 2.2: The different types of x-ray production in synchrotron facilities a) bending magnet, b) wiggler and c) undulator. The aperture is equal to 1/γ in a), greater than to 1/γ in b), and 1/(γ√N) in c). γ is the Lorentz factor and N is the number of magnetic dipoles. The sketches are taken from reference [84].

In undulators, the electrons are weakly deviated from a straight line, so the amplitude of the oscillations is small enough that it is possible for the X-rays emitted in the single periods of the electron's trajectory to interfere coherently. The produced spectrum has strong peaks at a specific X-ray energy (quasi-monochromatic wave) and its higher harmonics. On the other

hand, in wigglers, the deviation of the electrons is much stronger, so the amplitude of the oscillations is larger, and the cones of the emitted radiation do not superpose, and no more interference can occur. The produced spectrum presents a more continuous broad distribution (white peak).

2.2.2 Bragg diffraction

In crystalized materials, atoms are arranged in a repeating matrix, and within this matrix, different planes of atoms can be defined. The separation between these planes of atoms is determined by the interplanar distance d_{hkl} of a set of parallel planes belonging to the (h, k, l) family. In 1912, Max Von Laue [90] recognized that the X-ray wavelength is of the same order of magnitude as the interplanar distances in crystals (typically in the order of ångström). As a result, when X-rays strike a crystal, they are scattered in all space directions by the electron cloud surrounding the atoms arranged periodically in the crystal. The waves scattered from different atoms may have different phases due to taking different length paths, therefore some waves will arrive in phase leading to a constructive interference measured by the detector while those arriving in opposite phase will lead to a destructive interference by canceling each other.

According to Bragg's law [91] for diffraction, if the additional path taken by the second wave is equivalent to $\Delta L = 2d\sin\theta$, with θ being the diffraction angle, then the two waves will eventually interfere constructively and a series of diffraction spots will be produced in precise directions creating a diffraction pattern . The positions and shapes of the diffraction spots are inversely related to the distance between the crystal planes and size of the crystallites. Bragg's law derived by the physicists Sir W.H. Bragg and his son Sir W.L. Bragg in 1913 is the following:

$$n\lambda = 2d\sin\theta \quad \textit{Equation 2.1}$$

where λ is the x-ray wavelength, θ the Bragg angle, n an integer describing the diffraction order and d the atomic plane distance. This phenomenon is represented in figure 2.3 below. Equation (2.1) shows how from the measurement of diffraction angles, we can determine the interplanar distances of a crystal.

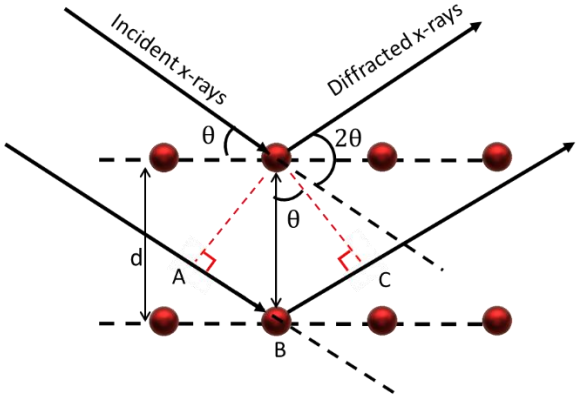

Figure 2.3: Representation of the X-ray diffraction conditions required to satisfy Bragg's law. The red points represent the atoms of two crystal planes separated by a distance d. The path difference for a given Bragg angle θ is ΔL=AB+BC.

To satisfy the Bragg's law, we must have:

$$\frac{n\lambda}{2d} \leq 1 \rightarrow d > \frac{\lambda}{2} \quad \textit{Equation 2.2}$$

Most XRD techniques are used to extract the diffraction pattern that gives information on the arrangement of atoms or molecules within the crystal i.e., its atomic structure. The absolute stress and strain (terms introduced in sections 1.3.1 and 1.3.2) inside the crystal can also be obtained by comparing the measured interplanar distance to the value found in the unstrained crystal (taken as reference). This latter can be derived from the lattice constants and the Miller indices (h, k, l) of the diffracting (h k l) plane following equation (2.3) for a hexagonal structure:

$$d_{hkl} = \sqrt{\frac{3}{4\left(\frac{h^2+k^2+hk}{a^2} + \frac{3l^2}{4c^2}\right)}} \quad \textit{Equation 2.3}$$

In the next section, we will introduce the three-dimensional (3D) reciprocal space in which we associate the crystal planes to real space and the diffraction spots to reciprocal space.

2.2.3 Diffraction in reciprocal Space

The reciprocal lattice is a mathematical construct that helps relate the crystal structure to the diffraction pattern produced by X-rays, it can be described by the Fourier transform of the real Bravais lattice. In the four-axis system, the reciprocal lattice basis vectors defined as $\overrightarrow{a_1^*}$, $\overrightarrow{a_2^*}$, $\overrightarrow{a_3^*}$ and $\overrightarrow{c^*}$ where $\overrightarrow{a_1^*}$, $\overrightarrow{a_2^*}$ and $\overrightarrow{a_3^*}$ lie in the plane of the crystal and are separated by angles of 120° angle and oriented in the same direction as the basis vectors $\overrightarrow{a_1}$, $\overrightarrow{a_2}$, $\overrightarrow{a_3}$ and $\vec{c}$ in the direct space of a four-axis system. But this is not the case with the three-axis system where the reciprocal

lattice basis vector $\overrightarrow{a^*}$ and $\overrightarrow{b^*}$ are at 60° angle and the reciprocal hexagonal lattice is rotated through 30° around the c-axis with respect to the direct lattice [92].

In the three-axis system, it is defined by three reciprocal space vectors $\overrightarrow{a^*}$, $\overrightarrow{b^*}$ and $\overrightarrow{c^*}$, but this is not the case with the four-axis system where the reciprocal lattice basis vector is used to describe the diffraction phenomenon in a more straightforward manner. The reciprocal vectors can be written as a function of the direct space unit vectors ($\vec{a}, \vec{b}, \vec{c}$) and the volume of one unit cell V such that:

$$\overrightarrow{a^*} = \frac{\vec{b} \wedge \vec{c}}{(\vec{a} \wedge \vec{b}) . \vec{c}} = \frac{\vec{b} \wedge \vec{c}}{V}$$

$$\overrightarrow{b^*} = \frac{\vec{c} \wedge \vec{a}}{(\vec{a} \wedge \vec{b}) . \vec{c}} = \frac{\vec{c} \wedge \vec{a}}{V} \qquad \textit{Equation 2.4}$$

$$\overrightarrow{c^*} = \frac{\vec{a} \wedge \vec{b}}{(\vec{a} \wedge \vec{b}) . \vec{c}} = \frac{\vec{a} \wedge \vec{b}}{V}$$

A set of lattice planes (h k l) in real space corresponds to one reciprocal lattice point in the reciprocal lattice space. This point corresponds to the end of a vector $\overrightarrow{H_{hkl}}$ pointing away from the origin in the direction of the normal to the (h k l) set planes. $\overrightarrow{H_{hkl}}$ is a linear combination of the reciprocal unit vector and can be expressed as:

$$\overrightarrow{H_{hkl}} = h\overrightarrow{a^*} + k\overrightarrow{b^*} + l\overrightarrow{c^*} \qquad \textit{Equation 2.5} \text{ ; } h, k, l \in \mathbb{Z}$$

The length of this vector is equal to $\frac{1}{d}$, where d is the inter planar spacing. The reciprocal lattice of a 2D hexagonal lattice is also a hexagonal lattice rotated by 30° around the c-axis of the direct lattice, distances are inverted while the angles between (h k l) planes remain constant.

Diffraction can also be illustrated in the context of the reciprocal lattice. The scattering vector $\vec{Q}$ describes the change in the wave vector of the X-rays diffraction and is defined as $\vec{Q} = \overrightarrow{k_s} - \overrightarrow{k_i}$ where $\overrightarrow{k_i}$ is the incident wave vector and $\overrightarrow{k_s}$ is the diffracted wave vector with $|k_i| = |k_s| = \frac{1}{\lambda}$. The diffraction phenomena in the reciprocal space are illustrated in figure 2.4 where the components Q_x and Q_z of the scattering vector $\vec{Q}$ represent the unit vectors of the reciprocal space system.

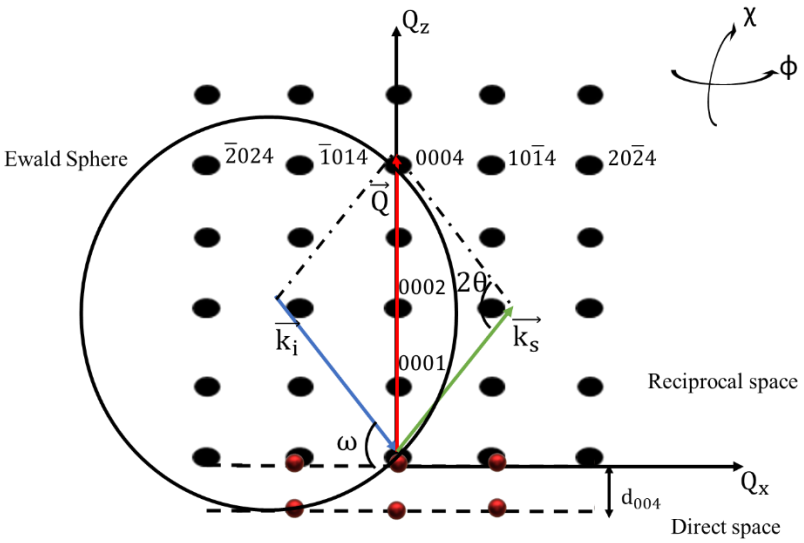

Figure 2.4: Illustration showing the direct space of (0004) plane, reciprocal lattice points corresponding to different direct space planes (h k i l), the scattering vector $\overrightarrow{Q_{0004}}$ with its corresponding $\overrightarrow{k_i}$ and $\overrightarrow{k_s}$, the incidence angle ω and the diffraction angle θ. The Ewald sphere is also shown.

Figure 2.4 shows the reciprocal lattice points, each representing one Miller plane (h k l), and we can visualize that $|\overrightarrow{Q_{hkl}}| = \frac{\sin\theta}{|k_i|} + \frac{\sin\theta}{|k_s|} = \frac{2\sin\theta}{\lambda} = \frac{1}{d_{hkl}}$ which means that we have:

$$\overrightarrow{Q_{hkl}} = \overrightarrow{H_{hkl}} \quad \textit{Equation 2.6}$$

This represents the vectorial translation of Bragg's law, called the Laue condition, and it implies that to satisfy Bragg's condition, the scattering vector $\vec{Q}$ must lie exactly on a reciprocal lattice point H. Hence, the scattering vector $\vec{Q}$ can be referred to as the diffraction vector and Bragg's law is satisfied in the reciprocal space for any point located on a diffraction spot. The position of these spots will shift due to the presence of macrostrains (the inter planar distance within the same family of plane is not constant). The Ewald sphere shown in figure 2.4 is proposed by Paul Peter Ewald [93]. It is a sphere of radius $r = |k_i| = \frac{1}{\lambda}$ used to determine which regions of the reciprocal space (i.e. which diffraction spots) satisfy the Bragg's law with the scattering vector $\overrightarrow{Q_{hkl}}$ under the condition of keeping the same wavelength λ and the same diffraction angle θ while varying only ϕ and χ with ϕ being the rotation angle around the axis to the sample's surface and χ the rotation angle around a tilted axis. We can deduce that for a certain Bragg angle, diffraction takes place wherever the Ewald sphere intersects a spot (black point). The scattering vector's length increases with an increase in θ up to a maximum of $\frac{2}{\lambda}$ to respect the condition presented in equation (2.2).

We must note that in hexagonal structures, some (h k l) reflections have shown theoretically zero intensity and are then not allowed in X-ray diffraction techniques. In fact, the amplitude

of the total intensity comes from the sum of the contributions to the diffracted wave of each atom of the unit cell. This sum is equal to zero if the following two conditions are satisfied: (1) l coefficient is odd and (2) 2h+k=3n, n∈ℕ.

2.2.4 Different scan types and measurement geometries

To define the scan types, we must first introduce the different rotations axes possible during a scan. Figure 2.5 illustrates a reference sample with the different axes of rotation. In this figure, we show the case of symmetrical planes where the incidence angle denoted as ω is the equal the Bragg angle θ. The different types of symmetries will be explained in detail later in this section. We define 2θ as the angle between the incident beam and the diffracted beam (taken with respect to the center of the detector).

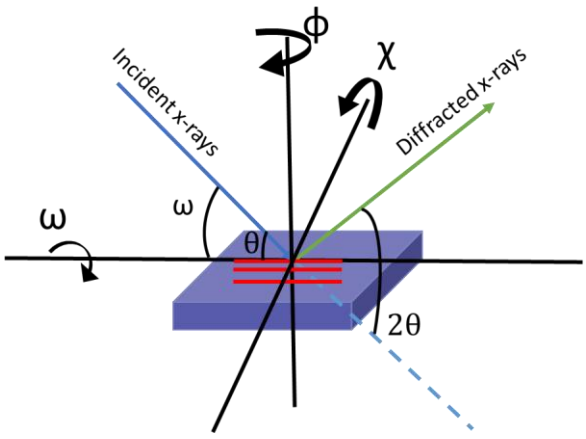

Figure 2.5: Illustration of reference sample, showing the axis of rotation. The angle ω refers to the incidence angle between the incident beam and the sample surface, θ to the Bragg angle, χ to the out of plane inclination of the sample with respect to the surface and ϕ to the rotation of the sample around the normal to the sample's surface.

Different scan types can be performed:

- ω scan: called "rocking curve", the incidence angle ω is changing with the rotation of the sample around the ω axis while the detector remains in its place so that 2θ remains constant. In reciprocal space (fig 2.5), the scattering vector $\vec{Q}$ traces an arc centered on the space origin and its length remains constant.
- 2θ scan: The detector is moved with the sample position remaining fixed. The scan follows the arc of the Ewald sphere, which means that the intensity will be collected along the Ewald sphere.
- ω - 2θ scan: The detector is rotated by 2θ and for each value of 2θ, the sample is rotated around ω. The length of the scattering vector $\vec{Q}$ changes, but its direction remains the same.

- ϕ scan: The sample is rotated around the ϕ axis (usually in the plane of the sample). The direction of the scattering vector $\vec{Q}$ changes, while its length remains same.
- χ scan: The sample is rotated around the χ axis. The direction of the scattering vector $\vec{Q}$ changes, while its length remains same.

Figure 2.6 shows the path of the scattering vector during ω scans, 2θ scans and ω-2θ scans.

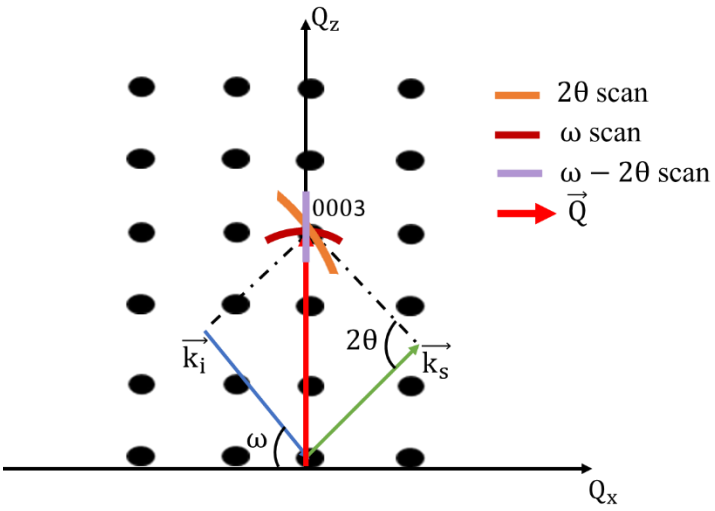

Figure 2.6: Schematic representation of the reciprocal lattice points of GaN with the scattering vector path for three different scan types (ω, 2θ and ω-2θ) measuring the (0003) planes.

To carry out a reciprocal space mapping, a sequence of ω - 2θ scans at various ω values can be made or 2θ scans at various ω values can be made. These scans take a lot of time, however the experimental set up in the beamlines we worked on has been upgraded so that the reciprocal space maps (RSM) can be built up over two-dimensional regions of the sample within a few minutes or even seconds instead of several hours, by using 2D detectors capable of measuring multiple 2θ positions simultaneously.
The specific experiments conducted at the ESRF will be discussed below in section 2.2.
Until now, we have only demonstrated diffraction in planes that are parallel to the surface with ω = θ, however some regions in reciprocal space (some lattice planes) are not accessible without adjustments in the diffraction angles (ω, 2θ, ϕ, χ). Therefore, we distinguish three distinct geometries possible that allow us to measure different areas of the reciprocal space providing different and complementary information. Figure 2.7 shows the three possible diffraction geometries i.e. three possible reflections: (a) symmetric reflection, (b) asymmetric reflection and (c) skew reflection.

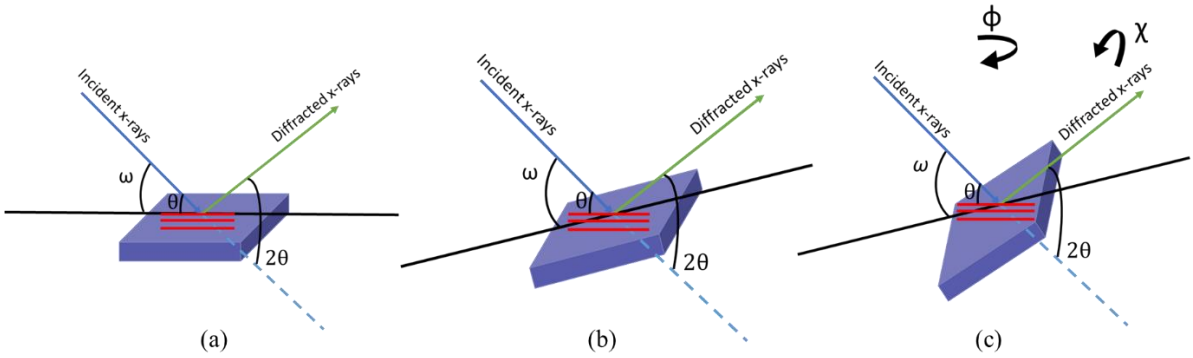

Figure 2.7: Possible diffraction geometries: (a) symmetric geometry, (b) asymmetric geometry and (c) skew geometry.

(a) Symmetric reflection: The incident and diffracted beams form equal angles with the sample surface ($2\omega = 2\theta$). It is used to measure (h k l) planes parallel to the surface of the sample. These reflections are used to measure the lattice tilt from mixed or screw dislocations [94]. Twisted planes cannot be measured with symmetric reflections.
(b) Asymmetric reflection: This is useful for measuring lattice planes that are inclined with respect to the surface of the sample (non-parallel to the surface). The sample should be rotated by θ plus an additional offset ω_0 so that the desired planes become horizontal, and we end up with incidence angle $\omega = \theta \pm \omega_0$ The ϕ scan of asymmetric reflections can be used to measure the twist (the sample is rotated around the normal to its surface) [29].
(c) Skew reflection: This is also useful for measuring lattice planes that are inclined with respect to the surface. The crystal is rotated 90° about the ϕ axis and tilted about the χ axis with an angle equal to the inclination of the diffracting planes with respect to the surface.

Despite these additional geometries, some (h k l) reflections remain forbidden: such as those where the amplitude of the intensity is equal to zero (section 2.2.3) or if the incident beam hits the back surface of the sample ($\omega<0$) or even if the direction of the diffracted beam points below the surface of the sample ($2\theta < \omega$).
Further constrains are brought by the angular limitations of the diffractometer and will be discussed further for each experiment.

As we already mentioned, the dimensions of our samples and the information needed require a synchrotron beam. In this thesis, we were allocated four synchrotron beamtime slots for three different X-ray diffraction techniques on three different beamlines at the ESRF: Scanning X-ray diffraction microscopy at the ID01 beamline, Macroscopic X-ray diffraction at the BM02 beamline and Dark field X-ray microscopy at the ID06 beamline. In section 2.2, we will present the characteristics of each technique as well as their experimental set up.

2.3 Synchrotron X-ray diffraction techniques

2.3.1 Macroscopic X-ray diffraction technique: BM02

The beamline BM02 installed at the ESRF uses high-brilliance X-ray synchrotron source to measure the structural properties of crystalline matter non-destructively at the macroscopic scale. It has been built and designed to combine many types of techniques like, macroscopic X-ray diffraction technique, wide-angle X-ray scattering and small-angle X-ray scattering, and it is distinguished by a high flux enabling fast data collection and reducing the time required for experiments compared to lab setup. In this thesis, we conducted the macroscopic X-ray diffraction technique.

This beamline is equipped with a beam size of 30 × 30 µm² and can perform tilt and twist scans within a small-time frame. Therefore, the objective from the experiment conducted at this beamline is (i) to determine the quality of large 40 x 40 µm² GaN platelet and (ii) to measure the tilt/twist of a large number of pillars (at the platelet scale) before and after coalescence.

To address the inherent divergence of the X-ray beam and to maximize the flux on the sample, the X-ray beam is refocused onto the sample using X-ray optical elements (mirrors, slits, crystal monochromators) placed in the optics cabin before entering the experimental cabin. The beam is monochromatized, at an energy ranging from 6 to 45 keV, by being diffracted from an initial Si(111) monochromator. Figure 2.8 displays a photo taken during the experiment showing the incident beam, the detector as well as the mounted sample.

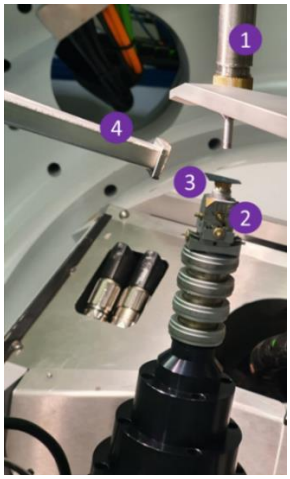

Figure 2.8: Experimental setup at ESRF BM02: (1) beamline, (2) sample holder stage (3) sample and (4) detector.

The different possible translations and rotations are explained in detail in [95]. We note that all rotation axes go through the center of rotation (COR) of the diffractometer and the only range-limiting parameter may be the sample environment mounted for in situ experiments and the maximum load of 20 kg on the sample stage.

In this thesis, one study was conducted on the BM02 beamline at the ESRF on different type of samples and at an energy of 9 keV with a 2D detector having a pixel size of 130 × 130 µm². During our experiment, issues with the optics caused the beam to oscillate, leading to a reduction in spatial resolution. To reduce the beam's oscillation, a 20 µm-diameter pinhole was added, however this came at the cost of reducing the beam's intensity. So, the monochromatic beam had a projected spot size ~30 x 80 µm². We performed ω-scans around symmetric Si reflection to measure the tilt in the pillars before and after coalescence. We performed ω-ϕ scans around asymmetric Si reflection by rotating the sample around its normal axis ϕ to measure the twist in the pillars before and after coalescence. Measurements around asymmetrical GaN reflection were also performed to determine the quality of 40 x 40 µm² GaN platelet. Figure 2.9 shows a geometrical scheme of the macroscopic X-ray diffraction at BM02 with a diffraction peak seen on the 2D detector.

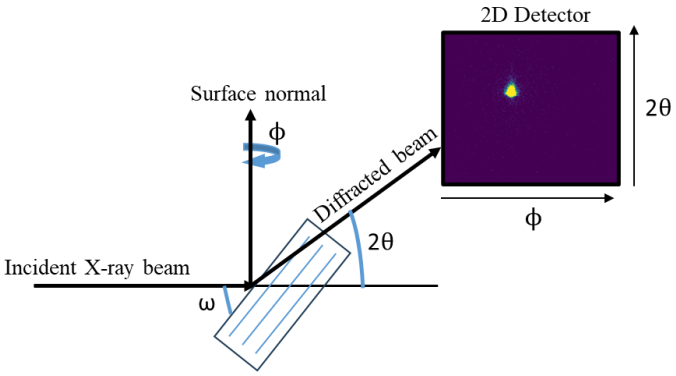

Figure 2.9: Schematic illustration of the geometry of the macroscopic *X-ray diffraction. The x axis of the 2D detector represents the ϕ values and the y axis the θ values.*

In chapter 3, we will describe the samples characterized at BM02, the performed measurements as well as the results obtained from the post-processing of the data followed by discussions. We will now explain the data treatment performed in this work to convert the raw data into the final results.

Post-processing tool

The recorded data sets are treated using python-based scripts developed by the beamline scientists. These scripts are then adjusted depending on the experimental setup we had and the information we would like retrieved due to the specificity and complexity of the conducted experiments.

Figure 2.10 shows the SEM image of one of measured samples at the BM02 beamline. It consists of two fully coalesced GaN matrices, each formed by 10 x 10 fully coalesced GaN platelets with a different pitch. One of the platelets measured during the experiment, is the one in the center position of the matrices with a pitch of 0.5 µm, it is highlighted with a red circle in the zoomed image in figure 2.10, however due to the deterioration of the spatial resolution,

we were measuring around two platelets in the y direction. The coalesced GaN and the Si nanopillars underneath the coalesced platelet were measured at BM02.

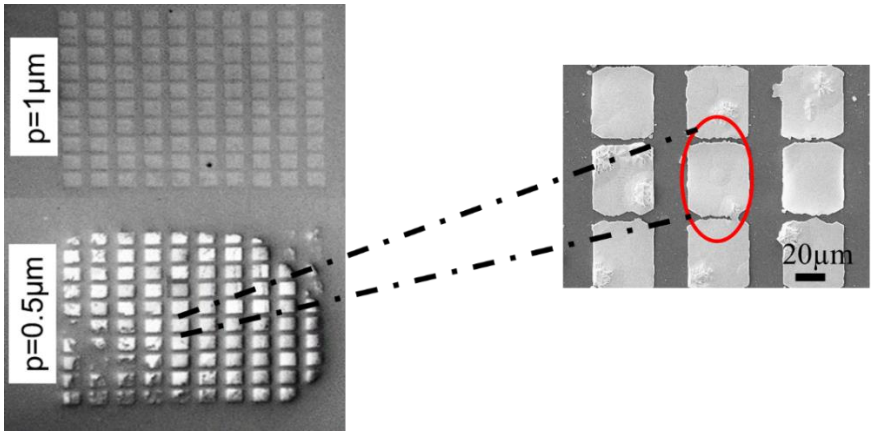

Figure 2.10: Two GaN matrices with coalesced platelets on different pitch arrays (p=0.5 µm and p=1 µm) and a zoomed in image on the measured platelet (marked with a red circle) at the BM02 beamline.

Measurements around the Si(111) reflection were conducted, the Bragg angle is equivalent to the incidence angle $\theta = \omega = 12.75°$. We performed ω rocking curves of 41 points with a step $\Delta\omega = 0.06°$ at a constant ϕ value and with $\Delta t = 0.5$ s. The acquired intensity can be seen on the 2D detector, and a region of interest (ROI) is chosen surrounding the position of the diffraction peak. We can also extract the diffraction pattern on the 2D detector of the integrated intensity and of the intensity at a precise ω value. Measurements like these performed on the Si before coalescence will allow comparing the full width at half maximum (FWHM) values before and after coalescence to determine any pillar tilt/twist.

2.3.2 Dark field X-ray microscopy: ID06

Dark-field X-ray microscope (DFXM) is installed on the ID06-HXM beamline at the ESRF [96] (now it is transferred to the ID03 beamline). This technique is a non-destructive full-field imaging technique able to provide 3D mapping of micro-structure and lattice strain of deeply embedded crystalline materials.

Unlike the macroscopic technique BM02, dark field X-ray microscopy provides a direct space image on the detector rather than just the diffracted beam. The beam can illuminate a large field of view (100 x 100 µm²) at once, and we obtain a real live image of the diffracted area. It has a better spatial then at BM02 reaching 30-100 nm [97]. Therefore, the objectives from the experiment conducted at this beamline is to (i) validate the results found from BM02 data and be able to measure only one 40 x 40 µm² GaN platelet of the same sample to get local information and (ii) measure new set of samples with different pillars pattern to determine the quality of small GaN islands.

The experimental set up allows the acquisition of far-field images or near-field images. Near-field images are non-magnified images recorded with 2D detectors placed directly downstream of the sample [97], they are used for classical diffraction topography and its extension like rocking curve imaging. In this present work, we used far-field imaging to characterize our samples. With this technique, we illuminate the whole sample at once with a focused monochromatic X-rays. Si(111) monochromator is used allowing a beam energy variation between 15 keV and 35 keV. The beam can be focused on the sample by Si-lenses and slits that limit the size of the beam at the expense of loss of intensity. The minimum beam size that can be obtained is of 30 x 30 µm² (h x v) and the maximum is of 5 x 5 mm² (h x v) [95]. The sample is mounted on a sample stage that can be tilted and moved by high precision motors.

The diffracted beam then passes through a compound reflective lens (CRL) comprising 88 2D Be lenses placed after the sample along the diffracted beam and serving as an objective. The far field detector is mounted at a distance equivalent to 5 m depending on the diffraction peak and the x-ray energy, as shown in figure 2.11. When applied as an objective, the CRL provides a magnification M in the direct space. For the present work, we produced a 10x magnified inverted (in both directions) real (x, y) image on the 2D far field detector. The pixel size of the 2D detector gives a real space resolution of 35 nm in the x direction while the resolution in the y direction depends on the beam incident angle of the measurement and the magnification. The 2D detector with a pixel size about 50-70 µm is able to capture all the different diffraction peaks in the far field. By altering the objective lens's focal length, the magnification and field of view can be changed and adapted to the experiment, enabling a zoom in and out of the measured area.

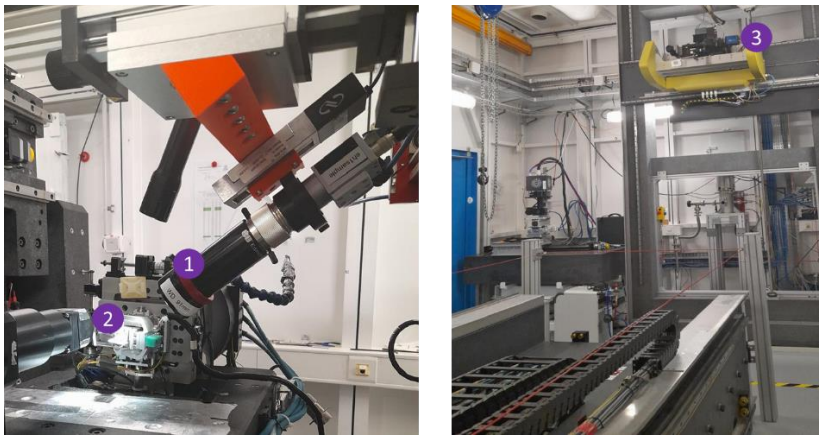

Figure 2.11: Experimental setup at ESRF ID06: (1)beamline, (2)sample and (3)far field detector.

Sets of $\omega - \phi$ scans and $\omega - \chi$ scans can be performed by rotating the sample around its normal axis or around its incidence angle ω to determine the tilt. An ω-2θ scan can also be performed by rotating the detector and performing a rocking curve for each 2θ value, this gives information on the spatial variations in the d spacing of a selected Bragg reflection to extract the strain in the material.

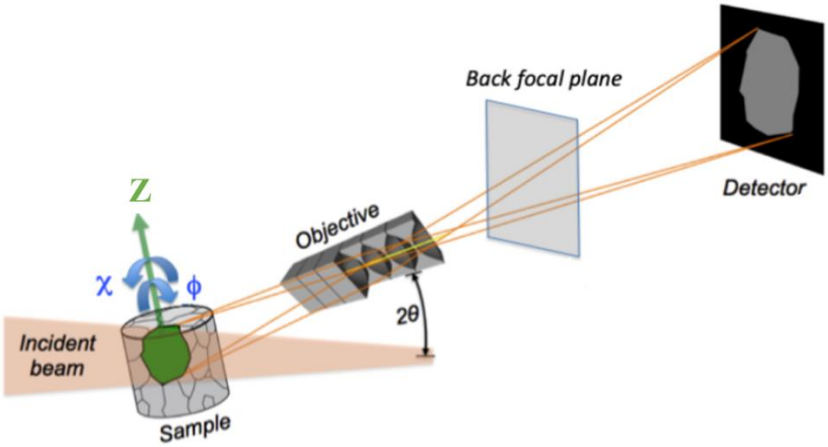

Figure 2.12: Geometry of the dark-field x-ray microscopy at ID06-HXM at the ESRF. The incident beam illuminates a crystalline element of interest, and the diffracted radiation is imaged by means of an x-ray objective and a 2D detector. The tilt can be obtained through rotations around ϕ and χ. The image is taken from ref. [97].

In this experiment, the energy of the incident beam was fixed at 16 keV. A set of ω-ϕ scans around GaN reflection was performed on the same 40 x 40 µm² GaN platelets studied at BM02 and on new samples with GaN coalesced on new different pillars pattern. We note that during the experiment at ID06, we were limited to low θ values (θ_{max}= 25°) which resulted in a wide projection of the beam, illuminating several 40 x 40 µm² GaN platelet. Therefore, we switched to a transmission configuration where the beam passes through the sample instead of reflecting off it without being absorbed by the Si and we were able to achieve a beam that was nearly perpendicular to the surface of the sample. The description of the characterized samples, the performed measurements as well as the results will be presented in chapter 3. A description of the data treatment process is presented below.

Post-processing tool

The data obtained from this experiment were extracted using darfix which is a python library developed by the ID06 beamline scientists [96]. This package provides initial data processing and visualization tools and includes Orange add-on [98] that allows the creation of computational workflows by linking the different tasks together using the darfix graphical user interface (GUI). The software can also provide the relevant instrument angles from the input files for each scan.

Darfix offers numerous task that can be accomplished independently through a workflow so that for every task there is a different dedicated widget. Figure 2.13 presents our workflow with the tasks we used for data selection, pre-processing and visualization. We used (1) raw data selection, (2) region-of-interest selection, (3) integrated intensity plot, (4) noise removal, (5) shift correction, (6) rocking curves and (7) grain plot.

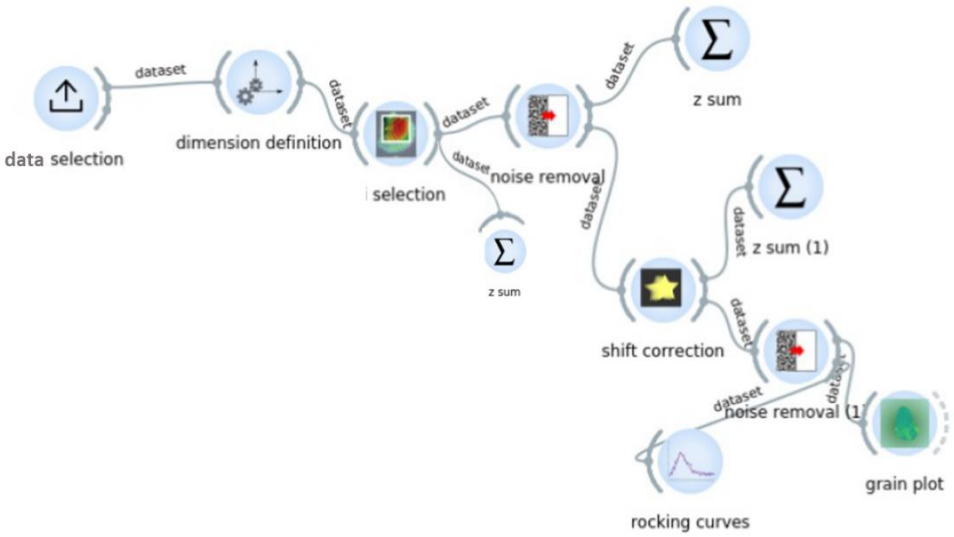

Figure 2.13: Darfix GUI showing the workflow used in this work composed by three modules: data selection, pre-processing algorithms, and analysis and visualization.

For the data selection, we will consider the data obtained from the measurements around the GaN(101) reflection on coalesced GaN lines shown in figure 2.14.

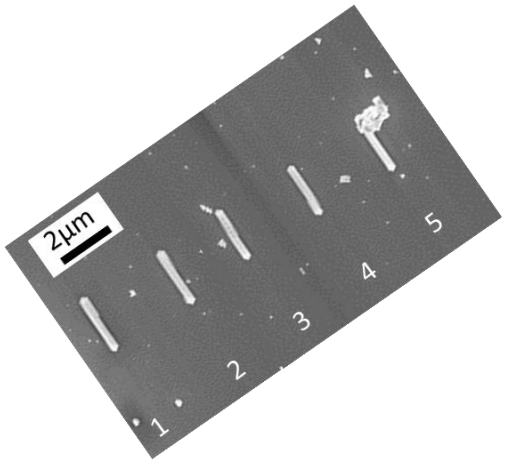

Figure 2.14: Inclined SEM image of five fully coalesced GaN lines (numbered from 1 to 5).

On these lines, we performed ω-ϕ scans, which means we performed rocking curves around the incidence angle ω for 21 different ϕ values. The obtained data is explored by the workflow presented in figure 2.12. Following the data selection, we selected a ROI that contains the entire peak. Next, we show in figure 2.15, the intensity map of the five lines at different ϕ values.

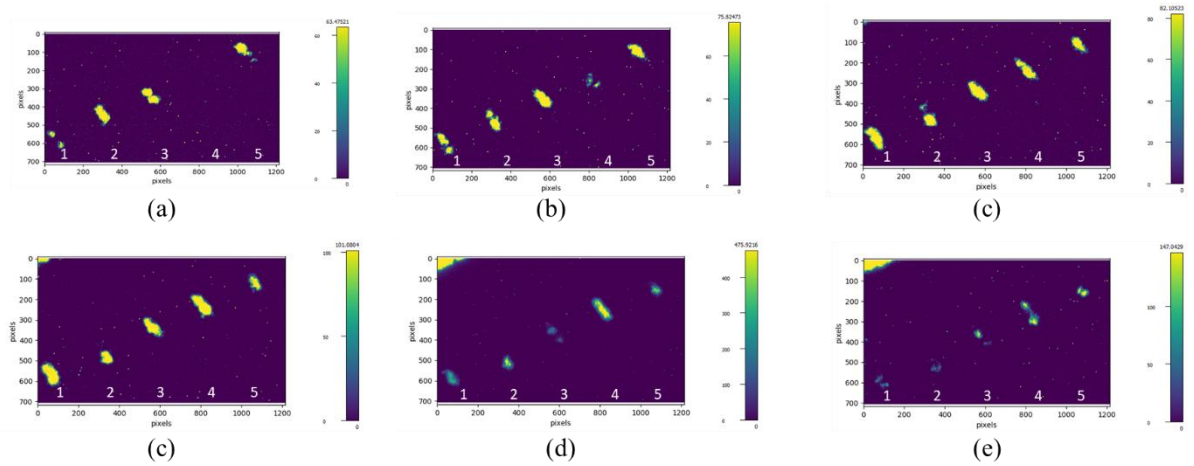

Figure 2.15: Integrated intensity from ω rocking curve at different ϕ angles.

We can observe that certain lines become visible at specific ϕ angles, while others disappear and reappear at different phi angles indicating that the lines have different orientations. These results will be more detailed in chapter 3.

We notice the presence of hot pixels in the map which can be removed by data cleaning process. Different tasks can be operated on the raw data to return a cleaner dataset such as:

- hot pixel removal: a hot pixel is an isolated pixel having a higher intensity than the other pixels around it, and it is usually not part of the object we want to analyze.
- shift detection and correction: a shift of the sample as a function of the rotation angle can be caused due to alignment errors in the experimental set up.

These techniques provided by darfix in the noise removal widget and shift correction widget. The algorithms used for these operations are explained in [96]. Following the filtering of the data, we check the integrated intensity over all ϕ angles in figure 2.16.

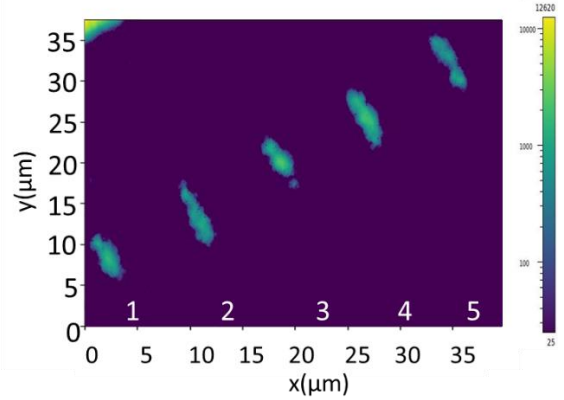

Figure 2.16: 2D map of the integrated intensity of the five GaN coalesced lines.

We notice how the map clarity has increased, however, some pillar information is lost, this means the intensity of the applied noise removal needs to be reduced.

Finally, in the analysis and visualization model, it is possible to extract, the ω center of mass map, FWHM map and many other plots. We show in figure 2.17 the center of map for of the five lines.

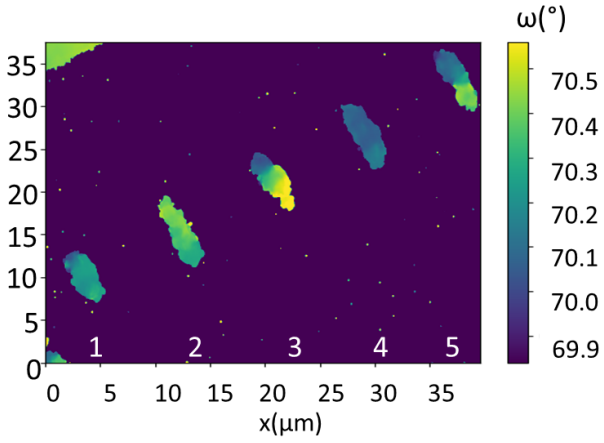

Figure 2.17: Centre of Mass map for ω of the five lines.

This same workflow is launched with different input data set from the rest of the performed measurements.

2.3.3 Scanning X-ray diffraction microscopy: ID01

Numerous techniques are available on the ESRF ID01 beamline, such as small-angle X-ray scattering, grazing-incidence diffraction, and highly focused beams for coherent diffraction imaging and nano-diffraction mapping (Scanning X-ray Diffraction Microscopy - SXDM) which is the technique used in this work.
This technique presents many advantages:

- Equipped with a nano-beam with high spatial resolution, the incident beam can be focused down to 25 nm which will allow us to retrieve local information from individual pillars unlike the macroscopic technique at the BM02 beamline where we were had large beam size.
- Not limited to the study of the surface of structures as the EBSD technique (explained later in section 2.4), instead it gives information from the overall probed volume (few microns at an energy of 10keV).
- The high flux of the nanofocused beam allows detecting on a 2D detector the diffracted intensity from the thin Si sections in the nanopillars contrary to the dark field X-ray microscopy at the ID06 beamline.
- Gives access to the 3D Bragg peak at each position of the sample which will give us the strain distribution, tilt distribution and peak broadening maps.

- Allows fast scans using the continuous scan mode which combines high-speed continuous motion of the positioning system (continuously moving the sample) while recording scattering images with a fast 2D detector for every point along a rocking curve.

Considering the advantages of this beamline over the others especially the nano size of the beam, the objectives of the experiments performed within are: (i) to measure different sets of pillars (at the nanoscale) prior to the regrowth and after coalescence, (ii) measure the orientation and strain distribution of coalesced GaN layers (at different growth time) and (iii) measure different patterns and different pitch values.

Figure 2.18 is a photo of the experimental set up taken during the experiment.

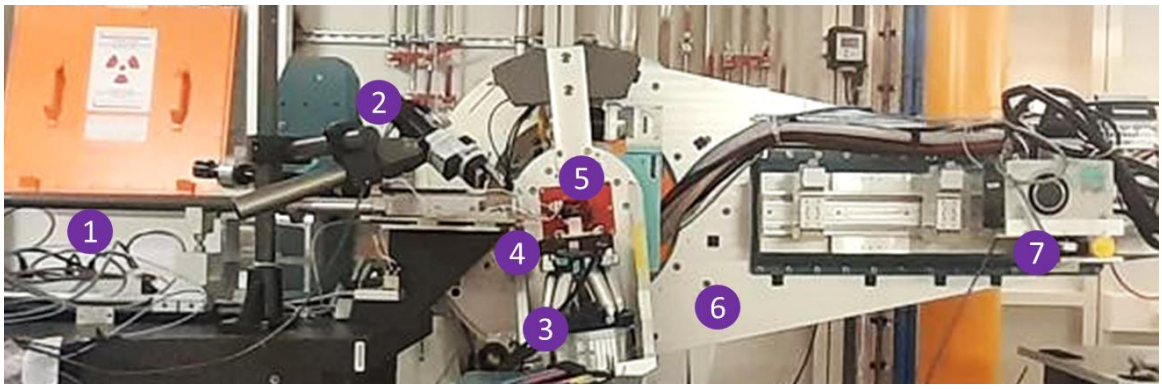

Figure 2.18: Experimental setup at ESRF ID01: (1) beamline and optics, (2) optical microscope, (3) hexapod with piezo stage, (4) piezo stage, (5) sample, (6) rotable diffractometer arm, and (7) detector.

The distance separating the experimental hutch and the x-ray source is 118 meters [99]. Many monochromators and optical elements are placed between the source and the sample, changing the characteristics of the synchrotron beam. Typically, the beam passes by small size slits to (1) shape the white beam as a function of required illumination and to (2) clean the beam and limit the heat load on all optical elements. This helps to minimize thermal deformation when only a small fraction of the beam is needed, such as for nano diffraction. The monochromator used in ID01 is made of Si(111), and by precisely adjusting the angle of the crystal, the monochromator selects the desired wavelength from the broad spectrum.

The beam is then focused at the rotation center of the diffractometer using a Fresnel zone plate (FZP) combined with molybdenum order sorting aperture (OSA) needed to remove high diffraction orders produced by the FZP [100]. An optical microscope is used to locate regions of interest on the sample allowing to set up a coordinate system. The sample is mounted on a hexapod with a piezo stage on top. The piezo motors provide a few nanometers spatial resolution.

In practice, the sample can be tilted by ω so that the Bragg condition is satisfied. Then a rocking curve is performed by slightly changing the value of ω. For every incidence angle ω of the rocking curve around the theoretical Bragg angle, an x-y piezo scan was performed, and

diffraction images (2D detector) were taken with a nanometer spatial resolution at each position for each value of ω creating a diffraction pattern on the detector for each position on the sample. The 2D detector has a large 2θ aperture which means the ω scan is performed simultaneously for different values of 2θ, which then provides a 3D RSM for each position on the sample. A schematic overview of the experimental set up is shown in figure 2.19.

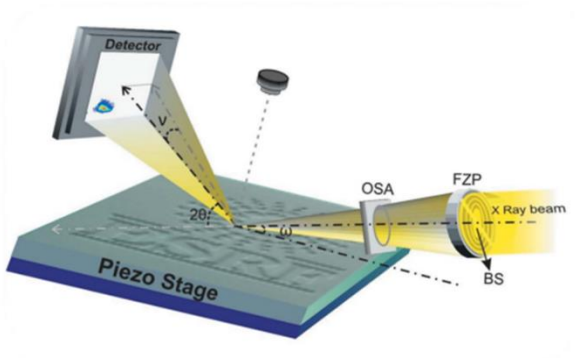

Figure 2.19: Schematic overview of the ID01 experimental setup: the X-ray beam is focused using an FZP and OZA , ω is the incidence angle, θ the Bragg angle and υ the deviation angle of the signal from the coplanar geometry. The optical microscope is positioned above the sample. This schematic is taken from ref [100].

The diffracted beam is collected by the detector placed on the arm rotating which is moved to the appropriate 2θ angle to capture the diffraction spots of interest. The ID01 beamline offers two types of detectors [99]: a two-dimensional (2D) Maxipix™ detector (square of 4 chips, 516 × 516 pixels with pixel size= 55 x 55 µm²) [101], and a 2D Eiger detector (1030 x 2164 pixels with pixel size= 75 x 75 µm²). We used Maxipix for one experiment and Eiger for another depending on their availability in order to save time. Maxipix presents limits in the sample-to-detector distance up to 2.36 m and 2θ = 68° and the Eiger presents limits in the sample-to-detector distance up to 1.76 m and 2θ = 120°. The two detectors are ultra-fast and recently developed, making it possible to acquire the data fast enough to realize such an experiment because for every incident angle ω of the rocking curve, an x-y scan was performed with Δx and Δy steps in the nanometers order (e.g. 80nm, 100nm, 200nm). So, at the end, we were scanning huger number of points (e.g. 40000 points, 25600 points) at each ω value for a certain duration that's why the measurement must be fast, and even with that it takes few hours.
ID01 developed a scanning approach called K-map to execute the scan and the sample's rocking curve in a reasonable amount of time (a data volume of about 1 TB was recorded in about 3 h). It is based on combining high-speed continuous motion of the positioning system, with a continuous readout and a high-frequency image recording system. This is done by using a pixel detector, a piezo scanning stage (P-563 PIMars XYZ Piezo System, PI GmbH and Co.) and a hardware module that synchronizes the detector and the scanning stage. It is fully described by the authors [100].

In this thesis, two experiments were realized on the ID01 beamline at the ESRF. X-ray diffraction measurements were conducted on the GaN and the Si in the pillars on different type of samples using a monochromatic nano-beam with an energy of 10 keV. In chapter 3, we will describe the samples characterized at ID01, the performed measurements as well as the results obtained from the post-processing of the data followed by discussions. We will now give a detailed explanation on the post process work conducted to convert the raw data into its corresponding reciprocal space maps for one dataset associated with one chosen sample.

Post-processing tool

The complete acquisition consists of a five-dimensional dataset for each scan to process and analyze: two dimensions for real space positions on the sample x and y, one for the incidence angle ω and two x' and y' positions on the detector taken with respect to the center of the detector. With this huge amount of data, there is a need to make the experiment as efficient and as feasible as possible, therefore, enormous efforts have been made over the years in numerous fields (engineering, physics, computer science) to develop algorithms to treat the acquired data and extract three-dimensional reciprocal space maps at each spatial position. In this work, the data was processed and analyzed using specific python library developed at the ID01 beamline [102]. These post treatment scripts undergo ongoing adjustments depending on the experimental setup and the information that needs to be retrieved due to the specificity and complexity of the conducted experiments. However, in addition to the generic scripts provided by the ESRF, significant amount of additional processing is required in order to extract the desired data. A lot of work has been done in this thesis to comprehend and adapt the python codes for the data treatment and image analysis work.

During one of the SXDM experiment, we investigate a reference sample denoted sample A that contains only GaN GaN/AlN/Si/SiO_2 etched nanopillars before coalescence (prior to the pyramids growth) separated by 0.5 µm in order to extract the orientation of the GaN pillars prior to any regrowth. An area of 20 x 20 µm² has been scanned, ω rocking curves were performed around the asymmetrical Bragg reflection GaN (105) with a step size $\Delta\omega = 0.05°$ and an angular range of $59.5° < \omega < 61°$. For every incidence angle ω of the rocking curve, an x-y piezo scan was performed, and diffraction images were taken every 80 nm in the x direction and 80 nm in the y direction. Figure 2.21 shows the intensity measured at each (x, y) for one SXDM scan i.e. for one ω value = 60.21° (given its maximum peak intensity, the ω value corresponding to the midpoint of the rocking curves is chosen) during the experiment. The GaN pillars can be easily distinguished as a dot-like pattern of high intensity while regions with no diffracted signals correspond to damaged area of sample A (missing pillars, fallen pillars) due to a problem in the pillar fabrication process that is undergoing continuous optimization.

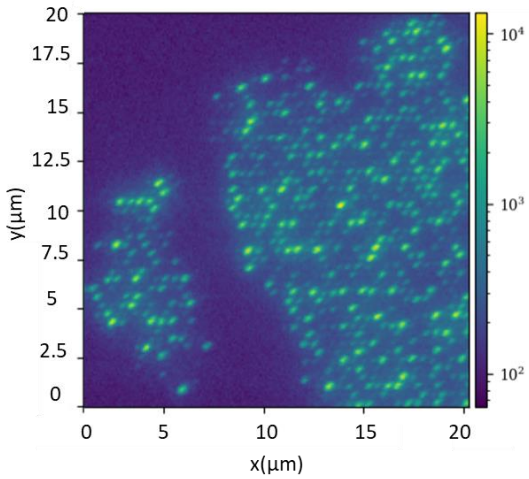

Figure 2.20: 2D map of the intensity measured at each (x, y) of sample A for one ω value of the SXDM scan.

The next step is computing the integrated intensity of sample A over all the scans at every position (x, y) for all the ω values as shown in figure 2.21(a). We notice from figure 2.21(a) that the image is unclear and blur, this is due to a sample drift that occurred during the experiment. This shift may happen if the sample is not quite sitting at the center of rotation of the diffractometer so the scanned area will move while changing the values of the incidence angle during the rocking curve. Therefore, a drift correction is required, and one way to solve the problem is to use an interactive widget and manually mark identical points in successive images to estimate the shift. For most of the datasets in this work, this method was used; otherwise, a linear interpolation can be used if the sample drift is linear: one can simply discard the scan where the intensity changes abruptly and use the rest to estimate the shift; then, the missing shift point is found by interpolation. Figure 2.21(b) shows the integrated intensity of sample A over all the scans at every position (x, y) after drift correction.

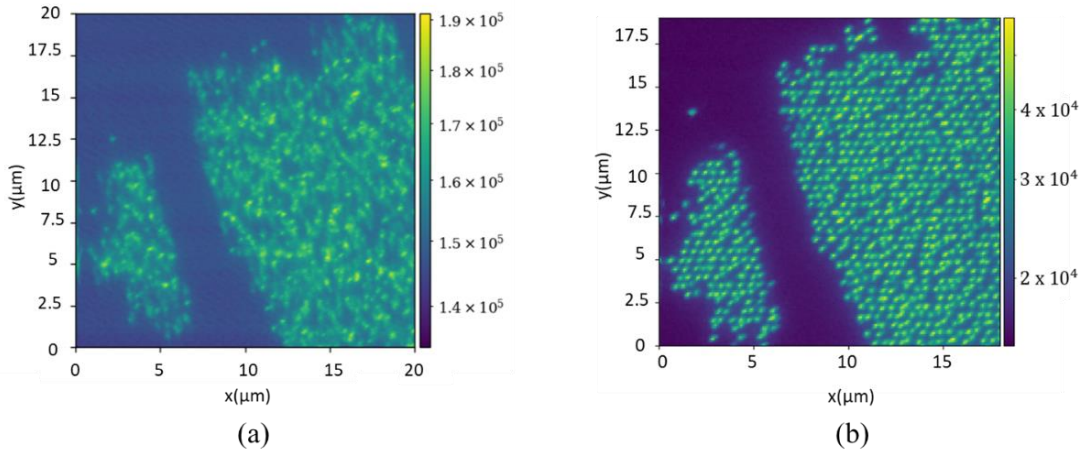

Figure 2.21: 2D map of the integrated intensity of sample A shown in logarithmic scale (a) before drift correction and (b) after drift correction.

The dimensions of the map after shift have changed and we have lost part of the scanned area due to the shift correction. Once the drift correction is done, a check if any discrepancies between the "real" and "experimental" value of the motor angle (2θ) exists due to alignment imprecisions is needed. This test will be presented in chapter 3 for each dataset (each measurement) and an angular offset is estimated.

Once angular offsets have been established, we proceed to the transformation from angular to reciprocal space. The dataset obtained is a 5-dimensional dataset in the form I(x, y, ω, detx, dety) with I being the scatter intensity, (x, y) are the position of the sample relative to the beam and (detx, dety) are the horizontal and vertical directions of the 2D detector active area.
The incidence angles and the angles made by the scattered beam with respect to the 'straight-through' incident beam are converted into reciprocal lattice units [103]. Therefore, the diffracted intensity can be expressed in reciprocal space to obtain I(x, y, q_x, q_y, q_z) with q_x, q_y and q_z being the q-space coordinates.
Figure 2.22 displays the projections of the Bragg peak along q_x, q_y and q_z which represents the average reciprocal space volume. A volume of interest (VOI) (red rectangle) is selected in order to fit a Gaussian function to the intensity contained within it, as a function of the position which will gives us the Q_x, Q_y, Q_z components of the reciprocal vector $\vec{Q}$ at each position (x ,y).

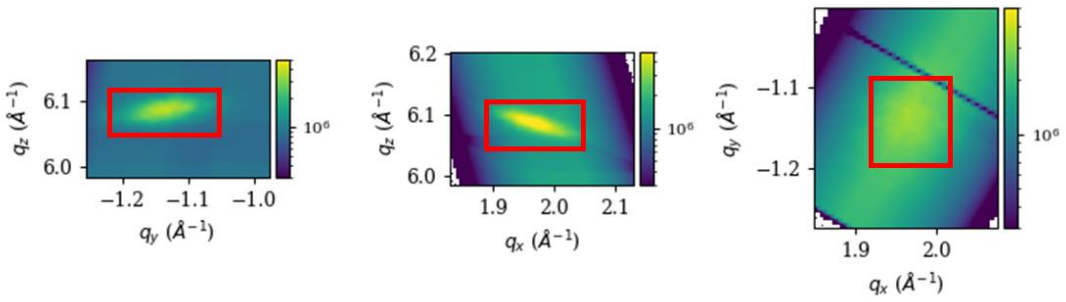

Figure 2.22: Projection of the Bragg peak intensity along q_x, q_y and q_z.

This acquisition of $\vec{Q}$ at each sample position allows the computation of the local structural parameters such as interplanar distance and the tilt (intensity + orientation) relative to a reference axis. The average peak position over (x, y), $\vec{Q}_{mean}$, is computed and taken as reference. The relative angular distance between $\vec{Q}$(x, y) and $\vec{Q}_{mean}$ is calculated from their dot product equation. Figure 2.23(a) shows the result of such calculation for sample A, as it displays a 2D map of the angular deviation of the normal of the 105 planes in each pixel from the mean orientation, we will refer to it as relative rotation map.

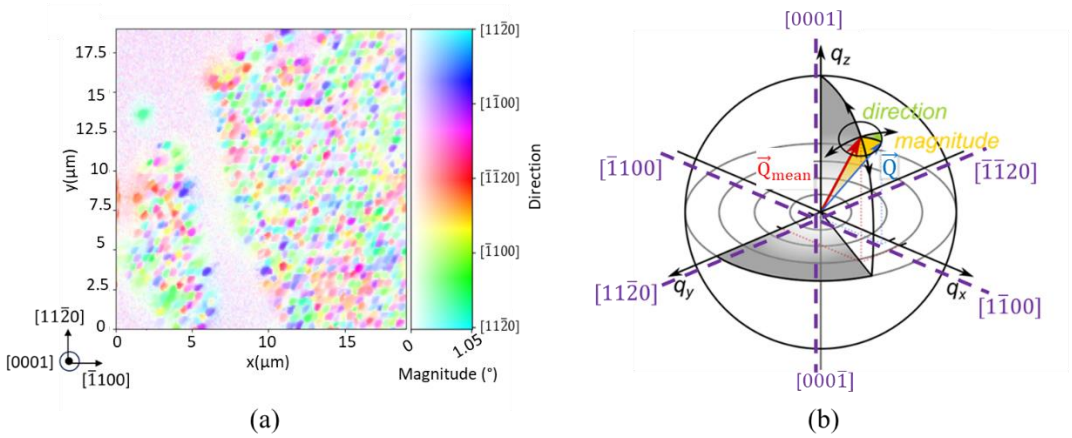

Figure 2.23: (a) 2D map of $\vec{Q}_{105}$ relative rotation of sample A. The hue and saturation of the colors in the map represent tilt direction and magnitude, respectively. (b) Schematic representation of $\vec{Q}_{105}$ deviation from q_{av} in reciprocal coordinate system.

Figure 2.23(a) presents two kinds of information: (i) the magnitude of the tilt between each (x, y) position and the mean orientation and (ii) the direction at which the (105) plane are inclined at each position (x, y). We will use the information presented in figure 2.23(b) to interpret figure 2.23(a).

The blue vector in figure 2.23(b) corresponds to the reciprocal space vector $\vec{Q}$ at a certain (x, y) position in the sample in figure 2.23(a), the red vector in figure 2.23(b) corresponds to the chosen reference orientation and that is $\vec{Q}_{mean}$. The yellow colored angle in figure 2.23(b) represents the relative angular distance between $\vec{Q}_{mean}$ and $\vec{Q}(x,y)$ at a certain (x, y) position. This angular deviation is presented as the tilt magnitude with respect to the mean orientation for each (x, y) position in figure 2.23(a); we notice that a maximum tilt (inclination) magnitude between $\vec{Q}(x, y)$ and $\vec{Q}_{mean}$ is equal to 1.05°.

It is also essential to compare the direction of the two vectors: we notice that in the reciprocal space in figure 2.23(b), the two vectors $\vec{Q}_{mean}$ and $\vec{Q}(x,y)$ are pointing at different directions. This means that in the real space on the sample, the family of the (105) planes at the position (x, y) are tilted along a different direction compared to the average orientation. In figure 2.23(a) if two pixels (two positions) have different colors, it means the corresponding $\vec{Q}(x,y)$ vectors at those points are pointing in different directions in the reciprocal space and the corresponding (105) planes are inclined towards different directions in real space. For instance, if a point is colored by red, this means that in the real space direction, the (105) planes at this point are inclined along the [$\bar{1}\bar{1}$20] direction. Therefore, we notice from figure 2.23(a) that the pillars exhibit a variety of colors, indicating that their corresponding $\vec{Q}(x,y)$ point at different directions in the reciprocal space which means they are disoriented with respect to each other. This data treatment process is repeated for every SXDM scan and for different samples.

2.4 Electron backscatter diffraction technique

2.4.1 Set up and description of the technique

As mentioned in section 2.1, the number of beamtime possible that can be allocated, and its duration are very limited. Therefore, we employed additional characterization techniques such as the electron backscatter diffraction technique, suitable for characterizing crystal structure of thin films at the microscale.

EBSD is a technique used for characterizing the microstructure of crystalline and polycrystalline materials. It offers significant advantages such as: (i) it can identify different grain properties such as size, shape, orientation, grain boundaries and phase distributions for polycrystalline materials with high spatial resolution [104], (ii) it provides local crystal orientation, and (iii) it is relatively fast, enabling large areas of the film to be scanned efficiently.

Given these advantages, we used the EBSD tool in the CEMEF laboratory to (i) compare the EBSD results with the XRD results and (ii) to measure the orientation of coalesced GaN platelets on larger number of samples with different pillars distribution. We note that EBSD presents certain limitations that restricted us from measuring the GaN pillars. These limitations will be discussed just after explaining the EBSD principles.

The EBSD measurements were conducted on a ZEISS Supra40 microscope equipped with a field emission gun-scanning electron microscopy (FEG-SEM). We used the EBSD tool in the CEMEF laboratories to characterize more samples and extract the GaN crystalline orientations along with other properties.

EBSD technique consists of sending a focused electron beam to the surface of the sample. The sample is generally tilted by 70° sample towards the detector to increase the quality of the signal obtained. The electron beam scans the surface of the sample over a discrete grid (rectangle in this work) with a fixed step size. The electrons interact with the atomic nuclei of the crystal and are then scattered backward out of the sample, they are referred to as backscattered electrons (BSE). As these electrons penetrate the crystal, they interact with the periodic arrangement of atoms within the crystal lattice and since they have short wavelengths, they will fulfill the Bragg condition with respect to the atomic planes. This means they will diffract in the form of two cones whose tips are at the point where the electron hits the plane. The EBSD detector has a phosphor screen that captures these scattered electrons. The intersection of the diffraction cones with the phosphor screen forms hyperbolic shapes. However, because the angles are very small, these hyperboles look like pairs of parallel lines on the screen forming an electron backscatter pattern (EBSP).

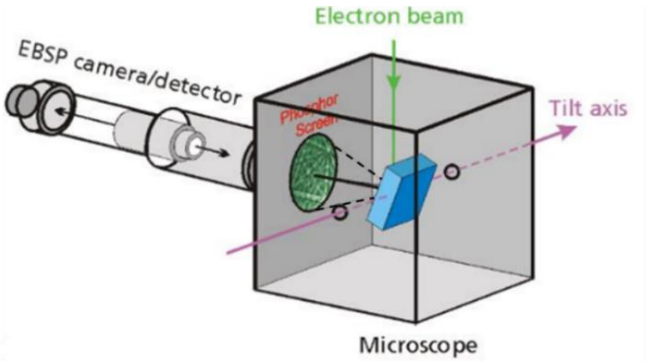

Figure 2.24: Schematic illustration of the EBSD set up taken from [105]*, the lines in green color on the surface of the Phosphor screen illustrate the Kikuchi bands and the dashed lines represent the cone*

The resulting EBSP is a diffraction diagram composed of an overlapping of these lines that are called Kikuchi bands while each Kikuchi band corresponds to a different diffracting plane [106][107]. An example of Kikuchi pattern is shown in figure 2.25(a).

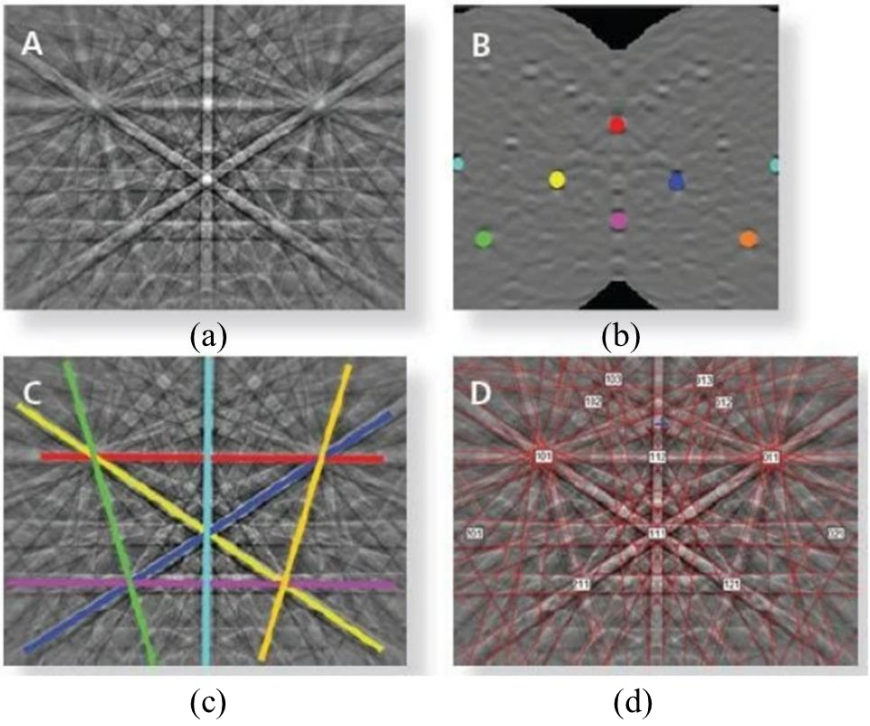

Figure 2.25: (a) example of EBSP composed of Kikuchi bands (b) the Hough transform image showing the identification of the highest intensity peaks; (c) the corresponding Kikuchi bands in the EBSP and (d) the indexed diffraction pattern. This figure is taken from ref.[108].

The EBSP is used to identify the phase and the orientation of the crystal lattice at the point of the sample that generated the EBSP though Hough transform [109] [110]. Hough transform identifies the positions of the Kikuchi bands by converting the bands with the highest intensity

from lines to points called peaks that can be easily located as shown in figure 2.25(b). The corresponding Kikuchi bands are shown in figure 2.25(c).

Once EBSPs have been transformed into the Hough space, the indexation of Kikuchi band can be achieved. Given the structure geometry (wurtzite in our case), and knowing the Kikuchi band positions, it is possible to calculate the angle between each pair of bands. The computed angles are compared with a predetermined list of interplanar angles between the atomic planes for the structure present within the sample (GaN in our case). If a coherent match between the two lists of angles is found, each detected Kikuchi band is assigned to a certain crystallographic plane. The indices on the Kikuchi bands shown in figure 2.25(d) correspond to the Miller indices of the crystal planes that produced those bands. From this, the crystal orientation is formulated. We note that the image acquisition and calculation of the crystallographic orientations are fully automated and fast. Following the Hough transform, a more sophisticated Kikuchi pattern indexing method is used. It is based on kinematic simulation that would model the expected positions of the Kikuchi Band. This will enable a refinement of the original solution and an improvement of the angular resolution up to 0.2° [112]. It is also possible to extract lattice strains from EBSD patterns, but this requires advanced processing methods such as image cross-correlation of diffraction patterns [111]. In this work, the classical Hough-transform-based analysis is employed, so only crystal lattice rotations are considered.

In this work, EBSD mapping of c-plane GaN layer has been performed on different samples tilted by 70° and the step size along x and y is 0.1 µm. To avoid any non-indexed points coming from noise and most often correspond to diffraction diagrams of bad quality, three frames are measured at each position (x, y), with t=15 ms for each frame and then the average result is considered.

Now that we have defined the interests of EBSD as well as the way it operates, it is important to present its limitations:

- EBSD is only sensitive to the sample surface, as it can only penetrate 10 nm below it.
- EBSD can only be used on smooth surfaces so that high quality Kikuchi bands appear. Samples are often chemically or electrically polished before measurement. However, in our case, the surface was smooth enough to allow the acquisition of high quality bands, therefore we did not do any polishing prior to the measurements.
- The non-conductive nature of GaN and SiO_2 present in our samples causes the incident electrons to accumulate in their location instead of being evacuated which can lead to a localized charge buildup and therefore can shift the beam trajectory as the electrons can interact with the accumulated charge [113]. During our experiment, this issue was avoided by decreasing the beam voltage to 15 kV, which reduced the number of electrons that remained present and therefore prevented a large beam drift.

In chapter 3, we will describe the samples characterized at with EBSD, as well as the results obtained. We will now give a detailed explanation on the post process work conducted to convert the raw data into results.

2.4.2 Post-processing tool

The acquired EBSD data were analyzed with the MTEX library [114], an open-source MATLAB toolbox specifically developed for analyzing crystallographic textures of EBSD data.

The MTEX library allows the generation of multiple plots like grain reference orientation deviation (GROD), pole figures, grain sizes… GROD map shows the misorientation between the orientation θ_i at a position (x_i, y_i) and the mean orientation. In this work, we mostly extracted the GROD maps to investigate the misorientation in the GaN film with respect to the mean orientation as shown in figure 2.26.

Filtering the data is necessary to reduce the orientation measurement noise that manifests in unclear Kikuchi band positions and is caused by experimental inaccuracies. The MTEX library provides several methods for filtering EBSD data. For example, it is possible to set a misorientation angle threshold in order to exclude the impact of high-angle grain boundary (HAGB) (higher than 10°). This method, typically employed for polycrystalline materials, was not utilized in this study. The GaN material under examination has a nearly monocrystalline structure with boundaries that exhibit much lower misorientation angles. In this study, a different filtering tool was used which consists of removing all grains with size < 5 pixels. Due to the small beam drift during the experiment, the plots obtained had some pixels that did not correspond to any diffracted GaN grain. The difference before and after the filtering process of the data is shown in figure 2.26.

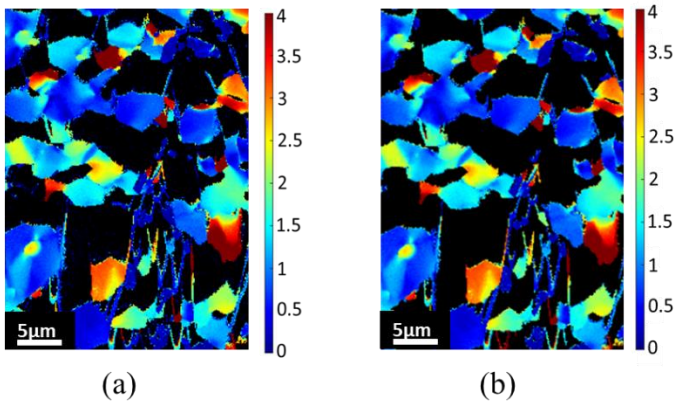

Figure 2.26: GROD map of a sample characterized in this thesis with (a) raw data and (b) with filtered data displaying grains larger than 5 pixels only. The intensity scale is in (°).

Further analysis of the acquired EBSD data is possible, such as determining the geometrically necessary dislocation densities (GND) present at the grain boundaries required to accommodate a measured misorientation. In other words, GND represent the minimum number of dislocations necessary to result in a given misorientation angle. Since EBSD data provides local orientation θ over each spatial position (x, y) of the measured grid, it is possible to partially compute the elastic curvature tensor for every pixel in the EBSD map.
From a local angle misorientation ($\Delta\theta = \theta_1 - \theta_2$) between two neighboring positions (neighboring pixels) separated by a distance equal to Δx on the surface of the specimen (as shown in figure 2.27), we can extract from equation (2.7) the lattice curvature tensor (rank-2 tensor denoted as $\underline{\underline{K}}$) for every pixel in the EBSD map [115].

$$K_{ij} = \frac{\Delta\theta_i}{\Delta x_j} \quad \textit{Equation 2.7}$$

where subscripts (i, j) are taken in $i \in \{1,2,3\}$ (for the nine components of the rank-2 K_{ij} tensor shown in equation (2.8)) and $j \in \{1,2\}$ (along the x and y directions).

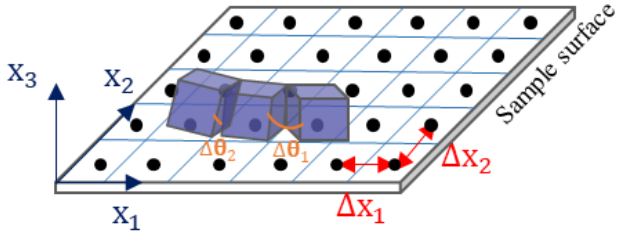

Figure 2.27: Schematic representation of lattice misorientation ($\Delta\theta_1$ and $\Delta\theta_2$) between neighbooring pixels (black points) distant by Δx_1 and Δx_2.

For example, we have $K_{11} = \frac{\Delta\theta_1}{\Delta x_1}$ and $K_{21} = \frac{\Delta\theta_2}{\Delta x_1}$, however the K_{i3} components (highlighted in bold in equation (2.8)) cannot be obtained because the local lattice orientations are determined only in the plane of analysis (i.e., along x_1 ad x_2), but not perpendicular to it (along x_3), so the orientations along this direction are considered as uniform.

$$\underline{\underline{K}} = \begin{bmatrix} K_{11} & K_{12} & \mathbf{K_{13}} \\ K_{21} & K_{22} & \mathbf{K_{23}} \\ K_{11} & K_{12} & \mathbf{K_{13}} \end{bmatrix} \quad \textit{Equation 2.8}$$

According to Nye [116] and then Kröner [117], the curvature tensor $\underline{\underline{K}}$ is directly related to the GND tensor density tensor denoted as $\underline{\underline{\alpha}}$ through equation (2.9) [118]:

$$\underline{\underline{\alpha}} = \underline{\underline{\text{curl}}}\ \underline{\underline{\varepsilon_{el}}} - \text{tr}\ \underline{\underline{K}}\ \underline{\underline{I}} + \underline{\underline{K}}^T \quad \textit{Equation 2.9}$$

where $\underline{\underline{\varepsilon_{el}}}$ is the rank-2 elastic strain tensor, $\underline{\underline{I}}$ is the rank-2 identity tensor of the three-dimension canonical vector space and superscript T denotes the transpose operation. As the classical Hough analysis of diffraction patterns cannot recover local elastic strain induced by dislocations

and since no boundary conditions are applied that can produce elastic strain, the first term on the right-hand side of equation (2.9) involving elastic strain is assumed to be null.
The total GND density denoted as ρ_{GND} is defined as the sum of the GND densities coming from all the possible dislocations modes (edge and screw) so that $\rho_{GND} = \sum_{m=1}^{M} \rho_{GNDm}$ with ρ_{GNDm} being the dislocation density and M being the total number of possible dislocations mode. Therefore, the total dislocation density tensor relating to all possible dislocation modes is defined in equation (2.10):

$$\sum_{m=1}^{M} \rho_{GNDm}\ b_m \otimes l_m = \underline{\underline{\alpha}} \quad \textit{Equation 2.10}$$

where b_m and l_m are, respectively, defined as the Burgers vector and the unitary line vector defining the m^{th} physically and crystallographically possible dislocation mode.

If the Bravais lattice of the crystal is simple cubic, the nine associated dislocation densities exist and are unique, resulting in a well-defined GND density. Otherwise, multiple sets of dislocations densities can satisfy equation (2.9), which means, a given rotation of the crystal lattice could be caused by different combinations of dislocations modes. Therefore, we used the approach proposed by Pantleon [115] to consider the set of dislocation densities that satisfies equation (2.10) and minimizes the internal energy. In this work, this calculation of the dislocation density was performed using the open source MTEX toolbox [114] within the MATLAB software.

2.5 Scanning electron microscopy

Scanning electron microscopy (SEM) is a powerful non-destructive tool used to get a close-up look at the surfaces of objects with a resolution in the 10s of nanometers. It has a wide range of applications in various fields like biology, material science and can reveal objects that are invisible to the naked eye. It has been used in this work to observe the samples before regrowth (only the pillars) to ensure that all the pillars were successfully obtained and were of good quality before proceeding to the growth. SEM images were also taken to observe the samples after regrowth and prior to their characterization.
An electron gun produces a beam of high-energy electrons, which passes through different lenses and is focused on the surface of the specimen. When the electron beam hits the sample, it interacts with the atoms, causing various signals to be emitted. These signals include secondary electrons, backscattered electrons, photons and X-rays, which are detected by specific detectors. In the case of SEM imaging, the primary signals utilized to create the image are backscattered electrons and secondary electrons (SE) [119]. Figure 2.28(a) shows a schematic diagram of the SEM while figure 2.28(b) displays the SEM image taken for pillars prior to growth. The SEM images presented in this work were taken with the SEM microscope installed in CHREA.

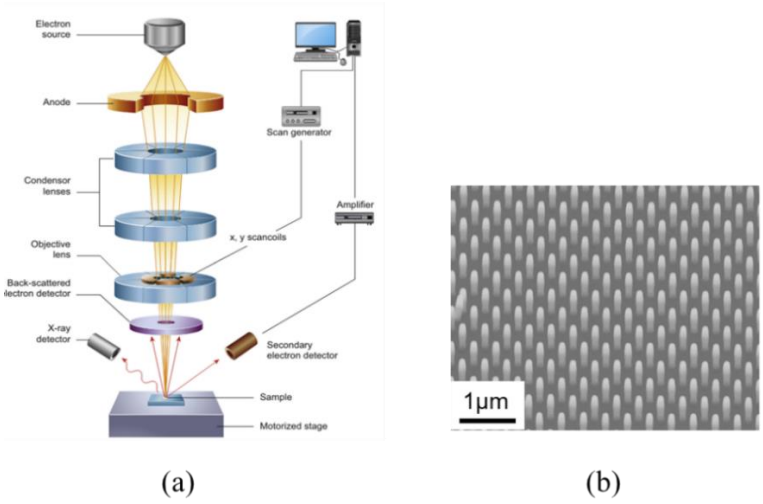

Figure 2.28: (a) Illustration of the main components of an SEM microscope taken from ref. [120] and (b) SEM image for the nanopillar before regrowth.

- Backscattered electrons have high energy, they come from a depth of the order of a micron below the surface. These electrons interact strongly with the sample and are subsequently re-emitted thanks to elastic interactions between the beam and the sample. BSE signal increases with the atomic number (Z) of the targeted material [121], this correlation between BSE signal strength and atomic number provides insights about the elemental composition of a multiphase sample. Heavier elements (greater Z) scatter electrons more strongly than lighter elements (lower Z), as a result, areas with heavier elements having greater Z appear brighter, while areas with lighter elements having lower Z appear darker. This helps distinguish between different materials present though the contrasts seen in the images corresponding to the different material.
- Secondary electrons typically have low energy (less than 50 eV), which means they can only escape from atoms present at the top few nanometers of the sample surface. The number of SEs emitted is directly related to the surface topography and since they are collected from a small volume near the surface, they can provide detailed images of the surface morphology (including edges, roughness, and textures) [119].

2.6 Cathodoluminescence microscopy

CL consists of a focused beam of high-energy electrons directed at a sample. When the electron beam interacts with the sample, it excites the electrons within the material. These excited electrons are then unstable (in excited states) and eventually return back to their lower energy states by releasing the excess energy in various forms. CL detectors collect the emitted visible light and analyze it. CL is a powerful technique used for the investigation of the optical properties of materials [122], its emission can be used in different fields like nano-photonics, semiconductors and geology. It is highly used to determine dislocations in epitaxial layers of

GaN since these dislocations act as non-radiative recombination centers preventing light emission from their relevant positions. Figure 2.29 presents a SEM image (figure 2.29(a)) and cathodoluminescence image (figure 2.29(b)) conducted in this work of GaN clusters that are not fully coalesced.

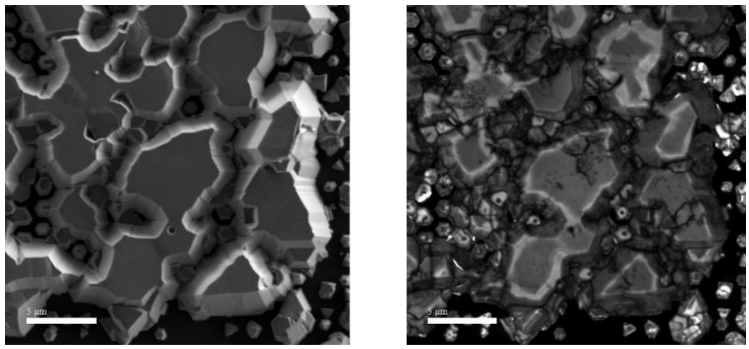

Figure 2.29: GaN clusters observed using (a) SEM, and (b) cathodoluminescence.

The non-flat irregular surfaces at the edges of the grain might scatter the incident electron beam, causing variations in the intensity and distribution of the CL signal. This scattering can result in a broader emission spectrum, contributing to the appearance of white color at the edges of the grain as we can see in figure 2.29(b).

2.7 Conclusion

This chapter presented a comprehensive overview of the characterization techniques employed in this study that provided us with complementary information required to achieve the objectives of this work. Additionally, we presented in detail an explanation of the post-processing procedures applied to the data generated through these techniques. This stage of processing was a crucial part of the overall work. The following chapter will describe the different samples measured and provide a comprehensive analysis of the results obtained from the processed data.

Chapter 3: Experimental assessment of pillars rotation and GaN quality

3.1 Introduction

Following the presentation of the PEGADIS growth approach in chapter 1 as well as the objectives of this thesis, different samples with different geometries have been characterized by the various characterization techniques described in chapter 2. The results of these experimental measurements are presented in this chapter. For clarity, we will use the concept of "twist" to define a rotation around the pillar length (around an axis that is normal to the sample's horizontal surface), the concept of "tilt" to define a rotation an axis in the plane of the sample's surface and the concept of "rotation" to define a twist + tilt. First, measurements of the twist and tilt of the pillars are presented in order to test the principle of the twisting and tilting of the pillars that this growth approach is based on. Second, the GaN crystalline orientation before coalescence and during coalescence is determined in order to gain a deeper physical understanding of the processes operating during our proposed growth approach followed by a calculation of the geometrically necessary dislocations. Additionally, the tilt between neighboring pillars is calculated and the quality of the GaN layer after fully coalescence is determined. The obtained results are discussed and validated by different characterization techniques.

3.2 Verification of the pillar's rotation in a set of three pillars

3.2.1 Orientation of coalesced GaN lines

The idea behind the PEGADIS growth approach is based on the rotation of the pillars. The work previously presented in chapter 1 that was done within the PEGADIS project did not provide clear evidence of the rotation of the pillar after coalescence. Therefore, the first objective of this work is to test whether the pillars indeed rotate. Thus, samples with simple geometry (sets of three GaN/AlN/Si/SiO_2 nano pillars with coalesced GaN lines on top them) were prepared for an SXDM experiment at the ID01 beamline at the ESRF. We aim (i) to determine the quality of the GaN lines and (ii) to test if a misorientation between neighboring pillars induced by the rotation during the coalescence is observed since before coalescing the Si(111) layer in the nanopillars should be perfectly aligned and they could only become disoriented by a rotation of the pillars during coalescence.

A first SXDM experiment conducted at the ID01 beamline focused on one sample containing eight sets of three pillars with coalesced GaN on top of them. The first four sets (region 1) are

formed by pillars with a diameter of 200 nm and a pitch of 1 µm and are shown in the SEM image in figure 3.1(a). Figure 3.1(b) displays the coalesced GaN layer on top of them. The other four sets (region 2) of pillars are distant by 0.5 µm and have a diameter equal to 100 nm as shown in the SEM image in figure 3.1(c). The coalesced GaN lines on top of them are shown in figure 3.1(d). We etched a label for each region, marked with a blue arrow in figure 3.1, to easily locate the areas during measurements.

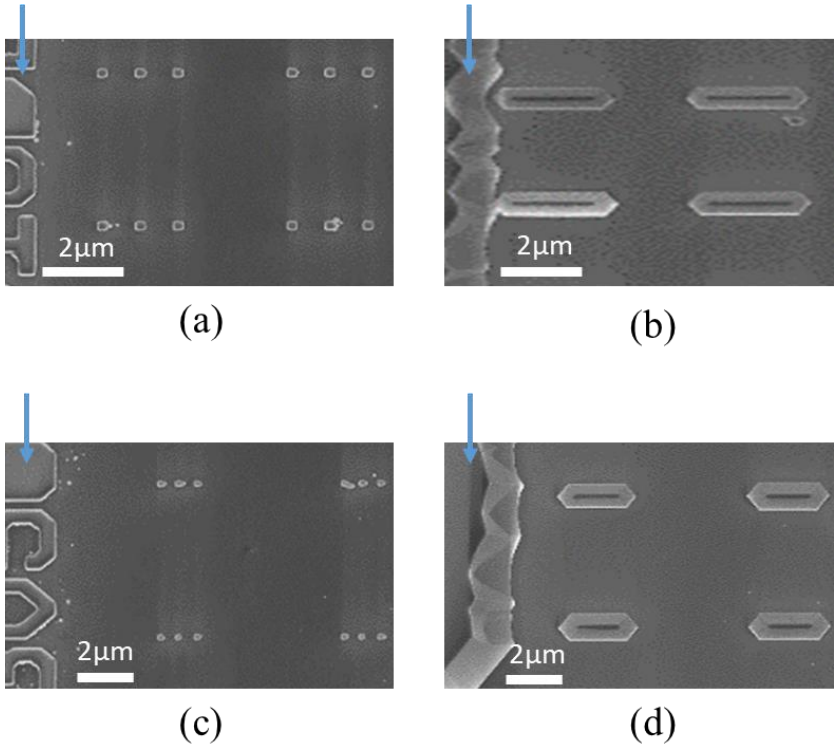

Figure 3.1: SEM image of (a) region 1: four sets of three pillars prior to regrowth with p=1 µm and D=200 nm, (b) coalesced GaN lines on top of the corresponding pillars in region 1, (c) region 2: four sets of three pillars prior to regrowth with p=0.5µm and D=100 nm and (d) coalesced GaN lines on top of the corresponding pillars in region 2.

Using a monochromatic nano-beam with a focal spot size of ~25 nm at an energy of 9 keV, measurements around the symmetrical Bragg reflection GaN(004) have been performed on the eight lines of GaN shown in figures 3.1(b) and 3.1(d) from which we can obtain information on the tilt of the GaN. We define ϕ being the rotation angle around the axis perpendicular to the sample surface - $\phi = 0°$ corresponds to the straight horizontal direction pointing towards the right in figure 3.1(d). Our sample is at $\phi = 0°$ and the Bragg angle θ of GaN(004) reflection is equal to the incidence angle $\omega = 32.0918°$ which makes the projected beam size equal to ~47 nm. For the GaN lines in region 1 and in region 2 (figures 3.1(b) and 3.1(d)), an area of 11.2 x 11.2 µm² has been scanned, and ω rocking curves were performed with a step size $\Delta\omega = 0.1°$ and an angular range of $31.0918° < \omega < 33.0918°$ (i.e., 20 points for each rocking curve). For every incidence angle ω of the rocking curve, an x-y piezo scan was performed, and diffraction images were taken every 70 nm in the x direction (160 positions) and 70 nm in the y direction (160

positions) with a measurement time t =0.01 s for each position. Therefore, for each region, we scanned 25600 positions (160 x 160) 20 times (20 ω values) with 0.01 s/point. The diffracted beam is detected by a 2D Eiger detector (pixel size= 75 x 75 µm²), for every ω and at each position. Thus, a slice of the Bragg peak is obtained, and the sum of the whole rocking curve allows the extraction of the 3D Bragg peak at each position. After reconstruction, a 3D reciprocal space map around the Bragg reflection is obtained at each (x, y) position. Figure 3.2 is a schematic representation of the SXDM geometry. The Bragg peak seen on the 2D detector corresponds to one slice of the 3D Bragg peak colored red in the figure.

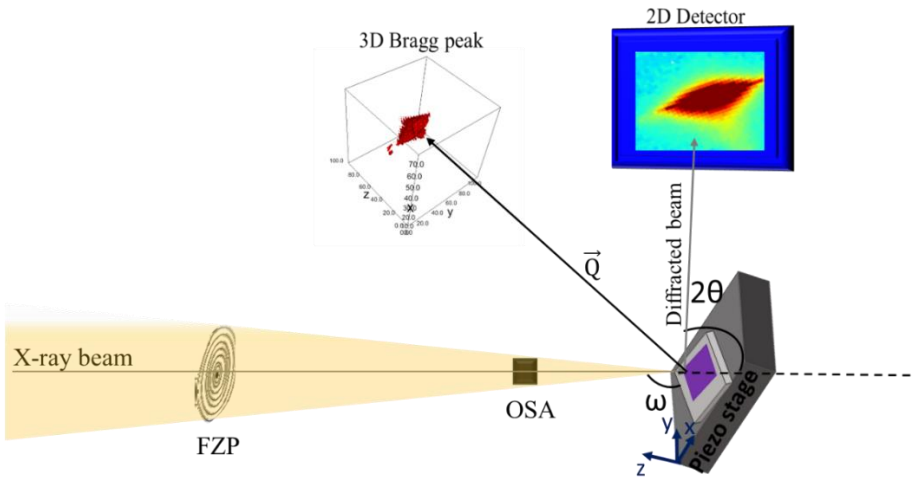

Figure 3.2: A schematic of the SXDM geometry.

In order to determine the quality of the GaN lines, the crystalline orientation map of the GaN layers is required. Therefore, a conversion from angular space to reciprocal space is performed using the data treatment procedure explained in section 2.3.3.

First, to reduce the computation time and to discard the data noise, a region of interest (ROI) is selected within the detector. This is achieved by identifying the position of a single diffraction peak on the detector using one rocking curve in one position only. Specifically, we choose the ω angle positioned in the middle of the series, where the highest intensity is anticipated. Figure 3.3(a) shows the entire detector with the detected diffraction peak inside the red square (missing pixels due to damage in the detector are indicated by a green arrow) and figure 3.3(b) shows the relevant area of the detector used for the GaN(004) measurements (the cross sign seen in the background split the detector into frames).

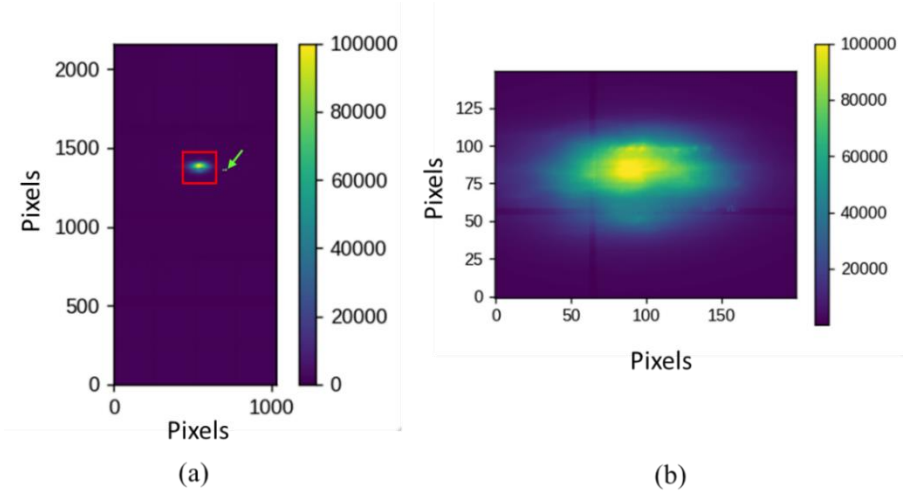

Figure 3.3: (a) Image of a 2D Diffraction peak within the entire detector and (b) zoomed in image at the relevant area.

The chosen ROI coordinates are between 1300 and 1450 pixels along the y direction and 450 and 650 pixels along the x direction. Figure 3.4 shows the integrated intensity over all the rocking curves around the (004) reflection for the eight GaN lines inside the ROI. We notice that the outline of the lines is not exactly as seen in the SEM images because there are areas which diffract at higher/lower ω angles, or with lower intensity (due to difference in thickness). We note that the intensity seen along the y direction at x between 0 and 1 µm is the intensity diffracted from the GaN grown on the sample's label seen in the SEM images (figure 3.1).

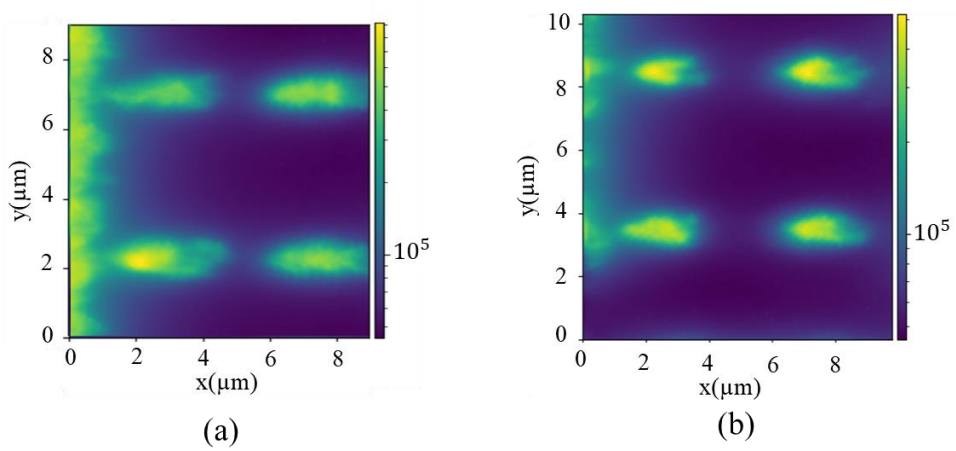

Figure 3.4: 2D map of the integrated intensity of (a) coalesced GaN lines on top of pillars in region 1 and (b) coalesced GaN lines on top of pillars in region 2. The color bar represents intensity on a logarithmic scale.

Before computing the reciprocal vector $\vec{Q}_{004}$ (Q_x, Q_y, Q_z) at each position on the scanned areas, we must consider the impact of imprecisions in the alignment (such as sample not being centered on the goniometer) on the final results. We note that the y axis of the detector represents the 2θ values while the x axis represents the ϕ values composed of both the tilt in the

orthogonal direction to ω, and the rotation around the pillar's height. With only a single orientation measured, it is not possible to separate these two.

Offset calculation

The 2θ values are extracted from the position of the diffracted beams on the 2D detector. To estimate any angular offset from a previously calculated setup, we measured the silicon substrate and performed one rocking curve around the Si(004) reflection. The offset found for the Si(004) can be applied to the measurements around the GaN(004) since they have very close 2θ values ($2\theta_{Si004}$=61° and $2\theta_{GaN004}$=64°) and thus the diffraction geometry is similar, so the errors encountered during alignment for the Si(004) measurements are similar to the ones encountered during the GaN(004) measurements. We based our calculations on the Si measurements rather than the GaN ones because the GaN layer we measured is strained, whereas we expect that the thick silicon substrate is relaxed. The chosen 2θ parameter corresponds to the "real" angle of an unstrained Si(004). This approach ensures that the calculated offset represents an absolute value rather than a relative one.

The offset can be calculated using equations (3.1):

$$\text{Offset in } 2\theta = 2\theta \text{ (theoretical)} - 2\theta \text{ (experimental)} \quad \textit{Equation 3.1}$$

From the Si(004) measurements , we obtain the experimental 2θ by extracting the sum of the intensity over the entire measured area in the reciprocal space. The extracted slice of the Bragg peak from the detector is shown in figure 3.5. It is possible to integrate the pixels over y to calculate the measured 2θ and apply equation (3.1), alternatively, we can extract the position of the center of the peak from figure 3.5 and compare it to the position of the central pixel (the pixel that corresponds to the center of the direct X-ray beam on the detector when all motor angles are zero). The difference between the pixels position in y will be equal to the offset in 2θ.

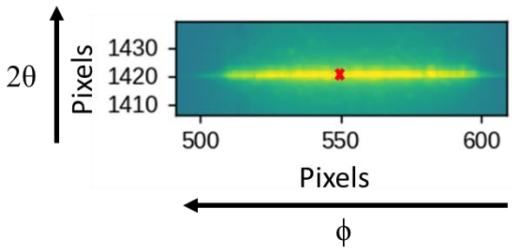

Figure 3.5 Sum of the intensity of the Si(004) reflection in the reciprocal space.

From the alignment measurements at the beginning of the experiment, the central pixel ordinate coordinate was saved as: y=1374. From figure 3.5, we obtain the ordinate of the center of the peak (y=1420) which leaves us with an offset of 46 pixels in the negative y direction. With the size of one pixel equal to 75 µm and the distance from sample to detector of 75 cm, the angular

offset in $2\theta = \frac{-46 * 75}{750000} = -0.0046°$. This offset value is then used for the rest of the data analysis.

Once the angular offset has been established, we proceed with the shift correction and ROI selections steps as explained in section 2.3.3 to finally obtain the reciprocal space vector $\vec{Q}$. The local rotations are only meaningful if defined relative to a reference axis, and for this study the average peak position over (x, y) $\vec{Q}_{mean}$ is computed and taken as a reference. The relative angular distance (referred to as relative tilt) between $\vec{Q}$ and $\vec{Q}_{mean}$ is calculated at every (x, y) position as:

$$\text{Relative Tilt (°)} = \left(\frac{180}{\pi}\right) \text{ x arcos } \left(\frac{\vec{Q}_{mean} \cdot \vec{Q}}{|\vec{Q}_{mean}| \text{ x } |\vec{Q}|}\right) \quad \textit{Equation 3.2}$$

Figure 3.6(a) shows the result of this calculation, i.e. a 2D map of the tilt magnitude at each position of the scanned region relative to the mean orientation of the four GaN lines on top of pillars distant by 1.5 µm and D=200 nm. The same map is shown for the four GaN lines on top of pillars distant by 0.5 µm and D=100 nm in figure 3.6(c). We visualize in figures 3.6 (b) and (d) the angular deviations of $\vec{Q}_{004}$(x, y) from its average $\vec{Q}_{mean}$ i.e. from the mean orientation, which describe the local lattice rotation.

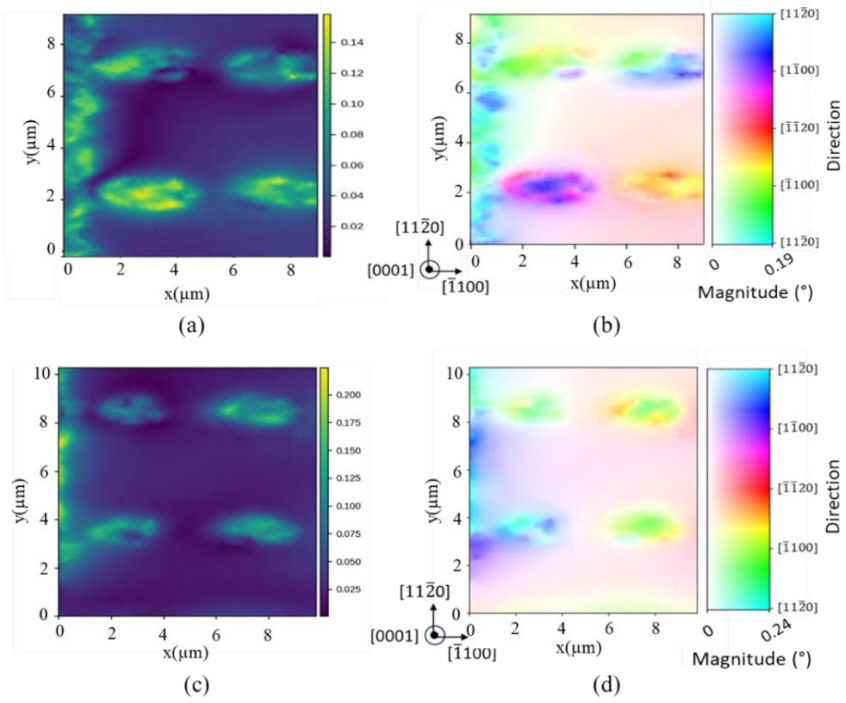

Figure 3.6:(a) 2D map of the tilt magnitude of GaN lines in region 1 from the GaN(004) measurements, (b) 2D map of $\vec{Q}_{004}$ relative rotation of the corresponding lines, (c) 2D map of the tilt magnitude of GaN in region 2 from the GaN(004) measurements, and (d) 2D map of $\vec{Q}_{004}$ relative rotation of the corresponding lines. The hue and saturation of the colors in (b) and (d) represent tilt direction and magnitude, respectively.

The map in figure 3.6(a) indicates the magnitude of the tilt between $\vec{Q}_{004}(x, y)$ and $\vec{Q}_{mean}$, i.e. it indicates the angular deviation of the normal of the 004 GaN planes in each pixel from the mean orientation. Across the whole of region 1, $\vec{Q}_{004}$ has a maximum angular deviation of 0.19° with respect to the mean orientation (note that the GaN in the label can play a role in increasing the maximum angular deviation) with an angular sensitivity of 0.001° [99]. The angle between any two adjacent directions indicated on the scale bar of the rotation maps is 90° and colors placed near each other correspond to nearby directions. We will conduct a qualitative assessment to identify lines with uniform and non-uniform orientations. But by examining each line within itself, we see in figure 3.6(b), that the two lines at the bottom are bicolored with colors corresponding to proximate directions indicating that, at any given position along the line, the diffracted vector $\vec{Q}_{004}$ is oriented more or less in the same direction, meaning that the epitaxial GaN is well oriented within the line.

The top right line in region 1 exhibits significant misorientation, indicating by its two colors representing entirely different orientations. The interpretation of the top left line in region 1 is not very clear.

The same results can be seen in the measurements over region 2, where we see a homogenous color in the GaN line at the bottom right of figure 3.6(d) which means we have a well oriented GaN layer, but at the same time the other GaN lines present misorientations within themselves.

The same measurements on both regions are repeated around the asymmetrical GaN(204) reflection from which we can obtain information on the rotation of the GaN. The Bragg angle for the (204) reflection is equal to 44.95°, the sample is rotated by ϕ= 29.2°, we performed ω rocking curves consisting of 20 points with a step size $\Delta\omega$=0.1° and an angular range of 93.55° < ω < 95.55°. The intensity is acquired for every position and the same data analysis have been performed to compute the reciprocal space vector at each position. Due to network errors encountered during the measurement of the Si(440) reflection for offset estimation, the offset from the Si(440) asymmetrical reflection could not be calculated and therefore could not be applied to the GaN(204) measurements, and the offset found from the Si(004) measurements cannot be applied either since the alignment differs between the GaN(204) and the Si(004) diffractions. Therefore, the offset is calculated between the GaN we measured and the relaxed GaN, it is derived by calculating the difference between the measured (204) peak position and the relaxed (204) GaN peak position. We will show directly the relative tilt magnitude map and the relative rotation map with respect to the mean orientation in figure 3.7.

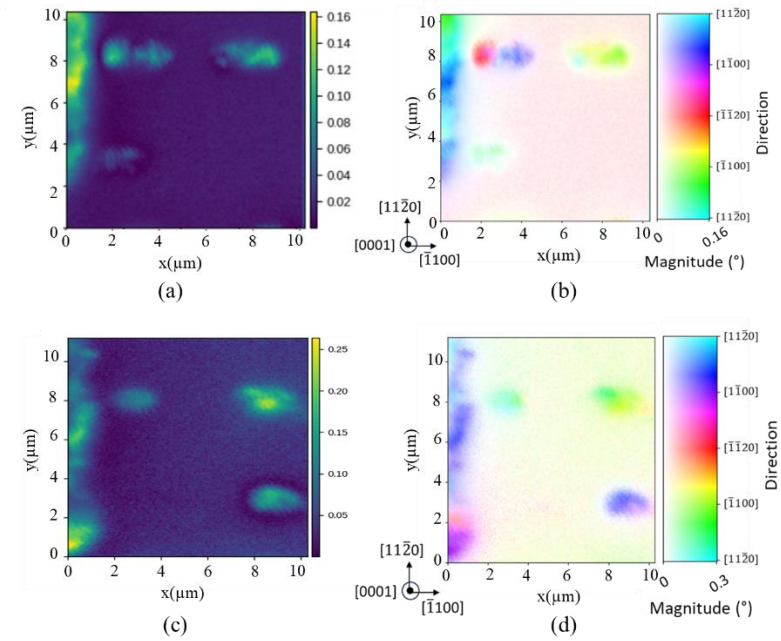

Figure 3.7: (a) 2D map of the tilt magnitude of GaN lines in region 1 from the GaN(204) measurements, (b) 2D map of $\vec{Q}_{204}$ relative rotation of the corresponding lines, (c) 2D map of the tilt magnitude of GaN lines in region 2 from the GaN(204) measurements and, (d) 2D map of $\vec{Q}_{204}$ relative rotation of the corresponding lines. The hue and saturation of the colors in (b) and (d) represent tilt direction and magnitude, respectively.

We notice that from each region one line is missing, this is probably because it is highly disoriented from the others so that the ω angular range selected for the (204) scans was insufficient and only permitted us to see GaN lines that were misoriented by a maximum of 2°. In both regions, we have lines that are very well oriented by themselves (uniform color within the line) and other lines that present various orientations (mix of colors).

We notice that within the same region, we have well-aligned and misaligned GaN lines, one explanation could be (i) multiple initial orientations within the same pillar making it impossible to align everything properly, (ii) significant initial misalignment between two adjacent GaN pillars. We can expect to have a limit in the initial GaN misorientation – if this is too high then the pillars are not able to rotate to align correctly.

We also notice that two regions with different pillar pitch and diameter produce both well-aligned and misaligned GaN lines. To statistically determine the optimal geometry, we would ideally collect more data from measurements on a larger number of samples. However, due to the limited number of measurements possible during the beamtime, our analysis is constrained by the available data and thus, the optimal pitch and diameter that leads to the growth of well-oriented GaN lines cannot be found statistically. Therefore, an optimization of different pillar parameters has only been possible through finite element simulations as will be discussed in chapter 4.

Measurements of the Si layer in the nanopillars underneath the coalesced GaN lines of region 1 were also conducted to compute the misorientation between neighboring pillars to test the rotation of the pillars during the proposed growth approach. These measurements will be shown and discussed in the next section.

3.2.2 Orientation of the corresponding Si pillars underneath the GaN lines

Following the determination of the orientation of various coalesced GaN lines, it is interesting to perform measurements on the Si layer in the pillars underneath the GaN lines to determine their orientation after coalescence and verify whether the Si layers that should be properly oriented before coalescence become disoriented after coalescence due to the rotation of the pillars and the reorientation of the GaN on top of them.

The Si layer in the pillars in region 1 shown in figures 3.1(a) have been measured after the coalescence of GaN on top of them which means the pillars underneath the GaN lines in figures 3.1(b) are the ones studied.

Using a monochromatic nano-beam with a focal spot size of ~25 nm at an energy of 9 keV, we wanted to avoid measurements around the Si(111) reflection since it has a very low Bragg angle which reduces the spatial resolution (the beam can be spread over several pillars and the intensity of the beam will be dispersed over several pillars instead of just one), so we tried to measure the Si(333) reflection but we did not see any diffracted intensity. Finally, measurements around the asymmetrical Bragg reflection Si(331) have been performed on the Si layers in the pillars underneath the four lines of GaN shown in figures 3.1(b). The sample is rotated by ϕ=29.2°, the Bragg angle of Si(331) is 33.625° while the incidence angle ω=55.43° means we had a projected spot size of ~30 nm. An area of 7 x 9 µm² is scanned, and 25 ω rocking curves were performed with a step size $\Delta\omega$=0.16° and an angular range of 53.43° < ω < 57.43°. Although, the Si is monocrystalline with minimal mosaicity, we selected a relatively large $\Delta\omega$ value for two reasons: (1) we expect the Si in the nanopillars to become disoriented after coalescence due to the rotation of the pillars and (2) size effect: the Si layer in the pillar is 100 nm wide and 50 nm thick which will cause a broadening of the peak in both directions since the broadening of the peak is inversely proportional to the thickness of the measured layer; in the case of the pillars with a diameter of 200 nm, the broadening along x inherited from the size effect is found equal to 0.042° using Scherrer equation [123].

For every incidence angle ω of the rocking curve, an x-y piezo scan was performed, and diffraction images were taken every 100 nm in the x direction (90 positions) and 100 nm in the y direction (70 positions) with a measurement time t =0.1 s for each position. We scanned 6300 points (70 x 90) 25 times (25 ω values) with 0.1 s/point.

Two scans were performed over the same region 1 while varying the spatial resolution from steps of 100 nm in both directions in the first scan to 140 nm in both directions in the second one. In each scan different sets of pillars appeared.

After selecting a ROI in the detector corresponding to the position of the peak, we show the 2D map of the integrated intensity of the Si(331) Bragg peak across all the ω values in region 1 from two different scans in figures 3.8(a) and 3.8(b). Figure 3.8(c) shows the 2D map of the $\vec{Q}_{004}$ relative rotation of the GaN lines on top of the studied pillars in figures 3.8(a) and 3.8(b). The pillars can be easily distinguished as a dot-like pattern of high intensity. To associate each set of three pillars with the corresponding coalesced GaN lines on top of them, the set of pillars and the corresponding lines, are marked using arrows of the same color. To simplify viewing the GaN lines and their underlying pillars, we have included the rotation map from figure 3.6(b) once again in figure 3.8(c).

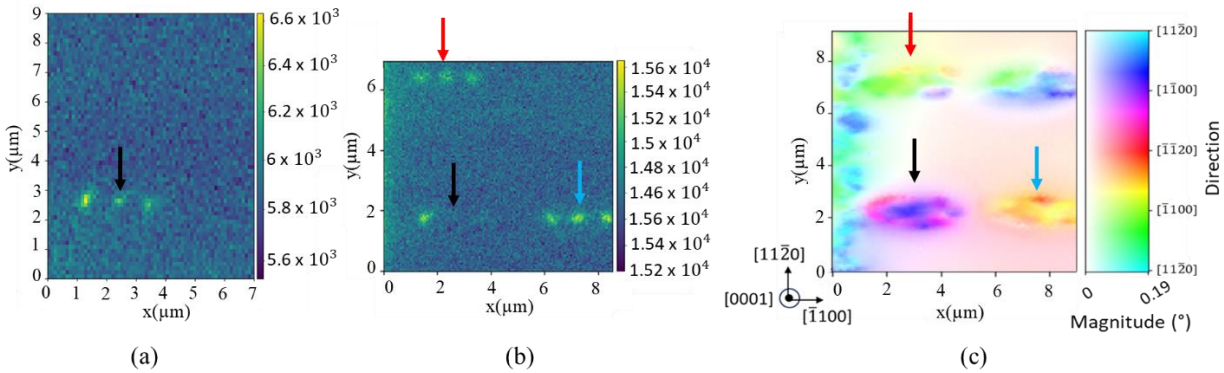

Figure 3.8: (a) 2D map of the integrated intensity of the Si(331) Bragg peak from the pillars of region 1 and during the first scan, (b) 2D map of the integrated intensity of the Si(331) Bragg peak from the pillars of region 1 during the second scan and (c) 2D map of $\vec{Q}_{004}$ relative rotation of the corresponding lines in region 1. Each set of three pillars and its corresponding GaN lines are marked using arrows of the same color.

From both scans, only three sets of pillars are seen in total (figures 3.8(a) and 3.8(b)). This could be due to several factors: (i) accumulation time t of the diffracted beam on the detector was not sufficient, (ii) the intensity of the diffracted beam is so low because Si layer in the nanopillars is only 50 nm thick with a diameter of 200 nm so we don't have enough material to diffract a beam with high intensity detectable by the detector, and (iii) too much background noise so that it is impossible to see the intensity of the pillars.

Following these results, the conversion to the reciprocal space is applied with the same procedure used for the GaN(004) and GaN(204). In figure 3.8(a), the pillar in the center pointed by the black arrow is taken as the reference and the angular deviation between this reference pillar and its neighboring pillar is calculated to test if the pillars become disoriented after coalescence. Figure 3.9(a) shows the magnitude of the tilt between each pillar and the reference one. From figure 3.9(a), we clearly see that after coalescence, the pillar on the left is disoriented

by approximately 0.1° from its neighboring pillar. The tilt between the pillar on the right and the reference pillar is nearly zero, indicating they share the same orientation. This suggests that either these two pillars did not rotate at all, or they both rotated in the same direction, and thus preserved a unique orientation.

For the pillars seen in the second scan (figure 3.8(b)), we choose the centered pillar from the bottom right pointed by the blue arrow as reference point. Figure 3.9(b) shows the magnitude of the tilt between each pillar and the reference. From figure 3.9(b), we notice that after coalescence, the pillar on the right side in the right bottom set of pillars is disoriented by approximately 0.1° from its neighboring pillar. To simplify viewing the GaN lines and their underlying pillars, we have included the rotation maps from figures 3.6(b) and 3.7(b) once again in figure 3.9(c) and 3.9(d) respectively.

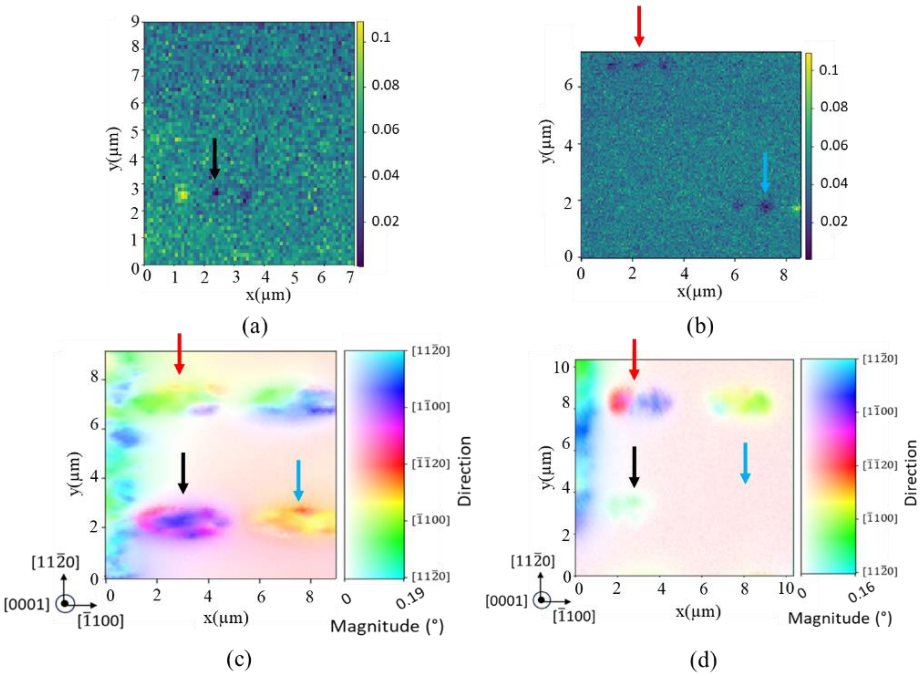

Figure 3.9: (a) 2D map of the tilt magnitude of the pillars in region 1 from the first scan, (b) 2D map of the tilt magnitude of the pillars in region 1 from the second scan, (c) 2D map of $\vec{Q}_{004}$ relative rotation of the corresponding lines in region 1, and (d) 2D map of $\vec{Q}_{204}$ relative rotation of the correspond lines. Each set of three pillars and its corresponding GaN lines are marked using arrows of the same color in region 1.

The misorientation between the pillars seen in the two bottom sets (indicated by black and blue arrows) in figures 3.9(a) and 3.9(b), confirms the rotation of the pillars during coalescence. We also notice that the GaN on top of these pillars is well oriented as seen in figure 3.9(c) and 3.9(d) from the GaN(004) and GaN(204) measurements. We note that we also have a set of pillars that did not rotate: the three pillars at the top left side of figures 3.9(b) (indicated by red arrow) preserved the same orientation as the reference pillar, since we see that the angular deviation between their $\vec{Q}_{331}$ (x, y) and the $\vec{Q}_{331\ ref}$ is equal to zero. In this case, where no pillar

rotation occurred, the GaN lines on top is disoriented as seen in figure 2.9(d) (indicated by red arrow). This means that the GaN is aligned only when the pillars rotate.

Additionally, the fact that some pillars did not rotate implies that not all rotations are feasible as suggested in section 3.2.1. In other words, the degree of misorientation of the GaN pillars before regrowth may play a major role in the feasibility of the rotation. This suggests the existence of a limit tilt that could permit a rotation to take place from an energetic point of view. This possible explanation will be tested and discussed in chapter 4 through the finite element simulations results.

3.3 Evolution of the epitaxial GaN from pillars to coalesced domains

3.3.1 Reference sample: crystalline orientation of GaN pillars before coalescence

Following the validation of the pillar rotation, the next objective of this work is to examine the microstructural evolution of the GaN during growth to understand the coalescence process taking place at the nanoscale with more complex geometries. This is done by a detailed investigation into the behavior of the GaN before and during coalescence to compare the orientation of the GaN before and after coalescence. A second SXDM experiment was conducted at the ID01 beamline at the ESRF, to investigate the coalescence phenomena by studying two samples: a reference sample A that contains only GaN GaN/AlN/Si/SiO_2 etched nano pillars of 100 nm diameter before coalescence (prior to the pyramids growth) with pitch equal to 0.5 µm and taken as a reference sample (figure 3.10(a)), and a sample B with GaN grown on top of the GaN/AlN/Si/SiO_2 pillars with pitch= 1.5 µm (figure 3.10(b)). The thickness of the GaN pillars in sample A is equal to 250 nm while that of the coalesced GaN layer in sample B is equal to 1 µm. The growth of the GaN in sample B is deliberately interrupted before the platelet reaches full coalescence in order to characterize a sample with GaN at the early stage of coalescence. We note that the missing pillars and the fallen pillars in the probed area of sample A seen in figure 3.10(a) are due to a problem in the pillar fabrication process that has been optimized in parallel with this work, but which was not fully mature for these samples [124].

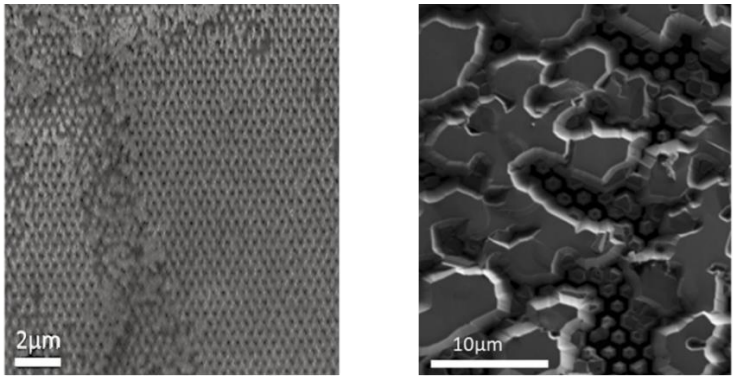

Figure 3.10: (a) SEM images of the measured area (a) of sample A with GaN pillars before regrowth (b) and of sample B with GaN at the early stage of coalescence.

In this experiment, we used a monochromatic nano-beam with a focal spot size of ~65 x 65 nm² at an energy of 10 keV. We measured the GaN(105) Bragg reflection with the sample being at ϕ=30°, the Bragg angle equal to θ=39.6°, the incidence angle ω=60.5°, and the projected beam size is 74 nm. The diffracted signal is recorded by a two-dimensional (2D) Maxipix™ detector (square of 4 chips, each of them 516 × 516 pixels with 55 µm pitch size) [100].

For sample A an area of 20 x 20 µm² has been scanned, and ω rocking curves were performed around the asymmetrical Bragg reflection GaN(105) with a step size $\Delta\omega$=0.05° with an angular range of 59.5° < ω < 61° (each rocking curve consisted of 30 points). For every incident angle ω of the rocking curve, an x-y piezo scan was performed, and diffraction images were taken every 80 nm in the x direction (200 positions) and 80 nm in the y direction (200 positions) with t=0.01s.

Figure 3.11(a) shows a two-dimensional (2D) map of the intensity of the (105) Bragg peak of sample A. The GaN pillars can be easily distinguished as a dot-like pattern of high intensity, and a zoomed area of the pillars is indicated by the red arrow. In order to determine the orientation of each GaN pillar before regrowth, a conversion from angular to orthonormal reciprocal space is performed using the python library ID01-sxdm developed on the ID01 beamline [102]. We did not perform measurements on the silicon substrate; therefore, the offset is calculated between the GaN we have (that might be stressed) and the relaxed GaN, it is derived by calculating the difference between the measured (105) peak position and the relaxed (105) GaN peak position (theoretical position) which means the length of the diffraction vector is relative and not absolute and thus the strain values obtained are relative strain values. An offset in phi of 0.25° was found due to imperfect alignment of the sample and this was applied to the analysis. The reciprocal space coordinates (Q_x, Q_y, Q_z) of the diffraction vector $\vec{Q}_{105}$ are determined for every (x, y) position of the probed sample area. The average peak position over (x, y) $\vec{Q}_{mean}$ is then computed. The relative angular distance between these two quantities is calculated at every (x, y) position following equation (3.2). Figure 3.11(b) shows the result of

such calculation for sample A, i.e. a 2D map of the angular deviation of the normal of the (105) planes in each pixel from the mean orientation, thus describing the local lattice rotation.

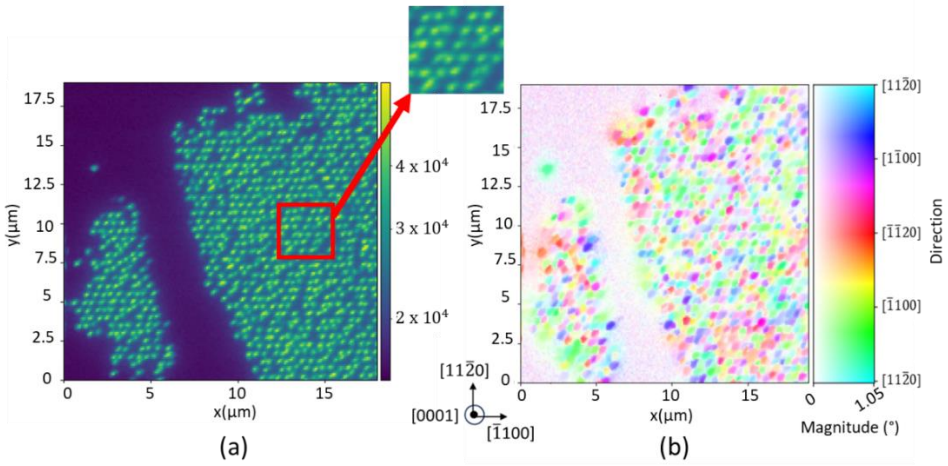

Figure 3.11: (a) 2D map of the integrated intensity of sample A shown in logarithmic scale. (b) 2D map of $\vec{Q}_{105}$ relative rotation of sample A. The hue and saturation of the colors in the map represent tilt direction and magnitude, respectively.

We notice how the damaged area of sample A seen in figure 3.11(a) has no diffracted signal in the intensity map. The results found in figure 3.11(b) indicate that GaN pillars, before regrowth and coalescence, are misoriented with a relatively large distribution of orientations up to ±1° (color distribution is heterogeneous).

3.3.2 Reorientation of the GaN during coalescence

For sample B, with partially coalesced zones, an area of 30 x 40 µm² has been scanned, and ω rocking curves were performed around the asymmetrical Bragg reflection GaN(105) with a step size Δω=0.1° and an angular range of 58.5° < ω < 62.5° (each rocking curve consisted of 40 points). For every incidence angle ω of the rocking curve, an x-y piezo scan was performed, and diffraction images were taken every 150 nm in the x direction (200 positions) and 200 nm in the y direction (200 positions) with t=0.01 s.

Figure 3.12(a) shows a two-dimensional (2D) map of the intensity of the (105) Bragg peak of sample B. The same offset and the same data processing as described above for sample A are applied on data collected on sample B; the 2D map of $\vec{Q}_{105}$ relative rotation is shown in figure 3.12(b).

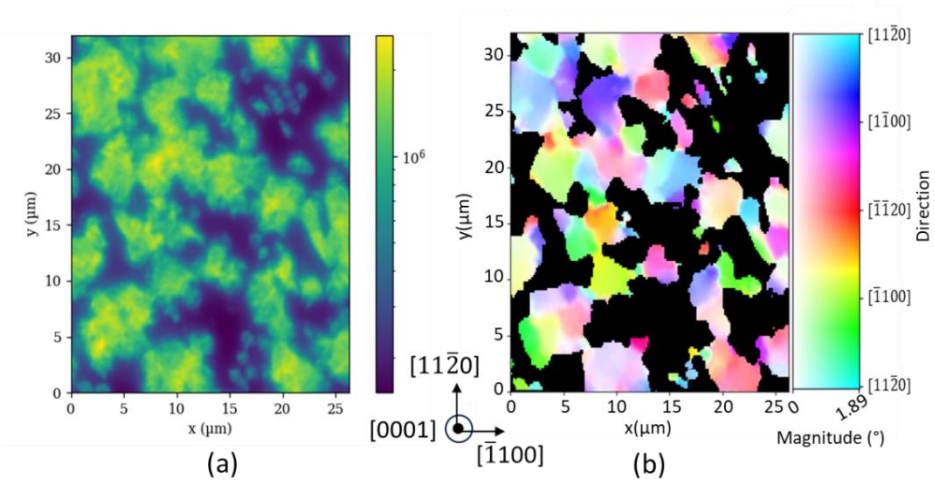

Figure 3.12: (a) 2D map of the integrated intensity of sample B shown in logarithmic scale. (b) 2D map of $\vec{Q}_{105}$ relative rotation of GaN at the early stage of coalescence (sample B).

Here, it is evident that GaN pillars (seen in figure 3.11(b)) have coalesced into larger well-defined GaN domains up to 3.9 ±1.3 µm with a unique and narrow orientation distribution within each domain. We note that the black regions seen in figure 3.12(b) correspond to the uncoalesced GaN regions diffracting with extremely low intensity seen in figure 3.12(a) and thus they were masked throughout the data treatment. Hence, by comparing a crystalline orientation map of the GaN before coalescence and at the early stage of coalescence, it has been demonstrated that with this novel growth approach, the initially disoriented GaN pillars transformed into well-defined and well-oriented GaN domains. We have gained in the size of the highly oriented GaN domains (3.9 µm) compared to our reference sample (0.1 µm) and compared to GaN domains obtained in 2D GaN on Si (the size of the well oriented GaN grains in 2D GaN on Si was found by the author of [125] to be equal to 2 µm), thus we reduced the number of grain boundaries. However, the misorientation between the large GaN grains has nearly doubled compared to the misorientation in our reference sample, and the reason behind it is not clear. Additionally, we cannot predict if this tilt and twist will vary so that the misorientation will be compensated once the GaN becomes thicker and fully coalesced Therefore, it is difficult to compare the obtained misorientation at the early stage of coalescence to the misorientation between grains in fully coalesced 2D GaN on Si. XRD measurements on fully coalesced GaN platelets are presented in section 3.5.1 but with different pitch values and different techniques.

3.3.3 Grain boundaries formation at the early stage of coalescence

To establish the reciprocal space coordinates of the (105) peaks, one-dimensional projections of the data along Q_x, Q_y, and Q_z are computed and fitted to Gaussians. This fit allows the determination of the peak FWHM in each direction at each (x, y) coordinate. The map of

FWHM along Q_z and Q_x for sample B is displayed in figures 3.13(a) and 3.13(b), respectively. We notice a broadening of the peak along both Q_z and Q_x at the boundaries of the same grains identified in the relative tilt map in figure 3.12(b). This peak broadening implies a distorted lattice and/or the presence of a strain gradient between two neighboring GaN grains. This gradient could be introduced by the presence of geometrically necessary dislocations and elastic strain required to accommodate the misorientation between two large rigid grains.

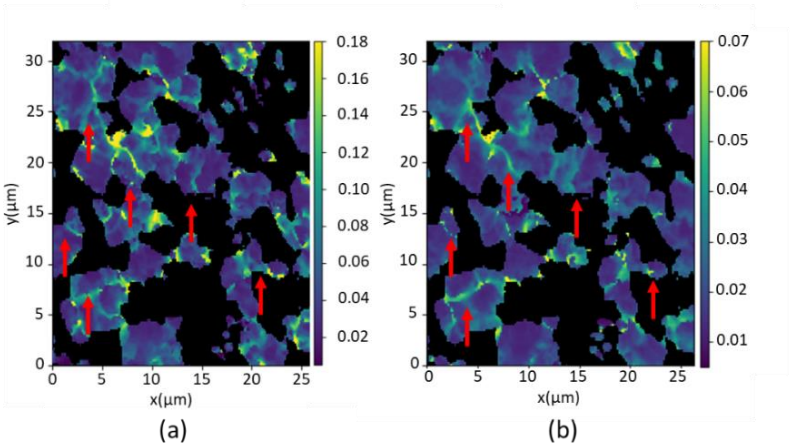

Figure 3.13: (a) FWHM of the Bragg peak intensity as a function of Q_x, (b) FWHM of the Bragg peak intensity as a function of Q_z. The color bar on the right represents the values in (Å) and the peak broadening is designated by the red arrow.

Having the 3D reciprocal Bragg peak information at each (x, y) position allowed us to perform a strain analysis on the GaN at the early stage of coalescence (sample B). However, it is not possible to obtain the full strain tensor because it requires measuring three independent diffraction peaks from different crystallographic directions [126], which was not possible due to the limited time of this experiment. The relationship between strain and lattice spacing is described with equations (3.3) and (3.4):

$$\varepsilon_{105} = \frac{d_{105,meas} - d_{105,mean}}{d_{105,mean}} \quad \textit{Equation 3.3}$$

And

$$d_{105} = \frac{2\pi}{|\vec{Q}_{105}|} \quad \textit{Equation 3.4}$$

where ε_{105} represents the relative strain along the (105) direction and d_{105} the lattice spacing between (105) planes. Figure 3.14 the relative strain ε_{105} map along the (105) direction for the corresponding region.

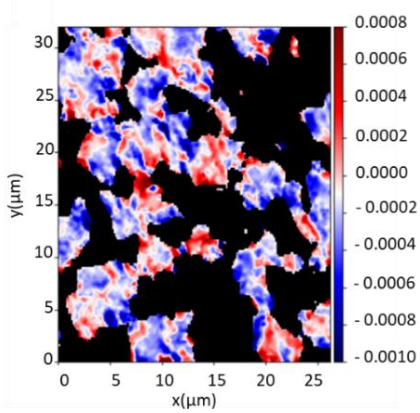

Figure 3.14: Relative strain distribution ε_{105} as function of the real beam position on the corresponding area.

The relative strain map indicates the homogeneity of the strain inside the GaN domains. However, it is hard to retrieve firm conclusions from this spatially-resolved strain analysis since we don't have an absolute strain map. The strain map is quite complex to understand since it implies both residual strains due to coalescence between misoriented grains but also strain relaxation coming from the edge of these islands of few microns.

3.3.4 Validation by EBSD measurements

To validate the SXDM results, EBSD measurements were performed on the same area of sample B studied by SXDM. A scanning electron microscopy (SEM) image of the scanned region in sample B is shown in figure 3.15(a). Pillars with uncoalesced GaN on top are seen (designated by red arrows) as well as coalesced GaN regions. EBSD mapping of the c-plane GaN layer has been performed on sample B tilted by 70° in the SEM to enhance the detection of backscattered electrons. The angular resolution is around 0.2° [21] and the step size along x and y is 0.1 µm. At each position (x, y), three frames were obtained with t=15 ms for each frame and the average result was then considered. The resulting EBSP consists of overlapping Kikuchi bands where each Kikuchi band corresponds to a set of planes. Following the data treatment procedure explained in section 2.4.2, the crystal orientation can be extracted. Figure 3.15(b) shows the GROD map which corresponds to the local misorientations of each pixel relative to the mean orientation; we note that the area colored in black is masked out because it corresponds to non-indexed pixels with low signal. We note too that the GROD maps seem to be expanded along the vertical axis compared to the SEM image, which is associated to the angle of the sample during the EBSD measurement. Figure 3.15(c) shows the GROD axis map with the standard crystallographic triangle presenting the crystallographic axes used to describe the orientation of the grains; in other words, it indicates the rotational axis that each grain must turn around to align with the mean orientation.

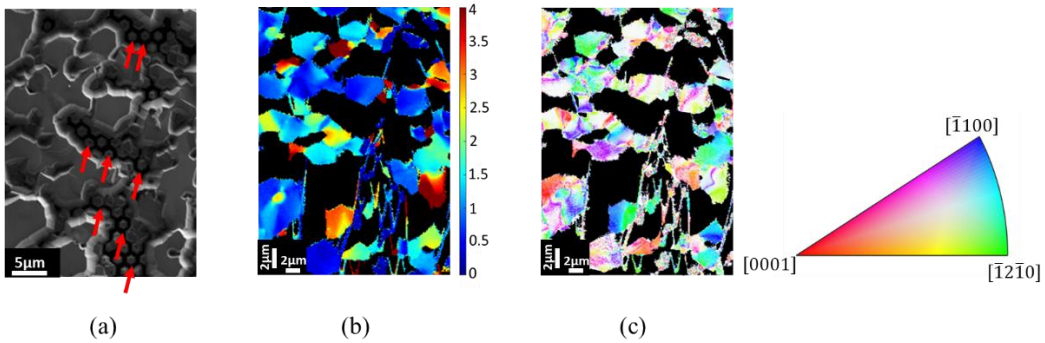

Figure 3.15: (a) SEM image of the measured area of sample B, (b) GROD map of the scanned area in (°) and (c) GROD axis map of the scanned area. The black regions in (b) and (c) correspond to undetectable points with no signal.

We observe the formation of GaN grains with small GROD angles (<0.5°) and we can also see that certain grains exhibit a large misorientation of 4° compared to the mean orientation. These results are in good agreement with those found in the SXDM measurements; we can clearly see the formation of well-defined grains with a unique orientation within themselves.

For clarity, we shown in figure 3.16, the tilt magnitude and orientation of the same area measured by SXDM and EBSD.

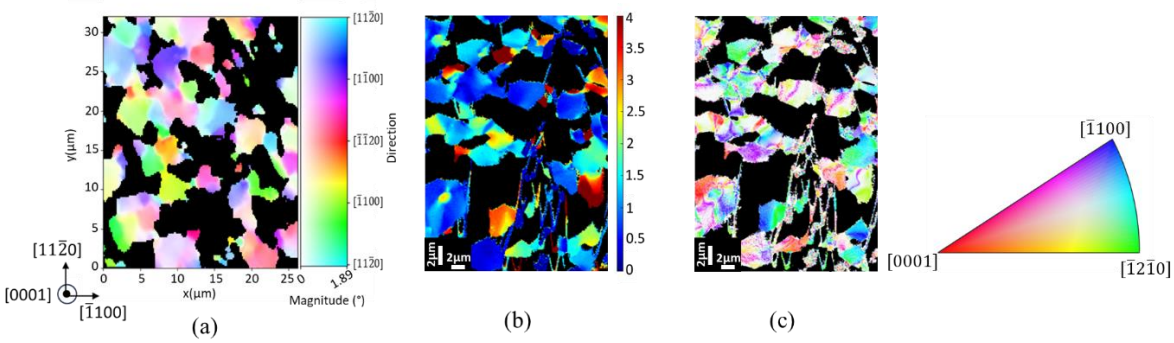

Figure 3.16: (a) 2D map of $\vec{Q}_{105}$ relative rotation of GaN at the early stage of coalescence measured by SXDM, (b) GROD map in (°) of the same region measured by EBSD and (c) GROD axis map of the corresponding area.

In the GROD angle map (figure 3.16(b)), we are able to identify a larger number of islands and a greater angular deviation than in the relative rotation map by SXDM (figure 3.16(a)). This implies that the ω angular range that was selected for the ESRF scans was insufficient and only permitted us to see GaN grains that were misoriented by a maximum of 2°. Therefore, conducting EBSD measurements prior to the synchrotron measurements would be extremely helpful to determine the ω angular range that should be considered during the SXDM experiments allowing us to be more time-efficient by avoiding unnecessary angular measurements, while at the same time, detecting all grains, including those with significant misalignments in their orientations.

To accommodate the misorientations between adjacent domains, GNDs are required, as the grain boundaries can be described in terms of arrays of dislocations for low angle boundaries

(<10°) to accommodate the tilt and twist components [127]. Therefore, in section 3.3.5, further analysis is conducted to estimate the GND densities present at the grain boundaries.

3.3.5 Geometrically necessary dislocations

From the EBSD data, it is possible to calculate the number of dislocations between neighboring grains required to put them back to exactly the same orientation. As we have shown in section 2.4.2, we can extract the lattice curvature tensor K_{ij} [115] between two consecutive positions (x1, y1) and (x_2, y_2) from equation (2.7) which is directly related to the dislocation density tensor using Nye [116] and Kröner [117] relations. Defining the active GaN slip systems for the (a+c) -type dislocation as $\{10\bar{1}1\}\langle 11\bar{2}3\rangle$, $\{11\bar{2}2\}\langle 11\bar{2}3\rangle$, and for the a-type dislocation as $\{0001\}\langle 11\bar{2}0\rangle$ [32][33], we obtain in figure 3.17(c) the distribution of the geometrically necessary dislocation densities in GaN at early stage of coalescence. To distinguish clearly the grains as well as their boundaries, figures 3.17(a) and 3.17(b) show the SEM image and the GROD map image of the same area measured by EBSD respectively. To confirm the presence of the dislocations, cathodoluminescence measurements were carried out on the same sample area with a 3 kV scanning electron beam and a step size $\Delta x=\Delta y=0.1$ µm. The acquired CL image is shown in figure 3.17(d). To help identify the same zones and grains in each of the four maps, specific zones are highlighted by color-coordinated arrows in each figure.

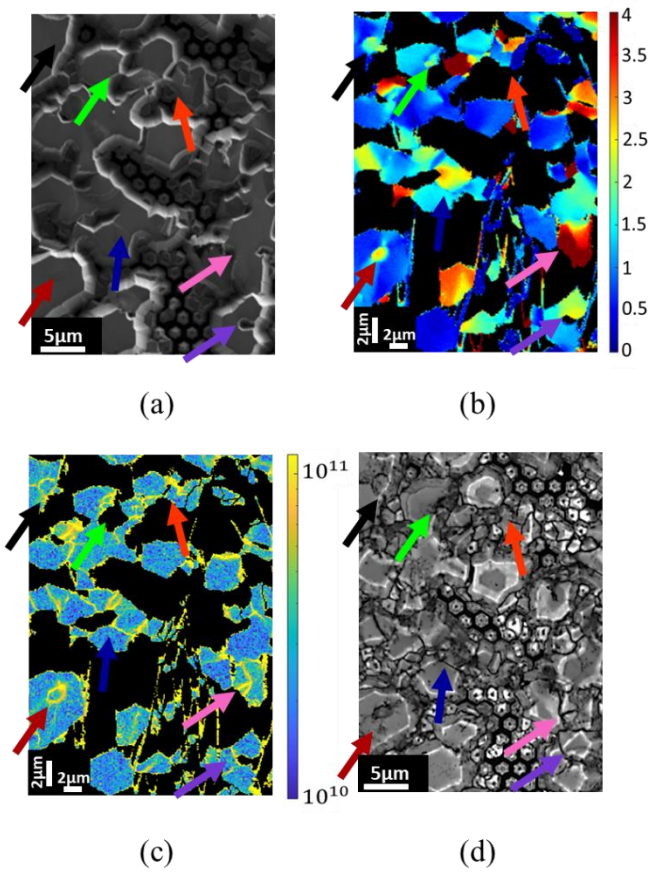

Figure 3.17: (a) SEM image of the measured area of sample B, (b) GROD map in (°) of the corresponding region, (c) Estimation of the geometrically necessary dislocation density distribution (color scale indicates logarithmic values in cm^{-2}), and (d) CL image of the corresponding area.

We observe large GND values around 2 x 10^{11} cm^{-2}, present at the grain boundaries when the difference in GROD values is higher than 2°, while areas with a misorientation lower than 2° present lower GND values of the order of 10^{10} cm^{-2}. We detected GND at the free edges of some of the GaN grains which we attribute to scan distortion . In fact, the quality of the Kikuchi band used for indexing depends on the local surface topography and it is very poor at the edges and voids. As a result, the precision of orientation determination is reduced at these edges, and the noise measurement is greater, which means the increase in the GND density in these areas is an artifact since its evaluation is based on the orientation variation [128]. CL images were collected at the corresponding sample area; we can confirm that the high-value (~10^{11} cm^{-2}) dislocations in the GND map (figure 3.17(c)) are indeed the same dislocations lines observed in the CL image on the surface of the flat grains, as indicated by arrows of matching colors. CL measurements across the non-flat area that contain pillars only (with no coalesced GaN on top) are not discussed because the surface irregularities could affect photon extraction.

We note that noise in measurement leads to overestimated GND density especially in lightly deformed grain structures and local measurements (small step size). In our case, this precision limit has set the lowest measurable GND density to 10^{10} cm^{-2}.

Nevertheless, this study confirms the growth of large GaN domains (3.9 µm) of homogeneous orientation with large dislocation densities at the interfaces between highly disoriented domains and reveals that the grain boundaries are the major issue because of the GND that can extend all the way to the top of the device, negatively impacting the efficiency of light emission in µLEDs.

3.3.6 Testing model to compute the tilt between neighboring pillars

Further data treatment allows us to analyze the tilt between neighboring pillars that, according to our measurements allow the formation of grains that are well aligned within themselves (figure 3.12(b)). Our earlier tilt measurements on sets of three pillars in section 3.2.2 suggested a potential initial misorientation (tilt limit) between adjacent GaN pillars. Therefore, from the measurements on the new samples presented in sections 3.3.1 and 3.3.2, we will calculate a tilt limit that corresponds to the maximum tilt possible between adjacent pillars that leads to the formation of pillar domains similar in size to the GaN domains forming at the early coalescence stage. This size comparison will be made between pillar groups before coalescence, with a pitch of 0.5 µm (sample A) and coalesced GaN grains grown on top of pillars with a pitch of 1.5 µm (sample B). These different pitch sizes are used due to the lack of available data on structures with the same pitch. It is assumed that the distribution of the orientation of pillars would be unchanged for different pitch values, since these pillars are formed by etching from 2D layers.

First, we set a tilt limit between adjacent pillars, and then determine how many pillars would be contained in a group within this limit. The size of groups of pillars is then analyzed for different tilt limit values. Figure 3.18(a) shows the tilt magnitude of the GaN pillars before coalescence (sample A) and figure 3.18(b) shows also the tilt distribution of the same sample but with a conversion from pillars to pixels spaced by 0.5 µm, meaning each pixel represents one pillar.

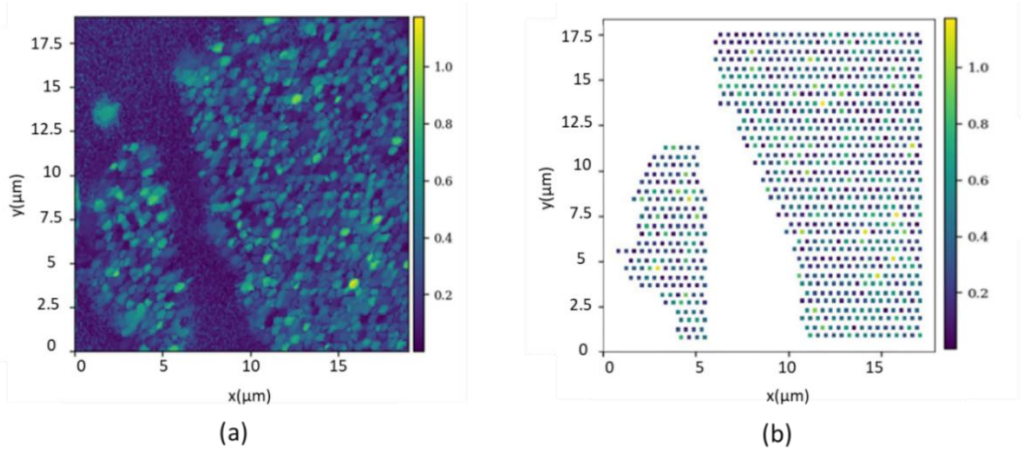

Figure 3.18: (a) Tilt magnitude distribution of the GaN pillars before coalescence and (b) tilt magnitude of the GaN pillars before coalescence each represented by one pixel.

We define the adjacent pillars as the pillars' first neighbors and choose a set of tilt limits from 0.2° to 0.04°. The test condition is that the tilt between two adjacent pillars is less than the tilt limit specified. In the next step, each pillar is considered as a starting point and the tilt between all its neighboring pillars is calculated. If the condition is satisfied, in other words if the tilt between the two pillars is less than the specified tilt limit, these two pillars are considered to belong to the same pillar group. Figure 3.19 shows the pillars group obtained for three tilt limit values (0.2°, 0.1° and 0.04°). We note that the groups formed by one pillar only were removed from the maps.

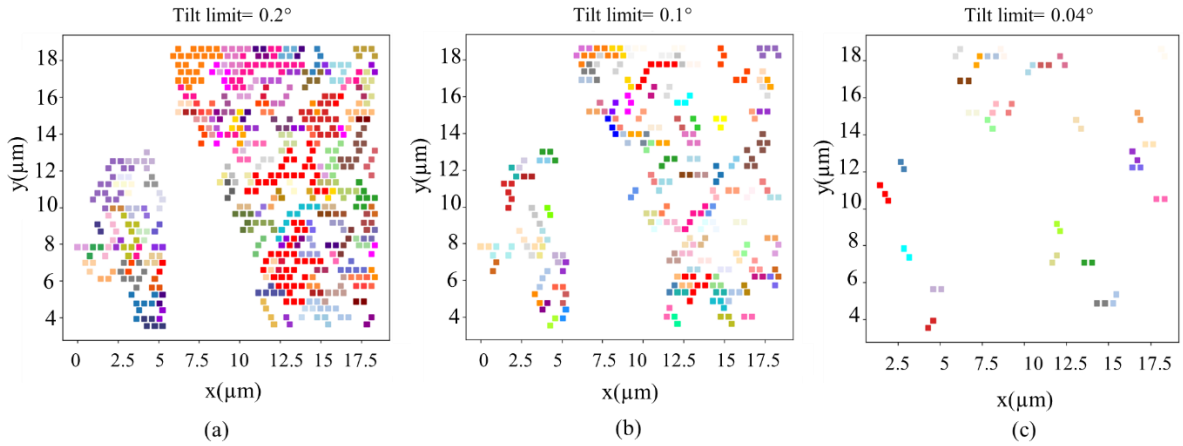

Figure 3.19: (a) Groups of pillars with tilt between neighboring pillars <0.2°, (b) groups of pillars with tilt between neighboring pillars <0.1° and (c) groups of pillars with tilt between neighboring pillars <0.04°. The pillars having the same color belong to the same group.

The pillars belonging to the same group have the same color. We notice that for a tilt max=0.2° (figure 3.19(a)), we have large groups of pillars formed much bigger than the coalesced GaN domain size, meaning that the tilt limit specified is too high. After decreasing the tilt limit, we notice the formation of smaller groups.

The final step is to compare the sizes of these groups to the size of the GaN domains to find the max tilt possible that allow us to obtain groups of pillars similar in size to the GaN domains. To clearly display the groups, the GaN domains are drawn as red contours in figure 3.20(a) and the pillars group of tilt limits 0.1° and 0.04° are designated in red contours in figures 3.20(b) and 3.20(c) respectively.

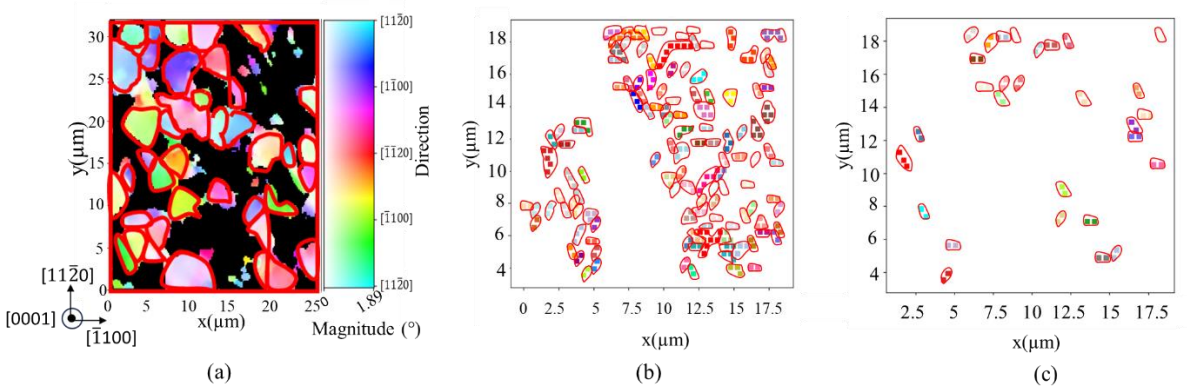

Figure 3.20: (a) 2D map of $\vec{Q}_{105}$ relative tilt of GaN at the early stage of coalescence with GaN domains encircled by a red border, (b) group of pillars encircled by a red border with tilt between neighboring pillars <0.1°, and (c) group of pillars encircled by a red border with tilt between neighboring pillars <0.04°.

However, as we mentioned in the beginning of this section, the GaN domains in figure 3.20(a) are grown on top of pillars with a pitch of 1.5 µm while the GaN pillars in figures 3.18, 3.20(b) and 3.20(c) have a pitch of 0.5 µm. In order to properly compare the sizes, we assume that the distribution of the pillars before coalescence is the same whether the pitch is equal to 0.5 µm or 1.5 µm because regardless of the pitch, the pillars undergo the same etching process. If we now consider that the pillars in figures 3.18, 3.20(b) and 3.20(c) have a pitch of 1.5 µm instead of 0.5 µm while maintaining the same orientation, this means that the size of the pillar groups obtained from figure 3.20(b) and 3.20(c) should also be multiplied by three. Now we can compare them to the GaN domain size from figure 3.20(a).

From figure 3.20(a), we find the GaN domains mean size is 3.9 µm with a standard deviation σ=1.3 µm. We note that GaN domains smaller than 1.5 µm across were excluded from the calculation of the mean domain size and were not outlined in figure 3.20(a) because we consider that these groups are formed on top of a single pillar, and they were removed from the tilt limit maps shown in figure 3.19.

From figure 3.20(b), the size of pillar groups for a tilt limit of 0.1° is found to be equal to 1.7 µm on average, and that with a tilt limit of 0.04° is equal to 0.5 µm on average as seen in figure 3.20(c). Once multiplied by three, the tilt limit of 0.1° between neighboring pillars before coalescence allows the formation of group pillars slightly larger than the coalesced GaN domains which are 3.9 µm on average (figure 3.20(a)). The tilt limit of 0.1° shows strong consistency with the tilt measured directly using SXDM in the sets of three pillars in section

3.2.2. This tilt can be generated due to the excess surface energy present on the interface of each GaN pyramid and might be facilitated by the compliant SiO_2 that could present viscoelastic properties at high growth temperature [129]. Further analysis of this surface energy will be performed in the next chapter 4 to test the feasibility of theses tilt values from an energetic point of view.

Additionally, we notice that in the case of a tilt limit of 0.1° (figure 3.20(b)) that each group typically consists of 2 to 5 pillars, so we would expect each island of GaN in figure 3.20(a) to have this number of pillars. To verify our work, we show in figure 3.21 the superposition of the outline of the GaN domains on top of a map containing pillars with pitch= 1.5 µm distributed in a hexagonal pattern.

Figure 3.21: Superposition of the outline of the GaN domains with the map of pillars (seen as black points) having a pitch of 1.5 µm and distributed a hexagonal pattern.

The pillar map is obtained from the GDS (graphic design system) file used for the patterning process. We notice the presence of typically 2 to 6 pillars in each GaN island which is in good agreement with the results found in figure 3.20(b) where the tilt limit was set to 0.1°.

These results also illustrate the importance of combining EBSD, CL and SXDM to provide complementary structural information on the evolution of GaN crystalline structure from pillars to well-defined coalesced domains. This advances the understanding of the coalescence process at the nanoscale and highlights the potential of this novel pendeo-epitaxy technique in producing well-oriented GaN layers employed in the future in the production of micro-LEDs. Following the study of the GaN at the first growth stages, new samples with fully coalesced GaN layers are characterized to assess their quality and determine if they are suitable for use in microLEDs.

3.4 Demonstration of highly oriented GaN lines on top of a set of ten pillars

3.4.1 Crystalline GaN orientation

Now that we have measured the rotation of pillars in sets of three pillars and studied the GaN coalescence in non-fully coalesced GaN samples, the next goal is to determine the quality of fully coalesced GaN epitaxial layers along a 1D array of ten pillars with a pitch of 0.5 µm. The coalesced GaN lines on top of five lines each consists of ten pillars shown in figure 3.22 are characterized with DFXM using the GaN (101) reflection. The choice of DFXM technique is based on its potential to illuminate the whole sample (the five coalesced lines) at once and give direct real image of the sample. Additionally, the measurements as well as the data treatment are relatively fast, and it is still possible to perform mosaicity scans (ω-ϕ scans) that provide information on the crystallographic misorientations in the sample.

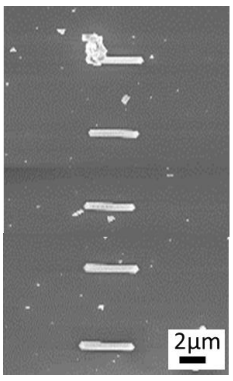

Figure 3.22: SEM image of five fully coalesced GaN lines.

As we have mentioned in section 2.3.2, the measurements were performed in the transmission mode due to the limitations of 2θ on the experimental setup. We measured the GaN(101) Bragg reflection to study the GaN structures using a diffraction angle θ=9.16° and incidence angle ω=65°. We performed ω-ϕ scans, meaning rocking curves around the incidence angle ω while rotating the sample around its normal axis ϕ (ω rocking curve for each value of ϕ) as illustrated in figure 3.23. We typically performed ω rocking curves with 40 points, with a step Δω of 0.02° for 21 values of ϕ with Δϕ=0.08°. The spatial resolution is 100 nm, the beam size ~50 µm and the beam energy is 16 keV. Measurements on the Si layers in the nanopillars were attempted, however the diffracted intensity from the thin Si layers was not enough to be registered by the detector due to the small size of the Si pillars, and the limited collection time on the detector of only 2 seconds.

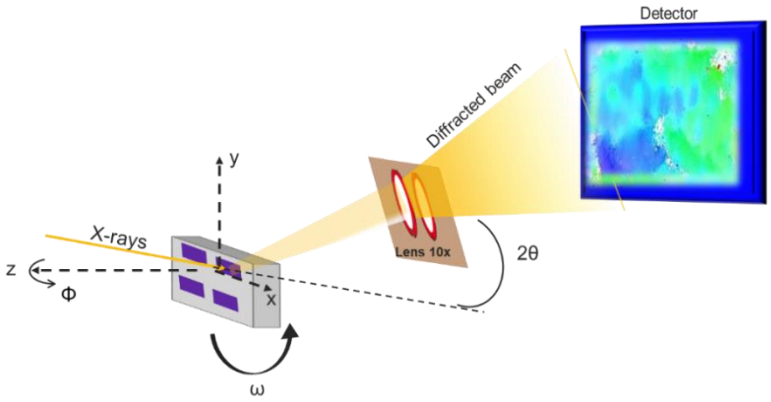

Figure 3.23: Schematic of dark-field X-ray microscopy geometry including the rotational axes ω, Φ and 2θ. The grey box is our sample, and the purple rectangle represents the GaN coalesced structures.

The data obtained from the ω-ϕ scans was extracted using the darfix library [130]. Figure 3.24(b) shows the center of mass (COM) map for the incidence angle ω obtained for the five lines.

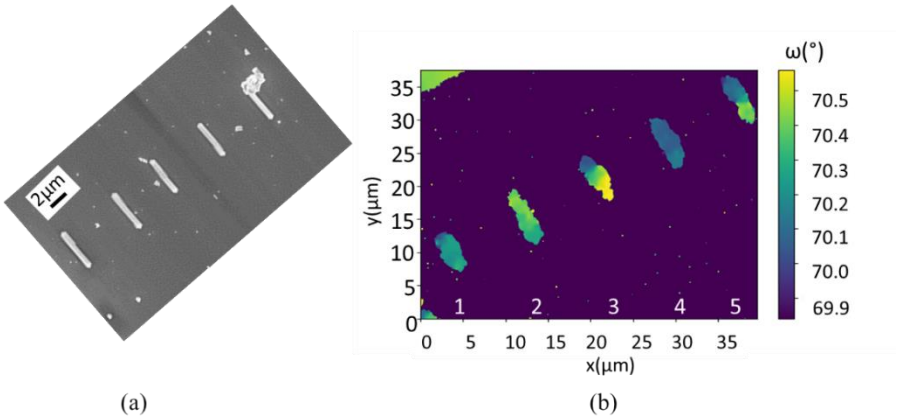

Figure 3.24: (a) Inclined SEM image of five fully coalesced GaN lines, (b) Centre of Mass map for ω of the five lines.

The results show significant differences between the lines. For lines 1, 2 and 4, we have homogeneous lines with a very small ω variation along the line itself ($\Delta\omega<0.1°$), implying that the GaN crystallites are very well oriented and that few, if any, coalescence boundary dislocations are required to accommodate any misorientation [131] . In contrast, lines 3 and 5 have strong ω variations ($\Delta\omega>0.1°$) along their length, implying the generation of dislocations at the interfaces between pillars.

3.4.2 Dislocation density in the GaN lines

In figures 3.25(a-e), we show histograms of the ω values obtained in figure 3.24(b) for each pixel with a Δω of 0.1° for the five lines and the standard deviation (σ) values calculated from a Gaussian fit.

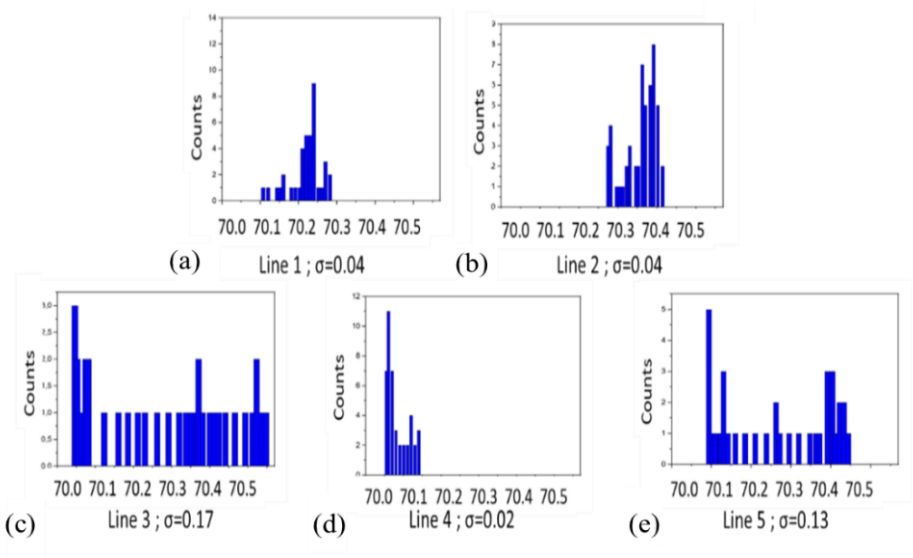

Figure 3.25: Histograms showing the distribution of ω along each line (with a binning step of 0.1°).

The values of σ found in lines 1, 2 and 4 are very small, in the order of 0.04°. In lines 3 and 5, we have a much wider range of ω values and higher σ values of 0.17° and 0.13° respectively. Kurtz et al. [132] created a model that relates the FWHM (β) of ω scan peaks to the dislocation density ρ and the Burgers vector b through equation (3.5):

$$\rho = \frac{\beta^2}{9b^2} \quad \textit{Equation 3.5}$$

Based on this equation, the dislocation density for the well oriented lines (1, 2, 4) is calculated to be 1.2 x 10^7 cm^{-2} while previous studies of 2D GaN on silicon reported that FWHM values depend on the growth rate and the range of AlN growth temperature: the rocking curve width of (002) GaN varies from 0.18° to 0.66° [133], other studies reported a FWHM of 0.13° for the (002) GaN reflection [132] and of 0.19° for the (101) GaN reflection [132] corresponding to dislocation densities in the order of 1 x 10^9 cm^{-2}. This shows that for the good lines (1, 2, 4), there is a significant improvement. However, lines 3 and 5 are comparable to a standard 2D growth with a dislocation density of 1.7 x 10^9 cm^{-2} meaning that improvements are still required to better control the growth process. These results are promising, as they show that it is possible to have excellent alignment of the pyramids during coalescence.

3.5 Promising results of small highly oriented islands of GaN on Si suitable for µLEDs

3.5.1 Measurements of the quality of GaN platelets up to 40 x 40 µm²

The next objective is to investigate larger GaN platelets suitable for microLEDs, therefore, fully coalesced GaN structure of 40 × 40 µm^2 grown on top of nanopillar array with hexagonal symmetry. Once again, we used dark field X-ray microcopy at the ID06 beamline. Figure 3.26(a) shows GaN/AlN/Si(111)/SiO_2/Si(100) nanopillars in a hexagonal distribution before GaN regrowth. Following the 2-step growth, we obtain a 40x40 µm^2 fully coalesced GaN structure with a thickness of 3 µm, as shown in figure 3.26(b). A matrix formed by fully coalesced structures is presented in figure 3.26(c) and two fully coalesced matrices are shown in figure 3.26(d) with 1 µm pitch (top) and 0.5 µm pitch (bottom). We should note that some platelets in figure 3.26(d) (bottom part) are damaged due to a problem in the pillar fabrication process. In parallel, this process to optimize the pillar etching has been worked on elsewhere [73]. Therefore, all measurements in this work were performed only on the better quality GaN platelets.

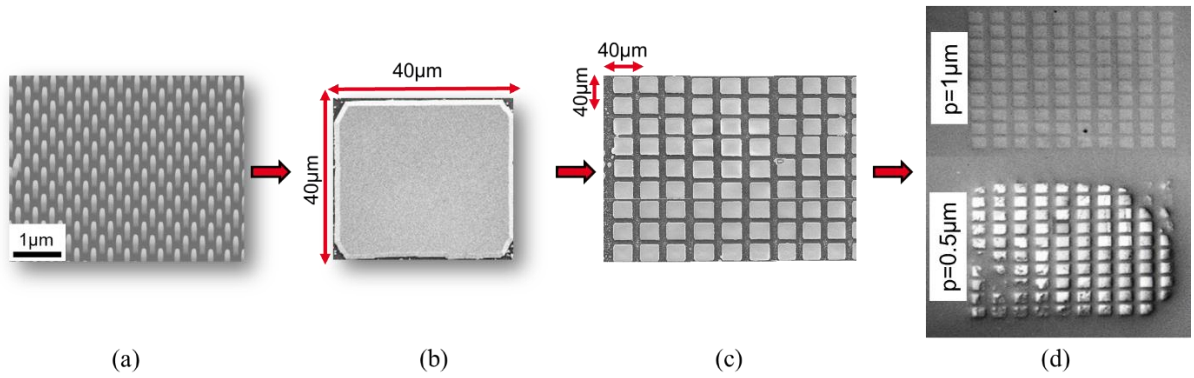

Figure 3.26: Scanning Electron Microscope (SEM) images of (a) GaN/AlN/Si(111)/SiO_2/Si(100) nanopillars before GaN pyramid growth, (b) single fully coalesced 40 × 40 µm^2 GaN platelet, (c) matrix of fully coalesced GaN platelets, (d) two GaN matrices with structures coalesced on different pitch arrays (p=0.5 µm and p=1 µm).

The same measurements as for the lines of 10 pillars were performed on two 40 x 40 µm² GaN platelets: structure 1 with a pitch of 0.5 µm and structure 2 with a pitch of 1 µm. Figures 3.27(a) and 3.27(b) show the COM of the two structures for ω using the GaN(101) reflection from ω-ϕ scans. From structure 1, we can see three separate areas. Clusters 1 and 3 in structure 1 are very well oriented areas, with standard deviations of 0.04° and 0.07° respectively, as presented in the histograms (figure 3.27(c)). These values are similar to those found in the homogenous lines discussed in section 3.4.3. The resulting dislocation density for cluster 1 is calculated as 1.1 x 10^8 cm^{-2} from equation (3.5), a value significantly better than standard GaN 2D on silicon

growth. However, cluster 2 has a higher standard deviation of 0.21°, which is larger than values seen for standard GaN 2D on silicon growth.

We should note that GaN structure 1 is not a full rectangle due to a parasite nucleation site whose different orientation prevents it from diffracting at the chosen Bragg angle. This parasite nucleation site originates from growth on top of improperly etched, missing, or fractured pillars.

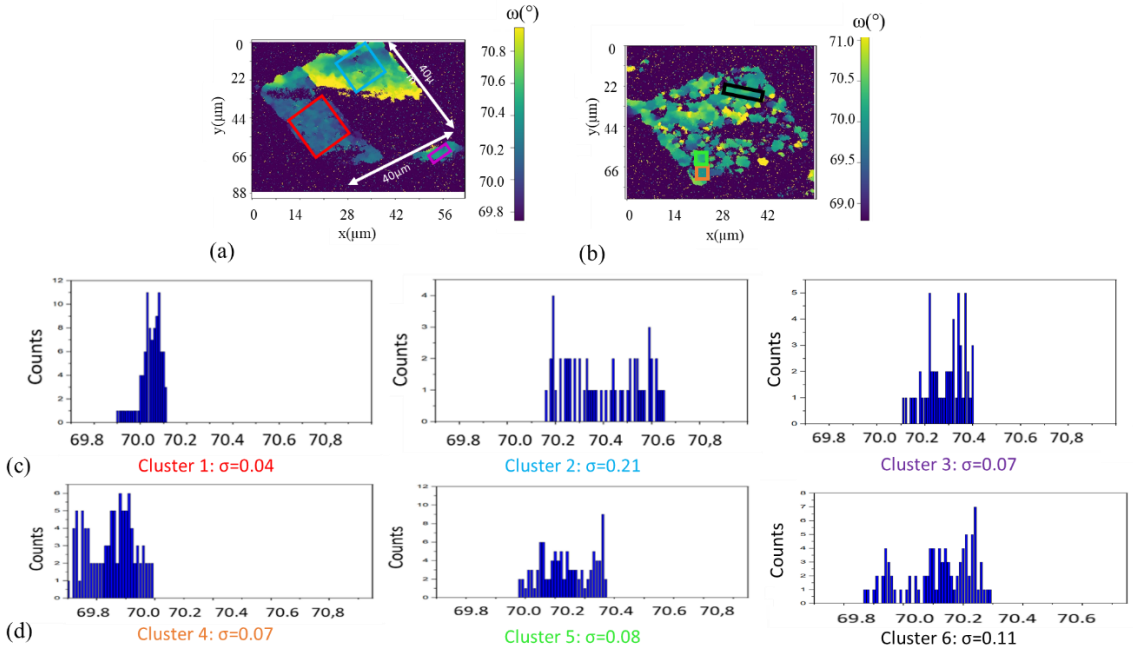

Figure 3.27: (a) Center of mass map for ω of GaN structure 1 with pitch=0.5 µm, (b) Centre of mass map for ω of GaN structure 2 with pitch=1 µm, (c) three histograms showing the distribution of ω in clusters 1, 2 and 3 inside structure 1, (d) three histograms showing the distribution of ω along clusters 4, 5 and 6 inside structure 2 (the binning step corresponds to 0.1°).

GaN structure 2 has a pitch of 1 µm (figure 3.27((b)), and since the spacing between the pillars is larger, the coalescence is not completely finished. As the coalescence is still ongoing, we can see that it appears to occur through a cluster phenomenon where each group of pillars coalesces to form small areas of well oriented GaN with low standard deviation values, as seen in figure 3.27(d). Cluster 4, 5 and 6 have standard deviation values of 0.07°, 0.08° and 0.11° respectively. Calculations using equation (3.5) translate these values into dislocation densities of 1.3 x 10^8 cm^{-2}, 2.6 x 10^8 cm^{-2}, and 9.2 x 10^8 cm^{-2} respectively.

Although not uniform across the platelets, these results are extremely promising since we are able to achieve high quality GaN across areas greater than 10 × 10 µm² (Structure 1, cluster 1) with our growth approach suitable for µLEDs.

3.5.2 Growth through cluster formation

The last experiment performed was on the macroscopic XRD at the BM02 beamline on the same samples characterized by DFXM in order to (i) analyze macroscopically the platelet samples and (ii) have access to the silicon (111) layer before and after coalescence, which was not possible to measure using DFXM because of the weak intensity of the diffraction peaks for this thin buried layer. The energy of the incident beam was 9 keV with an intensity of 2.4 × 10^{10} photons/s. Given that each GaN platelet is 40 x 40 µm², the incident beam arriving on the sample covers an area of approximately one platelet in the x direction and two in the y direction.

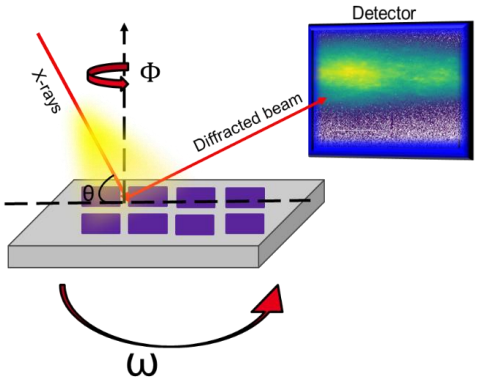

Figure 3.28: Schematic of macroscopic X-ray diffraction.

We performed ω - ϕ scans around the GaN(204) reflection on two structures with p=0.5 µm and two structures with p=1 µm positioned at the center of the matrix presented in figure 3.26(d). We performed ω rocking curves of 70 points with a step Δω= 0.11° for 25 values of ϕ with Δϕ=0.4° and with t=2 s. The Bragg angle θ=46.75° and the incidence angle ω=89.95° and the sample is rotated around ϕ such that ϕ=147°.

Figure 3.29(a) shows the diffraction pattern on the 2D detector of the integrated intensity, with the y-axis corresponding to values of 2θ, and the x-axis corresponding to ϕ. This image is from the GaN(204) Bragg reflection in the middle of a GaN platelet coalesced from pillars having a 0.5 µm pitch. For a given value of θ and ω, we have peaks at different values of ϕ, as shown by the red arrows. This implies that we are diffracting from zones or clusters of GaN with different values of twist. In addition, figure 3.29(b) shows the distribution of the intensity as function of ω for a given ϕ value, and we can see the presence of more than one peak at different values of ω: for example, for a pitch of 0.5 µm, we identify a peak at ω= 88.8° and another at ω = 89.5°. This also reinforces the cluster detection, but this time with different tilt orientation. Figure 3.29(c) shows similar results for the structures coalesced from pillars with a pitch of 1 µm.

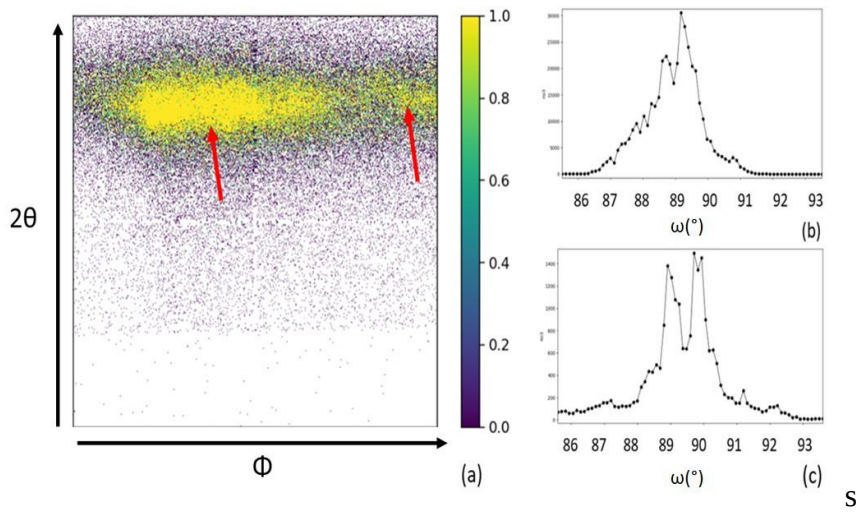

Figure 3.29:(a) 2D detector image of the GaN(204) Bragg peaks at one position in the GaN structure, with the x and y axis representing Φ and 2θ respectively. Intensity is displayed to the right of the image and two Bragg peaks at different values of Φ are shown with the red arrows, (b & c) rocking curves showing two Bragg peaks at different values of ω for pitch=0.5 µm (b) and pitch=1 µm (c).

These results reinforce the analysis of the growth seen by DFXM, which suggests that coalescence is happening by formation of clusters covering several pillars, which subsequently coalesce as large grains.

It is interesting to note also that by measuring the GaN(204) reflection, we obtained FHWM values around 0.6° in the GaN layers of the coalesced structure. This high value can be explained by the fact that with this technique we are scanning across two GaN structures and not just one like the DFXM case, thus the results presented correspond to multiple clusters across two structures. The divergence of the focused beam is around 0.004° along the vertical direction and around 0.01° along the horizontal direction, so this is not a significant factor in the peak width.

3.5.3 Measurement of the pillar's rotation on a macro scale

Lastly, we can benefit from this experiment to examine the orientation in the Si layers within the nanopillars beneath the GaN layers before coalescence and after coalescence. The tilt and twist are analysed by measuring the symmetrical Si(111) and asymmetrical Si(331) reflections, respectively. For the Si(111) reflection, the Bragg angle is equivalent to the incidence angle $\theta = \omega = 12.75°$ and $\phi = 123°$. We performed ω rocking curves of 41 points with a step $\Delta\omega = 0.06°$ at a constant ϕ value and with t=0.5s. For the Si(331) reflection, the Bragg angle is $\theta = 33.55°$ and the incidence angle $\omega = 55.6°$ and $\phi = 145°$. We performed ω rocking curves of 70 points with a step $\Delta\omega = 0.11°$ at for 25 values of ϕ with $\Delta\phi = 0.4°$ and with t=2 s.[2]

Two samples were measured: sample A is a reference sample that has only nanopillars, i.e. prior to the pyramid growth (figure 3.26(a)). Sample B is composed of the fully coalesced GaN structures described above in figure 3.26(d), with nanopillar pitch of 0.5 µm and 1 µm.

For the (331) reflection, the FWHM of the diffraction curve is broadened in sample B compared to sample A, from 1.1° for sample A to 2.5° for sample B for a pitch of 0.5 µm. It is likely that the initial value of FWHM is linked to the instrumental resolution and the coherently diffracting domains size and shape [134]. The broadening observed in the Si (331) peak due to size effects is approximately at 0.08°. The Si(111) reflection also shows an increase in FWHM between the reference sample A and sample B, going from 0.32° for sample A to 0.81° for sample B for a pitch of 0.5 µm and from 0.25° for sample A to 0.71° for sample B for a pitch of 1 µm. The broadening observed in the Si (111) peak due to size effects is approximately at 0.07°. The broadening of the two diffracted planes implies that the silicon layers are more twisted and tilted in the coalesced structures compared to the reference sample, as we have previously shown on different type of samples and different pitch values.

3.6 Conclusion

In this chapter, we first presented the SXDM characterization of simple samples consisting of sets of three pillars with coalesced GaN on top. The results allowed us to confirm the PEGADIS hypothesis about the rotation of the pillars by 0.1° during coalescence leading to the reorientation of the coalesced GaN lines on top. Second, a new set of samples has been characterized with SXDM at the ESRF at the early stage of coalescence to understand the coalescence process taking place at the nanoscale. The measurements on GaN coalescing at an early growth stage and on GaN pillars only (prior to growth) confirmed that the initially misoriented GaN pillars coalesce into larger well-defined GaN domains very well oriented within themselves but with a larger tilt/twist between them. A broadening of the diffraction peak at the boundaries of the same domains identified in the orientation map was seen and could be caused by elastic strain and the presence of geometrically necessary dislocations. The dislocations were also seen at domain boundaries by CL and the estimated GND density from EBSD measurements is equal to 2×10^{11} cm^{-2} . Additionally, from SXDM post processing, it was estimated that a tilt limit of 0.1° between neighboring pillars would lead to the formation of pillars groups similar in size to the domain size found in the GaN layers. This tilt limit is in good agreement with the tilt measured directly in the set of three pillars.
The next objective was to study larger coalesced GaN lines, therefore, GaN lines on top of 10 pillars was characterized with DFXM and we showed that with our unique growth approach,

we can achieve extremely well oriented lines, with barely any misorientation (σ= 0.04°) between pillars along the whole line, which is better than 2D GaN on Si. However, this only occurred for 3 out of 5 lines. Then, we studied fully coalesced 40 x 40 μm² platelets, where we achieve regions up to 10×10 μm^2 that are also extremely well oriented. These results are extremely promising for the fabrication of small highly oriented islands of GaN on silicon suitable for highly efficient light emission, in devices such as micro-displays or micro-LEDs, although more work needs to be done to improve the reproducibility of this approach. At the macro scale, large GaN peak widths were measured, implying that the coalescence occurs by cluster formation where different clusters have different orientations as seen from DFXM measurements. We also compared the orientation in the Si section in the nanopillars before coalescence and after coalescence to further confirm the self-orientation of the GaN pyramids during the coalescence, resulting in increased misorientation of the silicon layers in the pillars after coalescence.

To complete this work, finite element simulations using Abaqus software are presented in chapter 4. The objectives from the simulations will be to explain the pillar tilt values found from the experimental data and to find the optimal growth parameters that could help in the rotation of the pillar. Such optimization was not achievable in an experimental work because of the limited beamtime, the large number of measurements required, and the large time required to fabricate the samples.

Chapter 4: Finite element mechanical modeling of GaN pillars coalescence

4.1 Introduction

To complete this work, we intend to (i) provide explanation for the tilt/twist values acquired from the experimental data and (ii) optimize the pillar's parameters in a way that it increases the possibility of rotation. However, it is not possible to accomplish these goals through experiments only because synchrotron beamtime is very limited to test various tilt/twist configurations and conventional XRD lack the resolution (either spatial or temporal). Therefore, we will employ simulations to obtain this required information. Simulations offer a cost-effective and efficient means of exploring the behavior of complex systems under various conditions and across various scientific fields.

The goal of our simulations will be to (i) conduct mechanical analysis that allows us to simulate the rotation of the pillars taking place during the coalescence, (ii) compute the surface energy required for different rotation angles to check whether it is available at the GaN surface and (iii) optimize the pillar pitch and the GaN facet's thickness (e) to enhance the feasibility of rotation.

Considering the context of our project, simulation methods available can be broadly classified into two main families: (i) discrete simulations such as molecular dynamics (MD) and density functional theory (DFT), and (ii) continuous simulations such as finite difference method (FDM), fast Fourier transform (FFT) and finite element method (FEM). Each type of simulation has its distinct characteristics and applications. We show briefly the characteristics of each approach:

- MD is used for atomic and molecular scale simulations; it simulates the physical movements of atoms and molecules over time [135]. It relies on fundamental physical laws, such as Newton's equations of motion, and accurate interatomic potentials which reduces the need for strong hypotheses, however these simulations are confined to the nanometer scale and simulating large systems over long timescales is computationally demanding and therefore not adapted to our microscopic study.
- DFT provides detailed information about a molecule electronic structure, thus it limits the model to an even smaller system than the one simulated with MD [136].
- FDM tackles the approximation of partial differential equations (PDE) (e.g. Momentum and energy conservation) and is particularly well-suited for problems with regular geometries, such as rectangles or squares [137].
- FFT-based methods also tackle the approximation of PDEs all while having low computational cost, but these approaches often rely periodic domain which is a

limitation when dealing with non-periodic data [138]. FFT-based methods are not well-suited to handle complex geometries, such as those with voids or irregular shapes.

- FEM allows also to approximate the solution of PDEs using a non-structured discretization of the computational domain to provide a deterministic solution [139]. While FEM is based on rigorous mathematical principles, it does involve certain assumptions and approximations, such as the choice of element type, interpolation functions, and temporal integrating schemes. It is applicable to a wide range of scales, including micro-scale problems.

In this thesis, the purpose of the modelling is to simulate the rotation of pillars with non-periodic shape. Given the micro-scale and non-periodic nature of our system, finite element method is the optimal choice because of its capability to accurately represent micro-scale complex geometries, handle non-periodic boundary conditions (BC), and effectively model thermal and mechanical phenomena.

In addition to what we already mentioned, FEM supports coupled Multiphysics simulations allowing for the analysis of interactions between different physical phenomena, in our case, between the thermal and mechanical phenomena and it can handle complex geometries, making it suitable for modeling of structures with different parts and capable of performing detailed structural analyses. To implement the finite element simulations, Abaqus software will be used.

Using Abaqus, we establish a model of the entire system consisting of different components (substrate + GaN/AlN/Si/SiO_2 pillars + GaN). FEM relies on the use of discretization of the computational domain that is composed of nodes that are linked by the elements of the mesh. The generation of the discretization is referred to as meshing. The nodes of the mesh as used to build an interpolated solution of the PDE that is being solved, and the degrees of freedom of the problem are linked to the nodes. Therefore, by changing the position and the number of nodes of the mesh it is possible to control the accuracy of the solution. FEM transforms the original problem into a system of equations where nodal degrees of freedom (e.g. displacements in the case of a mechanical problem) are the unknowns. Once the degrees of freedom are found, they are interpolated inside every element in order to an approximated solution to the problem. Interested readers could refer to [140]. In the following, a detailed description of the model is presented as well as its limitations, the boundary conditions used, the assigned material properties, and the numerical results.

4.2 Modeling of the test model

4.2.1 Purpose of the test model

In section 4.2, we will define a simple geometrical model of one pillar only, bonded onto a Si (001) substrate prior to the growth. We will refer to it as “test model” and use it to define the boundary conditions, the applied constraint, the element size and type. The pillar will then be submitted to a torsion load and the strain energy is computed. The goal of this simulation is to validate the BC, constraints, element size and type defined in the “test” model. This validation will be carried out by comparing the numerical energy with the analytical energy.

4.2.2 Geometrical model and boundary conditions

We define in figure 4.1(a) a simple model of one pillar bonded onto a Si (001) substrate prior to the growth. As mentioned in section 4.2.1, this simple model is used as a “test model” to verify the applied boundary conditions and the applied constraint. The mesh size is examined to verify if our approach is well adapted to the micro-scale.

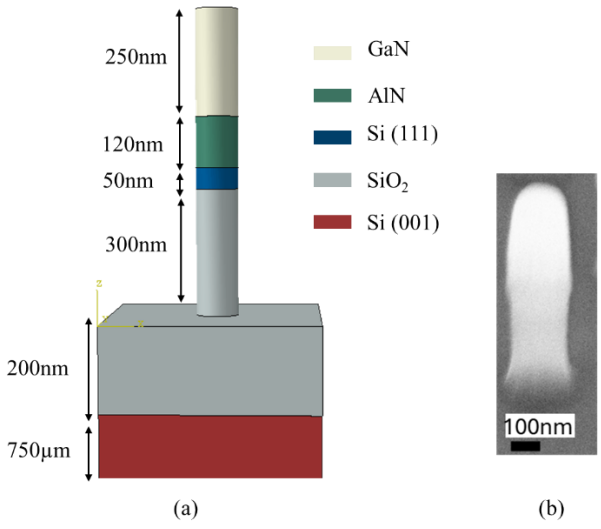

Figure 4.1: (a) A simple geometrical model of one pillar (GaN/AlN/Si111/SiO_2) bonded into a Si (001) substrate and (b) SEM image of the corresponding pillar prior to growth.

The pillar is considered to have a cylindrical shape with a diameter D =100nm. However, this is a simplification, because we can see in figure 4.1(b), that the pillar exhibits a slight variation in diameter between its base and upper section, and this geometry could change depending on the etching recipe. It would be complex to come up with a numerical strategy that allows geometries that change from one sample to another, and so a simplified cylinder is used for all the models. The material properties is presented in section 4.2.3.

As we see in figure 4.1(a), the model presents different parts (a part represents a section with a defined shape and size and is made out of a unique homogeneous material). The different parts are assembled together to fit the real geometry and they are linked mechanically by using different type of constraints offered by Abaqus. When using finite elements, the degrees of freedom are the displacements of the nodes of the mesh, and it is possible to add constraints to the kinematics of some of these nodes. A constraint named “tie” will be employed throughout this study to connect the parts unless otherwise specified.

A tie constraint in Abaqus is applied between two surfaces of two different parts that in reality are "glued" together. It is a surface-based constraint that allows us to fuse together two surfaces so that they behave as if they are perfectly bonded together, preventing any relative motion between them. The tie constraint links the degrees of freedom of the nodes of one surface (“slave” surface) to degrees of freedom of the nodes of another surface (“master” surface) by adding some algebraic equations to classic FEM system of equations. Thus, in a tie constraint, we define two types of surfaces:

- Master surface: The surface of the one part that will deform independently from its tied slave surface.
- Slave surface: The surface of the second part that will follow the master surface. i.e. the displacement of the nodes of the slave surface are interpolated as a function of the displacement of the nodes of the master surface.

Therefore, the tie constraint essentially forces corresponding nodes on the slave surface to follow the motion of the master surface. The surfaces pairs that are tied in our model are:

- The top surface of Si with the bottom surface of unetched SiO_2
- The top surface of unetched SiO_2 with the bottom surface of the SiO_2 part in the pillar
- The top surface of the SiO_2 part in the pillar with bottom surface of the Si part in the pillar.
- The top surface of the Si part in the pillar with bottom surface of the AlN part in the pillar.
- The top surface of the AlN part in the pillar with bottom surface of the GaN part in the pillar.

A mesh sensitivity analysis was conducted to determine the optimal mesh size. This involved simulating the model with varying mesh densities to identify the mesh size that yielded converged results while maintaining computational efficiency. The optimal mesh size found for the various parts forming the pillar is equal to 0.014 µm, for the unetched SiO_2 and the substrate it is 0.05 µm. This convergence in the mesh size is relevant only for the model presented in figure 4.1 and is validated in section 4.2.5 where we compare the numerical solutions with analytical ones. Therefore, the mesh size for the pillar and the substrate is adopted thought this study. Later in section 4.3.2, when defining new model with new parts, a new mesh size will be adopted for the new part, and supplementary nodes will be added in certain critical areas to

locally increase the accuracy of the model. More details on this new mesh size used in the complex models will be presented in section 4.3.2. As for the element shape, the hexahedral (cubic) shape was adapted and for the element type, the quadratic order was adapted.

As for the boundary conditions of the model shown in figure 4.1(a), the bottom surface of the substrate is blocked along the three directions (x, y and z), which means the displacements along x, y and z directions are set to zero over all the nodes of the bottom surface of the substrate. This boundary condition is adopted throughout the entire study. To validate the model, a new BC is applied: that of a torque on top of the pillar to rotate it around the Z-axis. This will be explained in section 4.2.5.

In the next section, we discuss the limitations of the proposed model before introducing the material properties assigned to each part.

4.2.3 Limitations of the model

Before presenting the simulations conducted, it is crucial to clearly define the limitations of our model. We had to make unavoidable approximations in our simulations that will be presented in this section. Hence, the results obtained will be considered as qualitative representative tendencies that help us make general conclusions.

- For simplification reasons, as we have mentioned above, the pillar geometry depends on the etching recipe and thus it would be complex to come up with a numerical strategy that allows to handle geometries that change from one sample to another. Therefore, the shape of the pillar is considered cylindrical (as seen in figure 4.1(a)). If the precise geometry of all samples was known, this simplification could be removed without causing complications.
- In our simulations SiO_2 is considered elastic (instead of viscoelastic). Depending on the velocity of the coalescence phenomena, this simplification might have an important impact on the results. If the coalescence is fast, SiO_2 might not have enough time to relax, then the elasticity simplification is acceptable. Whereas if the coalescence is slow, then SiO_2 might relax and in such case results could change significantly. The notion of fast or slow refer to the characteristic time of the viscoelastic behavior of the SiO_2. Considering that we do not know much about the kinetics of the coalescence process, it seems conservative to assume that the process is fast and thus that the SiO_2 rheology can be simplified using elasticity. Therefore, we will use this elasticity simplification in the energy computation and consider that only the surface energy of the GaN hexagon is responsible of the rotation. This computation is discussed in detail in section 4.4.
- The current understanding of GaN coalescence lacks clarity regarding the physical mechanisms taking place during the pillar twist/tilt. Therefore, the approach used to

simulate the rotation of the pillars (coalescence process) does not consider the underlying physical phenomena. Different approaches will be explored in order to account for the coalescence process from a mechanical viewpoint.

These assumptions will be displayed later in this chapter once they are explicitly applied, and as we have mentioned, they will require us to discuss the obtained results qualitatively in terms of order of magnitude and not quantitatively.

4.2.4 Mechanical anisotropic properties

The coalescence process occurs at a high growth temperature; hence, the numerical simulations involve a thermomechanical procedure, which means that the mechanical properties of the different materials are required over a specific range of temperatures. As explained in the limitations presented in section 4.2.3, for simplification purposes and without knowing if the coalescence duration is sufficient to allow the for SiO_2 to soften, the SiO_2 is assumed to be elastic.

GaN and AlN are transversely isotropic material, a bibliographic study was conducted to obtain the elastic constants for each material at ambient T=300K and at growth temperature T=1300K. If we replace the GaN and AlN elastic coefficient found in reference [44] in the rigidity matrix and calculate its inverse, we find the compliance matrix which gives us the engineering constants $E_1, E_2, G_{12}, G_{13}, \upsilon_{12}, \upsilon_{13}, \upsilon_{23}$ and υ_{31} required for the thermomechanical simulations in Abaqus. These properties are summarized in table 4.1. The elastic coefficients found in the literature [44] correspond to temperature values up to 900K, therefore a linear extrapolation up to 1500K was performed and the extrapolated elastic coefficient at T=1300K are presented in table 4.1.[44].

	T(K)	**E_1**	**E_2**	**E_3**	**υ_{12}**	**υ_{31}**	**υ_{13}**	**υ_{23}**	**G_{12}**	**G_{13}**	**G_{23}**
GaN	1300	293.2	293.2	323.6	0.32	0.18	0.17	0.17	111.1	96.3	96.3
	300	310.5	310.5	351.2	0.33	0.19	0.16	0.16	116.4	93.2	93.2
AlN	1300	335.5	335.5	337.8	0.31	0.172	0.171	0.171	127.2	122.3	122.3
	300	345.8	345.8	353.5	0.32	0.176	0.173	0.173	131	124.6	124.6

Table 4.1: Engineering constant of GaN and AlN at T=300K and T=1300K from ref. [44]. *The values of E_1, E_2, E_3, G_{12}, G_{13} and G_{23} are presented in GPa and $\upsilon_{12}, \upsilon_{13}, \upsilon_{23}$ are unit-less.*

For the cubic silicon Si crystal, there are three independent elastic constants C_{11}, C_{12}, and C_{44}. By symmetry, we have $C_{11}=C_{22}=C_{33}$, $C_{12}=C_{13}=C_{23}$ and $C_{44}=C_{55}=C_{66}$. Therefore, the stiffness matrix is more simplified as shown in equation (4.1).

$$\begin{bmatrix}\sigma_{11}\\ \sigma_{22}\\ \sigma_{33}\\ \sigma_{23}\\ \sigma_{13}\\ \sigma_{12}\end{bmatrix} = \begin{bmatrix} C_{11} & C_{12} & C_{12} & 0 & 0 & 0 \\ & C_{11} & C_{12} & 0 & 0 & 0 \\ & & C_{11} & 0 & 0 & 0 \\ & & & C_{44} & 0 & 0 \\ & \text{Symmetry} & & & C_{44} & \\ & & & & & C_{44} \end{bmatrix} \begin{bmatrix}\varepsilon_{11}\\ \varepsilon_{22}\\ \varepsilon_{33}\\ \gamma_{23}\\ \gamma_{13}\\ \gamma_{12}\end{bmatrix}$$ *Equation 4.1*

Table 4.2 shows the values of the elastic constant used for Si found in ref. [3] and addressed directly in Abaqus.

T(K)	C_{11}	C_{12}	C_{44}
300	161.5	62	79.5
1300	130	50	79.1

Table 4.2: Elastic constant (in GPa) of Si (001) at T=300K and T=1300K taken from ref. [3].

For Si (111), the Young modulus and Poisson ratio along the (111) direction are considered. The compliance coefficient can be derived from the elastic coefficient (stiffness coefficient) obtained in table 4.2 by the following equations (4.2) (4.3) and (4.4) [142]:

$$S_{11} = \frac{(C_{11}+C_{12})}{(C_{11}-C_{12})(C_{11}+2C_{12})}$$ *Equation 4.2*

$$S_{12} = \frac{-C_{12}}{(C_{11}-C_{12})(C_{11}+2C_{12})}$$ *Equation 4.3*

$$S_{14} = \frac{1}{C_{44}}$$ *Equation 4.4*

And $E_{(111)}$ and $\upsilon_{(111)}$ can be expressed as [143]:

$$E_{(111)} = \frac{4}{2S_{11}+2S_{12}+S_{44}}$$ *Equation 4.5*

$$\upsilon_{(111)} = -\frac{1}{6} E_{(111)} \left(S_{11}+5S_{12}-\frac{1}{2}S_{44}\right)$$ *Equation 4.6*

Table 4.3 summarizes the elastic properties of Si (111) at T=300k and T=1300K.

T (K)	$E_{(111)}$ (GPa)	$\upsilon_{(111)}$
300	167	0.259
1300	149.5	0.251

Table 4.3: Elastic properties of Si (111) at T=300k and T=1300K.

SiO_2 is amorphous isotropic, therefore it has a Young's modulus E = 64 GPa and Poisson ratio ν of 0.24 [4] at T=300K.

Following the assignment of material properties, the next step is to validate the "test model" to use it further in this study.

4.2.5 Validation of the model

To validate the model, a new BC is applied and that is the application of a torque on top of the pillar to rotate it around the Z-axis. The analytical solution of a beam under torsion has been used in order to validate the "test model" and in particular, to validate the applied constraints, the applied boundary conditions and the element type and size by comparing the strain energy computed numerically with the one computed analytically. Analytical energy calculation requires homogenous material composition across all parts, thus in the "test model", we will consider that all parts are now made of one material only, in this case AlN. A torque T is applied on top of one pillar at the RP-1 point seen in figure 4.2 which induces a rotation of the pillar by an angle ϕ around the Z-axis.

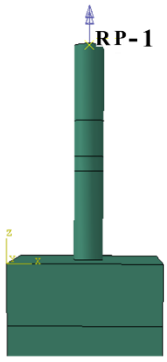

Figure 4.2: Geometrical Model of one AlN pillar under a torque load.

We compare the strain energy for different rotation angles calculated analytically and obtained numerically using our proposed FEM model.

Analytically, the relationship between the rotation angle ϕ (in rad) and the applied torque T is described in equation (4.7) from the theory of torsion [145]:

$$T=\frac{G * J * \phi}{L} \quad \textit{Equation 4.7}$$

With J being the polar moment $\frac{\pi D^4}{32}$.

The pillar diameter and length are denoted by D and L respectively, while the shear modulus is represented by G. For simplification purposes, we consider the isotropic mechanical properties (Young modulus and Poisson ratio) of the AlN at ambient temperature. Therefore using the values found from ref. [146] and equation (1.4) of the shear modulus, we have G= 155 GPa.

Torque values are obtained for various ϕ values, and the strain energy stored U is equal to the work done, hence:

$$U=\frac{T*\phi}{2} \quad \textit{Equation 4.8}$$

Figure 4.3 shows the strain energy values obtained numerically and analytically from equation (4.8) for different rotation angles.

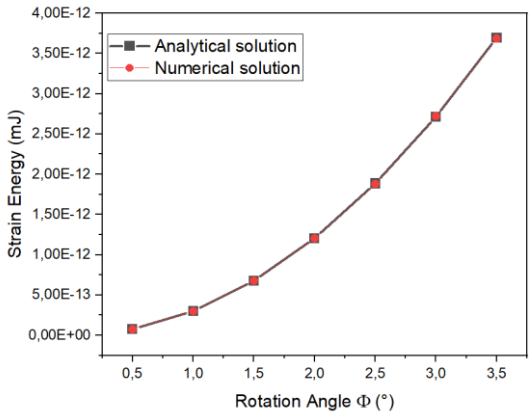

Figure 4.3: Numerical and analytical solution for strain energy variation as function of rotation angle ϕ.

The numerical and analytical solutions are in good agreement as shown in figure 4.3, which indicates that the chosen element size and type, the tie constraint between different parts and the boundary conditions are appropriate for our model. We also note that this serves as a validation of the scale. Our model, which is approximately 1 µm in size, achieves results consistent with theoretical predictions, demonstrating that the model remains effective at this scale. Following the validation of our model, further simulations can be carried out.

4.3 Modeling of the twist and tilt of GaN hexagons

4.3.1 Purpose of simulating the hexagons rotation

Following the validation of the tie constraint, BC, element type and mesh size used in "test model", a new model is defined to simulate the rotation of one GaN pyramid (grown on top of the 250 nm GaN nanopillar during the first step of the regrowth) that will then coalesce with its adjacent GaN pyramid. The objective of this new model is to compute the required GaN surface energy for the different rotation angles tested experimentally in chapter 3, sections 3.2.2 and 3.3.6 and then compare it to the available GaN surface energy to determine the energetically feasible rotation angles.

The excess energy present on the vertical facets at the edge of the GaN pyramid indicated by double red arrow in the SEM image in figure 4.4(a) is the driving force that might induce the rotation of the entire pyramid. Therefore, in order to decrease the computational time associated with modeling the entire GaN pyramid, we adopted a simplified approach by focusing and modeling only on the facets at the edge of the pyramids forming a hexagonal base (seen clearly from the top view SEM image of the pyramids in figure 4.4(b)). Figure 4.4(c) shows the schematic representation of the GaN pyramid on top of the pillar and figure 4.4(d) shows the schematic representation of the facets at the edge of the pyramids forming a hexagonal base that we will model in our simulations. At this stage of growth, the thickness of the facets we obtain is approximately equal to 0.1 µm.

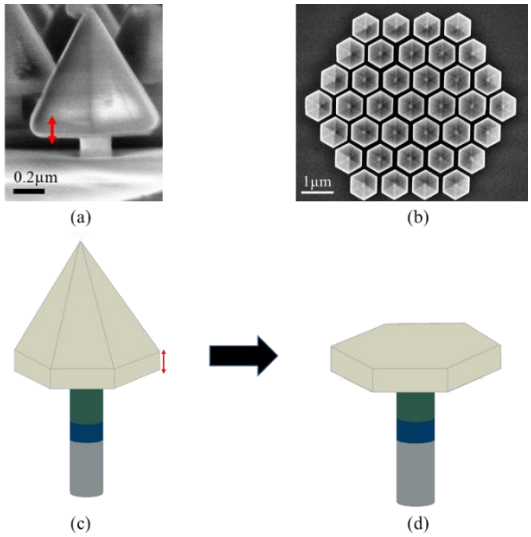

Figure 4.4: (a) SEM image of one uncoalesced GaN pyramid on top of one pillar. The double arrow sign designates the thickness of the facets at edge of the pyramid responsible for rotation. (b) Top view SEM image of a set of GaN pyramids showing clearly their hexagonal base, (c) schematic representation of the GaN pyramid on top of one pillar, and (d) schematic representation considering only the facets at edge of the pyramid forming the hexagonal base on top of one pillar.

It is worth mentioning again that since we neglected the viscoelastic properties of the SiO_2 layer (limitation presented in section 4.2.3), it will not introduce any compliance behavior to the pillar in our simulations to facilitate the rotation.

4.3.2 Testing different twist approaches

As mentioned in section 4.2.3, the mechanism by which rotation occurs during pyramid coalescence remains unclear. To overcome this limitation, we propose a new approach that is to model only the pre- and post-coalescence of the GaN pyramid + pillar configuration, which means bypassing the complexities of the intermediate coalescence process. This approach will be explained in detail in this section.

Two different methods to simulate the rotation are explored. We will start by explaining the approach used in method 1. For clarity, we define twist as a rotation around an axis that is normal to the sample's horizontal surface while a tilt it is a rotation around an axis in the plane of the sample's horizontal surface. For simplicity, we will test these two methods by performing a "twist".

Method 1

As we have seen in chapter 3, in the pre-coalescence phase (prior to any rotation), the GaN pillars are initially tilted and/or twisted. Therefore, the GaN pyramids on top of them are also disoriented, and since we are only considering the facets at the edge of the pyramid forming a hexagonal base of the GaN in our simulation, the initial model will use disoriented GaN hexagons as a starting point. This method is based on different steps and the boundary conditions will change between each step.

In the initial step, we consider two pillars with one GaN hexagon on top of each. To reproduce the initial misorientation between the GaN hexagons, one hexagon (on the left side in figure 4.5) is considered fixed and straight while the other (on the right side in figure 4.5) is twisted by an angle θ around the Z-axis.

Figure 4.5(a) shows the defined model with pillars and GaN hexagon on top of each and figure 4.5(b) shows a magnified image of this model highlighting the twist of the GaN hexagon placed on the right side by an angle θ.

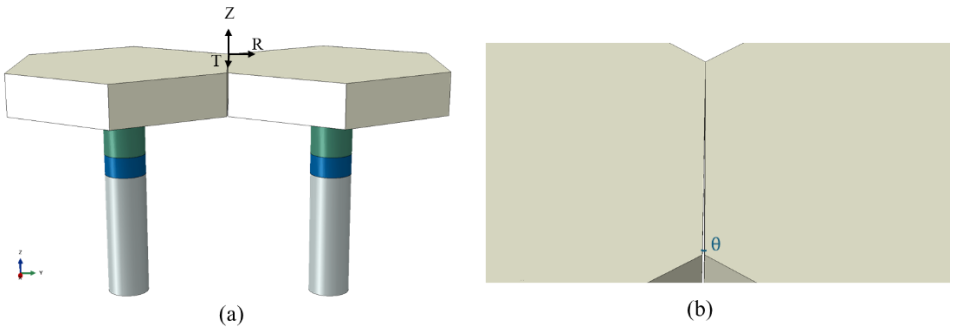

Figure 4.5: (a) Geometrical model of two pillars with GaN hexagon on top (the hexagon on the right is twisted by an angle θ), (b) zoomed in and top view image of the corresponding model.

For clarity, the facet of the fixed GaN hexagon (on the left side) is called facet "A", and the facet of the twisted GaN hexagon (on the right side) is called facet "B" as shown in figures 4.6(a) and (b). The nomenclature of these two facets is employed throughout the rest of this study. A tie constraint is applied between the overlaid surfaces of the different parts. However, no tie constraint is applied between the two GaN surfaces that are not in contact in this initial step.

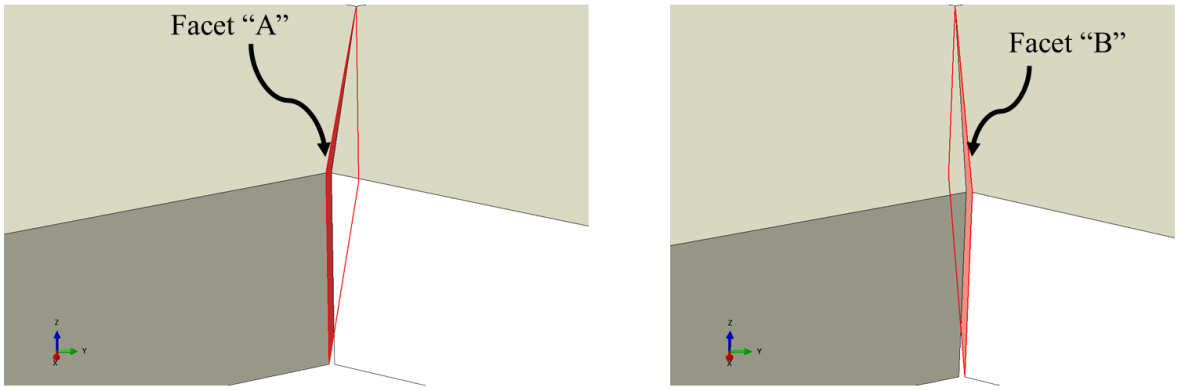

Figure 4.6: Zoomed in view showing (a) the fixed facet “A” and (b) the twisted facet “B”. The coordinate system on the bottom left side of each figure represents the global coordinate system defined by Abaqus.

The mesh elements and size for the pillar parts remain the same as presented in section 4.2.2 (in the “test model”). A new part (GaN hexagon) requiring meshing is added to this model with a thickness of 0.1 µm. After testing various mesh size to identify the size that yielded converged results while maintaining computational efficiency, the element size of the GaN hexagon has been chosen equal to 0.01 µm. The mesh size of the hexagon’s facets plays a crucial role in this simulation and thus a finer (smaller) element size equal to 0.005 µm is used on the six facets of the GaN hexagon along the z direction of the global coordinate system (shown in figure 4.6).

Now that the initial model is defined, we perform the simulation in two steps.

- Step 1: consists in rotating the twisted hexagon so it comes into contact with the fixed hexagon. To execute a rotation in three-dimensional space, a cylindrical coordinate system is used because it simplifies the transformation as rotations can be directly implemented by modifying the angular component, while the radial distance and height remain unaffected. We created a cylindrical coordinate system, with three axes: radial R-axis, tangent T-axis and Z-axis such that the Z-axis is coincident with the axis used to induce the misorientation (the rotation). The defined cylindrical coordinate system is shown in figure 4.7 (colored in black) and is used to apply a twist with method 1. Note that in further simulations, the initial misorientations are different (e.g. tilt instead of twist), therefore, we will define new coordinate system at different positions and with different axis direction in order to simulate a tilt and to find an optimal coordinate system.

  Now that we have defined our coordinate system , we apply a displacement load U_2 on the twisted facet “B” along the tangent T-axis of the defined cylindrical coordinate system, such that $U_2 = \theta$*radius with the radius equal to the distance from the origin to any point on the R-axis. This load will allow the rotation of the GaN hexagon around the Z-axis of the cylindrical coordinate system, so it comes into contact with the adjacent

GaN hexagon (facet “A”). The pillar will follow the behavior of the GaN hexagon because it is tied to it. We note that the displacements over x, y and z are set to zero along the facet “A” and along the bottom surface of the pillars. Figure 4.7 shows the displacement load applied on facet “B”.

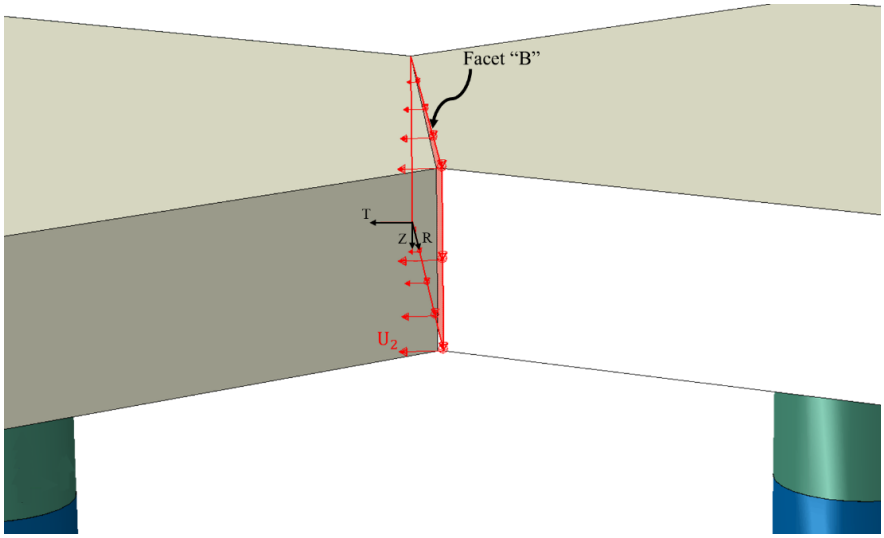

Figure 4.7: Displacement load along T-axis on facet “B”.

- Step 2: now that the two facets are close to each other, step 2 consists of removing the displacement load (the rotation load) applied in step 1 and applying simultaneously a constraint that would keep the two facets “A” and “B” in contact. Since applying a tie constraint in the middle of a simulation is not an option in Abaqus, a new type of constraint is applied between the two facets “A” and “B” of the GaN hexagons that are now close together to keep them stuck together and that is the surface-to-surface contact constraint. Contact constraints are used to model realistic interactions between surfaces that may come into contact, separate, or slide against each other. They do not eliminate the degrees of freedom of the nodes like the tie constraint but instead they define how surfaces interact when they come into contact [147].

By using this technique, we have simulated a rotation of one GaN hexagon (step 1) and coalesced it into the neighboring GaN hexagon (step 2). We expect the two facets to stay in contact, however in the obtained results, we noticed that with the surface-to-surface contact interaction, the facet “B” reopens and revert to its original position once the displacement load is removed.

This issue might be related to limitations of the contact algorithm used by Abaqus and which we cannot modify. Abaqus propose alternatives to the surface-to-surface contact constraint such as the node-to-surface contact constraint. This algorithm relies on the use of a master and a slave surface. For a general contact condition, this algorithm might lead to penetration of the master surface into the slave one [147]. However, due to this simple contact geometry, the numerical model that we handle is not affected by this problem. After using the node-to-surface

contact constraint, we see improvement of the model convergence and the twisted facet "B" remains in its new position close to the fixed GaN facet "A" as seen in figure 4.8(a) that displays the maximal principal stress (S. Max. Principal) (maximum stress among the normal stresses in the x, y, and z directions). However, to identify any potential issues in the final model assembly, we show in figure 4.8(b) the distance between the slave surface node and the closest point on the master surface. This variable is called COPEN in Abaqus, a positive COPEN value represents an open contact between the surfaces while a negative value represents an overclosure. From figure 4.8(b), we can see the existence of positive COPEN values across a big part of the facet "B", indicating the presence of regions that are not actually touching the GaN facet "A".

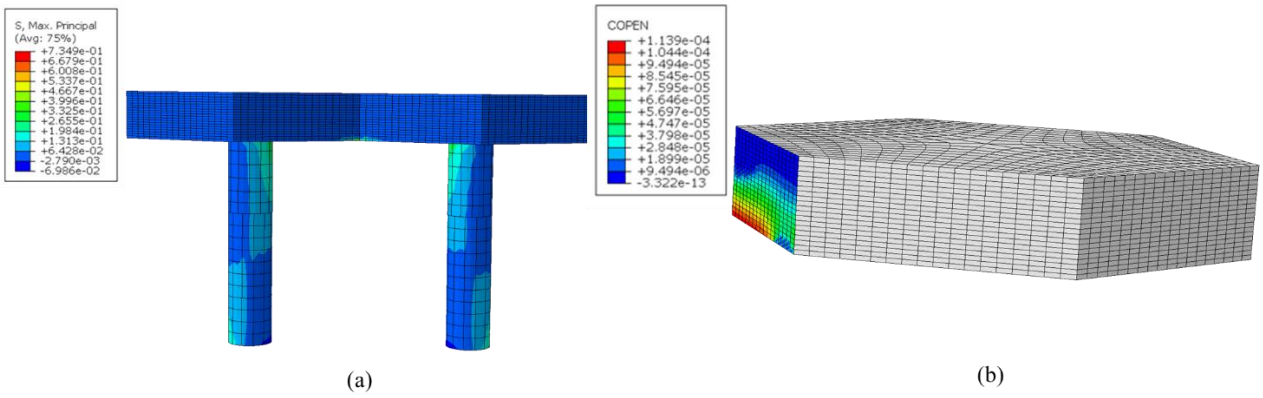

Figure 4.8: (a) Stress distribution between the hexagons following the node-to-surface contact constraint, the values are shown in GPa, (b) COPEN distribution along the twisted GaN facet "B", the values are shown in µm.

This result suggests incomplete contact or gaps between the surfaces, which could affect the overall simulation results. Additional adjustments suggested in the Software documentation have been tested, however each of them introduced a new issue:

- Supplementary contact by selectively adding nodes: model did not converge, and no results were obtained.
- Applying a tolerance (specifying a threshold distance to determine when two surfaces or nodes are considered to be in contact): a small threshold led to tie the two surfaces from the initial step which is not we want because in this case, we will not be able to rotate the GaN hexagon.

To conclude, using method 1, we encountered technical problems in the contact constraint applied once the rotation of the hexagon has been accomplished and this led to convergence problems and contact inconsistencies.
Thus, an alternative method 2 is proposed to be able to rotate the GaN and tie the two hexagons without facing the earlier difficulties.

Method 2:

Method 2 consists in splitting the simulation into two separate simulations: simulation 1 represents the rotation phase of the hexagon before any coalescence, i.e. it represents the initial misalignment between the hexagons, this simulation will allow us to extract the generated stress in the hexagon and the pillar due to a rotational load. Simulation 2 represents the tie up phase between the GaN facets "A" and "B" when they come close together after the rotation (after coalescence). This method is also based on different steps and the boundary conditions will change between each step. We will explain in detail the two simulations:

In the first simulation, we start with a model of two pillars with non-twisted GaN hexagon on top of them (as shown in figures 4.9) as initial step. A tie interaction is applied between the overlaid surfaces of the different parts expected between the two GaN facets "A" and "B". No contact constraint is used. We note that the displacements over x, y and z are set to zero along the bottom surface of the pillars. The mesh elements and size are identical to that used for method 1.

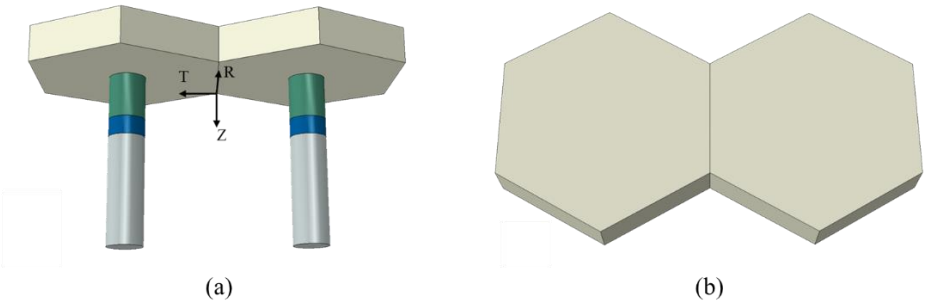

Figure 4.9: (a) Geometrical model of two pillars with GaN hexagon on top, (b) top view of the corresponding model.

Only one step is required for this first simulation:

- We apply a rotation on the facet "B" to twist one of the hexagons. This rotation will twist the hexagons apart instead of towards each other and will create a gap between them, but it generates the same stress as if they were rotated to approach each other. We use the same coordinate system employed in method 1 (shown in black in figure 4.9). This step consists of applying a displacement load U_2 on the facet "B" along the tangent T-axis, i.e. along the 2nd axis in the cylindrical coordinate system colored in black in figure 4.9(a) such that $U_2 = \theta$*radius. This step will allow the rotation of the GaN hexagon around the Z-axis of the cylindrical coordinate system so that one of the GaN hexagons is twisted. Based on its tie to the GaN hexagon, the pillar's behavior will follow. This step is identical to the first step in method 1.

Figure 4.10 shows the distribution of the Maximum Principal Stress in the entire model caused by the rotation of the facet "B" by an angle θ.

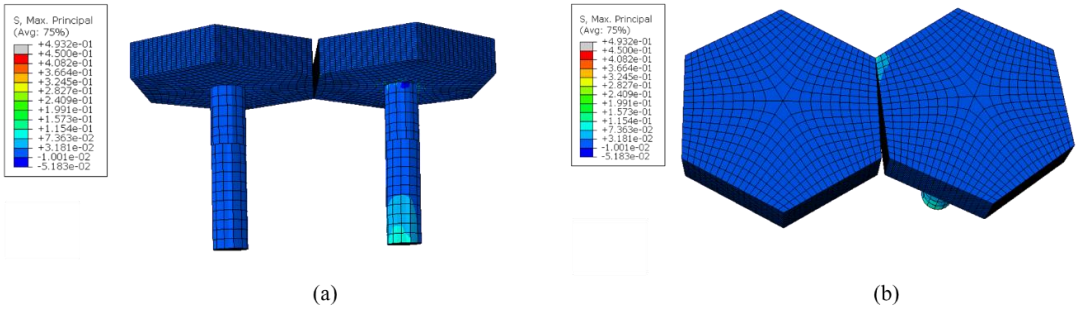

Figure 4.10: (a) Distribution of maximum principal stress in GPa induced by the rotation of the right-side hexagon and (b) top view of the corresponding model. The values of the stress are shown in GPa at the top left side of each figure.

We can see that the twisted hexagon and its corresponding pillar are under stress while the fixed hexagon and its pillar remain relaxed with zero stress.

Next, simulation 2 describes the post-coalescence phase (after the rotation). We define a new model formed by two pillars with non-twisted GaN hexagon on top. In this model, a tie constraint is applied between all the overlaid surfaces of the different parts even between the two GaN facets "A" and "B" that are now considered coalesced.

One step is required in this simulation:

- We import the residual stress obtained in simulation 1 (induced by the rotation) and apply it as initial stress in the new model in simulation 2. This method imports only the stress variations, excluding any initial displacement variations resulting from simulation 1. Now that the two facets "A" and "B" are tied in this simulation, we expect the stressed hexagon to relax and part of the stress is transferred to the fixed hexagon and its pillar.

Figure 4.11 shows the distribution of the Maximum Principal Stress in the entire model after relaxation.

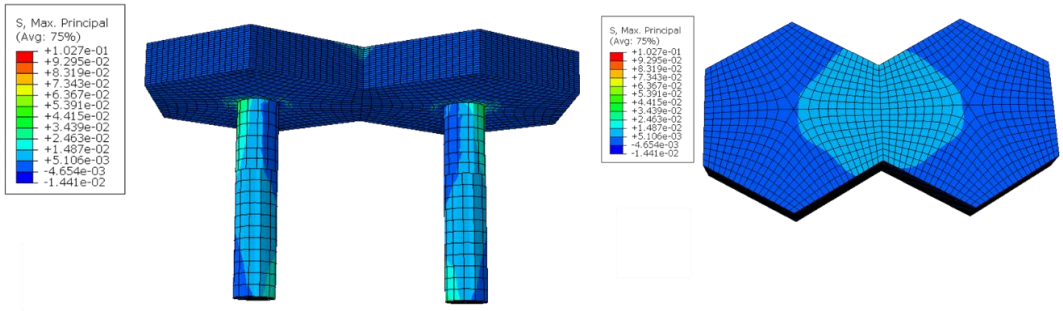

Figure 4.11: (a) Distribution of maximum principal stress in GPa after relaxation and (b) top view of the corresponding model.

We observe in figure 4.11, that both the fixed hexagon and pillar, which initially had no stress (as shown in figure 4.10(a)), now exhibit a significant stress distribution. This means that the facet “B” remained in contact with the facet “A” and relaxed by transferring part of its stress to its adjacent hexagon and pillar. With this expected equal symmetrical distribution of stress across both hexagons and their respective pillars obtained from method 2, we will go further in our work using method 2.

The next step is to apply method 2 for a tilt case, the primary change will be in defining a new cylindrical coordinate system that allows us to perform a tilt instead of a twist. After presenting the model for the tilt, different rotation axes are considered to find the optimal one that requires from the system the least amount of energy to rotate, then the energy required for different twist/tilt angles is calculated. This energy is needed to compare it with the available GaN surface energy in order to determine the energetically feasible rotation angles. Finally, an optimization of the pillar’s pitch and the height of the GaN facet is conducted to determine the optimal parameters that would contribute to an energetically feasible rotation.

4.3.3 Twist and Tilt model

From now on, the method 2 (section 4.3.2) will be used for the twist simulations. In order to draw comparisons with the findings from the experiment work, in the rest of this work, the distance between pillars is considered equal to 1.5 µm (equal to the experimental pillars pitch in section 3.3.6) and the diameter equal to 100 nm unless said otherwise.

The tilt model employed in this work also uses method 2 (section 4.3.2), but with a new defined coordinate system. To simulate a tilt, the rotation should take place around an axis that is not normal to the surface. Consequently, a new coordinate system is established for the tilt model at a new position and with different axis direction as shown in black in figure 4.12(a).

As explained in section 4.3.2, we start with simulation 1 that requires one step: the facet “B” is rotated around the inclined Z-axis of the new coordinate system. The maximum principal stress distribution in the model after the tilt is shown in figure 4.12(b). For clarity, we applied a displacement magnification equal to 50 which means the displayed scale is multiplied by 50 in figure 4.12(b).

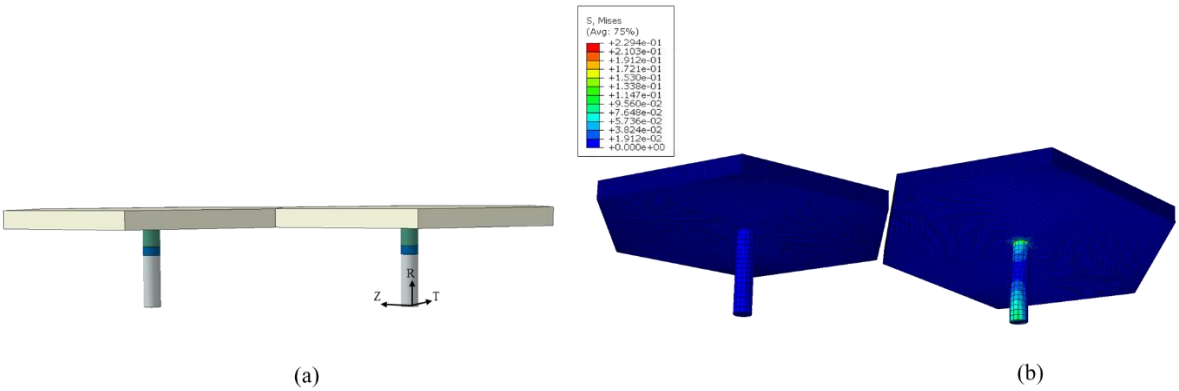

Figure 4.12: (a) Geometrical model of two pillars with GaN hexagon and (b) Distribution of maximum principal stress induced by the rotation of the right-side hexagon.

The stress distribution is extracted from figure 4.12(b) and applied as initial stress in simulation 2 where the GaN facets are tied up from the beginning. Figures 4.13(a) and 4.13(b) show the obtained displacement U_3 along the Z-axis of the global coordinate system (shown on the left bottom side of the figure) of the model in simulation 1 after tilt and in simulation 2 after relaxation, respectively. The displacement values are very small, therefore, to clearly visualize the deformation in the model in figure 4.13, we magnified the deformation by a factor of 100.

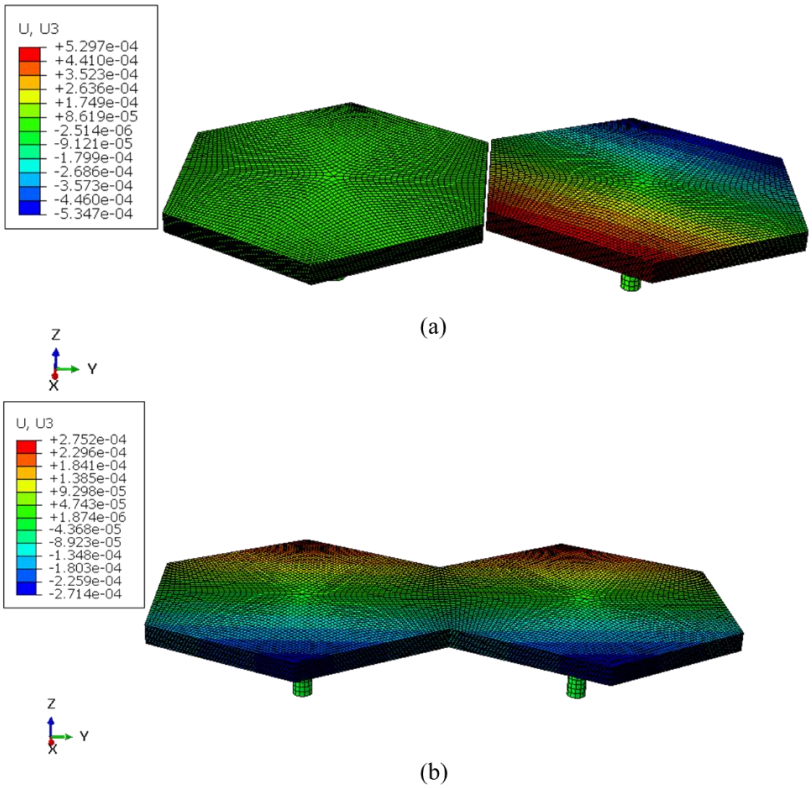

Figure 4.13: (a) Displacement U_3 along the Z-axis of the global coordinate system (shown on the left bottom side of the figures) of the tilted hexagon (a) in simulation 1 after rotation and (b) in simulation 2 after relaxation. The values are shown in µm.

We can see in figure 4.13(a) how the top edge of the tilted hexagon exhibits a displacement towards negative Z-axis due to the applied rotation. In figure 4.13(b), we see that the top edge of the tilted hexagon now exhibits a displacement in the positive Z-axis direction because it returned to its equilibrium position by transferring part of its stress to the adjacent hexagon.

Now that we have tested different approaches to model the tilt and twist, we will use method 2 that we proved to give robust solutions to optimize the rotation axis and compute the rotational energy in section 4.4 in both tilt and twist cases.

4.4 Computation of the rotation energy

4.4.1 Purpose of computing the rotation energy

Now we have a model that allows the simulation of the pillar's tilt and twist. We can compute the rotation energy per surface required for various tilt angles obtained in chapter 3 from experimental data. In sections 3.2.2 and 3.3.6, a tilt of 0.1° between adjacent pillars was measured and found as a tilt limit between neighboring pillars results to form groups of pillars similar in size to the coalesced perfectly aligned GaN domain measured experimentally in figure 3.20(a). The question that arises is then: do we have sufficient GaN surface energy on the facet "B" to tilt the pillar by 0.1°?

4.4.2 Energetic feasibility of the experimental tilt results

To address this question, we need to first determine the amount of energy required in order to tilt a pillar with a pitch=1.5 µm with diameter equal to 100 nm to align the GaN hexagons. This energy can be provided by our simulation model. Then we will compare the required energy found numerically with the available energy using the GaN surface energy found in literature. We will test three tilt values 0.04°, 0.1° and 0.2° and compute using Abaqus the surface energy required for each angle. The model used in our simulations relies on many hypotheses; therefore, we will focus on comparing the results based on their order of magnitude rather than the precise numerical values to determine which tilt magnitude is feasible energetically.

The absolute surface energy δ available at the GaN surfaces is calculated by T. Kawamura et al. [148] and C.E. Dreyer et al. [149]. Although δ varies depending on the crystallographic plane, it remains within the same order of magnitude, and since we are not looking at precise numerical values, we are only concerned with the order of magnitude of the surface energy, thus, the available GaN surface energy is considered approximately equal to $\delta = 0.2$ eV/Å^2.

However, before computing the energy numerically, we should choose which tilt axis (coordinate system) to consider. In our model, the choice of the coordinate system is completely arbitrary as we lack knowledge of the mechanics behind the rotation. Therefore, we tested four different tilt axes (four different coordinate system) and two different twist axes chosen randomly (two different coordinate system). The axis that yields the lowest surface energy will be considered for the rest of this work, as it will be considered as the most privileged orientation.

Tilt axis optimization

Figure 4.14 shows the four distinct coordinate system for a tilt axis test in this work on a model of two pillars with pitch=1.5 µm and GaN's hexagon thickness equivalent to 0.1 µm. In figure 4.14(a) and (b), we provide a close-up view of two of these coordinate systems (inside the dashed blue rectangle). The coordinate system in figure 4.14(c) is identical to the one in 4.14(a) but is located in a different area. Likewise, the coordinate system in figure 4.14(d) is identical to the one in 4.14(b) but is positioned elsewhere. For the four cases, the rotation is applied on the facet "B" along the Z-axis of the defined coordinate system.

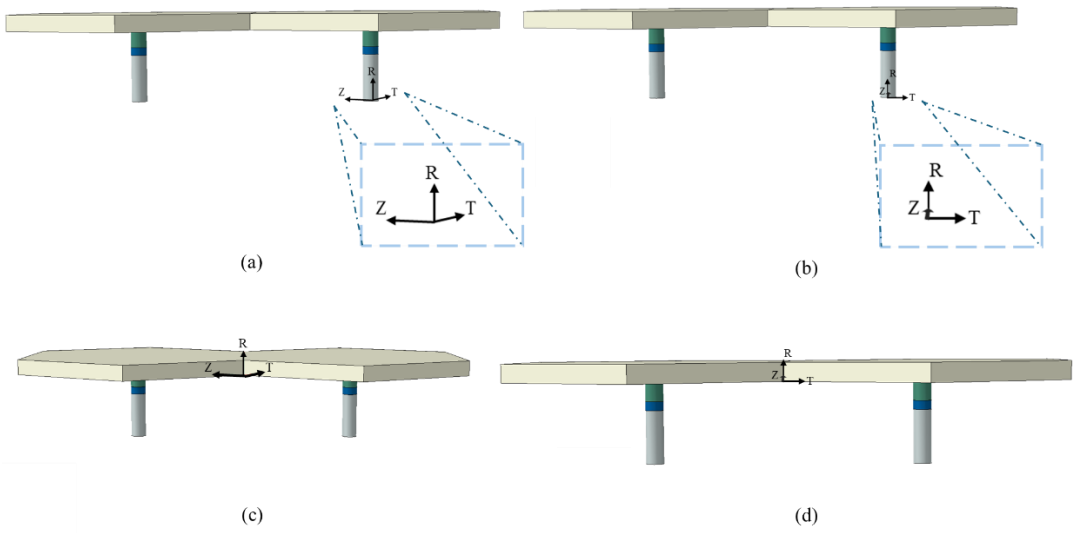

Figure 4.14: Geometrical model showing the position and direction of the tested coordinate system for a tilt: (a) coordinate system 1 with a close-up view, (b) coordinate system 2 with a close-up view, (c) coordinate system 3 and (d) coordinate system 4.

Method 2 presented in section 4.3.2 is applied for each of the four cases, therefore two simulations were performed for each case. In simulation 1, the tilt angle is set to 0.04° (chosen randomly), subsequently, in simulation 2, the residual stress induced by the tilt of 0.04° is applied as initial stress and the required energy is calculated from Abaqus and shown in table 4.4 for the four coordinate systems.

Coordinate system	1	2	3	4
Required energy (eV)	1.21×10^6	2.72×10^6	1.59×10^6	3.46×10^6

Table 4.4: Required energy for a tilt of 0.04° with respect to various coordinate systems.

To compare the computed required energy with the available energy coming from both facets "A+B", we calculate the available energy using equation (4.9):

$$\text{Available energy} = 2 * \text{Area}_{facet} * \delta \qquad \textit{Equation 4.9}$$

With δ being the absolute GaN surface energy found in literature [148] [149].

For a pitch = 1.5 µm and facet thickness = 0.1 µm, the available energy= $2 * \text{Area}_{facet} * \delta = 2 * 8610000 * 0.2 = 3.4 \times 10^6$ eV.

We can see that a tilt of 0.04° around the Z-axis in coordinate systems 1, 2 and 3 is energetically feasible because the two facets provide sufficient energy for such tilt. In fact, the required energy for the tilt test-cases 1, 2 and 3 is lower that the available energy (3.44×10^6 eV). On the other hand, a tilt in the coordinate system 4 requires 3.46×10^6 eV, an amount of energy slightly higher than the one actually present. This could mean that if the initial misorientation is the result of a rotation around an axis close to the case 4, then the probability of having enough energy to induce a realignment (a tilt) between the GaN hexagons is much lower than in the other three cases.

We will keep the system that requires the least energy since the system usually tends to be in a situation that demands the least energy, therefore, the coordinate system 1 will be considered for the rest of the calculation.

The next goal is to test whether a tilt of 0.1° (found experimentally) and 0.2° (to test higher tilt values) is energetically possible. Following new simulations, we obtain in table 4.5 the computed energy required for a tilt of 0.04°, 0.1° and 0.2° compared to the absolute GaN surface energy found in literature [148] [149].

	Numerical results		
Tilt angle (°)	0.2	0.1	0.04
Required energy (eV)	3.0×10^7	7.6×10^6	1.2×10^6
Available energy (eV)	3.4×10^6		

Table 4.5: Required energy for different tilt values with respect to coordinate system 1 between two pillars with a pitch of 1.5 µm along the available energy from the facets "A+B".

Table 4.5 shows that the energy required varies as a quadratic function of the tilt angle (proportional to θ_{tilt}^2) which means the required energy highly depends on the angle of tilt. We realize from table 4.5 that a tilt of 0.04° is possible energetically as the required energy is less than the available energy (1.2×10^6 eV < 3.4×10^6 eV), however, a tilt of 0.1° and 0.2° is less likely to be energetically possible since the energy available on facets "A+B" of the GaN

hexagon might not be enough to induce the hexagon's realignment, (7.6×10^6 eV > 3.4×10^6 eV and 3.0×10^7 eV > 3.4×10^6 eV). The tilt of 0.1° that seemed less likely to be energetically possible in our simulations, was measured and proved in the set three of pillars, this could mean that (i) the rotation is taking place around an axis that was not considered in the simulation tests, resulting in a lower required energy to rotate, or (ii) the SiO_2 enables a compliant behavior in the pillar during its rotation which will facilitate the rotation. Additionally, we emphasize that the fabrication processes and cylinder geometries differ between the experimental samples on one hand and the simulated data on the other hand. Therefore, these numerical results are used to prove the rotation of the pillars and its feasibility from an energetic point of view as well as to give a range of tilt values without providing a precise tilt threshold.

Twist axis optimization

Figure 4.15 shows the two distinct coordinate systems (coordinate system 5 and 6) for a twist test in this work on a model of two pillars with pitch=1.5 µm and a GaN hexagon thickness of 0.1 µm. The coordinate system 6 is identical to the 5 but is positioned elsewhere.

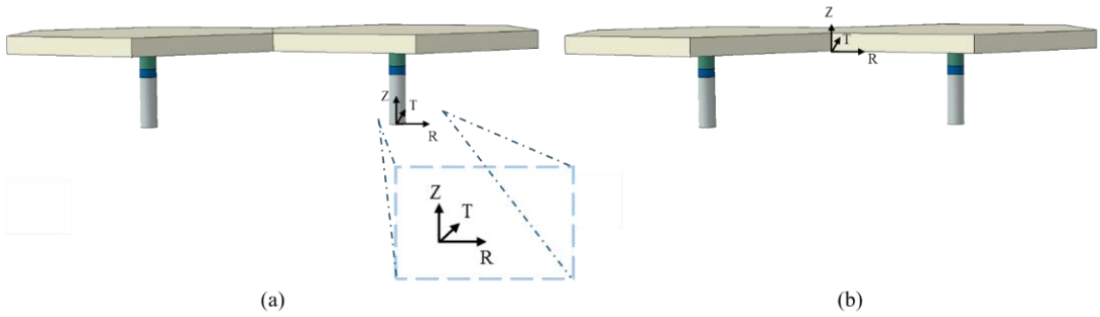

Figure 4.15: Geometrical model showing the position and direction of the tested coordinate system for a twist: (a) coordinate system 5 with a close-up view, and (b) coordinate system 6.

Similar to the optimization of the tilt axis, the energy required for a tilt of 0.04° is calculated in both coordinate system (5 and 6). Using the coordinate system 5, the required energy is found to be 1.1×10^6 eV, while using the coordinate system 6, it is found to be equal to 7.3×10^6 eV. Comparing both required energy to the available energy (3.4×10^6 eV), we choose the coordinate system 5 for the twist test. We calculate numerically the energy required for a twist of 0.1° and 0.2° (rotation around the Z-axis). Table 4.6 displays the computed energy required for a twist of 0.04°, 0.1° and 0.2° compared to the absolute GaN surface energy.

	Numerical results		
Twist angle (°)	0.2	0.1	0.04
Required energy (eV)	2.7×10^7	6.8×10^6	1.1×10^6
Available energy (eV)	3.4×10^6		

Table 4.6: Numerical energy for different twist values with respect to coordinate system 5 between two pillars with a pitch of 1.5 µm along the available energy from the facets "A+B".

The obtained results are similar to the one obtained in the tilt case simulations. We see from table 4.6 how the required energy varies as a quadratic function of the twist angle (proportional to θ_{tilt}^2) which means the required energy highly depends on the angle of twist and how only a tilt of 0.04° (among those tested) is energetically feasible under the conditions we used.

4.4.3 Optimization of the pillars pitch

As we have seen, the control and understanding of this growth approach is complicated, with numerous parameters influencing the etching process and the growth process which define the quality of the epitaxial GaN layer grown on nanopillars. Therefore, understanding if and how the pitch affects the pillar's rotation would be valuable for future studies whether for sample fabrication or sample characterization. Hence, it would be beneficial to optimize the pillars pitch in order to ensure the feasibility of the rotation that should allow the GaN pyramids to align and help in reducing the creation of dislocations.

For a fixed tilt angle of 0.04°, a fixed coordinate system 1, and a constant GaN thickness of 0.1 µm, three models are defined with varying pitch values: 0.5 µm, 1 µm, and 1.5 µm. These models shown in figure 4.16 aim to analyze how different pitch distances affect the energy surface required for a tilt.

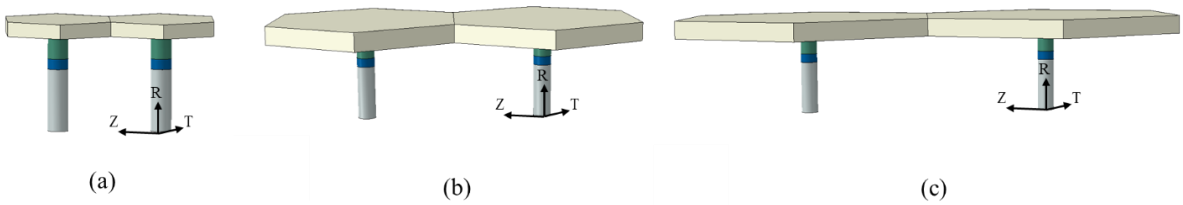

Figure 4.16: Geometrical model of two pillars with pitch equal to (a) 0.5 µm, (b) 1 µm and (c) 1.5 µm.

The available energy is calculated for each pitch value using equation (4.9) and the required energy is computed using our FEM model for each pitch value. Both values are shown in table 4.7 along with the required surface energy that depends on the surface of the facets.

Pitch (µm)	0.5	1	1.5
Required energy (eV)	1.4×10^6	1.3×10^6	1.2×10^6
Required surface energy (eV/Å²)	0.48	0.21	0.14
Available energy (eV)	1.2×10^6	2.3×10^6	3.4×10^6

Table 4.7: Variation of the required total energy, required surface energy and the available energy for a tilt of 0.04° as function of pitch.

We notice a slight variation in the required energy that decreased linearly with the increase of the pitch. This result demonstrates that the energy required to rotate the pillars and induce the alignment of the GaN hexagons is mainly concentrated in the pillars, therefore, since varying the pitch does not affect the pillars, the required energy will only change slightly. On the other hand, varying the pitch will modify the area of the facets that is directly related to the required surface energy and to the available energy. This is what we obtained in table 4.7, we see a decrease in the required surface energy and an increase in the available energy when the pitch increases.

This leads to a conclusion that the pitch has a less impact on the required energy compared to the rotation angle value, however, a rotation is more likely to occur between pillars at greater pitches. At a pitch of 0.5 µm, the required energy for a tilt of 0.04° is less than the available energy suggesting that a tilt of 0.04° is energetically feasible only when the pitch is 1 µm or 1.5 µm, and not for a pitch of 0.5 µm.

4.4.4 Optimization of the GaN thickness

Another parameter that can affect the available energy is the thickness of the GaN hexagon. When the facets "A" and "B" become larger, it means more atoms are present. A larger material with more atoms will have a greater total surface area and since surface energy is typically expressed as energy per unit area, a larger surface area will result in a higher total surface energy available. This means that an increase in atomic presence contributes to more energy, making it more likely to induce a realignment of the GaN hexagons

Therefore, to test the impact of the GaN facet's thickness, we define three models (shown in figure 4.20) with two pillars with a pitch=1.5 µm and calculate numerically the energy for a tilt of 0.04° around the Z-axis of the coordinate system 1. Three thickness are tested: 0.1 µm, 0.15 µm and 0.2 µm. The choice of these three values is based on (i) the length measured from figure 4.4(a) and (ii) given that after full coalescence the GaN platelet can be at least 1 µm thick means that the GaN hexagon should have a significantly smaller thickness.

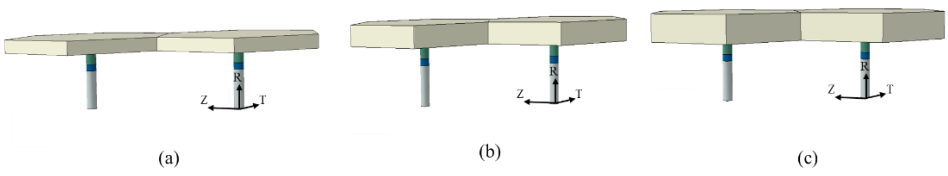

Figure 4.17: Variation of GaN facet thickness: (a) 0.1 µm, (b) 0.15 µm and (c) 0.2 µm.

The required surface energies/Å^2 to tilt the GaN hexagon by 0.04°, are obtained numerically and shown in table 4.8 along the available energy calculated using equation (4.9) for each

thickness value since the area of the facet varies with its thickness, so the available energy depends on the facet's thickness.

Facet's thickness (µm)	0.1	0.15	0.2
Required energy (eV)	1.24×10^6	1.23×10^6	1.22×10^6
Required surface energy (eV/Å^2)	0.14	0.1	0.07
Available energy (eV)	3.44×10^6	5.16×10^6	6.88×10^6

Table 4.8: Required total energy and required surface energy variation and the available energy as function of the facet's thickness.

We notice that the thickness does not highly impact the amount of energy required in order to induce a rotation in the pillars. But as the thickness increases, the available energy on the surface of each facet increases (linearly) and the required energy per surface decreases, this means that the thicker the GaN hexagon is, the more easily the rotation can take place. Therefore, we recall what we obtained in the pitch optimization study in section 4.4.3 and deduce that both the pitch and the facet's thickness are parameters with second order impact on the required energy while the rotation angle have a first order impact.

The numerical simulation that we presented is highly valuable offering plenty of information, such as stress distribution, displacement distribution and energy calculation, however it is computationally demanding making it challenging to explore all possible parameters. This is why the use of analytical methods, where appropriate, can be highly beneficial to acquire certain data in a fast simple way. We have seen from the numerical results that the part that mainly deforms during the mechanical rotation is the pillar, therefore we will present in the next section, an analytical study of the pillar's rotation (only the pillar). This analysis is expected to be valid for the entire system (with GaN hexagon). It is based on a mechanical geometrical approach and aims to provide a formulation that will allow us to assess the impact of each pillar's parameter (radius, height, pitch, elastic behavior) on the twist and tilt angles without having to carry out simulations. The results will be compared to the numerical ones to determine whether the analytical method is valid and can replace the numerical one in the case where we only want to study the effect of the pillars parameter on the rotation.

4.5 Analytical study of pillars rotation

4.5.1 Twist case

For simplicity, we start by considering two homogenous pillars ((all the parts made of unique material) with twisted GaN hexagon on top of each as shown in figure 4.17(a). As we have shown, the possible twist angle is quite small and thus the two twisted hexagons remain closely aligned preserving a pillar-to-pillar distance of approximately p as shown in figure 4.17(a). To

determine the impact of the parameters on the pillar's twist, we will calculate analytically the required twist energy; as the two pillars are symmetric, they have the same energy level thus we perform the analytical calculation for a single pillar and without the GaN hexagon on top as already mentioned.

The mechanism of the rotation is not clear; it seems natural to say that as two surfaces get closer, a "coalescence" force might appear, and this force is higher when the distance is small. Therefore, we will consider a simple hypothesis: the resulting force $\vec{F}$ inducing the twist is distributed along a triangle profile with a maximum magnitude F_{max} occurring at the shortest distance between the two hexagons. While there are no tools available to validate our hypothesis, it is a hypothesis that produces twist and tilt torque, making the quantitative analysis both useful and valid. To clearly visualize the distribution of $\vec{F}$, we show in figure 4.17(b) an exaggerated image of the twisted hexagons.

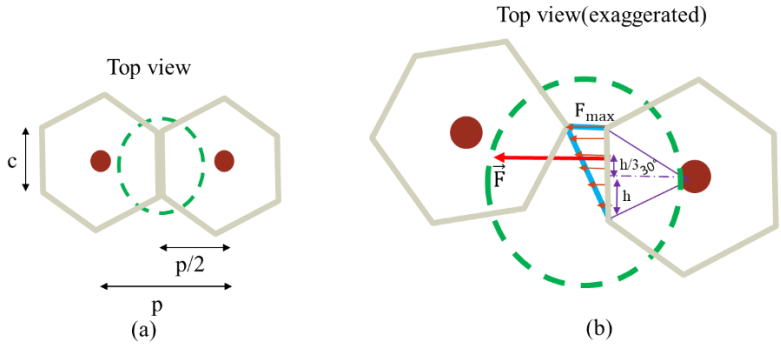

Figure 4.18: (a) Top view representation of the twist of two GaN hexagons with c being the length of the hexagonal side, (b) Exaggerated top view representation of the twist of two GaN hexagons. The green circle encloses the same area in both (a) and (b). The red circle represents the top surface of the pillar.

Geometrically we have:

$$\tan 30^{o} = \frac{h}{p/2} \rightarrow h = \frac{\sqrt{3}}{6} p \quad \textit{Equation 4.10}$$

And the magnitude of the force $\vec{F}$ is equal to the area of the blue triangle:

$$F = \frac{2h * F_{max}}{2} = h * F_{max} \quad \textit{Equation 4.11}$$

The distance between the force F and the center of the pillar, which is considered to be the rotation axis, is $d = \frac{h}{3}$ as seen in figure 4.17, so we can calculate the twist torque:

$$T_{twist} = F * d = h * F_{max} * \frac{h}{3} = \frac{h^2 * F_{max}}{3} \quad \textit{Equation 4.12}$$

Replacing equation (4.10) in equation (4.12), we obtain equation (4.13):

$$T_{twist} = \frac{p^2 * F_{max}}{36} \quad \textit{Equation 4.13}$$

The relation between the twist angle and the torque is defined by equation (4.14):

$$\theta_{twist} = \frac{T_{twist} * L}{G * I_p} \quad \textit{Equation 4.14}$$

With L being the length of the pillar, G the shear modulus of the chosen material equal to $\frac{E}{2(1+\nu)}$ (ν: Poisson ratio) (G value is unique since the beam is homogenous), and I_p the polar moment equal to $\frac{\pi}{2}r^4$ r: radius of the pillar).

By combining equations (4.8) and (4.14), the dissipated energy in one single pillar from a twist can be written as

$$U = \frac{1}{2} * \frac{\theta_{twist} * G * r^4}{2L} * \pi * \theta_{twist} \quad \textit{Equation 4.15}$$

As expected, the energy found in equation (4.15) does not depend on the pitch nor on the facet's thickness as we considered only one pillar (and without the GaN hexagon on top). It is proportional to the square of the twist angle (as obtained in the simulations results) and to the shear modulus. It highly depends on the radius of the pillar as it is proportional to r^4. Lastly, it is inversely proportional to the height L of the pillar.

We proceed with a numerical application to compare the energy from equation (4.15) to the required energy found from the numerical simulation results. We consider the homogenous beam made of AlN only (arbitrary choice), with a radius equal to 50 nm and the twist angle θ_{twist}= 0.1° (arbitrary choice). Using equation (4.15), the required analytical energy is found equal to 4.94 x 10^{-12} mJ. As for the numerical simulation, we consider the model defined in figure 4.15(a) (since the pitch and facet's thickness have negligible impact, we choose p=1.5 µm and e=0.1 µm) but with all the parts of made of AlN only. The required the energy required for a twist of 0.1° around the Z-axis shown in figure 4.15(a) (coordinate system 5) is found equal to 9.33 x 10^{-12} mJ. We obtain that the analytical energy is nearly the double of the numerical one, this means that the numerical and analytical results are in good agreement because the numerical energy obtained in Abaqus is for two pillars while the analytical energy is calculated for one single pillar. Thus, the analytical approach for the twist case is validated. Therefore, equation (4.15) can be used to estimate easily the required energy in one pillar for a precise twist angle.

We can now deduce the relation between the theoretical maximum possible twist angle θ_{twist_max} and the different pillars parameter. θ_{twist_max} depends on the available energy which is related to the facet's area: this means that the pitch and the facet's thickness will impact the value of θ_{twist_max}. The maximum twist angle is reached when the dissipated energy is equivalent to the available energy, therefore, to obtain the expression of θ_{twist_max}, equation (4.9) is considered equal to equation (4.15), this means:

$$\theta_{twist\_max}\ (\text{rad}) = \sqrt{\frac{L * Area_{facet} * \delta}{\pi * r^4 * G}} = \sqrt{\frac{2L * e * c * \delta}{\pi * r^4 * G}}$$

$$= 2\sqrt{\frac{L * e * p * \delta}{\pi\sqrt{3} * r^4 * G}} \quad \textit{Equation 4.16}$$

with e being equal to the thickness of the facet and c= $\frac{2p}{\sqrt{3}}$. From equation (4.16), we conclude that a pillar with a smaller diameter, greater height, a larger pitch, and lower shear modulus (indicating greater flexibility) is capable of achieving a larger twist angle. We notice that the radius has the impact of first order which means a smaller radius allows for a larger twist angle.

In the case of a non-homogenous pillar (each part is assigned a different material) which is our case, given the elastic analysis, θ_{twist} can be computed for each part separately using equation (4.14) and the properties of the material assigned to it. Then, θ_{twist} at the top of the pillar will be equivalent to the sum of the θ_{twist} contributed by each part with the torque T_{twist} being continuous all over the pillar. In our case, the pillar is composed of three different parts with three different material (SiO_2, Si and AlN), which means the ratio $\frac{L}{G}$ in equation (4.16) will be equal to the sum $\frac{L_1}{G_1} + \frac{L_2}{G_2} + \frac{L_3}{G_3}$ with L_1, L_2, L_3 and G_1, G_2, G_3 corresponding to the height and shear modulus of the SiO_2, AlN and Si sections in the pillar respectively. To maximize the twist angle, we should increase the thickness of the softest material, which is in our case, the SiO_2.

4.5.2 Tilt case

For the tilt case, we consider the pillar as one-dimensional homogenous beam. The pillar's bottom is fixed at point O and L is the length of the beam. We show in figure 4.18 two pillars with GaN hexagon on top of each from a lateral view. To determine the impact of the parameters on the pillar's tilt, we will calculate analytically the required tilt energy for a single pillar and without the GaN hexagon on top as already mentioned. The resulting force $\vec{F}$ inducing the tilt is considered the same one inducing the twist, therefore, from equation (4.11) we have, $F = h * F_{max}$.

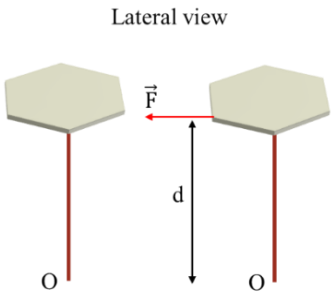

Figure 4.19: Lateral view representation of the force $\vec{F}$ that will induce a tilt within GaN pyramids (colored in blue) on top of two pillars.

With d being the distance from the axis of rotation to the point where the force $\vec{F}$ is applied, we can deduce that d is equal to L (length of the pillar), and we can calculate the tilt torque using equations (4.10) and (4.11).

$$T_{tilt} = F * d = h * F_{max} * L = \frac{\sqrt{3}}{6} p * F_{max} * L \quad \textit{Equation 4.17}$$

Therefore, we have:

$$\frac{T_{twist}}{T_{tilt}} = \frac{\sqrt{3}p}{18L} \quad \textit{Equation 4.18}$$

To define the relation between the tilt angle and the torque, we present a schematic representation of the pillar's tilt by an angle θ_{tilt} in figure 4.19. The pillar's bottom is fixed at point O. The displacement v of the pillar along the y direction is the deflection of the beam at a certain position x_A.

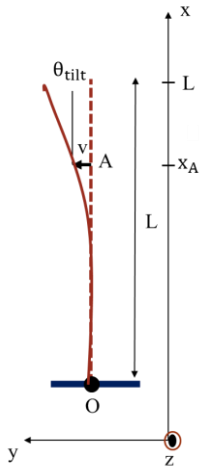

Figure 4.20: schematic representation of a beam bending (pillar's tilt).

The Euler-Bernoulli [143] beam deflection equation is given by:

$$v = \frac{T_{tilt} * x^2}{2E * I_Z} \quad \textit{Equation 4.19}$$

With E being the Young modulus along x, I_z the moment of inertia equal to $\frac{\pi}{4}r^4$ and x is the distance from point O to point A (if we consider the entire pillar → x_A=L).

Geometrically, and for small angles, we have $\tan \theta_{tilt} = \theta_{tilt} = \frac{dv}{dx}$, therefore, the relation between θ_{tilt} and T_{tilt} is expressed in equation (4.20)

$$\theta_{tilt} = \frac{T_{tilt} * L}{E * I_Z} \quad \textit{Equation 4.20}$$

By combining equations (4.8) and (4.20), the dissipated energy in one single pillar from a tilt can be written as

$$U = \frac{1}{2} * \frac{\theta_{tilt} * E * r^4}{4L} * \pi * \theta_{tilt} \quad \textit{Equation 4.21}$$

As seen in the twist case in equation (4.15), the required tilt energy does not depend on the pitch nor on the facet's thickness. It is proportional to the square of the tilt angle (as obtained in the simulations results) and to the shear modulus and highly depends on the radius of the pillar as it is proportional to r^4. Lastly, it is inversely proportional to the height L of the pillar.

We proceed with a numerical application to compare the energy from equation (4.21) to the required energy found from the numerical simulation results. We consider the same numerical test applied for the twist case, therefore using equation (4.21), the required analytical energy is found equal to 2.47 x 10^{-12} mJ. As for the numerical simulation, we consider the model defined in figure 4.14(a) (we choose p=1.5 µm and e=0.1 µm) but with all the parts of made of AlN only. The energy required for a tilt of 0.1° around the Z-axis shown in figure 4.14(a) (coordinate system 1) is found equal to 5.2 x 10^{-12} mJ. We obtain $E_{numerical}$=2.1 x $E_{analytical}$, this means that the numerical and analytical results are in good agreement because the numerical energy obtained in Abaqus is for two pillars while the analytical energy is calculated for one single pillar. Thus, the analytical approach for the tilt case is validated. Therefore, equation (4.21) can be used to estimate easily the required energy in one pillar for a precise tilt angle.

We can now deduce the relation between the maximum possible tilt angle θ_{tilt_max} and the different pillars parameter using the same approach used for the twist. By using equations (4.9) and (4.21), we obtain:

$$\theta_{tilt\_max}\ (\text{rad}) = 2\sqrt{\frac{2L * e * p * \delta}{\pi\sqrt{3} * r^4 * E}} \quad \textit{Equation 4.22}$$

From equation (4.22), we obtain the same conclusion found for the twist case: a pillar with a smaller diameter, greater height, a larger pitch, and lower young modulus is capable of achieving a larger tilt angle with the radius of the pillar being the parameter with the most impact.

In the case of a non-homogenous pillar, given the analysis is elastic, θ_{tilt} can be computed for each part separately using equation (4.14) and the properties of the material forming it. Then, θ_{tilt} at the top of the pillar will be equivalent to the sum of the θ_{tilt} contributed by each part. In our case, the pillar is composed of three different parts with three different material (SiO_2, Si and AlN), which means the ratio $\frac{L}{E}$ in equation (4.20) will be equal to the sum $\frac{L_1}{E_1} + \frac{L_2}{E_2} + \frac{L_3}{E_3}$ with L_1, L_2, L_3 and E_1, E_2, E_3 corresponding to the height and Young modulus of the SiO_2, AlN and Si sections in the pillar respectively. To maximize the tilt angle, we should increase the thickness of the softest material, which is in our case, the SiO_2.

This study permits to conceive a design that promotes θ_{twist} over θ_{tilt} or the opposite. By combining equations (4.14) and (4.20), we have:

$$\frac{\theta_{twist}}{\theta_{tilt}} = \frac{\frac{T_{twist} * L}{G * I_p}}{\frac{T_{tilt} * L}{E * I_Z}} = \frac{\frac{2\,(1+\nu) * T_{twist} * L}{E * I_p}}{\frac{T_{tilt} * L}{E * I_Z}} = (1+\nu) * \frac{T_{twist}}{T_{tilt}} = (1+\nu) * \frac{\sqrt{3}p}{18L} \quad \textit{Equation 4.23}$$

From equation (4.23), we can adjust the pitch/height ratio to have a twist angle that is greater than a tilt angle or the opposite.

4.6 Conclusion

In this chapter, we performed finite element simulations using Abaqus software to (i) validate and explain the feasibility of the tilt values found from the experimental data and (ii) determine the optimal pillars parameter for an energetically feasible rotation. Due to the different hypothesis we had to use, the obtained results are viewed as general qualitative conclusions. Following the validation of the applied boundary conditions, constraints type, element size and type, different approach were tested to simulate the rotation of the pillars. We have found that a tilt and a twist of 0.04° around a certain chosen rotation axis is energetically feasible, while a tilt of 0.1° and 0.2° requires higher energy orders not present on the GaN surface which is not in good agreement with the tilt of 0.1° measured from the experimental work, therefore, different explanations were discussed. We also found that the pitch and the GaN facet's thickness have the least impact on the required rotation energy. The numerical results allowed the development and validation of a simplified analytical model that only accounts for the mechanics of the nanopillar in both tilt and twist case. The analytical formulation allowed the determination of the impact of all the parameters (pitch, height, elastic property, radius, GaN facet thickness, rotation angle) in a simple way. The radius was found to be the most critical parameter as the required energy is proportional to r^4. This work opens the door to future numerical studies: the pillar model can be refined to match the experimental shape, a test of the pillar's cracking under certain conditions can be conducted… Furthermore, in this approach we considered only mechanical forces, but we believe that a better representation of the physical phenomena taking place during coalescence could be obtained by using a theory of rupture (or bonding) that uses an energetic approach to describe the kinetics of cohesion that takes place during the coalescence phase [150].

Chapter 5: New perspectives from optimization of pillars

5.1 Introduction

We have previously shown that the growth of GaN platelets on a hexagonal pillar pattern allowed us to obtain small (10 x 10 µm²) highly oriented islands of GaN. However, we were unable to produce larger well oriented GaN islands. We also achieved very well oriented GaN lines of 5 µm with dislocation densities of the order of 1.2 x 10^7 cm^{-2}, although this was only possible for 3 out of 5 lines. We also showed that for lines of 3 pillars, it is possible to perfectly orient the GaN layers, while disorienting the silicon of the pillars. Again, this did not occur for all zones that were examined.

From these results, we drew several conclusions:

1. It is possible to perfectly coalesce GaN pyramids on silicon/SiO_2 pillars.
2. Once two groups of pillars have coalesced, it would not be possible for them to accommodate another group, leading to dislocations at the boundary.
3. High mis-orientations between GaN pyramids, or multiple orientations of GaN in one pyramid would make perfect coalescence very difficult, or impossible.

These results allowed us to imagine new networks of pillars where we maintain the coalescence of the pyramids obtained from the lines of pillars, as this allows a pillar-by-pillar rotation, and we introduce the possibility to produce larger coalesced area than a line of GaN with a large smooth c-plane essential for the fabrication of µLEDs. This combination appeared in new samples with two different forms:

- star-shaped pattern: stars of 10 branches, with increasing distance between pillars along the arms.
- spiral-shaped pattern: pillars arranged in logarithmic spirals, where pillars are increasingly far from one another as they move away from the center of the pattern.

5.2 Towards new promising pillars pattern

5.2.1 Study of GaN reorientation within a star-shaped pillars pattern

New samples are prepared with pillars organized in star patterns in order to determine GaN orientation following a successive coalescence system (pillar by pillar). SXDM measurements at ID01 beamline and EBSD measurements were performed on these new samples.

SXDM analysis

In figure 5.1(a), we show two stars formed by branches of pillars with a diameter of 100 nm prior to regrowth; the label on the left side of the figure (1ET100) was etched to facilitate the localization of the star during the SXDM experiment. In figure 5.1(b), we observe the successive coalescence of the pyramids starting from the areas where the pillars are closest (at the center) to the more distant ones. In figure 5.1(b), the border of the star appears to have a different GaN thickness compared to its center, but this varying appearance is due to the semi-polar facets of the star, which create a visual effect that makes the border seem thicker while in reality the star has uniform GaN thickness.

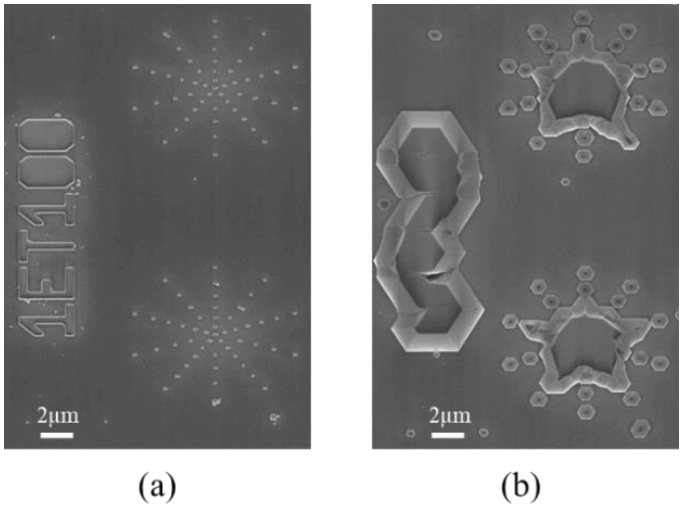

Figure 5.1: SEM images of star patterned pillars (a) before regrowth, and (b) after coalescence for 800 s at T=1030°C. Each figure includes two stars with a label placed on the left side.

To determine the orientation of the GaN after coalescence, SXDM measurements were performed on the two coalesced stars shown in figure 5.1(b). An area of 10 x 30 µm² has been scanned with the sample being rotated by ϕ= 29.2°, and ω rocking curves were performed around the asymmetrical Bragg reflection GaN (204) with a step size $\Delta\omega$=0.095° and an angular range of 93.55° < ω < 95.5° (each rocking curve consisted of 21 points). For every incidence angle ω of the rocking curve, an x-y piezo scan was performed, and diffraction images were taken every 100 nm in the x direction (100 positions) and 100 nm in the y direction (300 positions) with t=0.01 s. After selecting a ROI in the detector corresponding to the position of the peak, we display in figure 5.2(a), the 2D map of the integrated intensity of the GaN (204) Bragg peak across all the ω values.

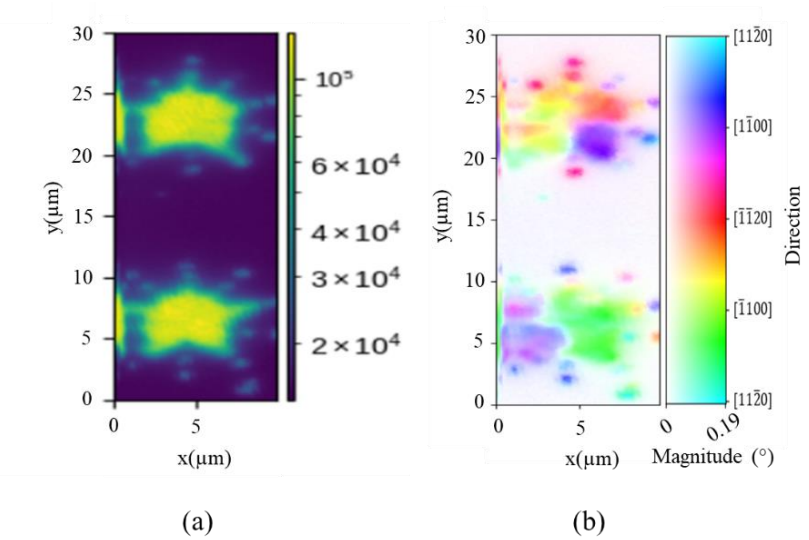

Figure 5.2: (a) 2D map of the integrated intensity at each point (x, y), the color bar represents intensity on a logarithmic scale, and (b) 2D map of $\vec{Q}_{204}$ relative rotation of the corresponding area.

From the intensity map in figure 5.2(a), we can clearly distinguish the coalesced lines forming the stars from the uncoalesced GaN pillars at the end of each branch presenting lower diffracted intensity. The results obtained in figure 5.2(b) show that the coalesced stars are actually made of several zones, with a lateral size < 5 µm, of homogeneous orientation (having the same color in figure 5.2(b)) but which have different tilts between them. These zones correspond to the branches of the initial star, which implies that the coalescence occurs branch by branch and not from a central nucleus. It may be because the central pillars are too close together to be able to effectively tilt or twist in order to form a perfectly oriented domain. The overall range of tilt in these structures is still low, only 0.19°.

EBSD analysis

A third coalesced star on top of pillars with a diameter of 100 nm was measured by EBSD, it is outlined by the red square in figure 5.3(b).

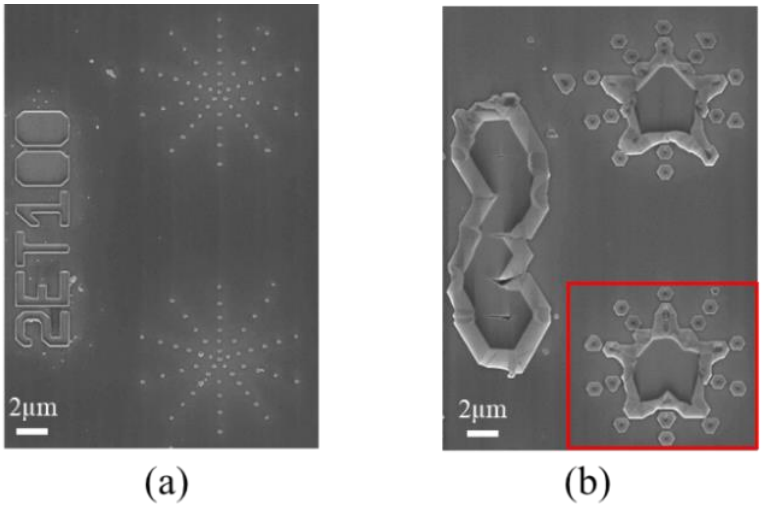

Figure 5.3: SEM images of star patterned pillars (a) before regrowth (b) after coalescence for 800 s at T=1030°C. Each figure includes two stars with a label placed to the right side. The measured star is outlined by red square.

The sample is tilted by 70° in the SEM, the step size along x and y is 0.1 µm, the voltage is 15 kV, and at each position (x, y), one frame was recorded with t=30 ms. We can obtain the angular deviation of each position from the mean orientation from the GROD map in figure 5.4(a). Figure 5.4(b) shows the GROD axis map with the standard crystallographic triangle presenting the crystallographic axes used to describe the orientation of the grains.

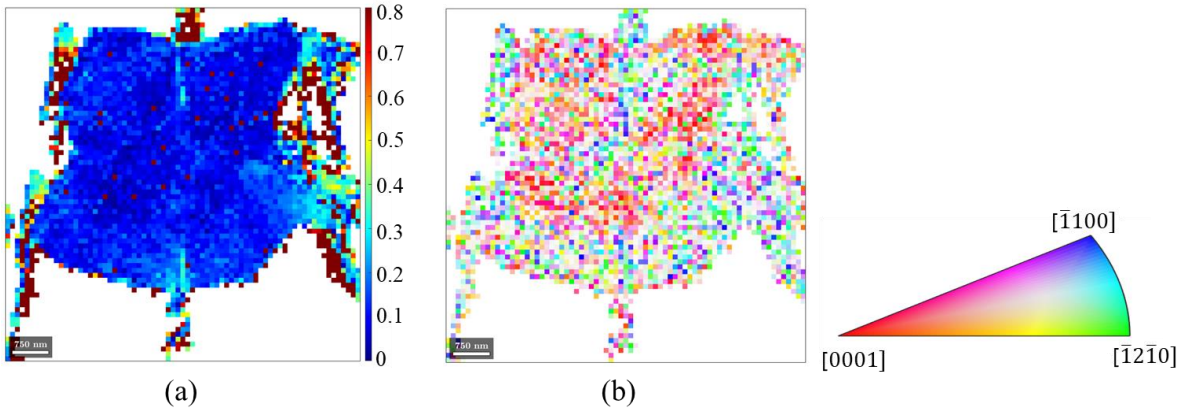

Figure 5.4: (a) GROD map of the measured coalesced star and (b) GROD axis map of the measured area.

In figure 5.4(a), we see that the tilt intensity is very low over the entire central surface and increases in the areas of the "branches" of the star. On the other hand, it is not possible to conclude on the different tilt directions from the GROD axis map (figure 5.4(b)) because the tilt values are low, and with the limited precision of EBSD, we are unable to distinguish the tilt directions, resulting in a noisy image.

The SXDM and EBSD analyses allowed us to observe that the progressive coalescence line by line does indeed take place, the different branches of the star patterns constituting distinct coalescence zones each having a unique homogenous orientation. However, the coalescence of the pillars on the edge of the branches is difficult to obtain quickly, and the homogeneity of the GaN orientation across all the coalesced branches is not evident, therefore, it is essential to adopt a different pillar distribution with reduced spacing. New samples, with spiral shaped pillars were prepared and analyzed by EBSD, and the results are shown in the next section.

5.2.2 Study of GaN reorientation within a spiral-shaped pillars pattern

The new studied samples are made of coalesced GaN on top of spiral-shaped pillars distribution such that the inter-pillar distance increases between the center and the edge of the pattern. Figure 5.5(a) shows a network of pillars in a spiral shape prior to regrowth. The 3D growth leads to the rapid coalescence of the pyramids in the center of the pattern, causing them to expand toward the edges. As for the previous samples, the growth is stopped after 800 s. The growth conditions should be optimized to allow complete coalescence of the spiral with relatively small height to obtain a large smooth c-plane rather than large semi-polar planes.

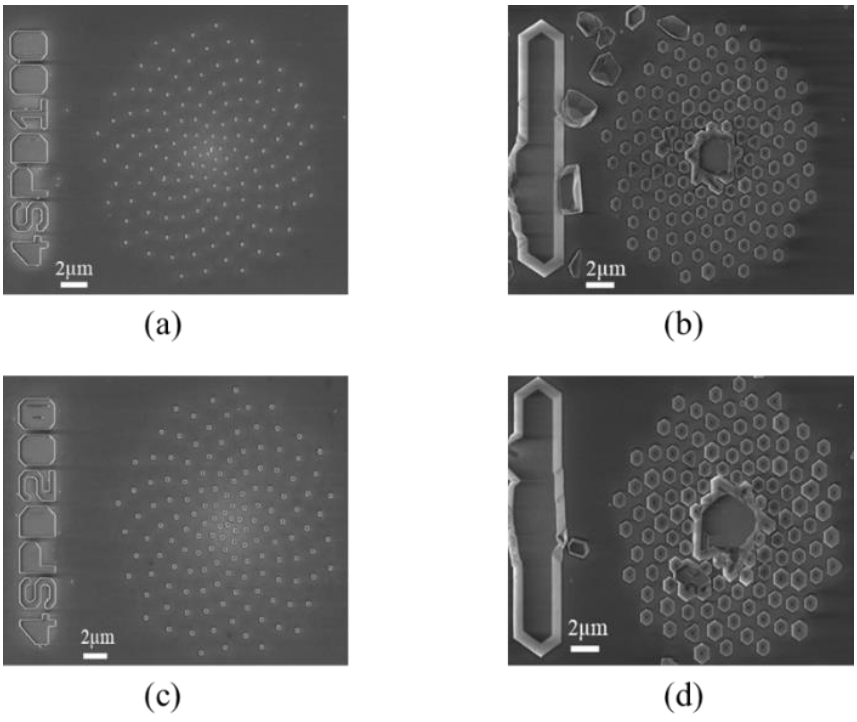

Figure 5.5 : SEM images of patterned pillars (a) before regrowth with a diameter of 100 nm, (b) after coalescence for 800 s with pillar diameter of 100 nm at T=1030°C, (c) before regrowth with a diameter of 200 nm, and (d) after coalescence for 800 s with pillar diameter of 200 nm at T=1030°C. Each figure includes the label on the left side.

The same EBSD measurements performed on the star samples were performed on the two spirals presented in figures 5.5(b) and 5.5(d). We obtain the angular deviation within the spiral on top of pillars with a diameter of 100 nm from its mean orientation from the GROD map in figure 5.6(a) and the tilt directions from the GROD axis map in figure 5.6(b). Figure 5.6(c) shows the GROD map of the spiral on top of pillars with a diameter of 200 nm and figure 5.6(d) shows the corresponding GROD axis map.

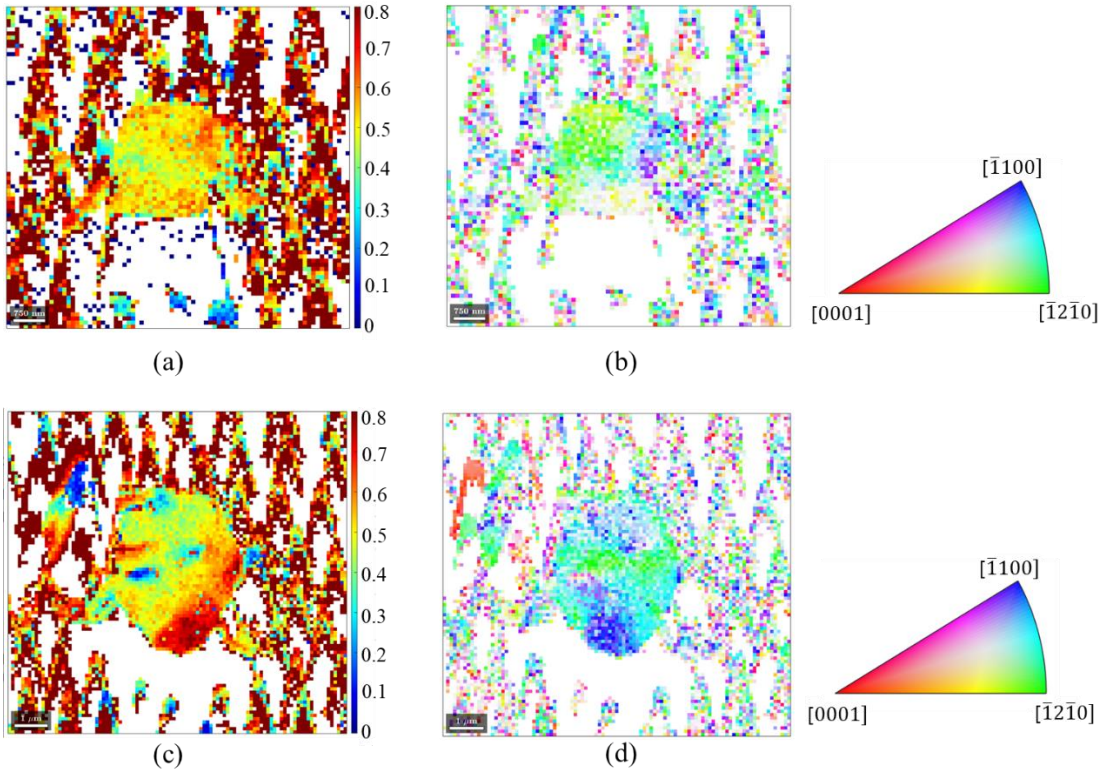

Figure 5.6: (a) GROD map of the measured coalesced spiral on top of the pillars with a diameter of 100 nm, (b) GROD axis map of the same area, (c) GROD map of the measured coalesced spiral on top of the pillars with a diameter of 200 nm, and (d) GROD axis map of the same area.

We observe that the amplitude of the tilt is more homogeneous and smaller on the patterns with pillars of smaller diameter than on the ones with larger diameter. In figure 5.6(a), the tilt across the whole coalesced spiral is between 0.4° and 0.6° while for the larger pillars (in figure 5.6(c)) it looks much bigger: from 0° to 0.7°. We lack statistics to determine whether the misorientation in figure 5.6(d) is due to the increased difficulty in rotating the pillars with a larger diameter (we have seen that the pillars rotation is inversely proportional to radius^4) or due to the parasitic growth visible in figure 5.5(d)) that caused a disruption of the coalescence on this pattern. These results show that successive coalescence in spiral pattern is a promising strategy to facilitate the rotation pillar by pillar to produce a well-oriented GaN layer with large smooth c-plane. However, more work is required to optimize the initial samples and the epitaxial process to be able to produce defect free islands several µm across.

5.3 Conclusion and perspectives

As a conclusion for the work done in this thesis, we have started by studying simple sets of three pillars where we measured directly the rotation of pillars by 0.1° after coalescence using SXDM at ID01 beamline. Following this confirmation of the tilt/twist of the pillars, SXDM measurements on GaN layers with incomplete coalescence (at the early growth stage) were carried out; the results confirmed that the initially misoriented GaN pillars coalesce into larger well-defined GaN domains (3.9 µm) very well oriented within themselves but with a larger tilt/twist between them. The grain boundaries between the large well oriented GaN grains thus led to the formation of dislocations in those areas to compensate the misorientation. This resulted in a dislocation density of 2 x 10^{11} cm^{-2} at the boundaries as approximated from EBSD measurements. From these measurements, we created a model that estimated the tilt limit between neighboring pillars underneath the GaN domains and found it equal to 0.1° coherent with the tilt in the sets of three pillars.

The next objective was to determine the quality of fully coalesced GaN in larger regions to fabricate µLEDs. Therefore, we characterized larger fully coalesced GaN samples (GaN on sets of ten pillars and GaN on large hexagonal pillars pattern) using DFXM at ID06 beamline. We achieved extremely well oriented GaN lines (σ =0.04°, implying a dislocation density of 1.2 x 10^{7} cm^{-2}) between pillars along the whole line better than 2D GaN on Si although this only occurred for 3 out of 5 lines. In addition, we achieved well oriented regions up to 10 x 10µm² in the GaN on hexagonal pattern samples. The comparison between the well oriented GaN island sizes observed during the early stage of coalescence (3.9 µm) and the well oriented fully coalesced GaN domains (10 µm) is not easy, because (i) we used different characterization techniques, so maybe the resolution of the ID06 method may not be sufficient to detect subtle differences in domain size forming the large region of 10 x 10 µm², given the very small orientation variations, (ii) the samples exhibit varying pitch sizes, which could also influence the results (iii) the samples were prepared at different times, meaning that the pillars may not be strictly identical. Nevertheless, in both samples, we have managed to increase the size of the well oriented GaN grains compared to the 2D GaN on Si case (2 µm). Regarding the misorientation between domains, in the case of GaN at the early stage of coalescence, the misorientation remains greater compared to 2D GaN on Si. However, for the GaN lines and platelets, the misorientation is reduced.

Based on the obtained results, we conclude that it is difficult to grow a fully coalesced and well-oriented 40 x 40 µm² GaN platelet on top of large number of pillars in a hexagonal pattern and with a fixed pitch value. As it is difficult or impossible to rotate large group of pillars once they have coalesced into domains, we end up having small homogenous GaN grains on top of a certain number of pillars, but with high misorientation between grains. As we obtained good results in coalescing lines of 10 pillars in 3 out of 5 cases, we produced new samples with star and spiral pillars pattern in a way that we used successive coalescence and allowed the

fabrication of larger GaN areas (larger than a line) that can be used as pixels. In this chapter, we showed and discussed SXDM and EBSD measurements of the GaN on top of star patterned pillars. Successive coalescence was seen, resulting in homogenous GaN branches. However, the orientation between the branches was not always identical, resulting in coalescence clusters each with its distinct orientation. From the EBSD measurements of the GaN on top of the spiral patterned pillars, homogenous GaN orientation was seen for pillars 100 nm across, but more the variation was much greater for pillars 200 nm across, maybe due to parasitic growth.

Many improvements are required to optimize the spiral patterned pillars, to eliminate the parasitic growth and improve the GaN reorientation, but following the experimental work and findings presented in this thesis, we found that this pattern represents the most optimized configuration because (i) it will facilitate the rotation pillar by pillar, and (ii) the coalescence will be successive and not by clusters.

To address the final objective of this thesis, which is to provide explanation for the experimental tilt/twist values and to evaluate how varying pillar parameters affect the pillar's rotation, we performed finite element simulations using Abaqus software. Testing the different pillar parameters was not feasible experimentally due to limited beamtime and long samples fabrication process. In chapter 4 we presented the numerical model which we defined and tested two approaches to simulate the pillar rotation using Abaqus. However, we were not able to consider the physical phenomenon taking place as it is not completely understood. Therefore, the results of the finite element simulations can only be interpreted in a qualitative way given the strong hypothesis we had to use. We computed the required energy for different rotation angles. We found that for a chosen twist and tilt axis, a tilt and a twist of 0.04° is energetically achievable but that was not the case for a rotation of 0.1° or 0.2°.

As for the pillar's parameter optimization in order to reduce the required energy for a rotation and increase the maximum energetically possible reorientation angle, the numerical simulations showed that a higher twist/tilt angle can be achieved with a larger pitch and an increased thickness of the vertical edge of the pyramid. However, the effect of these two parameters is not particularly significant, as their variation only causes a slight change in the required rotation energy. From the numerical results, we developed a simplified analytical model that considers only the mechanics of the nanopillars and allows an easy determination of the impact of all the parameters (pitch, height, radius, elasticity, thickness of the GaN facet) on the required rotation energy. The analytical model was validated, and we found that the effect of the pillar radius is particularly strong as the maximum energetically feasible rotation angle is inversely proportional to r^2, and the required energy is proportional to r^4.

From the work in this thesis, we have identified three key elements to be improved to enable defect free islands of GaN:

- Coalescence of structures pillar-by-pillar, to avoid formation of different domains within the island.

- Avoidance of different orientations within each pillar.
- Facilitating the coalescence of pillars without forming defects.

Therefore we propose the most promising strategy using the PEGADIS approach for fabricating small islands suitable for microLEDs: we have to (i) ensure that we have minimal misorientation in the 2D GaN on SOI (start from a GaN with good quality) to avoid having multiple orientation within a pillar, (ii) fabricate pillars with the smallest radius possible and with the maximum distance between the pillars to facilitate the rotation (this requires an optimization of the selective growth process to avoid parasitic growth between the pillars), and (iii) obtain a successive coalescence (pillar-by-pillar) which is what we had in the spiral structures case.

This means that the potential future experimental future work should mainly focus on the improvements of the spiral pattern and can include:

- Further characterization on spiral patterned samples at different growth levels is useful to follow the reorientation of the GaN step by step and with different diameters to determine whether an optimal diameter can be identified.
- An optimization of the growth conditions of the spiral patterned samples is required to produce GaN platelets of a few microns thick with a dislocation density below 10^8 cm^{-2}: (i) an optimization of the pillars spacing can help in reducing the parasitic growth within the spiral, and (ii) the distance between the pillars must be optimized in order to minimize the formation of semipolar planes and favor that of the c-plane.
- It is beneficial to reduce the number of pillars manufacturing steps to facilitate the structuring of samples. LTM is currently developing a process to avoid the lift-off step [124].
- Characterization of samples with GaN on Si instead of GaN on SiO_2 is needed, to determine clearly the impact of the SiO_2 on the rotation of the pillars and the reorientation of the GaN.

Future numerical work is feasible to improve our model and provide an optimal configuration to be fabricated and tested experimentally:

- Appling the rotation approach on larger number of pillars and hexagons to observe how the stress will be distributed in GaN.
- Refining the pillar geometric representation to resemble more to its actual shape.
- Considering a better representation (inspired from the cohesion theory) of the mechanical force between the pillars during coalescence (rotation).

General Conclusion

GaN based µLEDs are suitable for wide range of applications and their development is still in progress. The PEGADIS approach proposes an original method to grow high quality GaN layers used for the production of µLEDs. It is based on the growth of GaN pyramid on top of nanopillars that are intended to rotate during coalescence and allow the realignment of the GaN on top to form high quality GaN platelet. With the suggested architecture, pixel etching is not required, and the transfer procedure is facilitated. However, the rotation of the pillars had not previously been confirmed and the range of crystalline orientation GaN had not been determined. The understanding of the coalesces process was required to be able to control it and an optimization of the different growth parameters were necessary to determine the most promising strategy using the PEGADIS approach for fabricating GaN islands compatible for µLEDs.

In this thesis, we confirmed the hypothesis on the pillar rotation during coalescence and the realignment of the coalesced GaN on top of the pillars. Using SXDM, we measured at the pillar's level (nanoscale) the rotation of pillars by 0.1° after coalescence. At the macro scale, measurements performed by macroscopic X-ray diffraction showed that the Si sections in the nanopillars become significantly disoriented after coalescence compared with a reference sample prior to regrowth.

Following this confirmation of the tilt/twist of the pillars, it was crucial to examine the microstructural evolution during growth and to study the coalescence process taking place at the nanoscale in order to comprehend the growth approach. To carry out a complete structural characterization, new samples were characterized using three complimentary techniques: SXDM, EBSD, and CL. Crystalline orientation maps of the GaN before coalescence and at the early stage of coalescence showed that the initially misoriented GaN pillars transformed into well-defined and well-oriented GaN domains (3.9 µm). The presence of dislocations at the grain boundaries has been confirmed with CL observations and estimated from the EBSD measurements, providing an upper bound for their local density of ~10^{11} cm^{-2}. Additionally, we found that as long as the tilt between neighboring pillars does not surpass 0.1°, neighboring pillars contribute to forming a highly oriented crystalline domain similar in size to the ones formed at the early stage of coalescence. This tilt limit value is in good agreement with the tilt values measured directly using SXDM on the sets of three pillars. This study showed that once two groups of pillars have coalesced, it would not be possible for them to accommodate another group, leading to dislocations at the boundary. Therefore, new samples of sets of ten pillars were measured, where coalescence takes place pillar-by-pillar, which avoids the formation of different domains within the island.

We report the achievement of extremely well oriented GaN lines (dislocation density ~1.2 x 10^7 cm^{-2}), with barely any misorientation (better than 2D GaN) between pillars along the whole

line using our unique growth approach. When coalesced into platelets with hexagonal pillar pattern, we achieved regions up to 10 x 10 µm² that are also extremely well oriented. This study using DFXM, showed that it is possible to perfectly coalesce GaN pyramids on top of the nanopillars in sets of lines. For larger structures with hexagonal pillar pattern, prefect alignment can only be achieved over one part of the structure.

Based on the various characterizations, new optimized samples with star-shaped and spiral-shaped pillars pattern were fabricated. Their SXDM and EBSD characterization showed the achievement of homogenous GaN layers with a successive coalescence and the possibility to obtain larger coalesced areas than the lines of GaN. These results are promising for the fabrication of small highly oriented islands of GaN on Si, suitable for highly efficient µLEDs.

Lastly, finite element simulations were used in order to study the mechanical behavior of GaN hexagons on trop of nanopillars. This study relies on potentially strong hypothesis related to the mechanics and kinetics of the coalescence process. This process is not completely understood and therefore the results of the finite element simulations can only be interpreted in a qualitative way. Different geometrical configurations were studied by varying the pillars parameters (pitch, radius, height, shear modulus) and the thickness of the GaN hexagon (the edge of the GaN pyramid) in order to reduce the required energy for a rotation and increase the maximum energetically possible rotation angle. This study demonstrated that the energy required to induce the alignment of the GaN hexagons is mainly concentrated in the pillars. These numerical results permitted to develop a simplified analytical model that only accounts for the mechanics of the nanopillar. Using the finite elements simulations and the analytical model it was found that the highest energetically possible reorientation angle is proportional to the square root of the pitch and of the hexagon's thickness. The highest rotation angle energetically possible is also proportional to the square of the pillar’s height and inversely proportional to the shear modulus. The parameter with the greatest influence on the rotation angle (and the required energy) is the pillar's radius, as the maximum energetically feasible rotation angle is inversely proportional to r^2, and the required energy is proportional to r^4. Therefore, this study demonstrated the key parameters to rotate the pillars.

These findings open the door to future investigation on newly improved high-quality samples that could show the optimal potentials of this pendeo-epitaxy technique in producing well-oriented GaN layers employed in the future in the production of µLEDs. We propose new samples with high quality GaN on SOI, the smallest radius possible, the largest pitch possible without causing parasitic growth and with a successive coalescence (pillar-by-pillar) which makes the spiral samples an appropriate choice for continuous work and improvements.

Scientific Communications and Award

This PhD work has led to the following scientific communications and award.

Articles

- **M. Wehbe et al.**, "Demonstration of grain reorientation during GaN early stage coalescence grown by novel pendeo-epitaxy approach", *Journal of Applied Physics*, vol. 136, no. 22, (2024), https://doi.org/10.1063/5.0235955.

- **M. Wehbe et al.**, "Study of GaN coalescence by dark-field X-ray microscopy at the nanoscale," *Journal of Applied Crystallogr*aphy, vol. 56, no. 3, (2023), https://doi.org/10.1107/S160057672300287X.

- **M. Wehbe et al.**, "Mechanical modeling of GaN pillars coalescence for growth parameter optimization", to be submitted soon.

Presentations

- **M. Wehbe et al.**, "Combining dark-field X-ray microscopy with scanning X-ray diffraction microscopy to study GaN coalescence", *High Resolution X-ray Diffraction and Imaging (XTOP) Conference*, Carry-le-Rouet, France, March 17-22 2024. ***Oral***

- **M. Wehbe et al.**, "Strain and lattice rotation mapping of GaN at early stage of coalescence by synchrotron x-ray nano diffraction", *International Conference on Nitride Semiconductors (ICNS)*, Fukuoka, Japan, November 12-17 2023. ***Poster***

- **M. Wehbe et al.**, "Study of nanoscale GaN coalescence by synchrotron X-ray diffraction", *European Materials Research Society (EMRS) conference*, Warsaw, Poland, September 19-22 2022. ***Oral***

Award

- **Laureate of the Young and Early Career Scientist Award,** *granted by the International Union of Crystallography (IUCr) to reward young scientist based both on their academic records as well as on the quality of their presentation during the XTOP conference*, Carry-le-Rouet, France, March 22nd 2024. ***Oral***

Bibliography

[1] M. P. Thompson, G. W. Auner, and A. R. Drews, "Epitaxial growth of zinc-blende AIN on Si (100) substrates by plasma source molecular beam epitaxy," *J. Electron. Mater.*, vol. 28, pp. L17–L19, 1999.

[2] H. Morkoç and H. Morkoç, "General properties of nitrides," *Nitride Semicond. devices*, pp. 8–44, 1999.

[3] S. Kasap and P. Capper, *Springer handbook of electronic and photonic materials*. Springer, 2017.

[4] T. Hanada, "Basic properties of ZnO, GaN, and related materials," in *Oxide and nitride semiconductors*, Springer, 2009, pp. 1–19.

[5] V. Darakchieva, B. Monemar, and A. Usui, "On the lattice parameters of GaN," *Appl. Phys. Lett.*, vol. 91, no. 3, 2007.

[6] D. Schwarzenbach, "Note on Bravais–Miller indices," *J. Appl. Crystallogr.*, vol. 36, no. 5, pp. 1270–1271, 2003.

[7] K. Iga, "Forty years of vertical-cavity surface-emitting laser: Invention and innovation," *Jpn. J. Appl. Phys.*, vol. 57, no. 8S2, p. 08PA01, 2018.

[8] N. Zheludev, "The life and times of the LED—a 100-year history," *Nat. Photonics*, vol. 1, no. 4, pp. 189–192, 2007.

[9] M. G. Craford, "From holonyak to today," *Proc. IEEE*, vol. 101, no. 10, pp. 2170–2175, 2013.

[10] S. Nakamura, M. S. M. Senoh, and T. M. T. Mukai, "P-GaN/N-InGaN/N-GaN double-heterostructure blue-light-emitting diodes," *Jpn. J. Appl. Phys.*, vol. 32, no. 1A, p. L8, 1993.

[11] H. Amano, M. Kito, K. Hiramatsu, and I. Akasaki, "P-type conduction in Mg-doped GaN treated with low-energy electron beam irradiation (LEEBI)," *Jpn. J. Appl. Phys.*, vol. 28, no. 12A, p. L2112, 1989.

[12] H. Amano, N. Sawaki, I. Akasaki, and Y. Toyoda, "Metalorganic vapor phase epitaxial growth of a high quality GaN film using an AlN buffer layer," *Appl. Phys. Lett.*, vol. 48, no. 5, pp. 353–355, 1986.

[13] H. E. Lee *et al.*, "Micro light-emitting diodes for display and flexible biomedical applications," *Adv. Funct. Mater.*, vol. 29, no. 24, p. 1808075, 2019.

[14] K. Ahmed, "11-2: Micro LEDs efficiency targets for displays," in *SID Symposium Digest of Technical Papers*, 2019, vol. 50, no. 1, pp. 125–128.

[15] T.-Y. Lee *et al.*, "Technology and applications of micro-LEDs: Their characteristics, fabrication, advancement, and challenges," *Acs Photonics*, vol. 9, no. 9, pp. 2905–2930, 2022.

[16] F. Olivier, S. Tirano, L. Dupré, B. Aventurier, C. Largeron, and F. Templier, "Influence of size-reduction on the performances of GaN-based micro-LEDs for display application," *J. Lumin.*, vol. 191, pp. 112–116, 2017.

[17] R.-H. Horng *et al.*, "Study on the effect of size on InGaN red micro-LEDs," *Sci. Rep.*, vol. 12, no. 1, p. 1324, 2022.

[18] F. Templier *et al.*, "19-6: Invited Paper: A Novel Process for Fabricating High-Resolution and Very Small Pixel-pitch GaN LED Microdisplays," in *SID Symposium Digest of Technical Papers*, 2017, vol. 48, no. 1, pp. 268–271.

[19] S. X. Jin, J. Li, J. Z. Li, J. Y. Lin, and H. X. Jiang, "GaN microdisk light emitting diodes," *Appl. Phys. Lett.*, vol. 76, no. 5, pp. 631–633, 2000.

[20] T. P. Chow *et al.*, "SiC and GaN bipolar power devices," *Solid. State. Electron.*, vol. 44, no. 2, pp. 277–301, 2000.

[21] S. J. Pearton, F. Ren, A. P. Zhang, and K. P. Lee, “Fabrication and performance of GaN electronic devices,” *Mater. Sci. Eng. R Reports*, vol. 30, no. 3–6, pp. 55–212, 2000.
[22] Z. Liliental-Weber, J. Jasinski, and D. N. Zakharov, “GaN grown in polar and non-polar directions,” *Optoelectron. Rev.*, vol. 12, no. 4, p. 339, 2004.
[23] D. Feezell, “Nonpolar and Semipolar III-Nitride Optoelectronic Materials and Devices.” [Online]. Available: Center for High Technology Materials Department of Electrical and Computer Engineering,University of New Mexico.
[24] J. Neugebauer and C. G. Van de Walle, “Atomic geometry and electronic structure of native defects in GaN,” *Phys. Rev. B*, vol. 50, no. 11, p. 8067, 1994.
[25] A. H. Cottrell, “Theory of dislocations,” *Prog. Met. Phys.*, vol. 4, pp. 205–264, 1953.
[26] K. W. Böer and U. W. Pohl, “Crystal Defects BT - Semiconductor Physics,” K. W. Böer and U. W. Pohl, Eds. Cham: Springer International Publishing, 2019, pp. 1–51.
[27] H. Amano *et al.*, “The 2018 GaN power electronics roadmap,” *J. Phys. D. Appl. Phys.*, vol. 51, no. 16, p. 163001, 2018.
[28] R. Datta, M. J. Kappers, M. E. Vickers, J. S. Barnard, and C. J. Humphreys, “Growth and characterisation of GaN with reduced dislocation density,” *Superlattices Microstruct.*, vol. 36, no. 4–6, pp. 393–401, 2004.
[29] T. Metzger *et al.*, “Defect structure of epitaxial GaN films determined by transmission electron microscopy and triple-axis X-ray diffractometry,” *Philos. Mag. A*, vol. 77, no. 4, pp. 1013–1025, 1998.
[30] N. F. Mott, “Dislocations and the theory of solids,” *Nature*, vol. 171, no. 4345, pp. 234–237, 1953.
[31] M. F. Ashby and D. R. H. Jones, *Engineering materials 1: an introduction to properties, applications and design*, vol. 1. Elsevier, 2012.
[32] T. Markurt, T. Schulz, P. Drechsel, P. Stauss, and M. Albrecht, “A predictive model for plastic relaxation in (0001)-oriented wurtzite thin films and heterostructures,” *J. Appl. Phys.*, vol. 124, no. 3, 2018.
[33] B. Jahnen *et al.*, “Pinholes, dislocations and strain relaxation in InGaN,” *MRS Internet J. Nitride Semicond. Res.*, vol. 3, pp. 1–10, 1998.
[34] Q. Dai *et al.*, “Internal quantum efficiency and nonradiative recombination coefficient of GaInN/GaN multiple quantum wells with different dislocation densities,” *Appl. Phys. Lett.*, vol. 94, no. 11, 2009.
[35] K. Baril *et al.*, “High quality GaN microplatelets grown by metal-organic vapor phase epitaxy on patterned silicon-on-insulator substrates: Toward micro light-emitting diodes,” *J. Appl. Phys.*, vol. 133, no. 24, 2023.
[36] S. Y. Karpov and Y. N. Makarov, “Dislocation effect on light emission efficiency in gallium nitride,” *Appl. Phys. Lett.*, vol. 81, no. 25, pp. 4721–4723, 2002.
[37] J. Lähnemann, U. Jahn, O. Brandt, T. Flissikowski, P. Dogan, and H. T. Grahn, “Luminescence associated with stacking faults in GaN,” *J. Phys. D. Appl. Phys.*, vol. 47, no. 42, p. 423001, 2014.
[38] X. H. Wu *et al.*, “Dislocation generation in GaN heteroepitaxy,” *J. Cryst. Growth*, vol. 189, pp. 231–243, 1998.
[39] L. Zhang, “Energy of low angle grain boundaries based on continuum dislocation structure,” *Acta Mater.*, 2017.
[40] A. Béré and A. Serra, “Atomic structures of twin boundaries in GaN,” *Phys. Rev. B*, vol. 68, no. 3, p. 33305, 2003.
[41] J. Rychlewski, “On Hooke’s law,” *J. Appl. Math. Mech.*, vol. 48, no. 3, pp. 303–314, 1984.
[42] Allan F. Bower, *Applied Mechanics of Solids (1st ed.)*. CRC Press, 2009.
[43] W. Voigt, “Lehrbuch der Kristallphysik (Teubner, Leipzig, 1928),” *There is no Corresp.*

Rec. this Ref., 1908.
[44] R. R. Reeber and K. Wang, "High temperature elastic constant prediction of some group III-nitrides," *Mater. Res. Soc. Internet J. Nitride Semicond. Res.*, vol. 6, 2001.
[45] D. Mašín and J. Rott, "Small strain stiffness anisotropy of natural sedimentary clays: review and a model," *Acta Geotech.*, vol. 9, no. 2, pp. 299–312, 2014.
[46] Z. Peng, X. Chen, Y. Fan, D. J. Srolovitz, and D. Lei, "Strain engineering of 2D semiconductors and graphene: from strain fields to band-structure tuning and photonic applications," *Light Sci. Appl.*, vol. 9, no. 1, p. 190, 2020.
[47] A. Dussaigne *et al.*, "Full InGaN red (625 nm) micro-LED (10 μm) demonstration on a relaxed pseudo-substrate," *Appl. Phys. Express*, vol. 14, no. 9, p. 92011, 2021.
[48] O.-H. Nam, T. S. Zheleva, M. D. Bremser, and R. F. Davis, "Lateral epitaxial overgrowth of GaN films on SiO2 areas via metalorganic vapor phase epitaxy," *J. Electron. Mater.*, vol. 27, no. 4, pp. 233–237, 1998.
[49] H. Ishikawa, K. Yamamoto, T. Egawa, T. Soga, T. Jimbo, and M. Umeno, "Thermal stability of GaN on (1 1 1) Si substrate," *J. Cryst. Growth*, vol. 189, pp. 178–182, 1998.
[50] M. Khoury, O. Tottereau, G. Feuillet, P. Vennéguès, and J. Zúñiga-Pérez, "Evolution and prevention of meltback etching: case study of semipolar GaN growth on patterned silicon substrates," *J. Appl. Phys.*, vol. 122, no. 10, 2017.
[51] S. A. Kukushkin and S. S. Sharofidinov, "A new method of growing AlN, GaN, and AlGaN bulk crystals using hybrid SiC/Si substrates," *Phys. Solid State*, vol. 61, no. 12, pp. 2342–2347, 2019.
[52] J. W. Yang *et al.*, "High quality GaN–InGaN heterostructures grown on (111) silicon substrates," *Appl. Phys. Lett.*, vol. 69, no. 23, pp. 3566–3568, 1996.
[53] T. Takeuchi, H. Amano, K. Hiramatsu, N. Sawaki, and I. Akasaki, "Growth of single crystalline GaN film on Si substrate using 3C-SiC as an intermediate layer," *J. Cryst. Growth*, vol. 115, no. 1–4, pp. 634–638, 1991.
[54] P. Kung, A. Saxler, X. Zhang, D. Walker, R. Lavado, and M. Razeghi, "Metalorganic chemical vapor deposition of monocrystalline GaN thin films on β-LiGaO2 substrates," *Appl. Phys. Lett.*, vol. 69, no. 14, pp. 2116–2118, 1996.
[55] Z. Zhang *et al.*, "The melt-back etching effect of the residual Ga in the reactor for GaN grown on (111) Si," *AIP Adv.*, vol. 12, no. 9, 2022.
[56] A. Krost and A. Dadgar, "GaN-based optoelectronics on silicon substrates," *Mater. Sci. Eng. B*, vol. 93, no. 1–3, pp. 77–84, 2002.
[57] A. Dadgar, "Sixteen years GaN on Si," *Phys. status solidi*, vol. 252, no. 5, pp. 1063–1068, 2015.
[58] A. Watanabe, T. Takeuchi, K. Hirosawa, H. Amano, K. Hiramatsu, and I. Akasaki, "The growth of single crystalline GaN on a Si substrate using AIN as an intermediate layer," *J. Cryst. Growth*, vol. 128, no. 1–4, pp. 391–396, 1993.
[59] H. P. D. Schenk, E. Frayssinet, A. Bavard, D. Rondi, Y. Cordier, and M. Kennard, "Growth of thick, continuous GaN layers on 4-in. Si substrates by metalorganic chemical vapor deposition," *J. Cryst. Growth*, vol. 314, no. 1, pp. 85–91, 2011.
[60] T. S. Zheleva, S. A. Smith, D. B. Thomson, K. J. Linthicum, P. Rajagopal, and R. F. Davis, "Pendeo-epitaxy: A new approach for lateral growth of gallium nitride films," *J. Electron. Mater.*, vol. 28, no. 4, pp. L5–L8, 1999.
[61] U. T. Schwarz *et al.*, "Microscopic mapping of strain relaxation in uncoalesced pendeoepitaxial GaN on SiC," *Phys. Rev. B*, vol. 67, no. 4, p. 45321, 2003.
[62] H. Amano *et al.*, "Stress and defect control in GaN using low temperature interlayers," *Jpn. J. Appl. Phys.*, vol. 37, no. 12B, p. L1540, 1998.
[63] N. N. Morgan, Y. Zhizhen, and X. Yabou, "Evaluation of GaN growth improvement techniques," *Mater. Sci. Eng. B*, vol. 90, no. 1–2, pp. 201–205, 2002.

[64] E. Feltin *et al.*, “Epitaxial lateral overgrowth of GaN on Si (111),” *J. Appl. Phys.*, vol. 93, no. 1, pp. 182–185, 2003.
[65] B. Beaumont, P. Vennéguès, and P. Gibart, “Epitaxial lateral overgrowth of GaN,” *Phys. status solidi*, vol. 227, no. 1, pp. 1–43, 2001.
[66] M. Hao *et al.*, “Configuration of dislocations in lateral overgrowth GaN films,” *J. Appl. Phys.*, vol. 85, no. 9, pp. 6497–6501, 1999.
[67] S. Gradečak, P. Stadelmann, V. Wagner, and M. Ilegems, “Bending of dislocations in GaN during epitaxial lateral overgrowth,” *Appl. Phys. Lett.*, vol. 85, no. 20, pp. 4648–4650, 2004.
[68] P. Vennéguès, B. Beaumont, V. Bousquet, M. Vaille, and P. Gibart, “Reduction mechanisms for defect densities in GaN using one-or two-step epitaxial lateral overgrowth methods,” *J. Appl. Phys.*, vol. 87, no. 9, pp. 4175–4181, 2000.
[69] J. Cao, D. Pavlidis, Y. Park, J. Singh, and A. Eisenbach, “Improved quality GaN by growth on compliant silicon-on-insulator substrates using metalorganic chemical vapor deposition,” *J. Appl. Phys.*, vol. 83, no. 7, pp. 3829–3834, 1998.
[70] F. Richter, “Upsetting and viscoelasticity of vitreous SiO2: experiments, interpretation and simulation,” Doctoral Dissertation, 2006.
[71] K. Baril, “De la nano hétéroépitaxie aux microLEDs à base de GaN,” Doctoral Dissertation, 2023.
[72] J. Tallal, K. Berton, M. Gordon, and D. Peyrade, “4 inch lift-off process by trilayer nanoimprint lithography,” *J. Vac. Sci. Technol. B Microelectron. Nanom. Struct. Process. Meas. Phenom.*, vol. 23, no. 6, pp. 2914–2919, 2005.
[73] M. Mrad *et al.*, “Controlled SOI nanopatterning for GaN pendeo-epitaxy,” *Micro Nano Eng.*, p. 100110, 2022.
[74] C. Liu *et al.*, “Variations in mechanisms of selective area growth of GaN on nano-patterned substrates by MOVPE,” *Phys. status solidi c*, vol. 7, no. 1, pp. 32–35, 2010.
[75] R. Mantach *et al.*, “Semipolar (10-11) GaN growth on silicon-on-insulator substrates: Defect reduction and meltback etching suppression,” *J. Appl. Phys.*, vol. 125, no. 3, 2019.
[76] R. Dagher *et al.*, “Pendeo-epitaxy of GaN on SOI nanopillars: Freestanding and relaxed GaN platelets on silicon with a reduced dislocation density,” *J. Cryst. Growth*, vol. 526, p. 125235, 2019.
[77] B. Leung, Q. Sun, C. D. Yerino, J. Han, and M. E. Coltrin, “Using the kinetic Wulff plot to design and control nonpolar and semipolar GaN heteroepitaxy,” *Semicond. Sci. Technol.*, vol. 27, no. 2, p. 24005, 2012.
[78] W. T. Sproull, *X-rays in Practice*. McGraw-Hill Book, 1946.
[79] H. C. Pollock, “The discovery of synchrotron radiation,” *Am. J. Phys*, vol. 51, no. 3, p. 278, 1983.
[80] J. P. Blewett, “Synchrotron radiation–early history,” *J. Synchrotron Radiat.*, vol. 5, no. 3, pp. 135–139, 1998.
[81] A. Liénard, *Champ électrique et magnétique produit par une charge électrique concentrée en un point et animée d’un mouvement quelconque*. G. Carré et C. Naud, 1898.
[82] M. H. J. Koch and J. Bordas, “X-ray diffraction and scattering on disordered systems using synchrotron radiation,” *Nucl. Instruments Methods Phys. Res.*, vol. 208, no. 1–3, pp. 461–469, 1983.
[83] G. Shenoy, “Basic characteristics of synchrotron radiation,” *Struct. Chem.*, vol. 14, no. 1, pp. 3–14, 2003.
[84] F. Masiello, “X-ray diffraction and imaging with a coherent beam: application to X-Ray optical elements and crystal exhibiting phase inhomogeneities.” Université de Grenoble;

Università di Torino (Turin, Italie), 2011.
[85] P. Raimondi, “ESRF-EBS: The extremely brilliant source project,” *Synchrotron Radiat. News*, vol. 29, no. 6, pp. 8–15, 2016.
[86] D. Chenevier and A. Joly, “ESRF: inside the extremely brilliant source upgrade,” *Synchrotron Radiat. News*, vol. 31, no. 1, pp. 32–35, 2018.
[87] M. Levantino *et al.*, “Structural dynamics probed by X-ray pulses from synchrotrons and XFELs,” *Comptes Rendus. Phys.*, vol. 22, no. S2, pp. 1–20, 2021.
[88] M. Cotte, A. Genty-Vincent, K. Janssens, and J. Susini, “Applications of synchrotron X-ray nano-probes in the field of cultural heritage,” *Comptes Rendus. Phys.*, vol. 19, no. 7, pp. 575–588, 2018.
[89] D. Lübbert, “Strain and lattice distortion in semiconductor structures: a synchrotron radiation study,” *Ph. D. Thesis*, 2000.
[90] P. Forman, “The discovery of the diffraction of X-rays by crystals; a critique of the myths,” *Arch. Hist. Exact Sci.*, vol. 6, no. 1, pp. 38–71, 1969.
[91] W. H. Bragg and W. L. Bragg, “The reflection of X-rays by crystals,” *Proc. R. Soc. London. Ser. A, Contain. Pap. a Math. Phys. Character*, vol. 88, no. 605, pp. 428–438, 1913.
[92] A. Authier, C. A. Taylor, U. internationale de cristallographie. C. on C. Teaching, and U. of W. (Cardiff), *The reciprocal lattice*. University College Cardiff Press Cardiff, 1981.
[93] P. P. Ewald, *Fifty Years of X-Ray Diffraction: Dedicated to the International Union of Crystallography on the Occasion of the Commemoration Meeting in Munich July 1962*. Springer Science & Business Media, 2012.
[94] H. Heinke, V. Kirchner, S. Einfeldt, and D. Hommel, “Analysis of the defect structure of epitaxial GaN,” *Phys. status solidi*, vol. 176, no. 1, pp. 391–395, 1999.
[95] G. A. Chahine, N. Blanc, S. Arnaud, F. De Geuser, R. Guinebretière, and N. Boudet, “Advanced non-destructive in situ characterization of metals with the French collaborating research group D2AM/BM02 beamline at the European synchrotron radiation facility,” *Metals (Basel).*, vol. 9, no. 3, p. 352, 2019.
[96] J. Garriga Ferrer *et al.*, “darfix–data analysis for dark-field X-ray microscopy,” *J. Synchrotron Radiat.*, vol. 30, no. 3, 2023.
[97] M. Kutsal *et al.*, “The ESRF dark-field x-ray microscope at ID06,” in *IOP Conference Series: Materials Science and Engineering*, 2019, vol. 580, no. 1, p. 12007.
[98] J. Demšar and B. Zupan, “Orange: Data mining fruitful and fun-a historical perspective,” *Informatica*, vol. 37, no. 1, 2013.
[99] S. J. Leake *et al.*, “The Nanodiffraction beamline ID01/ESRF: a microscope for imaging strain and structure,” *J. Synchrotron Radiat.*, vol. 26, no. 2, pp. 571–584, 2019.
[100] G. A. Chahine *et al.*, “Imaging of strain and lattice orientation by quick scanning X-ray microscopy combined with three-dimensional reciprocal space mapping,” *J. Appl. Crystallogr.*, vol. 47, no. 2, pp. 762–769, 2014.
[101] C. Ponchut, J. M. Rigal, J. Clément, E. Papillon, A. Homs, and S. Petitdemange, “MAXIPIX, a fast readout photon-counting X-ray area detector for synchrotron applications,” *J. Instrum.*, vol. 6, no. 01, p. C01069, 2011.
[102] E. Zatterin, “id01-sxdm.” Zenodo, 2024, doi: https://doi.org/10.5281/zenodo.10777666.
[103] U. Pietsch, V. Holy, and T. Baumbach, *High-resolution X-ray scattering: from thin films to lateral nanostructures*. Springer Science & Business Media, 2004.
[104] A. J. Wilkinson and P. B. Hirsch, “Electron diffraction based techniques in scanning electron microscopy of bulk materials,” *Micron*, vol. 28, no. 4, pp. 279–308, 1997.
[105] K. Yvell, “Experimental Studies of Deformation Structures in Stainless Steels Using EBSD.” KTH Royal Institute of Technology, 2018.

[106] S. Vespucci *et al.*, "Digital direct electron imaging of energy-filtered electron backscatter diffraction patterns," *Phys. Rev. B*, vol. 92, no. 20, p. 205301, 2015.
[107] G. C. Sneddon, P. W. Trimby, and J. M. Cairney, "Transmission Kikuchi diffraction in a scanning electron microscope: A review," *Mater. Sci. Eng. R Reports*, vol. 110, pp. 1–12, 2016.
[108] O. A. Berkhemer *et al.*, "A randomized trial of intraarterial treatment for acute ischemic stroke," *N. Engl. J. Med.*, vol. 372, no. 1, pp. 11–20, 2015.
[109] P. V. C. Hough, "Method and means for recognizing complex patterns." Google Patents, Dec. 18, 1962.
[110] A. J. Wilkinson and T. Ben Britton, "Strains, planes, and EBSD in materials science," *Mater. today*, vol. 15, no. 9, pp. 366–376, 2012.
[111] S. Villert, C. Maurice, C. Wyon, and R. Fortunier, "Accuracy assessment of elastic strain measurement by EBSD," *J. Microsc.*, vol. 233, no. 2, pp. 290–301, 2009.
[112] A. Nicolaÿ *et al.*, "Discrimination of dynamically and post-dynamically recrystallized grains based on EBSD data: application to Inconel 718," *J. Microsc.*, vol. 273, no. 2, pp. 135–147, 2019.
[113] V. Randle, "Electron backscatter diffraction: Strategies for reliable data acquisition and processing," *Mater. Charact.*, vol. 60, no. 9, pp. 913–922, 2009.
[114] F. Bachmann, R. Hielscher, and H. Schaeben, "Texture analysis with MTEX–free and open source software toolbox," *Solid state Phenom.*, vol. 160, pp. 63–68, 2010.
[115] W. Pantleon, "Resolving the geometrically necessary dislocation content by conventional electron backscattering diffraction," *Scr. Mater.*, vol. 58, no. 11, pp. 994–997, 2008.
[116] J. F. Nye, "Some geometrical relations in dislocated crystals," *Acta Metall.*, vol. 1, no. 2, pp. 153–162, 1953.
[117] E. Kröner, "Der fundamentale zusammenhang zwischen versetzungsdichte und spannungsfunktionen," *Zeitschrift für Phys.*, vol. 142, pp. 463–475, 1955.
[118] A. Seret, C. Moussa, M. Bernacki, J. Signorelli, and N. Bozzolo, "Estimation of geometrically necessary dislocation density from filtered EBSD data by a local linear adaptation of smoothing splines," *J. Appl. Crystallogr.*, vol. 52, no. 3, pp. 548–563, 2019.
[119] K. Akhtar, S. A. Khan, S. B. Khan, and A. M. Asiri, *Scanning electron microscopy: Principle and applications in nanomaterials characterization*. Springer, 2018.
[120] B. J. Inkson, "Scanning electron microscopy (SEM) and transmission electron microscopy (TEM) for materials characterization," in *Materials characterization using nondestructive evaluation (NDE) methods*, Elsevier, 2016, pp. 17–43.
[121] F. J. Humphreys, "Review grain and subgrain characterisation by electron backscatter diffraction," *J. Mater. Sci.*, vol. 36, pp. 3833–3854, 2001.
[122] T. Coenen and N. M. Haegel, "Cathodoluminescence for the 21st century: Learning more from light," *Appl. Phys. Rev.*, vol. 4, no. 3, 2017.
[123] A. L. Patterson, "The Scherrer formula for X-ray particle size determination," *Phys. Rev.*, vol. 56, no. 10, p. 978, 1939.
[124] N. Labchir *et al.*, "Development of Nanopillar Arrays Nanopatterning Without Lift-Off for Transferable GaN-Based μLEDs," *Adv. Mater. Technol.*, p. 2400166.
[125] V. Yon, "Advanced X-ray characterization for the development of low consumption power transistors." Université Grenoble Alpes [2020-....], 2021.
[126] C. Corley-Wiciak *et al.*, "Nanoscale mapping of the 3D strain tensor in a germanium quantum well hosting a functional spin qubit device," *ACS Appl. Mater. Interfaces*, vol. 15, no. 2, pp. 3119–3130, 2023.
[127] R. Omar, "Grain boundary energies in copper." University of Warwick, 1987.

[128] B. Winiarski, A. Gholinia, K. Mingard, M. Gee, G. Thompson, and P. J. Withers, "Correction of artefacts associated with large area EBSD," *Ultramicroscopy*, vol. 226, p. 113315, 2021.
[129] G. C. Roda, F. Santarelli, and G. C. Sarti, "A simplified viscoelastic model for the thermal growth of thin SiO2 films," *J. Electrochem. Soc.*, vol. 132, no. 8, p. 1909, 1985.
[130] J. Garriga Ferrer *et al.*, "darfix: Data analysis for dark-field X-ray microscopy," *arXiv e-prints*, p. arXiv-2205, 2022.
[131] M. Wehbe *et al.*, "Study of GaN coalescence by dark-field X-ray microscopy at the nanoscale," *J. Appl. Crystallogr.*, vol. 56, no. 3, 2023.
[132] M. Charles, Y. Baines, A. Bavard, and R. Bouveyron, "High growth rate GaN on 200 mm silicon by metal-organic vapor phase epitaxy for high electron mobility transistors," *J. Cryst. Growth*, vol. 483, pp. 89–93, 2018.
[133] Y. Lu *et al.*, "Influence of the growth temperature of the high-temperature AlN buffer on the properties of GaN grown on Si (1 1 1) substrate," *J. Cryst. Growth*, vol. 263, no. 1–4, pp. 4–11, 2004.
[134] B. D. Cullity, *Elements of X-ray Diffraction*. Addison-Wesley Publishing, 1956.
[135] A. Hospital, J. R. Goñi, M. Orozco, and J. L. Gelpí, "Molecular dynamics simulations: advances and applications," *Adv. Appl. Bioinforma. Chem.*, pp. 37–47, 2015.
[136] E. S. Kryachko and E. V Ludena, "Density functional theory: Foundations reviewed," *Phys. Rep.*, vol. 544, no. 2, pp. 123–239, 2014.
[137] R. J. LeVeque, "Finite difference methods for differential equations," *Draft version use AMath*, vol. 585, no. 6, p. 112, 1998.
[138] P. Duhamel and M. Vetterli, "Fast Fourier transforms: a tutorial review and a state of the art," *Signal Processing*, vol. 19, no. 4, pp. 259–299, 1990.
[139] D. H. Norrie and G. De Vries, *The finite element method: fundamentals and applications*. Academic Press, 2014.
[140] T. Belytschko, W. K. Liu, B. Moran, and K. Elkhodary, *Nonlinear finite elements for continua and structures*. John wiley & sons, 2014.
[141] M. Karimi, H. Yates, J. R. Ray, T. Kaplan, and M. Mostoller, "Elastic constants of silicon using Monte Carlo simulations," *Phys. Rev. B*, vol. 58, no. 10, p. 6019, 1998.
[142] L. Zhang, R. Barrett, P. Cloetens, C. Detlefs, and M. Sanchez del Rio, "Anisotropic elasticity of silicon and its application to the modelling of X-ray optics," *J. Synchrotron Radiat.*, vol. 21, no. 3, pp. 507–517, 2014.
[143] W. A. Brantley, "Calculated elastic constants for stress problems associated with semiconductor devices," *J. Appl. Phys.*, vol. 44, no. 1, pp. 534–535, 1973.
[144] M. Bargmann *et al.*, "Temperature-dependent coefficient of thermal expansion of silicon nitride films used in microelectromechanical systems," *MRS Online Proc. Libr.*, vol. 605, 1999.
[145] S. P. Timoshenko, "Theory of bending, torsion and buckling of thin-walled members of open cross section," *J. Franklin Inst.*, vol. 239, no. 5, pp. 343–361, 1945.
[146] I. Yonenaga, T. Shima, and M. H. F. Sluiter, "Nano-indentation hardness and elastic moduli of bulk single-crystal AlN," *Jpn. J. Appl. Phys.*, vol. 41, no. 7R, p. 4620, 2002.
[147] V. A. Yastrebov, "Mechanics and Physics of Contact Interfaces." Sorbonne Université, 2021.
[148] T. Kawamura *et al.*, "Absolute surface energies of oxygen-adsorbed GaN surfaces," *J. Cryst. Growth*, vol. 549, p. 125868, 2020.
[149] C. E. Dreyer, A. Janotti, and C. G. Van de Walle, "Absolute surface energies of polar and nonpolar planes of GaN," *Phys. Rev. B*, vol. 89, no. 8, p. 81305, 2014.
[150] S. J. Marshall, S. C. Bayne, R. Baier, A. P. Tomsia, and G. W. Marshall, "A review of adhesion science," *Dent. Mater.*, vol. 26, no. 2, pp. e11–e16, 2010.

Résumé

Introduction générale

Le marché des micro-displays à haute résolution a connu une croissance rapide, en particulier pour les µLEDs (micro- Light-Emitting Diode) ayant de meilleures propriétés d'émission que les LEDs traditionnelles. Les applications des µLEDs sont nombreuses : la réalité virtuelle, réalité augmentée, secteur automobile et montres connectées [13].

Le nitrure de Gallium (GaN) est un matériau très intéressant pour les µLEDs mais les applications mentionnées demandent des µLEDs à très haute résolution ce qui pose des défis dans les techniques de fabrication et de développement des µLEDs. L'efficacité d'émission des µLEDs diminuent avec la gravure des micro-pixels. En plus, la qualité de la couche initiale du GaN epitaxiée influence énormément l'efficacité des couches actives des µLEDs.

Cette thèse fait partie du projet PEGADIS (Pendeo-Epitaxy of GaN for µDisplays) qui propose une méthode novatrice pour la croissance du GaN sur substrat SOI (Silicon-On-Insulator). La méthode proposée permet de surmonter les importants problèmes technologiques qui se produisent durant la fabrication des µLEDs et font diminuer leur efficacité. L'approche proposée par PEGADIS consiste à faire la croissance d'une couche de GaN non-dopée au-dessus de nanopiliers GaN/AlN/Si(111)/SiO_2 gravés sur SOI. L'objectif attendu est que les piliers permettent une rotation durant la coalescence des ilots de GaN qui sont au-dessus afin que ceux-ci s'alignent cristallographiquement, évitant ainsi la formation de dislocations aux joints de coalescence et permettant d'obtenir une couche de GaN de très bonne qualité adaptée aux µLEDs à haute efficacité. Cette étape est ensuite suivie par la croissance des couches actives. Une fois la couche de GaN formée, la faible résistance mécanique des piliers après croissance devrait faciliter le transfert de µLED.

Le projet PEGADIS s'inscrit dans un projet collaboratif financé par l'agence Nationale de la Recherche (ANR) et implique quatre laboratoires: le LTM (Laboratoire des technologies de la microélectronique) pour la partie gravure des piliers [124], le CRHEA (Centre de recherche sur l'hétéro-épitaxie et ses applications) pour la partie croissance [35], le CEA-LETI (Laboratoire d'électronique et de technologie de l'information) pour la partie fabrication et caractérisations des µ-LEDs, et le CEMEF (Centre de mise en forme des matériaux) pour la partie simulation numérique.

Cette thèse a été menée au CEA et au CEMEF ; elle a comme objectif la nano-caractérisation des couches epitaxiées non dopéees de GaN au-dessus des nanopiliers afin de mieux comprendre les phénomènes qui ont lieu durant le processus de pendéo-épitaxie et pour mieux le contrôler et améliorer la qualité des couches GaN obtenues. Les caractérisations ont été principalement faites à l'European Synchrotron Radiation Facility (ESRF) en utilisant des techniques avancées de diffraction des rayons X. Des simulations éléments finis et des calculs

analytiques ont aussi été menées pour évaluer le comportement mécanique des systèmes nano-structurés et optimiser les différents paramètres des piliers.

Cette thèse est organisée en cinq chapitres, structurés comme suit :

Le premier chapitre fournit une description des propriétés physiques essentielles du GaN et du concept de µLEDS à base de GaN nécessaires pour une bonne compréhension du manuscrit. Il introduit les concepts des défauts obtenus dans les cristaux lors de l'épitaxie et les différents défis auxquels est confrontée la croissance du GaN sur un substrat de différent type de matériau. Les techniques de croissance les plus courantes permettant de réduire la densité des défauts sont ensuite présentées, suivies d'une description de la technique de croissance proposée par PEGADIS. Les objectifs de la thèse sont ensuite présentés ainsi que le processus de gravure des piliers et de la croissance du GaN.

Le second chapitre présente les différentes méthodes de caractérisation utilisée dans cette thèse (macroscopic X-ray diffraction, dark field X-ray microscopy (DFXM), scanning X-ray diffraction microscopy (SXDM), electron backscatter diffraction (EBSD), microscopie électronique à balayage (MEB) and cathodoluminescence microscopy (CL)). Il présente les avantages et les limitations de chaque technique suivis d'une explication détaillée du traitement de données qui a été fait après chaque expérience. Plusieurs expériences ont été réalisées au synchrotron, ce chapitre couvre donc également les principes fondamentaux de la diffraction des rayons X et des installations du synchrotron.

Le troisième chapitre présente les résultats des caractérisations expérimentales. Il fournit une évaluation de la rotation des piliers et de la qualité du GaN à différents niveaux de croissance et pour différents types d'échantillons.

Le quatrième chapitre discute les résultats obtenus à partir de simulations par éléments finis à l'aide du logiciel Abaqus. Il définit un modèle test, ses conditions aux limites et les propriétés mécaniques de chaque matériau. Suite à la validation du modèle, il introduit plusieurs approches pour modéliser la rotation mécanique des piliers afin de calculer l'énergie de rotation et trouver une explication des valeurs d'angle de rotation maximal trouvées à partir des données expérimentales. Les hypothèses et limitations du modèle sont également discutés dans ce chapitre.

Le cinquième et dernier chapitre discute les conclusions et perspectives de ce travail de thèse. Il propose un nouveau type d'échantillons optimisé qui avait montré des résultats de caractérisation primaire prometteurs. En se basant sur ces résultats, ce chapitre présente trois éléments clés qui peuvent être développés pour optimiser l'approche pendéo-épitaxie proposée et pour produire des couches de GaN à haute qualité adaptées aux µLEDs.

Chapitre 1 : Les notions de base du GaN

Les matériaux cristallins ont des atomes disposés périodiquement dans les trois dimensions et les matériaux III-Nitrures sont formés par des atomes de groupe-V (azote dans notre cas) et des atomes de groupe-III (Ga, Al, In). Le nitrure de gallium est un III-N semiconducteur à avec une structure wurtzite hexagonale.

Le GaN est très intéressant pour des applications d'optoélectroniques et surtout pour les µLEDs car il offre des avantages distincts tels qu'une faible consommation d'énergie et une efficacité très élevée. Il a un gap d'énergie directe et large (3.4 eV) ce qui veut dire qu'il permet l'émission efficace de la lumière lorsque les électrons de la bande de conduction se recombinent avec les trous de la bande de valence.

L'arrangement des atomes dans les III-N semiconducteurs n'est pas parfaite. Il y a plusieurs types de défauts dans ses matériaux et qui peuvent impacter énormément leur comportement : défauts points, défauts de ligne, défauts planaires. Les défauts de ligne sont connus sous le nom de dislocations. Ces dislocations peuvent survenir lors de l'épitaxie en raison de la différence de paramètre de maille à l'interface entre deux matériaux. On distingue entre dislocation coin qui vient accommoder un twist et des dislocations vis qui viennent accommoder un tilt.

La croissance du GaN n'est pas commune car le substrat GaN est très cher et n'est pas disponible à large diamètre donc le recours à l'hétéroépitaxie est souvent la solution. Par contre, la croissance du GaN sur un substrat de matériau diifférent (Si, SiC ou sapphire) mène à la génération des dislocations qui vont diminuer l'efficacité des GaN-µLEDS car les dislocations agissent comme des centres de non-recombinaisons entre les électrons et les trous. La croissance du GaN sur SiC donne les couches de meilleure qualité car la différence de paramètre de maille est plus faible mais les substrats SiC sont chers. Dans cette thèse on va travailler sur du GaN sur Si.

La différence de paramètre de maille entre un substrat et la couche déposée induit une déformation dans la couche épitaxiée ce qui va créer des dislocations et la différence des coefficients d'expansion thermiques induit aussi des déformations dans la couche épitaxiée durant le refroidissement ce qui peut entrainer des fissures. Pour éviter les fissures, il faut déposer une couche de AlN entre le GaN et le Si pour mettre le GaN sous compression et lui permettre de se relaxer durant le refroidissement sans se fissurer.

Un autre problème d'épitaxie du GaN sur différents substrats est le « meltback etching » qui se produit dans le cas de croissance du GaN sur Si ; c'est une réaction chimique qui se produit lorsque les atomes de Ga et les atomes de Si entrent en contact à une température de croissance élevée. Pour éviter ses réactions, il faut insérer une couche AlN entre les deux.

Pour réduire la densité de dislocation, plusieurs méthodes ont été développés comme « Epitaxial lateral overgrowth (ELOG) » et « pendeo-epitaxy (PE) ». Dans le projet PEGADIS, on propose

une approche nouvelle qui permet aussi de diminuer les densités de dislocations mais aussi d'obtenir des pixels de petite taille sans étape de gravure et qui permet de faire le transfert facilement.

L'approche de PEGADIS est basée sur la croissance des pyramides de GaN au-dessus des nanopiliers de GaN/AlN/Si(111)/SiO_2 sur SOI (figure 1.16). A haute température, durant la croissance, on s'attend à ce que l'excès d'énergie présent à la surface des hexagones du GaN (bord vertical des pyramides) permet aux piliers de faire une rotation et au GaN au-dessus de s'aligner pour faire se coalescer des couches de GaN de bonne qualité adaptées pour des µLEDs à haute efficacité.

L'objectif de cette thèse est d'étudier l'orientation cristalline du GaN avant, durant et après coalescence pour mieux comprendre le phénomène de coalescence, et de déterminer la qualité du GaN obtenu. En plus, il faut aborder le sujet des rotations des piliers et déterminer si vraiment les piliers tournent et pouvoir mesurer les valeurs de tilt/twist. Une étude sur l'impact des différents paramètres des piliers est aussi nécessaire pour proposer un modéle optimisé à fabriquer favorisant l'effet PEGADIS. Pour accomplir ces objectifs, des techniques de diffraction des rayons X à l'ESRF ont été utilisés dans cette thèse ainsi que du EBSD et du CL. En plus, des simulations éléments finis ont été menés en utilisant ABAQUS.

Le substrat SOI a été fait au CRHEA, le LTM a fait la partie gravure des piliers en utilisant la technique nanoimprint suivi par une étape de lift off. Ensuite, la croissance sur les piliers a été faite au CRHEA en 2 étapes (croissance des pyramides + croissance 2D).

Chapitre 2 : Les techniques de caractérisation

Pour pouvoir tester l'hypothèse de rotation des piliers et pour déterminer la qualité du GaN, on a besoin de techniques avancées de diffraction des rayons X qui possèdent un faisceau à haute intensité et haute résolution. Trois techniques différentes ont été utilisé à l'ESRF : macroscopic X-ray diffraction, dark field X-ray microscopy (DFXM), et scanning X-ray diffraction microscopy (SXDM).

Macroscopic X-ray diffraction

Cette technique est installée à la ligne de lumière BM02 à l'ESRF ; elle est équipée d'n faisceau de taille 30 x 30 µm² à une énergie allant de 6 à 45 keV. Dans cette thèse, une étude a été menée sur la ligne de lumière BM02 sur différents types d'échantillons et à une énergie de 9 keV avec un détecteur 2D ayant une taille de pixel de 130 x 130 µm². Les expériences faites sur cette ligne avaient comme objectifs de déterminer la qualité du GaN sur une patelette de 40 x 40 µm² et de mesurer la désorientation des piliers avant coalescence et après coalescence pour voir si une rotation a eu lieu durant la coalescence. On a fait des mesures autour des raies de Si et du

GaN symétriques et asymétriques. Les données ont été traitées avec un code python développés par les chercheurs de la ligne.

Dark field X-ray microscopy

Cette technique, initialement développée sur la ligne de lumière ID06 à l'ESRF (maintenant transférée sur la ligne ID03), est une technique d'imagerie capable de fournir une image dans l'espace réel de notre échantillon sur le détecteur. Le faisceau X a une énergie allant de 15keV à 35keV et sa taille minimale peut être de 30 x 30 µm².

Dans cette technique, le faisceau diffracté passe au travers d'une lentille divergente afin d'être magnifié pour être capté sur un détecteur ayant une taille de pixel de 50-70 µm et situé à grande distance de la lentille. La résolution spatiale sur l'image du faisceau diffracté est donnée par le ratio entre la taille de pixel et la distance lentille caméra. Dans notre cas elle est de 35 nm. Il n'a pas été possible de mesurer le Si dans les nanopiliers car l'intensité diffractée était trop faible. Les ilôts de GaN ont pu être mesurés. Le traitement des données a été fait sur darfix qui est une librairie python avec une interface utilisateur.

Scanning X-ray diffraction microscopy

Cette technique est installée sur la ligne de lumière ID01 à l'ESRF. Le faisceau est focalisé à une taille nanométrique (25nm) et permet de récupérer des informations sur chaque pilier. Elle n'est pas limitée pas à l'étude de la surface des structures comme la technique EBSD (expliquée plus tard), et permet de récupérer plutôt des informations sur le volume global sondé. Deux études ont été menées dans cette ligne, et ont permis de tirer la désorientation des piliers dans des ensembles de trois piliers et une carte d'orientation du GaN avant coalescence et au début de la coalescence. Le traitement de données a été fait avec une librairie python.

Electron backscatter diffraction

Le temps de faisceau pouvant être alloués à l'ESRF est très limités. Par conséquent, nous avons aussi utilisé des techniques de caractérisation supplémentaires telles que la technique de diffraction par rétrodiffusion des électrons, adaptée à la caractérisation de la structure cristalline des films minces à l'échelle microscopique.

La technique EBSD consiste à envoyer un faisceau d'électrons focalisé à la surface de l'échantillon. L'échantillon est généralement incliné de 70° vers le détecteur pour augmenter la qualité du signal obtenu. Le faisceau d'électrons balaie la surface de l'échantillon sur une grille discrète avec un pas fixe. Les électrons interagissent avec les noyaux atomiques du cristal et sont ensuite diffusés vers l'arrière hors de l'échantillon ; ils sont appelés électrons rétrodiffusés. Le détecteur capte les électrons qui vont former de bandes de Kikuchi ou chaque bande correspond à un plan diffractant différent ce qui va permettre d'obtenir la carte d'orientation du GaN. Le traitement de données a été fait en utilisant la librairie Mtex sur MATLAB.

Microscopie électronique à balayage

La microscopie électronique à balayage est un outil non destructif puissant utilisé pour observer de près les surfaces d'objets avec une résolution de l'ordre de 10 nanomètres. Il a été utilisé dans ce travail pour observer les échantillons avant croissance (uniquement les piliers) pour s'assurer que tous les piliers ont été obtenus avec succès et étaient de bonne qualité avant de procéder à la croissance et pour observer le GaN une fois coalescé avant les expériences de diffraction des rayons X et d'EBSD afin de s'assurer que la coalescence s'est bien passée.

Cathodoluminescence microscopy

CL est une technique puissante utilisée pour l'étude des propriétés optiques des matériaux. Elle est très utilisée pour détecter les dislocations dans les couches épitaxiales de GaN puisque ces dislocations agissent comme des centres de recombinaison non radiatifs empêchant l'émission de lumière depuis leurs positions pertinentes.

Chapitre 3 : Evaluation expérimentale de la rotation des piliers et de la qualité du GaN

Suite à la présentation de l'approche de croissance PEGADIS dans le chapitre 1 ainsi que les objectifs de cette thèse, différents échantillons de géométries différentes ont été caractérisés par les différentes techniques de caractérisation décrites dans le chapitre 2. Les résultats de ces mesures expérimentales sont présentés dans ce chapitre.

Pour plus de clarté, nous utiliserons la notion de « twist » pour définir une rotation autour de la longueur du pilier (autour d'un axe normal à la surface horizontale de l'échantillon), la notion de « tilt » pour définir une rotation sur un axe dans le plan de la surface de l'échantillon et la notion de « rotation » pour définir un twist + tilt.

Dans un premier temps, des mesures de twist et de tilt sont présentées afin de tester le principe de twist et de tilt des piliers sur lequel repose cette approche de croissance.

Deuxièmement, l'orientation cristalline du GaN avant la coalescence et pendant la coalescence est déterminée afin d'acquérir une compréhension physique plus approfondie des processus opérant au cours de notre approche de croissance proposée, suivi d'un calcul de la densité de dislocations géométriquement nécessaires.

Finalement, le tilt entre les piliers voisins est calculé et la qualité de la couche GaN après coalescence complète est déterminée. Les résultats obtenus sont discutés et validés par différentes techniques de caractérisation.

Dans ce chapitre, on a présenté la caractérisation par SXDM d'échantillons consitutés d'ensembles de trois piliers avec une ligne de GaN coalescé au-dessus. Les résultats ont permis

de confirmer l'hypothèse de PEGADIS autour de la rotation des piliers durant la coalescence menant à la réorientation du GaN au-dessus (figures 3.9(a) et (b)).

Ensuite, des échantillons avec du GaN au début de la coalescence ont été caractérisé par SXDM à l'ESRF pour comprendre ce qui se passe durant la coalescence à l'échelle nanométrique. Les mesures sur le GaN au début de coalescence et sur des piliers de GaN avant croissance ont montré que les piliers de GaN qui étaient désorientés initialement ont été transformés en des domaines de GaN bien définis et bien orientés. Un élargissement de pic a été observé au niveau de joints de grains déterminés dans la carte d'orientation cristalline du GaN au début de coalescence. Des observations CL ont montrés la présence de dislocations au niveau de joints de grains et par EBSD, on a estimé leur densité vers 2 x 10^{11} cm^{-2} (figure 3.17(c)).

De plus, d'après les mesures SXDM, nous avons constaté que tant que le tilt entre les piliers voisins ne dépasse pas 0.1°, les piliers voisins contribuent à former des domaines cristallins très bien orientés similaire en taille à ceux formés au début de la coalescence. Cette valeur limite de tilt est en accord avec le tilt mesuré directement par SXDM dans des ensembles de trois piliers.

L'objectif suivant a été d'étudier des lignes de GaN plus larges. Des lignes du GaN au-dessus d'ensembles de dix piliers ont été étudiés par DFXM et on a pu montrer que, avec notre approche on peut réaliser des lines de GaN très bien orienté [131] (mieux que le 2D GaN sur Si). Cependant, cela ne s'est produit que pour 3 lignes sur 5. Ensuite, nous avons étudié des plaquettes entièrement coalescées de 40 x 40 µm², où nous obtenons des régions d'orientation homogène allant jusqu'à 10×10 μm^2 (figure 3.27(a)).

Ces résultats sont prometteurs pour la fabrication d'îlots de GaN hautement orientés sur silicium, adaptés à une émission lumineuse très efficace, dans des dispositifs tels que des micro-écrans ou des micro-LED, même si des travaux supplémentaires restent à faire pour améliorer la reproductibilité de cette approche.

Les mesures à l'échelle macro sur BM02 ont mis en évidence de grandes largeurs de pics de GaN, ce qui implique que la coalescence se produit par formation de clusters d'orientations différentes, en accord avec les mesures de DFXM.

Nous avons également comparé l'orientation du Si dans les nanopiliers avant et après la coalescence pour confirmer l'auto-orientation des pyramides de GaN pendant la coalescence, entraînant une désorientation accrue des couches de silicium dans les piliers après la coalescence.

Pour compléter ce travail, des simulations éléments finis utilisant le logiciel Abaqus sont présentées au chapitre 4 afin de déterminer l'impact de chaque paramètre des piliers sur la rotation de piliers.

Chapitre 4 : Modélisation mécanique par éléments finis de la coalescence des piliers

Pour compléter ce travail, l'objectif de ce chapitre est (i) de fournir un regard mécanique sur les valeurs de tilt et twist acquises à partir des données expérimentales et (ii) de proposer une méthodologie d'optimisation des paramètres du système de manière à augmenter la possibilité de rotation.

Il n'est pas possible d'atteindre ces objectifs par des séries expériences rayons X sur diverses configurations géométriques (taille des piliers, distance entre piliers…) parce que l'accès au faisceau synchrotron est très limité et que la diffraction X conventionnelle de laboratoire manque de résolution (spatiale ou temporelle).

Par conséquent, nous avons utilisé des simulations pour obtenir les informations requises. Les simulations offrent un moyen efficace d'explorer le comportement de systèmes complexes dans diverses conditions.

Compte tenu du contexte de notre projet, les méthodes de simulation disponibles peuvent être globalement classées en deux familles principales : (i) les simulations discrètes telles que la dynamique moléculaire (MD) et la théorie fonctionnelle de la densité (DFT), et (ii) les simulations continues telles que la méthode des différences finies. (FDM), transformée de Fourier rapide (FFT) et méthode des éléments finis (FEM). Chaque type de simulation a ses caractéristiques et ses applications distinctes. Pour notre étude on a choisi la méthode des éléments finis car elle est valable à notre échelle (micrométrique), ne demande pas de fortes approximations et donne des résultats précises.

À l'aide d'Abaqus, nous avons établi un modèle de l'ensemble de nos empilements avec ses différents composants (substrat + GaN/AlN/Si/SiO2 pilliers + GaN). La FEM repose sur l'utilisation de la discrétisation du domaine de calcul composé de nœuds liés par les éléments du maillage. La génération de la discrétisation est appelée maillage. La FEM transforme le problème d'origine en un système d'équations où les degrés de liberté nodaux sont les inconnues. Dans notre cas, on résout un problème mécanique puisqu'on souhaite simuler la rotation mécanique des piliers. Une étude bibliographique a été faite pour trouver les propriétés mécaniques anisotropiques pour tous les matériaux à haute température de croissance mais sans considérer le SiO_2 comme viscoélastique par manque d'informations.

Dans ce chapitre, grâce aux simulations par éléments finis à l'aide du logiciel Abaqus nous avons pu (i) valider et expliquer la faisabilité des valeurs d'inclinaison trouvées à partir des données expérimentales et (ii) déterminer le paramètre de piliers optimal pour une rotation énergétiquement réalisable. En raison des différentes hypothèses que nous avons dû utiliser, les résultats obtenus sont considérés comme des conclusions qualitatives générales.

Suite à la validation des conditions aux limites appliquées, du type de contraintes, de la taille et du type des éléments, différentes approches ont été testées pour simuler la rotation des piliers.

Les résultats ont montré qu'un tilt et un twist de 0.04° autour d'un certain axe de rotation est faisable énergétiquement alors qu'un twist et un tilt de 0.1° et 0.2° n'était pas faisable d'un point de vue énergétique. Par contre, un tilt de 0.1° a bien été mesurée et donc peut être la rotation se fait autour d'un axe qui n'a pas été testé numériquement ou bien le SiO_2 viscoélastique joue un rôle facilitant la rotation (ce qui n'a pas été pris en compte dans les simulations). Les résultats numériques ont aussi montré que le pitch (distance entre les centres des piliers) et l'épaisseur du GaN ont le plus faible impact sur l'énergie de rotation des piliers.

Les résultats numériques ont permis le développement et la validation d'un modèle analytique simplifié qui ne prend en compte que la mécanique du nanopilier dans les cas de tilt et de twist. La formule analytique a permis de déterminer l'effet des différent paramètres (pitch, longueur, rayon, propriété élastique, angle de rotation, épaisseur du GaN) par une méthode simple et rapide. On a trouvé que le rayon est le paramètre le plus critique car l'énergie requise est proportionnelle à r^4.

Ce travail ouvre la porte à de futures études numériques : le modèle du pilier peut être affiné pour correspondre à la forme expérimentale, un test de fissuration du pilier sous certaines conditions peut être réalisé…

Par ailleurs, nous n'avons considéré dans cette approche que les efforts mécaniques, mais nous pensons qu'une meilleure représentation des phénomènes physiques ayant lieu lors de la coalescence pourrait être obtenue en utilisant une théorie de la rupture (ou du collage) qui utilise une approche énergétique afin de décrire la cinétique de la cohésion qui a lieu pendant la phase de coalescence.

Chapitre 5 : Nouvelles perspectives à partir de l'optimisation des piliers

D'après les résultats trouvés, on a pu tirer plusieurs conclusions :

- Il est possible d'aligner parfaitement les pyramides des GaN coalescés sur pilier Si/SiO_2.
- Une fois deux groupes coalescés, il n'est plus possible qu'ils rejoignent un troisième groupe, ce qui va entrainer la formation de dislocations au niveau des joints de grains.
- Des pyramides désorientées ou bien de multiples orientations des piliers de GaN rendrait une coalescence parfaite très difficile, voire impossible.

Ces conclusions ont permis d'imaginer de nouveau types d'échantillons avec des motifs optimisés et spécifiques pour favoriser la coalescence successive (pilier par pilier) et pour produire de large zones bien coalescés et bien orientés efficaces pour la fabrication des µLEDs à très bonne efficacité d'émission.

Deux types d'échantillons ont été regardés :

- Motifs d'étoile : étoiles à 10 branches, avec une distance croissante entre les piliers le long des bras.
- Motifs de spirale : pilier arrangé en spirale logarithmique, avec la distance entre les piliers qui augmente au fur et à mesure qu'ils s'éloignent du centre du motif.

Dans ce chapitre, nous avons montré et discuté les mesures SXDM et EBSD du GaN au sommet de piliers à motifs en étoile et en spirale.

Pour les étoiles, des mesures EBSD et SXDM ont été réalisées. Une coalescence successive a eu lieu résultant en des branches GaN homogènes. Cependant, l'orientation entre les branches n'était pas toujours identique, cela entraine la formation d'ilots de coalescence avec chacun leur orientation distincte (figure 5.2(b)).

Pour les spirales, des mesures EBSD du GaN ont été faites, et une orientation homogène du GaN a été observée pour les piliers de 100 nm de diamètre (figure 5.6(a). Pour les piliers de 200nm, l'orientation n'était pas homogène (peut être due à une croissance parasite ou bien au fait que pour un rayon plus grand, il est plus difficile de faire tourner les piliers).

De nombreuses améliorations sont donc encore nécessaires pour optimiser les piliers à motif en spirale, éliminer la croissance parasite et améliorer la réorientation du GaN, néanmoins les résultats sur les motifs spirales sont prometteurs.

On a alors identifié trois éléments clés pour améliorer l'effet PEGADIS :

- Coalescence de structure pilier par pilier pour éviter la formation de différents domaines au sein du même ilot.
- Eviter la désorientation au sein d'un même pilier.
- Faciliter la coalescence des piliers sans formation de défauts.

Cela signifie que les futurs travaux expérimentaux potentiels devraient principalement se concentrer sur les améliorations du motif en spirale et peuvent inclure :

- Future caractérisation des échantillons spirales à différents niveaux de croissance.
- Optimisation de la croissance du GaN
- Optimisation de la gravure des piliers
- Caractériser des échantillons avec du GaN sur Si au lieu du SOI pour identifier réellement l'effet du SiO_2 sur la rotation.

De futurs travaux numériques sont aussi réalisables pour améliorer notre modèle et fournir une configuration optimale à fabriquer et tester expérimentalement :

- Appliquer l'approche de rotation sur de grand nombre de piliers pour observer la distribution des contraintes dans les hexagones.
- Affiner la représentation géométrique du pilier pour qu'elle ressemble davantage à sa forme réelle.
- Considérer une meilleure représentation mécanique du phénomène de coalescence.

Conclusion générale

Les µLEDs basées sur GaN sont bien adaptés pour une large gamme d'application et leur développement est toujours en cours. L'approche PEGADIS propose une méthode originale pour la croissance des couches minces de GaN de très bonne qualité utilisable pour la production des µLEDs. L'approche est basée sur la croissance de pyramides de GaN au-dessus de nanopiliers. Ces derniers sont destinés à tourner durant la coalescence ce qui va permettre au GaN au-dessus de s'aligner et former une couche de GaN bien orientée. Avec l'architecture proposée, il n'y a pas besoin de graver les pixels pour diminuer leur taille et le processus de transfert est facilité. Cependant, la rotation des piliers n'avait pas été confirmé auparavant et la plage d'orientation cristalline du GaN permettant cette réorientation n'avait pas été déterminée. La compréhension du processus de coalescence est nécessaire pour déterminer la meilleure stratégie pour fabriquer des ilots de GaN compatible avec les µLEDs.

Dans cette thèse, on a pu confirmer l'hypothèse autour de la rotation des piliers durant la coalescence et le réalignement du GaN coalescé. En utilisant le SXDM, on a mesuré à l'échelle nanométrique une rotation des piliers de 0.1° après coalescence. A l'échelle macro, des meures par diffraction des rayons X ont montré que les nanopiliers de Si deviennent significativement désorientés après la coalescence par rapport à un échantillon de référence (avant la croissance).

Après cette confirmation de la flexion/torsion des piliers, il était nécessaire d'examiner l'évolution microstructurale durant la croissance et étudier le processus de coalescence à l'échelle nanométrique pour comprendre ce dernier. Pour réaliser une caractérisation structurale complète, de nouveaux échantillons ont été caractérisés à l'aide de trois techniques complémentaires : SXDM, EBSD, et CL. Les cartes d'orientation cristalline du GaN avant coalescence et au début de coalescence ont montré que les piliers de GaN initialement désorientés sont transformés en gros ilots de GaN bien définis et bien orientés en eux-mêmes (3.9 µm). La présence des dislocations au niveau des joints de grains a été confirmé par les observations CL et estimé par les mesures EBSD, fournissant une limite supérieure pour leur densité locale de ~10^{11} cm^{-2}. De plus, nous avons constaté que tant que l'inclinaison entre les piliers voisins ne dépasse pas 0.1°, les piliers voisins contribuent à former des domaines cristallins très bien orientés similaire en taille à ceux formés au début de la coalescence. Cette valeur limite de tilt est en accord avec le tilt mesuré directement par SXDM dans des ensembles de trois piliers. Cette étude a montré qu'une fois que deux groupes de piliers coalescent, il ne sera plus possible qu'ils rejoignent en se réorientant un autre groupe, aboutissant à la formation de dislocations aux joints de grains. Des échantillons constitués d'ensemble de dix piliers ont été mesurés, où la coalescence se produit pilier par pilier pour éviter la formation de différents domaines au sein d'un gros domaine.

Nous démontrons la réalisation de lignes de GaN bien orientées (densité de dislocation ~1.2 x 10^7 cm^{-2}), avec pratiquement aucune désorientation (meilleure que le GaN 2D) entre les piliers tout au long de la ligne grâce à notre approche de croissance. Une fois coalescés en vignette

avec un motif de pilier hexagonal, nous avons pu fabriquer des régions allant jusqu'à 10 x 10 μm^2 qui sont aussi très bien orientées. Cette étude en utilisant le DFXM a montré qu'il est possible d'aligner parfaitement les pyramides de GaN au-dessus des lignes de nanopiliers. Pour les structures plus larges avec un motif de piliers hexagonaux, un alignement parfait ne peut être obtenu que sur une petite partie de la structure.

En se basant sur les différentes caractérisations, des échantillons optimisés avec des motifs d'étoiles et de spirales ont été fabriqués. Les mesures SDXM et EBSD ont montré la réalisation des couches de GaN homogènes avec une coalescence successive et la possibilité d'obtenir des surfaces de GaN coalescées plus larges que celles obtenues avec les lignes de GaN. Ces résultats sont prometteurs pour la fabrication de petits îlots de GaN très bien orientés adaptés aux µLEDs.

Finalement, des simulations éléments finis ont été utilisées afin d'étudier le comportement mécanique du GaN au-dessus des nanopiliers. Cette étude est basée sur une forte hypothèse sur la mécanique et la cinétique du phénomène de coalescence. Le phénomène de coalescence n'est pas complétement compris et donc les résultats des simulations éléments finis peuvent être interpréter uniquement dans un contexte qualitatif. Différentes configurations géométriques ont été étudiées en faisant varier les paramètres des piliers (pitch, rayon, hauteur, module de Young) et l'épaisseur de l'hexagone GaN (le bord de la pyramide GaN) afin de réduire l'énergie demandé pour une rotation et d'augmenter l'angle de rotation maximale énergétiquement possible. Cette étude a démontré que l'énergie nécessaire pour induire l'alignement des hexagones de GaN est principalement concentré au niveau des piliers. Ces résultats numériques ont permis le développement d'un modèle analytique simplifié qui ne considère que la mécanique des piliers. En utilisant les simulations éléments finis et le modèle analytique, on a trouvé que l'angle de rotation le plus élevé possible sur le plan énergétique est proportionnel à la racine carrée du pitch et de l'épaisseur de la facette de GaN. Il est aussi proportionnel à la racine carrée de la longueur du pilier et inversement proportionnel au module de Young. Le paramètre ayant la plus grande influence sur l'angle de rotation (et l'énergie nécessaire) est le rayon du pilier parce que l'angle de rotation est inversement proportionnel à r^2, et l'énergie demandée est proportionnel à r^4. Donc, cette étude a démontré les paramètres clés pour favoriser la rotation des piliers.

Ces résultats permettent d'examiner des échantillons optimisés et améliorés qui pourraient montrer tout le potentiel de cette technique de pendéo-épitaxie pour produire des couches de GaN bien orientées utilisables pour la fabrication des µLEDs. On propose de déposer le GaN sur des piliers de SOI avec le plus petit rayon possible, le plus grand pitch possible (sans causer des croissances parasites) et avec une coalescence successive (pilier par pilier) ce qui fait des spirales un bon choix pour des améliorations continus.

Abstract

Gallium nitride (GaN) is a promising semiconductor for microLEDs, but heteroepitaxial growth of GaN generates dislocations that reduce their emission efficiency. To improve the quality of the GaN, we propose novel approach based on growing GaN pyramids on top of GaN/AlN/Si(111)/SiO_2 nano-pillars. The approach relies on the excess surface energy at each pyramid's interface to allow the pillars to tilt/twist, coalescing and aligning the GaN on top. The main objective of this work is to gain a physical understanding of the processes operating during coalescence, determine the GaN quality, investigate the tilt/twist of the pillars and propose an optimal pillars pattern. Therefore, different samples were studied by electron backscatter diffraction, cathodoluminescence and advanced X-ray diffraction techniques at the European Synchrotron Radiation Facility. The results demonstrated the rotation of pillars by 0.1°. We showed that achievement of homogenous GaN layers in lines of pillars (dislocation density ≈ 1.2 x 10^7 cm^{-2}). We were able to follow the behavior of the GaN at the early stage of coalescence, in fact, the initially misoriented GaN pillars, were found to coalesce into larger well-defined GaN domains with a unique orientation distribution within each domain and a tilt limit of 0.1° between neighboring pillars was found. Geometrically necessary dislocations were found at the grain boundaries of the GaN domains. To complete the work, finite element simulations and analytical calculations are performed to identify the optimal parameters that make the pillars rotation energetically feasible; the radius (r) of the pillar was identified as the parameter with the greatest impact as the energy required to rotate is proportional to r^4. These results allowed the realization of new optimized pillars pattern that showed promising results and will allow the fabrication of high quality GaN islands suitable for microLEDs.

Résumé

Le nitrure de gallium (GaN) est un semiconducteur prometteur pour les microLEDs, mais la croissance hétéroépitaxiale du GaN génère des dislocations qui réduisent leur efficacité d'émission. Afin d'améliorer la qualité du GaN épitaxiée, on propose une approche qui consiste à faire la croissance des pyramides de GaN au-dessus de nanopiliers de GaN/AlN/Si(111)/SiO_2. L'excès d'énergie à l'interface de chaque pyramide permettra aux piliers de subir une rotation durant la coalescence des pyramides de GaN qui sont au-dessus afin que ceux-ci se coalescent en s'alignant cristallographiquement. Les objectifs de cette thèse sont de comprendre les phénomènes qui ont lieu durant la coalescence, déterminer la qualité des couches GaN obtenues, étudier la rotation des piliers et proposer un modèle de piliers optimales. Ainsi, différents échantillons ont été caractérisés par la diffraction d'électrons rétrodiffusés, la cathodoluminescence et différentes techniques avancées de diffraction des rayons X réalisées à l'European Synchrotron Radiation Facility. Les résultats ont confirmé la rotation des piliers de 0.1° après coalescence ainsi que la réalisation des lignes de GaN très homogènes (densité de dislocations ≈1.2 x 10^7 cm^{-2}). Nous avons pu suivre le comportement du GaN au début de la coalescence ; les piliers de GaN initialement désorientés sont transformés en gros îlots de GaN bien définis et bien orientés en eux-mêmes. La présence des dislocations au niveau des joints de grains a été confirmé. De plus, nous avons constaté que tant que l'inclinaison entre les piliers voisins ne dépasse pas 0.1°, les piliers voisins contribuent à former des domaines cristallins similaire en taille à ceux formés au début de la coalescence. Des simulations éléments finis et des calculs analytiques ont permis d'optimiser les différents paramètres des piliers. Le rayon (r) du pilier a été identifié comme le paramètre ayant le plus grand impact sur l'énergie nécessaire à la rotation car cette dernière a été trouvé proportionnelle à r^4. Ces résultats ont permis la réalisation d'un nouveau modèle de piliers optimisé qui a montré des résultats prometteurs et permettra la fabrication d'îlots GaN de haute qualité adaptés aux microLEDs.